Intracontinental Deformation Caused by Gravitational Lithosphere Removal

by

Huilin Wang

A thesis submitted in partial fulfillment of the requirements for the degree of

Doctor of Philosophy

Geophysics

Department of Physics
University of Alberta

Abstract

Gravitational removal of the dense lower lithosphere is proposed to be a fundamental process in continental tectonics. This has been used to explain seismological observations of an abnormally thin lithosphere beneath some regions and evidence for detached lithospheric materials at 100-200 km depth. In addition, geochemical arguments suggest that a significant portion of the lower lithosphere may have been recycled into the deeper mantle. The removal process should significantly affect the overlying crust, causing transient uplift/subsidence, crustal contraction/extension and pulses of volcanism. As removal can occur in continental plate interiors, it may provide an explanation of areas of anomalous intraplate deformation that can not be readily linked to tectonic processes. This thesis uses two-dimensional thermal-mechanical numerical models to explore the surface deflection and magmatism induced by gravitational lithosphere removal. Removal is widely believed to be associated with surface subsidence and widespread asthenospheric magmatism. However, the models show that the surface expression depends strongly on the thermal and rheological structure of the lithosphere. If the crust is weak, the descending dense lithosphere induces lateral crustal flow, leading to crustal thickening and surface uplift. Crustal flow

in a mid-crustal channel will smooth the surface subsidence caused by the dense lithosphere; crustal flow in a lower-crust channel can cause the surface to invert to become a topographic high. Magmatism caused by lithosphere removal depends on the removal style and the initial thermal structure of lithosphere. During a Rayleigh-Taylor instability (drip), three types of magmas are found: (1) for a hot lithosphere (e.g., back arc), the foundering lithosphere can melt as it is descends and the asthenosphere can undergo decompression melting as it upwells to replace the removed lithosphere; (2) for a warm lithosphere (e.g., average Phanerozoic lithosphere), only asthenospheric melt is predicted; (3) for a cold and thick lithosphere (e.g., craton), no magmas are generated during removal. If removal occurs through delamination, the dense mantle lithosphere rapidly peels along the Moho and sinks into the deep mantle before it can melt. However, significant decompression melting of the asthenosphere may occur as it upwells to the base of crust. Delamination is associated with an asymmetric surface signature, where crustal deformation and magmatism migrate with the detachment hinge. In a Rayleigh-Taylor instability, the deformation and magmatism are symmetric. Observational data from a number of regions (e.g., southern Sierra Nevada in North America, Puna plateau in the central Andes, and Tibet in western China) are consistent with the numerical models, suggesting that intracontinental deformation and magmatism in these areas are related to lithosphere removal.

Preface

This thesis is an original work by Huilin Wang. Chapters 3 and 4 are slightly modified from publications listed in the References. Chapters 5 and 6 are prepared to submit. I am responsible for majority of the model design, interpretation and manuscript composition. Peter G DeCelles provided the evolution data of Arizaro basin and contributes to manuscript edits for Chapter 3; Yan Zhan gave suggestions for the lithosphere structure in Tibetan plateau for Chapter 4.

Acknowledgments

My thanks to my supervisor, Claire Currie, are endless … Through the years, she encouraged and supported me, and lead me to do solid science. This study came from her inspiration. She also kept encouraging me to develop my own ideas and stories. I am grateful to her for patiently editing my manuscripts, and teaching me how to improve writing skills.

My committee, Drs. Jeff Gu, Martyn Unsworth, Russell Pysklywec, Thomas Chacko and David Potter, gave many constructive suggestions and insightful thoughts for this thesis. Thank you.

Dr. Peter DeCelles is thanked for guiding me to use geological observations to understand this study. He is a great source of inspiration.

I owe great thanks to my family. My parents set no requirement for me but to be a decent person. My family teaches me to be strong in difficult times and do so with humor.

I also want to thank my friends. They greatly enriched my life and gave me many stories. I am inspired by their enthusiasm for work and life.

Contents

List of Figures

List of Tables

Chapter 1

Introduction

1.1 Lithospheric removal

This thesis addresses the origin of anomalous topographic deflection and magmatism that has been observed in the interior regions of many continental plates Such features can not be readily linked to tectonic processes. One hypothesis is that the anomalous activity is caused by gravitational instability and removal of the lower lithosphere. Lithosphere removal has been inferred from a range of geophysical and geochemical observations. In several areas, seismic tomography studies find small-scale (30-100 km wide) high-velocity anomalies at sublithospheric mantle depths (100-200 km). These have been observed beneath the southern Sierra Nevada and the Great Basin in North America, the western Mediterranean in southern Spain and northern Morocco, and the Puna plateau in the central Andes of South America (Schurr et al., 2006; West et al., 2009; Bianchi et al., 2012; Saleeby et al., 2012; Thurner et al., 2014). The high-velocity anomalies are commonly interpreted to be pieces of lithosphere that have detached from the upper plate. Further, recycling of the lower lithosphere is interpreted to be an important process in the geochemical evolution of continental crust. In order to explain the relationship between the composition of continental lithosphere and its parental basalt, it appears that a significant portion of the mafic lithospheric root needs to be recycled into the mantle (e.g., Plank, 2005).

Lithosphere removal is driven by the presence of high-density rocks in lower lithosphere (lithosphere mantle and/or lower crust). The high-density could originate from (1) thermal contraction because of the cooler temperature in lithosphere relative to the underlying mantle (e.g., Houseman and Molnar, 1997) and/or (2) accumulation of dense compositions (e.g., eclogite) from magmatic and metamorphic processes (e.g., Kay and Kay, 1993). As a result, the lithosphere may be 20-250 kg/m^3 denser than underlying mantle (e.g., Ducea and Saleeby, 1996; Djomani et al., 2001; Jull and Kelemen, 2001) and therefore, it is susceptible to gravitational removal.

Lithosphere removal is typically believed to occur in the deep crust or at mantle depths. However, many ancient and present removal events have been inferred based on their surface signature. This includes the formation of sedimentary basins or orogens (i.e., surface deflections), crustal contraction/extension, magmatic eruption, and increased surface heat flow (e.g., Kay and Kay, 1993; Pysklywect and Beaumont, 2004;

Elkins-Tanton, 2007, Göğüş and Pysklywec, 2008; Ducea et al., 2013; DeCelles et al., 2015). This surficial evidence provides a window to investigate the dynamics occurring in the deep lithosphere.

One surface expression of lithosphere removal is a localized (diameter of ~100's km; DeCelles et al., 2015) surface deflection. The presence of a high-density lithospheric root exerts a normal stress on overlying crust and depresses the surface (Figure 1.1, left panel). Several sedimentary basins in continental interiors have been proposed to be linked to a dense lithosphere root, such as the Williston basin in North America and the Arizaro basin in the central Andes with width of 100's km (Naimark and Ismail-Zadeh, 1995; DeCelles, et al., 2015). After the dense lithosphere root detaches, the surface will isostatically uplift. This pattern of surface deflection is widely accepted, but observations show that the lithosphere removal may exhibit more diverse topographic signatures. Some intracontinental orogens are proposed to be formed by foundering of dense lithosphere, including the Wallowa Mountains in North America, Southern Alps in New Zealand and Tien Shan in western China (Neil and Houseman, 1999; Hales et al., 2005). In other places, lithosphere removal may have little or no topographic expression. For example, lithospheric foundering has been inferred based on magmatism in the Tibetan Plateau in China (Turner et al., 1993), but no localized surface deflection has been observed (e.g., Horton, 2012).

Geodynamic studies show that foundering of dense lithosphere can induce lateral crustal flow, leading to crustal thickening (e.g., Neil and Houseman, 1999; Pysklywec and Shahnas, 2003; Göğüş and Pysklywec, 2008). Thickened crust has been found in many regions with inferred lithospheric foundering, such as the southern Sierra Nevada in North America and intracontinental orogens in Australia (Zandt et al., 2004; Pysklywec and Beaumont, 2004). Because of the greater density contrast between crust and mantle than that between lithosphere mantle and asthenosphere, the varying crustal thickness may significantly change the surface topography. Previous studies demonstrate that the thickened buoyant crust can balance the surface subsidence caused by the dense root and may even cause the surface to uplift as a topographic high (e.g., Neil and Houseman, 1999) (Figure 1.1, right panel).
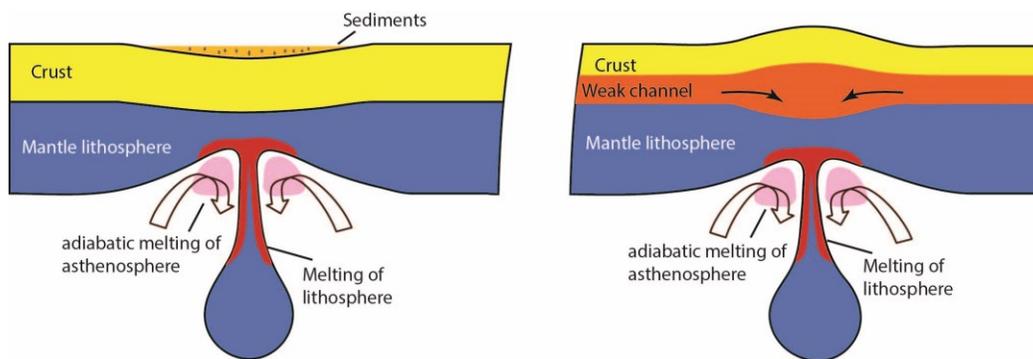
Figure 1.1. Schematic diagrams of lithosphere removal. The left figure shows the formation of a sedimentary basin by surface subsidence induced by lithospheric foundering. The right panel shows the generation of a topographic high above the sinking lithosphere. The descending lithosphere induces crustal flow in a weak channel, which thickens the crust and causes surface uplift. In both cases, lithosphere removal may be accompanied by crustal shortening, and melting of asthenosphere and lithosphere.

The surface deflection associated with lithospheric foundering depends on the combined effects of the dense lithospheric root and the induced crustal deformation. Thus, studying the surface deflection provides a way to investigate how the dynamics of the deep lithosphere interact with the overlying crust, and in turn modify the surface topography. In addition, because crustal deformation strongly depends on its rheology structure (Neil and Houseman, 1999) and interconnection with the underlying mantle (Pysklywec and Shahnas, 2003), the observed surface deflection can also be used to constrain the lithospheric rheology.

In addition to transient surface topography, magmatism is another important indicator of gravitational lithosphere removal (e.g., Kay and Kay, 1993). The loss of lithosphere causes a sudden overturn in composition and temperature at the lithosphere-asthenosphere boundary, which can trigger melting of lithosphere and asthenosphere. The classic view is that lithosphere removal induces magmatism through decompression melting of asthenosphere as it upwells to replace the removed lithosphere (Figure 1.1). Asthenospheric melts have been found in regions such as the southern Sierra Nevada

and western Canadian Cordillera in North America, and Puna Plateau in the central Andes (e.g., Kay and Kay, 1993; Farmer et al., 2002; Manthei et al., 2010). But to link such melts with lithosphere removal, additional information is needed, because decompression melting of asthenosphere can also be caused by lithosphere extension (Ducea, 2011). Recent studies show the magmatism caused by lithosphere removal may be characterized by temporal change in the geochemistry of the magmas (Ducea et al., 2013; Murray et al., 2015). The sinking lithosphere may undergo conductive heating and melting as it descends into the hot mantle; this will be followed by melting of asthenosphere as it upwells to replace the removed lithosphere (Elkins-Tanton, 2005 and 2007; Ducea et al., 2013). In addition, magmas sourced from lithosphere should have an increasing melting temperature with time, reflecting gradual heating; asthenospheric melts will show a decreasing melting temperature with time as the asthenosphere migrates upward along the adiabatic gradient (Ducea et al., 2013). These composition and temperature shifts has been observed in the young (5 Ma to present) magmas in the Puna plateau of South America and have been interpreted to reflect recent small-scale lithosphere removal (Ducea, 2013; Murray et al., 2015).

Magmatism induced by lithosphere removal has been identified in a number of places, such as the North China Craton, the Tibetan Plateau in China, and the central Andes of South America (Turner et al., 1993; Manley et al., 2000; Gao et al., 2008; Ducea et al., 2013). There are also regions in cratonic interiors where lithospheric removal is inferred but there is no associated magmatism (Elkins-Tanton, 2005). The diverse magmatic expressions of removal appear to reflect differences in the scale of removal and the initial lithosphere thermal structure. However, only a few geodynamic studies have investigated magmatism caused by lithosphere removal (e.g., Elkins-Tanton, 2005 and 2007; Gorczyk and Vogt, 2013).

This thesis investigates the surface expressions of lithosphere removal in continental interiors. The relationship between lithosphere removal (input) and the observable output parameters (i.e., surface deflection, crustal deformation and magmatism) are examined for different thermal and rheological settings, in order to understand the fundamental physical mechanisms. My research initially looked at local-scale removal processes in the central Andean orogen, but it has expanded to consider

lithosphere removal for continental plates in general.

1.2 An example of lithospheric removal – the central Andes

A global compilation of places with inferred lithosphere removal is shown in Figure 1.2. This is compiled from published papers that infer removal based on tomography, surface deformation, magmatism, xenolith and gravity data. In this study, we focus on the lithosphere removal process in the central Andes (Altiplano-Puna plateau).
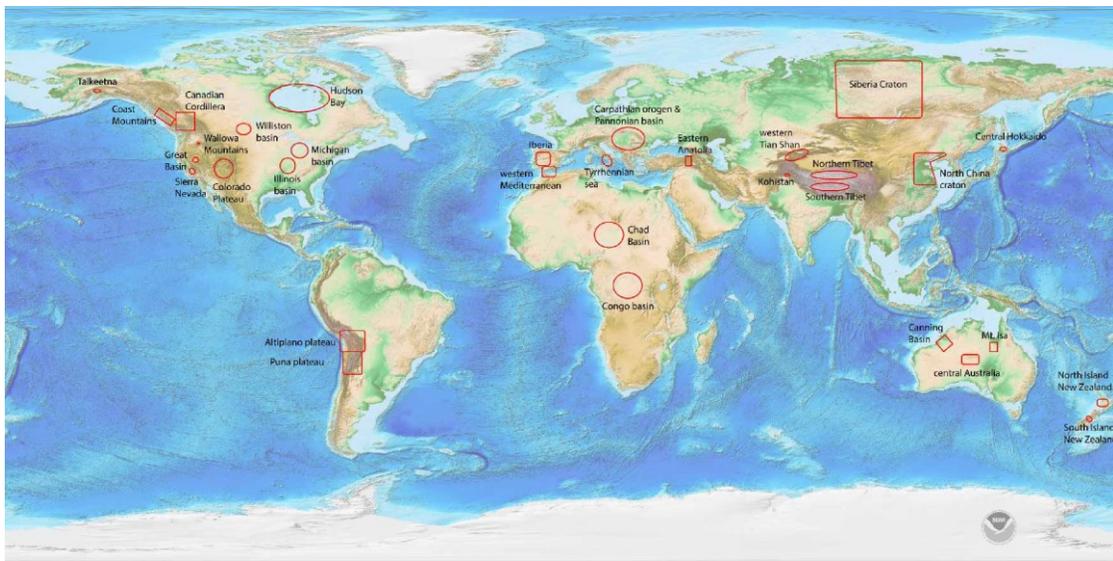
Figure 1.2. Global distribution of lithosphere removal events (e.g., Heidlauf et al., 1986; Middleton, 1989; Turner et al., 1993 & 1996; Naimark and Ismail-Zadeh, 1995; Sandiford and Hand, 1998 ; Tsumura et al., 1999; Elkins Tanton and Hager, 2000; Sobel and Arnaud, 2000; Stern et al., 2000; Houseman and Molnar, 2001; Gao et al., 2004; Pysklywec and Beaumont, 2004; Chung et al., 2005; Hales et al., 2005; Gok et al., 2007; Gemmer and Housman, 2007; Dowey and Gurnis, 2009; West et al., 2009; van Wijk et al., 2010; Calkins et al., 2010; Gutlerrea-Alonso et al., 2011; Manthei et al., 2010; Saleeby et al., 2012; Gorczyk et al., 2012; Darold and Humphreys, 2013; Jagoutz and Behn, 2013; Stern et al., 2013; Thurner et al., 2014; Bao et al., 2014; DeCelles et al., 2015; Schoenbohm and Carrapa, 2015).

The central Andes of western South America is the second largest active orogen

on Earth, and it is the only plateau along the 60,000 km length of modern subduction margins. In contrast to orogens formed through continental collision, such as the Himalayas, the central Andes developed in association with subduction of Nazca Plate. At present, the central Andes has an average elevation of ~4 km and lateral extent of ~1800 km from north to south and 300-400 km from west to east (Figure 1.3). The low relief Altiplano plateau (~3.7 km elevation) is located in the north of the central Andes and the high relief Puna plateau (~4.2 km elevation) is in the south.
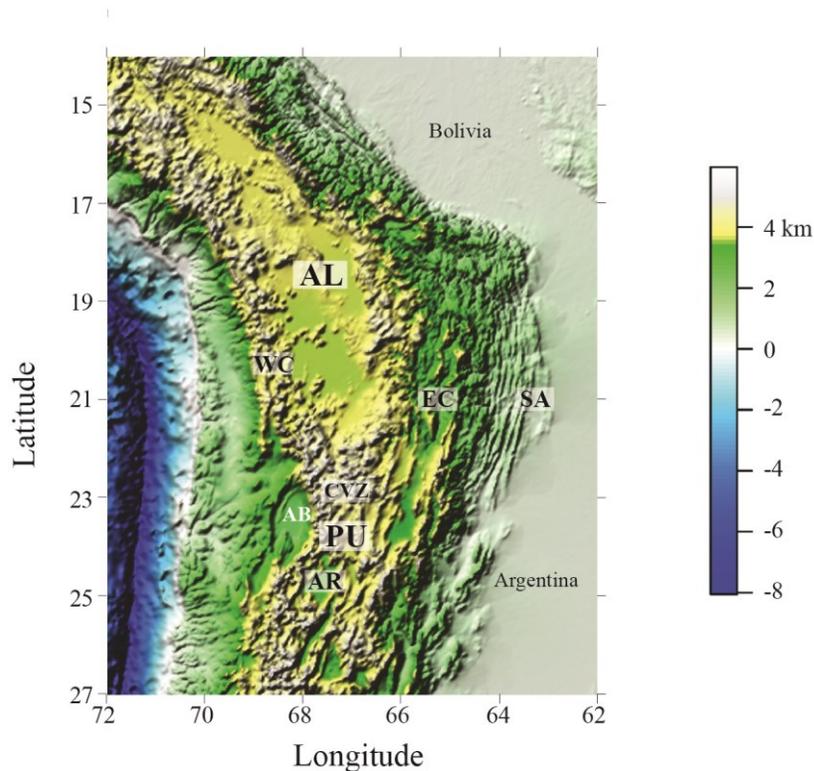
Figure 1.3. Surface topography in the central Andes. AL=Altiplano, PU=Puna, WC=Western Cordillera, EC=Eastern Cordillera, SA=Subandes, CVZ=Central Volcanic Zone, AR=Arizaro basin, AB=Atacama basin.

In the central Andes, the average shortening rate has ~1 cm/yr over the last 45 Ma (Oncken et al., 2006). The accumulated shortening in the last 30 Ma is at least 275 km in the Altiplano plateau and 120 km in the Puna plateau. Shortening has produced a

thick crust throughout the central Andes. The current crustal thickness varies from 65-80 km in the Altiplano Plateau and 50-65 km in the Puna Plateau (Beck et al., 1996; Beck and Zandt, 2002; Yuan et al., 2002).

The central Andes crust has nearly doubled in thickness during shortening. According to conservation of mass, the thickness of mantle lithosphere should have doubled as well. However, it is inferred that the mantle lithosphere for much of the plateau is anomalously thin at present-day, which does not support a simple linear relationship between the shortening rate and the thickness of the lithosphere. In the northern central Andes, seismic tomography studies (Myers et al. 1998; Heit et al., 2008) show low velocities and high attenuation in the shallow mantle beneath the Altiplano plateau and at the Eastern Cordillera boundary. Heit et al. (2008) point out that the lithosphere-asthenosphere boundary is only at ~100 km depth at the eastern part of Eastern Cordillera boundary, which is ~30 km shallower than the Altiplano plateau and ~70 km shallower than the Subandes. Higher seismic velocities are found in the shallow mantle below the central part of the Altiplano plateau (Myers et al. 1998; Heit et al., 2008), suggesting thicker lithosphere in this area. For the Puna plateau, low velocities and high attenuation are observed throughout the crust and shallow mantle (Schurr et al., 2006; Bianchi et al., 2012). The mantle lithosphere is interpreted to be completely removed under most of the Puna, which may explain why this region sits at higher elevation than the Altiplano, despite having a thinner crust. Further, seismic topography images show a high-velocity block (dimensions 30-100 km) sitting on the top of subducting oceanic slab at a depth of ~150 km under the Puna (Schurr et al., 2006). This is interpreted to be a piece of detached upper plate lithosphere. At present, the most of mantle lithosphere in Puna probably has been removed (Schurr et al., 2006). Note that seismic images provide a present-day snapshot of subsurface structure but do not constrain the timing of lithosphere removal.

For the crust of the central Andes, Beck and Zandt (2002) and Yuan et al. (2002) both conclude that seismic velocities are consistent with a felsic to intermediate bulk composition and that there appears to be a lack of mafic lower crust across the whole plateau. The thick crust reaches the critical depth at which mafic crust will be in the eclogite stability field. Eclogitized mafic crust is difficult to distinguish from mantle

lithosphere because it has a similar seismic velocity (Beck and Zandt, 2002). Therefore, it could be that either lower crust is intact but is eclogitized, or both lower crust and mantle lithosphere have been removed below much of the central Andes. Removal of lower crust and mantle lithosphere below much of the plateau is supported by seismic tomography images, as discussed above. Eclogitized lower crust can have a high density and would provide a driving force to initiate the lithosphere removal process (Beck and Zandt, 2002; Kay and Coira, 2009; Krystopowicz and Currie, 2013).

At the surface, the high plateau in the central Andes is not as smooth as in Tibet; instead, the plateau is characterized by numerous sedimentary basins that sit at relatively low elevation (Horton, 2012) (Figure 1.3). These basins tend to be fairly localized (diameter of ~100 km) and appear to be transient, with a sedimentation history of 10-20 Myr (DeCelles et al., 2015). Many of these basins have also experienced subsidence and crustal contraction, followed by surface uplift and crustal extension (Carrapa et al., 2011; Schoenbohm and Carrapa, 2014; DeCelles, et al., 2015). The formation of these basins cannot be directly linked with regional orogenic deformation. DeCelles et al. (2015) propose that these transient basins are caused by formation and removal of dense lower lithosphere. However, prior to this thesis, this hypothesis had not been tested by geodynamic studies. In particular, the magnitude and depth of removed lithosphere required to generate these basins are not well-known.

Mafic magmatism also supports lithospheric thinning in the central Andes (Kay and Kay, 1993; Hoke and Lamb, 2007; Kay and Coira, 2009). The magmatic history in the central Andes dates back to the Jurassic but the most voluminous magmas were erupted across the whole plateau in the last 30 Ma (Trumbull et al., 2006; Kay and Coira, 2009). Volcanism spread from the Western Cordillera (the present-day volcanic arc) to much of the plateau between 30 Ma and 10 Ma, which is commensurate with the migration of deformation. In the last 10 Ma, volcanism has shifted back to the Western Cordillera, while orogenic deformation propagated eastward to the foreland area (Trumbull et al., 2006). In the Altiplano region, Garzione et al. (2006) found a temporal relation between the paleoelevation and magmatism, and they suggest that there has been more than 1.5 km of uplift in last 10 Ma. This corresponds to a time of mafic and ignimbritic (felsic) magmatism. They propose that a large piece of lithosphere was

removed beneath the Eastern Cordillera, leading to heating, magmatism and abrupt surface uplift between ~10 and 6 Ma. In the Puna plateau, Ducea et al. (2013) suggest that the young (5 Ma to present) magmas were sourced from lithospheric pyroxenites in the first 1-2 Myr of magmatism, and then the magma source changed to asthenospheric peridotites. The geochemistry shift may indicate recent small-scale lithosphere removal in this region (Ducea et al., 2013; Murray et al., 2015).

The central Andes is a classic region for studying lithosphere removal process (e.g., Kay and Kay, 1993; Ducea, 2013; DeCelles et al., 2015). In this thesis, I examine whether the formation of transient sedimentary basins in the central Andes may be related to lithosphere removal. I also investigate the crustal deformation and magmatism accompanied by loss of lithosphere and compare the results of numerical models with observations from the central Andes and elsewhere.

1.3 Thesis objectives

In this thesis, numerical models are used to study the continental deformation caused by gravitational lithosphere removal. This is motivated by the many geological, geophysical and geochemical observations suggesting that a large portion of lower continental lithosphere is "missing", which indicate that it has been recycled into deeper mantle. The objectives are:

(a) to investigate the formation mechanism of localized, transient sedimentary basins in the central Andean plateau;

(b) to study the crustal deformation and surface deflection caused by lithosphere removal for diverse rheological and thermal structures;

(c) to explore the magmatic expression of removal for a range of lithosphere thermal-mechanical structures.

1.4 Thesis organization

This thesis is organized as follows:

- Chapter 2 reviews the numerical modeling method, governing equations, and the material rheology and density properties used in the computational code (SOPALE).

- Chapter 3 investigates the origin of hinterland basins in the central Andes.

Numerical models are used to explore the hypothesis that these hinterland basins are formed by lithosphere removal.

- Chapters 4 and 5 focus on the crustal deformation and topographic deflection induced by lithosphere removal. First, the relation between surface deflection and the lithosphere thickness/thermal structure is presented (Chapter 4). Then, the crustal deformation style, magnitude of crustal thickening and resulting surface deflection are investigated in detailed (Chapter 5).

- Chapter 6 tests the magmatism associated with lithosphere recycling for a range of lithosphere structures that correspond to different tectonic regions (e.g., backarc and craton). This chapter assesses how the magmatic source rocks, volume of melt and the pressure-temperature evolution of magmas are affected by variations in the initial lithosphere thermal structure and style of removal.

- Chapter 7 presents the main conclusions of this thesis and provides suggestions for future research.

Chapter 2

Numerical model methodology

The numerical modeling code used in this thesis is SOPALE, which was developed at Dalhousie University (Fullsack, 1995). The code has been widely applied to studies of lithosphere dynamics (e.g., Pysklywec and Beaumont, 2004; Beaumont et al., 2006; Göğüş and Pysklywec, 2008; Warren et al., 2008; Currie and Beaumont, 2011). The models are two-dimensional (2D) vertical cross-sections subjected to plane strain. In order to study continental plate evolution, all the models are at a regional, upper mantle scale.

In this chapter, the details of the numerical modeling method are presented. In the next chapters, the numerical modeling code will be used address each of the thesis objectives. The models vary between each study and therefore the specific model geometry, parameters and boundary conditions will be given in the individual chapters.

2.1 Governing formulae

The modeling code uses the finite element method to solve for the coupled thermal-mechanical evolution of the lithosphere-upper mantle system. Models evolve self-consistently according to the assumed thermal and mechanical boundary conditions and the properties of the materials within the model domain.

In the SOPALE modeling code, the Arbitrary Lagrangian-Eulerian (ALE) numerical technique (Fullsack, 1995) is used to solve for the evolution of the geodynamic system, based on conservation of momentum, mass and energy. In the ALE technique, all governing equations are solved on an Eulerian mesh, which is fixed in space except that it can stretch vertically to conform to the top surface of the models (the ground surface). The temperature, velocity and pressure fields are calculated on the Eulerian mesh. These are then interpolated onto a Lagrangian mesh, which consists of tracer particles. In each time step, the particles are advected with the model velocity field and carry information about the material properties (e.g., rheology, density, temperature, strain) which can be discontinuous at the boundaries between different

rock types. At the end of every time step, the new distribution of rock material properties is used to update the properties of the Eulerian mesh (Fullsack, 1995). As a result, the SOPALE code is able to model large deformation of materials. The other key advantage of the SOPALE code is that the upper boundary of the models is a free surface (i.e., no stress), and thus topography can develop self-consistently during model evolution.

Conservation of Momentum. This is the Stokes equation of creeping flow for a continuous medium under the assumptions that the material is incompressible and that inertial forces are negligible compared to viscous resistance and gravitational forces,

$$-\frac{\partial P}{\partial x_j} + \eta_{eff}\frac{\partial}{\partial x_i}\left(\frac{\partial v_i}{\partial x_j} + \frac{\partial v_j}{\partial x_i}\right) + \rho g_j = 0 \quad i,j = 1,2 \tag{2.1}$$

where P is mean stress, η_{eff} is effective viscosity, $x_i,$ x_j are spatial coordinates and v_i, v_j are the two components of velocity (i=1, 2), ρ is density, and g is gravitational acceleration.

The relation between stress (σ_{ij}), mean stress (P) and deviatoric stress (σ'_{ij}) is

$$\sigma_{ij} = -P\delta_{ij} + \sigma'_{ij} \tag{2.2}$$

δ_{ij} is the Kronecker delta (1 when i=j and 0 otherwise). The deviatoric stress (σ'_{ij}) can be expressed by the effective viscosity η_{eff} and strain rate $\dot{\varepsilon}_{ij}$

$$\sigma'_{ij} = 2\eta_{eff}\dot{\varepsilon}_{ij} \tag{2.3}$$

The strain rate tensor is

$$\dot{\varepsilon}_{ij} = \frac{1}{2}\left(\frac{\partial v_i}{\partial x_j} + \frac{\partial v_j}{\partial x_i}\right) \tag{2.4}$$

Conservation of Mass for an incompressible material follows the equation

$$\frac{\partial v_i}{\partial x_i} = 0 \tag{2.5}$$

This condition is modified when there is a metamorphic phase change which

involves a change in material density. During the time step in which the metamorphic phase change occurs, the incompressibility condition is relaxed and Eulerian elements that experience densification are compressed (Warren et al., 2008).

Conservation of Energy (heat equation). The thermal field is modeled by accounting for temperature changes due to advective and conductive heat transport and several types of internal heat generation and consumption:

$$\rho C_P \frac{DT_k}{Dt} = -\frac{\partial q_i}{\partial x_i} + H_r + H_s + H_a + H_{other} \tag{2.6}$$

where C_p is specific heat, T_k is absolute temperature. The operator $\frac{D}{Dt}$ is equal to $\frac{D}{Dt} = \frac{\partial}{\partial t} + v_i \frac{\partial}{\partial x_i}$. q_i is conductive heat flux in direction i, with $q_i = k\frac{\partial T_k}{\partial x_i}$. H_r is volumetric radioactive heat production. Shear heat production is $H_s = \sigma'_{ij}\dot{\varepsilon}_{ij}$. The adiabatic production/consumption is $H_a = T_k\alpha\frac{DP}{Dt} = v_2\alpha gT_k\rho$, where v_2 is the vertical velocity and α is the volumetric thermal expansion coefficient. H_{other} is the other heat source (e.g., phase change heating).

The thermal and mechanical fields are coupled in several ways: (1) the advection of material (redistribution of the thermal properties); (2) the strain heating term; (3) the rheology and density of the materials depend on temperature.

2.2 Material properties

Frictional Plastic Deformation. All materials in the numerical models have a viscous-plastic rheology. Frictional-plastic deformation occurs when the stress is above the frictional-plastic yield stress based on the Drucker-Prager yield criterion

$$J'_2 = P\sin\phi_{eff} + c_0 cos\phi_{eff} \tag{2.7}$$

with

$$P\sin\phi_{eff} = P(1-\lambda)\sin\phi \tag{2.8}$$

where J_2' is the square root of second invariant of the deviatoric stress, $J_2'^2 = \frac{1}{2}\sigma_{ij}'\sigma_{ij}'$. ϕ_{eff} is the effective internal angle of friction. c_0 is the cohesion. Equation (2.8) shows how ϕ_{eff} depends on the dry internal angle of friction ϕ, the Hubbert-Rubey fluid pressure ratio λ, and pressure P. The frictional-plastic deformation is modeled as viscous creep by defining a viscosity that places the state of stress on yield (Fullsack 1995; Willett, 1999).

Materials can undergo softening or hardening as they are strained, where the cohesion c_0 and/or effective angle of friction ϕ_{eff} can vary with strain owing to pore fluid pressure variations, mineral reactions and infiltration of fluids (Huismans and Beaumont, 2003; Babeyko et al., 2006; Warren et al., 2008).

Viscous Deformation. When the stress is less than the frictional-plastic yield stress, the flow is viscous. The power law creep effective viscosity is

$$\eta_{eff}^{V} = f(B^*)(\dot{I}_2')^{\frac{1-n}{n}}\exp(\frac{Q+PV^*}{nRT_K}) \tag{2.9}$$

η_{eff}^{V} is the effective viscosity. $\dot{I}_2'^2$ is the square root of the second invariant of the strain rate tensor, $\dot{I}_2'^2 = \frac{1}{2}\dot{\varepsilon}_{ij}\dot{\varepsilon}_{ij}$. R is the gas constant (8.3145 J mol^{-1} K^{-1}). The pre-exponential factor (B^*), stress exponent (n) and activation energy (Q) are rheological parameters derived from laboratory data. $B^* = (2^{(1-n)/n}3^{-(n+1)/2n})A^{-1/n}$; the term in brackets converts the pre-exponential viscosity parameter from uniaxial laboratory experiments (A) to the tensor invariant state of stress of the numerical models. The factor f is a scaling factor to scale the model viscosity linearly up or down relative to laboratory flow laws. This approach accounts for uncertainties in laboratory-derived parameters, which are based on deformation of individual rock/mineral samples. In addition, there may be differences between the laboratory results and rock deformation under natural conditions owing to variations in composition, water fugacity, the presence of melt or other fluids, and deformation mechanisms and strain rates. In order to simplify the

construction and interpretation of the models, we follow the approach of Beaumont et al. (2006) and choose a base set of rheological parameters from a few reliable laboratory data sets. We then scale the flow laws up/down by the scaling factor *f* to approximate the effects of a moderate change in composition or the effects of water fugacity. This is also a way to test the effects of reasonable changes in strength, instead of changing all the parameters in the flow law individually. The advantage of using f is we can easily scaling up/down the viscosity of a layer without affecting its dependence on temperature and pressure, and the ration of strength contrast within the layer.

Density. All materials have a temperature-dependent density, given by

$$\rho(T) = \rho_0[1 - \alpha(T - T_0)] \tag{2.10}$$

where ρ_0 is the reference density at temperature T_0 and α is the volumetric thermal expansion coefficient.

Chapter 3

Hinterland basin formation and gravitational instabilities in the central Andes

A version of this chapter has been published. Wang, H., Currie, C. A., & DeCelles, P. G. (2015). Hinterland basin formation and gravitational instabilities in the central Andes: Constraints from gravity data and geodynamic models. Geological Society of America Memoirs, 212, 387-406. Preliminary subduction models with an oceanic slab (Section 3.6) have been added for this thesis.

Abstract

The evolution of surface topography in an orogen provides information about the dynamics of the deep lithosphere. Within the high elevation Altiplano-Puna Plateau of the central Andes, there are several local basins (~100 km wide) that sit >500 m lower than the surrounding plateau. These areas correspond to positive gravity anomalies, indicating high density in the lithosphere. There are also examples of former basins that are now at high elevation (e.g., the Miocene Arizaro basin), suggesting that the basins are transient features that may be related to convective removal of lithosphere. Two-dimensional numerical models are used to investigate the topographic expression associated with removal of a high-density lithosphere root. A key result is that the presence of thick orogenic crust, as found in the Altiplano-Puna plateau, can greatly affect the surface deflection above the detaching root. Three types of deflection are observed: (1) >500 m subsidence, followed by uplift, (2) little subsidence, and (3) uplift followed by collapse. The main control on the deflection is the viscous coupling between the root and surface, which decreases with increased root depth or weaker crust. If the crust is weak, the dense root induces crustal flow, resulting in thickened crust and either limited subsidence or uplift above the dripping lithosphere. Significant subsidence only occurs if the deep crust is relatively strong and the density anomaly is located within the crust. To produce surface deflection over a width of ~100 km, the near-surface rocks must be relatively weak.

3.1 Introduction

Subduction zones are regions of crustal deformation and continental growth through both lateral lithosphere accretion and magmatism. They are also areas where removal of continental lithosphere may occur, for example through subduction erosion or gravitational foundering. Here, we examine gravitational removal of lithosphere from the central Andes orogen of South America (Figure 3.1a). This orogen formed in association with subduction of the Nazca plate below South America, with the majority of shortening in the last ~30 Ma (Oncken et al., 2006 and references therein). This has produced the Altiplano-Puna plateau, which has a 50-80 km thick crust (e.g., Beck et al., 1996; Yuan et al., 2002; Oncken et al., 2006; Bianchi et al., 2013). In contrast, the mantle lithosphere below most of the plateau does not appear to be anomalously thick. Seismic tomography images of the shallow mantle show that much of the plateau is characterized by low seismic velocities and high attenuation (e.g., Myers et al., 1998; Beck and Zandt, 2002; Schurr et al., 2006; Bianchi et al., 2013; Beck et al., 2014). A seismic receiver function study indicates that the thickness of lithosphere is only ~100 km in eastern Altiplano plateau, which is ~30-70 km thinner than the surrounding areas (Heit et al., 2008). Magmatism throughout the plateau (e.g., Kay and Coira, 2009) and high surface heat flow (e.g., Springer and Förster, 1998) also suggest high mantle temperatures and a thin lithosphere. These observations have been interpreted to indicate the removal of mantle lithosphere, and possibly lower crust, from the orogen (e.g., Beck and Zandt, 2002; Schurr et al., 2006; Kay and Coira, 2009).

Mantle lithosphere is generally cooler and denser than the underlying mantle, and therefore it is gravitationally unstable. During orogenic shortening, lithospheric thickening may initiate convective removal of the deep lithosphere, through either a Rayleigh-Taylor-type instability (RT-drip) (e.g., Houseman and Molnar, 1997; Molnar and Houseman, 2004) or delamination (e.g., Bird, 1979). Foundering may also be triggered by the presence of high-density eclogitic rocks in the lower crust or mantle

lithosphere, associated with metamorphic or magmatic processes (Kay and Kay, 1993; Leech, 2001; Ducea, 2002; Saleeby et al., 2003).
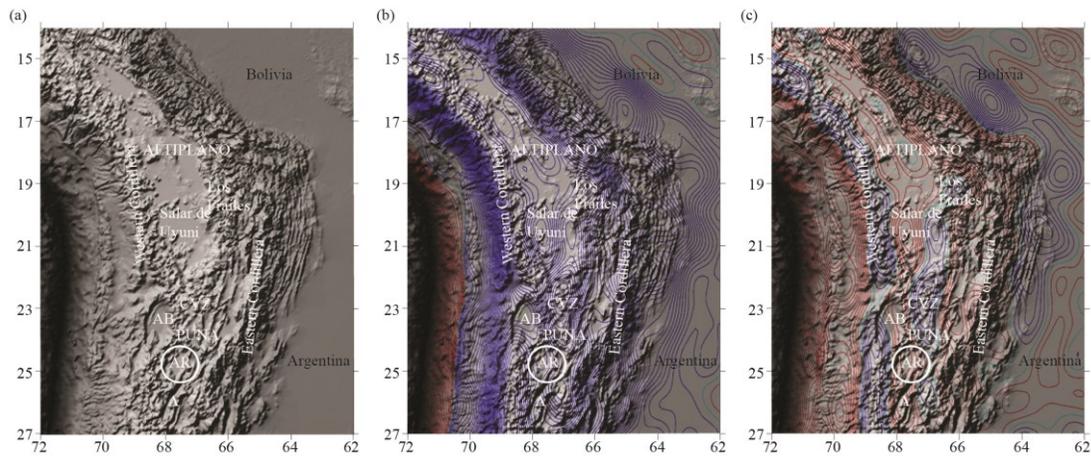
Figure 3.1. (a) Topography in the central Andes. CVZ= Central Volcanic Zone; AB=Atacama basin; AR= Arizaro basin. The Arizaro basin region consists of the Miocene basin in the east (now at high topography) and the modern Salar de Arizaro in the west. (b) Bouguer gravity map in the central Andes from gravity model Delft Gravity Model-1S. The red lines indicate positive gravity anomalies; the green line is zero anomaly and the blue lines are negative anomalies. The contour interval is 10 mGal. (c) Isostatic gravity map in the central Andes (contours as in Fig. 1b).

Lithosphere removal will modify the density and thermal structure of the orogen, and therefore removal events may be identified in the magmatic and elevation record. Localized magmatism in the Altiplano-Puna plateau has been linked to convective removal of lithosphere (e.g., Kay et al., 1994; Kay and Coira, 2009). Ducea et al. (2013) show that the composition of mafic magmas is consistent with small-scale lithosphere removal (<50 km diameter). As dense lithosphere is convectively removed, isostatic adjustment should produce uplift of the Earth's surface. Garzione et al. (2006) and Leier et al. (2013) compiled paleoelevation data for the Altiplano and inferred a period of rapid >1 km uplift in the Miocene. The spatial extent of uplift appears to

require large-scale foundering of the lithosphere across the width of the plateau (e.g., Hoke and Garzione, 2008).

In this chapter, we examine the topographic expression of lithosphere removal on a more local scale (100-200 km), similar to the scale inferred from magmatism (Ducea et al., 2013). Our work is motivated by observations of surface topography in the Altiplano-Puna plateau. Regionally, the plateau has low relief and is internally drained, with an average elevation of ~4 km. On a smaller scale, there are several basins within the high elevation hinterland (e.g., Horton, 2012). For example, the Atacama basin and Salars de Arizaro and Uyuni stand out as areas of relatively low elevation within the modern high plateau (Figure 3.1a). There are also examples of areas that were formerly basins but now sit at high elevation. The most well-studied of these is the Miocene Arizaro basin in the Puna plateau of northwest Argentina (DeCelles et al., 2015, and references therein). This basin is approximately circular, with a diameter of ~100 km. Basin subsidence initiated at ~21 Ma, at a time when paleoelevation data indicate that this part of the plateau had already undergone orogenic shortening and crustal thickening and was sitting at ~4 km elevation, close to its modern elevation (Carrapa et al., 2009, 2011; Quade et al., 2014). From 21 to ~8 Ma, the basin accumulated ~3400 m of lacustrine, fluvial, and eolian sedimentary rocks. Subsequently, the basin fill was internally shortened and then topographically inverted to its present ca. 4200 m elevation. It is now ~500 m higher than its surroundings and is located between the modern Salar de Arizaro in the west and the Salar de Pocitos in the east.

The formation of the Miocene Arizaro basin within the high Puna plateau is enigmatic. It does not appear to be controlled by neighboring thrust-faulted uplifts, loading associated with orogenesis, or extension (Schoenbohm and Carrapa, 2011; DeCelles et al., 2015). Given its roughly circular shape and transient nature, it has been proposed that the basin may be related to local removal of dense lithosphere as an RT-drip (DeCelles et al, 2011 and 2015; Schoenbohm and Carrapa, 2011). The goal of this

study is to assess whether an RT-drip can produce a surface deflection that is consistent with the observed characteristics of the Miocene Arizaro basin. We first present gravity data for the central Andes. This provides information about the present-day density structure of the orogen and demonstrates that modern hinterland basins coincide with regions of high gravity suggesting anomalously high density within the underlying lithosphere. We then use numerical models to examine the dynamics of RT-drips of either dense lower crust (Model Set A) or dense mantle lithosphere (Model Set B). The predicted surface deflection is compared to the geological record of the Arizaro basin to constrain the relationship between RT-drips and the temporal evolution of surface topography in an orogen.

3.2 Isostatic gravity data

Figure 3.1b shows the Bouguer gravity data for the Central Andes, based on the satellite model Delft Gravity Model-1S (Delft Gravity Model, 2013) with spherical harmonic coefficients up to degree 250. The Altiplano-Puna plateau appears as a negative Bouguer anomaly, with an average value of -300 mGal (Figure 3.1b). In order to assess whether the present-day topography (Figure 3.1a) is in isostatic equilibrium, we calculate the isostatic gravity anomaly. This calculation uses the present-day topography (Figure 3.1a, ETOPO2v2 database with 2 minutes resolution) to determine the expected crustal root thickness (w(x,y)), based on Airy-Heiskanen isostasy, as given by Whitman (1999):

$$w(x, y) = -\frac{\rho_t}{\Delta\rho} \times h(x, y) \quad \text{(onshore)} \quad (3.1)$$

$$w(x, y) = \frac{\rho_t - \rho_w}{\Delta\rho} \times h(x, y) \quad \text{(offshore)} \quad (3.2)$$

where ρ_t (2850 kg/m^3) is the topographic (crustal) density, ρ_w (1030 kg/m^3) is the water density, $\Delta\rho$ (450 kg/m^3) is the density contrast across the Moho, and h(x,y) is the topography or bathymetry, taken every 2 minutes. The zero elevation crustal thickness is 40 km.

The expected crustal thickness is then gridded into rectangular prisms (x and y spacing of 0.25 degrees) and the associated gravity field at the surface is computed by combining the effects of all the prisms. Finally, the calculated gravity field is subtracted from the Bouguer gravity field to obtain the isostatic gravity field. We also subtract the gravitational effect of the Nazca plate (20 mGal, Whitman, 1999) from the entire region.

This approach provides a first-order view of the lithospheric density structure of the central Andes. Figure 3.1c shows the calculated isostatic gravity field, which is similar to the isostatic gravity field presented by Whitman (1999) and Götze and Krause (2002). Regions that have a non-zero gravity anomaly are areas that are not in Airy isostatic equilibrium. On a regional scale, the Western Cordillera exhibits negative anomalies (~ -30 mGal), which may be associated with the modern volcanic arc. In the Altiplano-Puna Plateau, the isostatic gravity anomaly is close to 0 mGal. The Eastern Cordillera has positive anomalies (>30 mGal), which have been related to plate flexure caused by underthrusting of Brazilian shield (Whitman, 1999).

On a smaller scale, areas with active volcanism, such as the Los Frailes volcanic field and Central Volcanic Zone, are characterized by negative residual anomalies of approximately -30 mGal. This indicates low densities that may be associated with local thinning of the lithosphere and/or heating of the crust by volcanism. In contrast, modern salars and basins (e.g., Salar de Arizaro, Salar de Uyuni and Atacama basin) exhibit positive isostatic gravity anomalies, possibly related to anomalously high density in the lithosphere. In the Arizaro region, the largest positive anomaly is associated with the Salar de Arizaro in the west, and the gravity anomaly decreases to the east over the Miocene Arizaro basin, which is now a topographic high. This suggests that the Salar de Arizaro is presently underlain by high-density material, whereas the Miocene basin is closer to isostatic equilibrium. For the Puna plateau, seismic studies indicate low velocities in the shallow mantle, which have been interpreted to indicate a thin mantle lithosphere in this region (Schurr et al., 2006). Therefore, it is unlikely that the inferred

high density corresponds to unusually thick mantle lithosphere. The wavelength of the isostatic gravity anomalies is 100-200 km, which is consistent with anomalously dense material in either the deep crust or shallow mantle (<100 km depth). However, the wavelength of the gravity anomaly depends on both the depth and width of the density anomaly, and therefore the exact depth of the anomaly can not be determined from the gravity field alone.

3.3 Numerical modeling methods

3.3.1 Model geometry and methods

The gravity data presented in the previous section are consistent with the idea that hinterland basins may form above areas with high-density material in the lithosphere. We now develop numerical models to address the dynamics of this material, in order to assess whether densification followed by gravitational removal is a viable mechanism to explain the Miocene Arizaro basin. The initial geometry of the 2D thermal-mechanical numerical models is shown in Figure 3.2a. The model domain is 900 km wide and 400 km deep, with a 60 km thick continental lithosphere overlying sublithospheric mantle. The lithosphere has an 800 km wide weak zone (proto-orogen) between two stronger blocks. The initial (pre-orogenic) continental lithosphere consists of a 40 km thick crust (25 km upper-mid crust and 15 km lower crust) and 20 km mantle lithosphere. The mantle lithosphere is thin because the Puna plateau probably already underwent deformation and destruction before the Arizaro basin was formed (DeCelles et al., 2015). In the models below, we consider gravitational instability of anomalously dense material ("root") in either the orogen lower crust (Model Set A) or mantle lithosphere (Model Set B). The initial width of each of these zones is ~100 km (black material in Figure 3.2a).
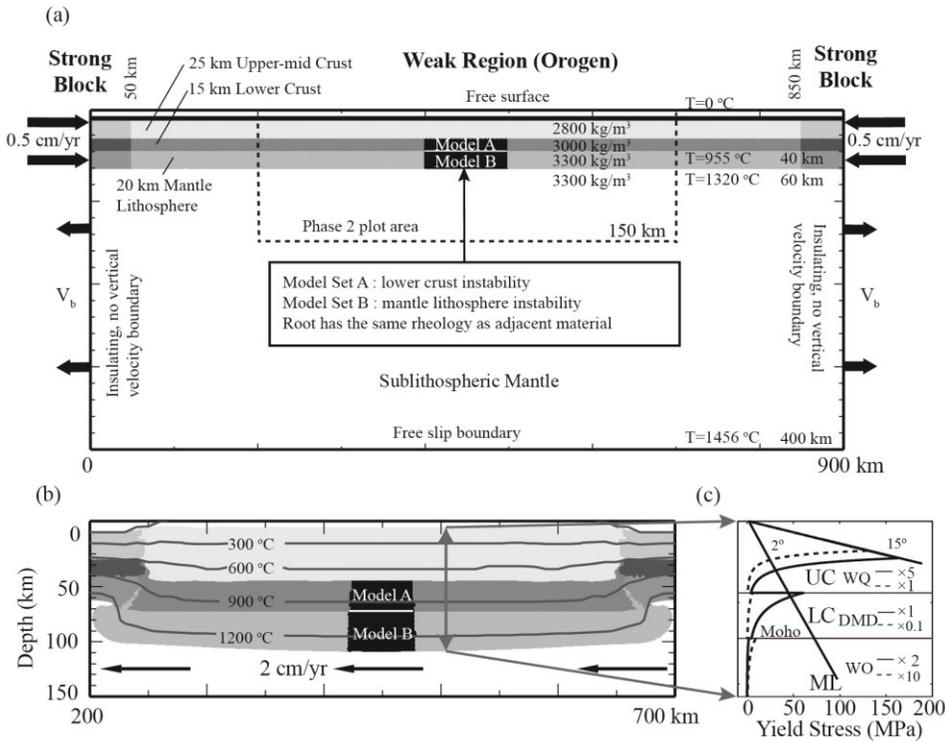
Figure 3.2. Numerical model set-up. (a) Initial model geometry and thermal-mechanical boundary conditions for Phase 1. Material parameters are given in Table 3.1. V_b is a small uniform outflux velocity assigned to the side boundaries of the sublithospheric mantle in order to maintain constant mass in the model domain. (b) Model geometry at the beginning of Phase 2, after 380 km of shortening. In this phase, the lithosphere boundaries have zero velocity and a 2 cm/yr flow to the left is assigned to the boundaries of the sublithospheric mantle to simulate mantle wedge flow. (c) Strength profiles for orogen lithosphere. The lines, 15° and 2°, show the frictional-plastic yield stress for unsoftened and softened materials, respectively. Solid lines show the viscous rheology used in the reference models; dashed lines are the strength variations that are tested this study, based on variations in the scaling factor f (Equation 3.4). The model thermal structure and a strain rate of 10^{-15} s^{-1} are used for the calculations. UC=upper-mid crust; LC=lower crust; ML=mantle lithosphere; WQ=wet quartzite; DMD=dry Maryland diabase; WO=wet olivine.

26

Using the finite element code SOPALE, thermal-mechanical calculations are carried out on an Eulerian mesh, which has 180 elements in the horizontal direction (5 km width) and 82 elements in the vertical direction, with 56 elements in the upper 140 km (2.5 km height) and 26 elements below (10 km height). Benchmark tests show that this resolution is sufficient to obtain growth rates of Rayleigh-Taylor instabilities within 6% of expected values (Houseman and Molnar, 1997; Molnar et al., 1998). Material properties are tracked using Lagrangian particles which are advected with the model velocity field and are used to update the Eulerian mesh every time step. The Eulerian mesh is fixed horizontally but can stretch vertically to conform to the top boundary of the models (ground surface) as topography develops.

3.3.2 Material properties

Crustal materials undergo frictional-plastic strain softening by decreasing the effective angle of friction (ϕ_{eff}) (Equation 2.7) with increasing strain. This approximates rock weakening due to pore fluid pressure variations, fault gouge formation and mineral reactions during deformation (Huismans and Beaumont, 2002 and 2003; Warren et al., 2008). In the models, ϕ_{eff} is linearly reduced from 15° to 2° over accumulated strain (I_2') of 0.5 to 1.5 (Table 3.1) (e.g., Huismans and Beaumont, 2003).

Table 3.1. Material parameters in the reference numerical models (A1 and B1)

	Upper-mid crust	Lower crust	Mantle lithosphere	Sublithospheric mantle
Model geometry				
Initial Thickness (km)	25	15	20	340
Thickness after Phase 1 (km)	48	28	36	292
Plastic rheology				
c_0 (MPa)	2	2	0	0
ϕ_{eff}	15º - 2º	15º - 2º	15º	15º
Viscous rheology				
f	5	1	2	1
A (Pa^{-n} s^{-1})	1.10×10^{-28}	5.05×10^{-28}	3.91×10^{-15}	3.91×10^{-15}
B* (Pa s$^{1/n}$)^a	2.92×10^{6}	1.91×10^{5}	1.92×10^{4}	1.92×10^{4}
n	4.0	4.7	3.0	3.0
Q (kJ mol^{-1})	223	485	430	430
V* (cm^3 mol^{-1})	0	0	10	10
Thermal parameters				
k (W m^{-1} K^{-1})	2.25	2.25	2.25	102.5
A_T (μW m^{-3})	1	0.4	0	0
c_p (J kg^{-1} K^{-1})	750	750	1250	1250
Density ^{b}				
ρ_0 (kg m^{-3})	2800	3000	3300	3300
T_0 (K)	900	900	900	900
α (K^{-1})	3.0×10^{-5}	3.0×10^{-5}	3.0×10^{-5}	3.0×10^{-5}

^{a} $B^* = \left(2^{(1-n)/n}3^{-(n+1)/2n}\right)A^{-1/n}$. The term in brackets converts the pre-exponential viscosity parameter from uniaxial laboratory experiments (A) to the tensor invariant state of stress of the numerical models

^{b} All materials have a temperature-dependent density, given by $\rho(T) = \rho_0[1 - \alpha(T - T_0)]$ where ρ_0 is the reference density at temperature T_0 and α is the volumetric thermal expansion coefficient.

When deformation is viscous, we choose rheological parameters from a few reliable laboratory studies following previous studies (e.g., Beaumont et al., 2006). We use the parameters for wet quartzite (Gleason and Tullis, 1995), dry Maryland diabase

(Mackwell et al., 1998) and wet olivine (Karato and Wu, 1993) for the upper-mid crust, lower crust and mantle, respectively (Table 3.1). We then use the scaling parameter (f) (Equation 2.9) to linearly scale the model viscosity relative to the laboratory data to approximate materials that are stronger or weaker than this base set. This provides a way to test reasonable variations in strength owing to moderate changes in composition or temperature, the effects of water fugacity, or uncertainties in the rheological parameters under the same ambient conditions (Beaumont et al., 2006). In the reference model, we use f=5 for the upper-mid crust, f=1 for the lower crust, and f=2 for the mantle lithosphere in the orogen (Table 3.1). This is designed to approximate a strong, dry quartzo-feldspathic upper-mid crust, a strong lower crust with refractory, intermediate granulite rocks and a relatively water-poor continental mantle lithosphere due to dehydration and melt depletion effects during lithosphere formation. The side blocks have values of f that are 5 times larger for each of the three units, so that the deformation is focused in the orogen region during shortening (Phase 1).

3.3.3 Initial thermal structure

The initial thermal structure of the model is calculated using a surface temperature of 0°C, a temperature of 1456°C at the base of the model (z=400 km) and the thermal conductivity (k) and radiogenic heat production (A_T) values given in Table 3.1. A high thermal conductivity is assigned to the sublithospheric mantle to maintain a nearly constant heat flux to the base of the lithosphere and produce an adiabatic thermal gradient of 0.4°C/km in the sublithospheric mantle, in order to simulate heat transfer by a convecting mantle (Pysklywec and Beaumont, 2004). The resulting thermal field has a surface heat flow of 72 mW/m^2, with temperatures of 955°C at the Moho and 1320°C at the base of the lithosphere (60 km depth). The assumption is that this lithosphere is in the backarc region of a subduction zone, and therefore the lithosphere is heated by convection associated with subduction (e.g., Currie and Hyndman, 2006).

3.3.4 Modeling approach and boundary conditions

For the Miocene Arizaro basin, subsidence occurred after orogenic shortening, uplift, and shallow regional exhumation (Carrapa et al., 2009; Canavan et al., 2010 and 2011; Quade et al., 2014). This is simulated by running the numerical models in two phases. During the first phase, the continental lithosphere is shortened to produce an orogen. Strong lithosphere is introduced through each of the side boundaries at 0.5 cm/yr (Figure 3.2a) and shortening localizes within the region of weaker lithosphere. After 38 Myr, the orogen is ~400 km wide and has a ~76 km crust, similar to the geometry of the Puna plateau (Figure 3.2b). Note that we have not attempted to model the details of shortening but instead create the orogen through pure shear. One consequence is that at the end of shortening, the lithosphere thermal gradient has decreased, such that the model surface heat flow is somewhat lower than that observed (~50 mW/m^2 vs. >60 mW/m^2, Springer and Forster, 1998), although the model Moho temperatures (~950°C) are similar to those inferred in the central Andes (Babeyko et al., 2002).

In the second phase, shortening is stopped and the density of the root region in the lower crust (Model Set A) or mantle lithosphere (Model Set B) is progressively increased to initiate gravitational instability. As discussed below, the density change is attributed to either metamorphic eclogitization of the lower crust or the emplacement of dense, mafic magmas in the mantle lithosphere. During this phase, the mechanical boundary conditions are as follows: 1) a free surface, which allows topography to develop in response to the underlying dynamics, 2) a free slip basal boundary, 3) no vertical velocity on the side boundaries, 4) no horizontal velocity on the lithosphere side boundaries, and 5) a velocity of 2 cm/yr to the left through both side boundaries of the sublithospheric mantle. This flow simulates mantle wedge corner flow associated with Nazca Plate subduction below the Puna plateau. The thermal boundary conditions are: 1) insulating (no heat flux) side boundaries, 2) a constant temperature of 1456°C for the

basal boundary, and 3) a constant temperature of 0°C for the top boundary.

We conducted a number of model experiments to examine the dynamics of gravitational removal of dense lower crust or mantle lithosphere, focussing on variations in the root density and rheological structure of the orogen (Table 3.2). The rheology variations in the lithosphere are shown in Figure 3.2c. All experiments were carried out in Phase 2 of the models (after shortening has stopped) and the times reported are the times in Myr since the start of Phase 2.

Table 3.2. List of models showing parameter variations tested in this study, focusing on the frictional angle (ϕ_{eff}) and viscosity scaling factor (f) for crust and mantle materials. In all models, $c_0 = 2$ MPa in the upper-mid crust and lower crust and $c_0 = 0$ MPa in the mantle lithosphere. Ref.=reference; FPSS is frictional-plastic strain softening; ML is mantle lithosphere.

Model	Model type	Parameter	Upper-mid crust	Lower crust	Mantle lithosphere	Figure number
MODEL SET A: Lower crust instability						
A1	FPSS	ϕ_{eff}	15° - 2°	15° - 2°	15°	3.3
(Ref.)	Strong crust & weak ML	f	5	1	2	
A2	High root densification rate (80 kg/m^3/Ma); other parameters as in A1					
A3	FPSS	ϕ_{eff}	15° - 2°	15° - 2°	15°	3.5
	weak crust & weak ML	f	1	0.1	2	
A4	FPSS	ϕ_{eff}	15° - 2°	15° - 2°	15°	
	Strong crust & strong ML	f	5	1	10	
A5	No FPSS	ϕ_{eff}	15°	15°	15°	
	Strong crust & weak ML	f	5	1	2	
A6	No FPSS	ϕ_{eff}	2°	2°	15°	
	Strong crust & weak ML	f	5	1	2	
Lower crust instability with sedimentation in basin						
A7	sediment density =2000 kg/m^3; other parameters as in A1					3.8
A8	sediment density =2400 kg/m^3; other parameters as in A1					
A9	sediment density =2000 kg/m^3; other parameters as in A2					
MODEL SET B: Mantle lithosphere instability						
B1	FPSS	ϕ_{eff}	15° - 2°	15° - 2°	15°	3.10
(Ref.)	Strong crust & weak ML	f	5	1	2	
B2	FPSS	ϕ_{eff}	15° - 2°	15° - 2°	15°	
	Strong crust & strong ML	f	5	1	10	
B3	FPSS	ϕ_{eff}	15° - 2°	15° - 2°	15°	
	Weak crust & weak ML	f	1	0.1	2	
B4	FPSS	ϕ_{eff}	15° - 2°	15° - 2°	15°	
	Weak crust & strong ML	f	1	0.1	10	

3.4 Lower crust instability

3.4.1 Origin of the crustal density anomaly

Model Set A addresses gravitational removal of a local region of high-density material in the lower crust of the orogen (Model A block in Figure 3.2). The high-density may be related to metamorphic eclogitization of the lower crust. During orogenic shortening, the lower crust enters the eclogite stability field (generally temperatures >600°C, pressures >1.2 GPa; Bousquet et al., 1997), but it may not immediately transform to eclogite. Eclogitization appears to be triggered by the presence of water, whereby localized shear zones or faults may enable the phase change in discrete regions (e.g., Austrheim, 1991; Leech, 2001; Jackson et al., 2004). Here, we test the idea that the granulitic lower crust remains metastable during orogenesis and then undergoes progressive eclogitization in the "root" region shown in Figure 3.2b, possibly associated with localized lithosphere hydration. This is simulated by gradually increasing the density of this zone, assuming that eclogitization occurs throughout the block. The material within the root initially has the density of lower crust (3000 kg/m^3) and its density is increased until it attains the density of mafic eclogite, 3550 kg/m^3 (Christensen and Mooney, 1995; Bousquet et al., 1997). We test densification rates of 40 kg/m^3/Myr and 80 kg/m^3/Myr, corresponding to 7.2% and 14.5% eclogitization every Myr for the 1500 km^3 (per unit km along strike) root region. Another possibility is that the local region of high density is related to the emplacement of mafic magmas in the deep crust (Kay and Kay, 1993; Ducea, 2002; Kay and Coira, 2009)

In the models, only the root density is changed. Studies of the rheology of eclogite show that dry eclogite has a similar strength to the dry Maryland diabase used for the lower crust (Jin et al., 2001; Zhang and Green, 2007). Therefore, we assumed that the root has the same rheological properties as its protolith. In the reference model, both the root and lower crust use f=1 to represent dry, strong crust. Later, we test the case of weak, hydrated material (f=0.1). Laboratory studies show that water may

significantly weaken granulitic and eclogitic lower crust by ~1 order (Zhang and Green, 2007).

3.4.2 Effect of root densification rate (Models A1 and A2)

Reference Model A1 uses the model parameters given in Table 3.1, and the lower crustal root undergoes densification at a rate of 40 kg/m^3/Myr. Figure 3.3a shows the evolution of this model. Over time, the density of the root increases and at ~7 Myr, it becomes more dense than the mantle, initiating gravitational instability. It starts to descend into the mantle and the deep root detaches at ~13 Myr, leaving the uppermost part of the root intact. Figure 3.3d shows the model at the time of root detachment. The deeper root entrains the surrounding weak mantle lithosphere, and thus there is no gap created in the deep lithosphere. The removed material is swept sideways by the 2 cm/yr mantle flow, as is the mantle lithosphere at the edges of the thickened orogen. The flow appears to only affect the root after detachment, and there is little effect on crustal dynamics or surface topography.

At the surface, the presence of the dense root results in the formation of a local basin with a width of ~100 km (top plot in Figure 3.3a). Figure 3.4 shows the evolution of the depth of the basin. During the first 3 Myr, the subsidence rate is slow, as an isostatic response to root densification. It then increases to ~0.2 km/Myr between 3 Myr and 8 Myr. By 9 Myr, the subsidence rate decreases to zero and basin is at its maximum depth of ~1.2 km. Between 9 and 13 Myr (the time of root detachment), the basin becomes shallower, with an uplift rate of ~0.2 km/Myr. The uplift rate then decreases and by 20 Myr, the basin has uplifted ~1.1 km from its deepest point but is still ~0.1 km lower than the surroundings.
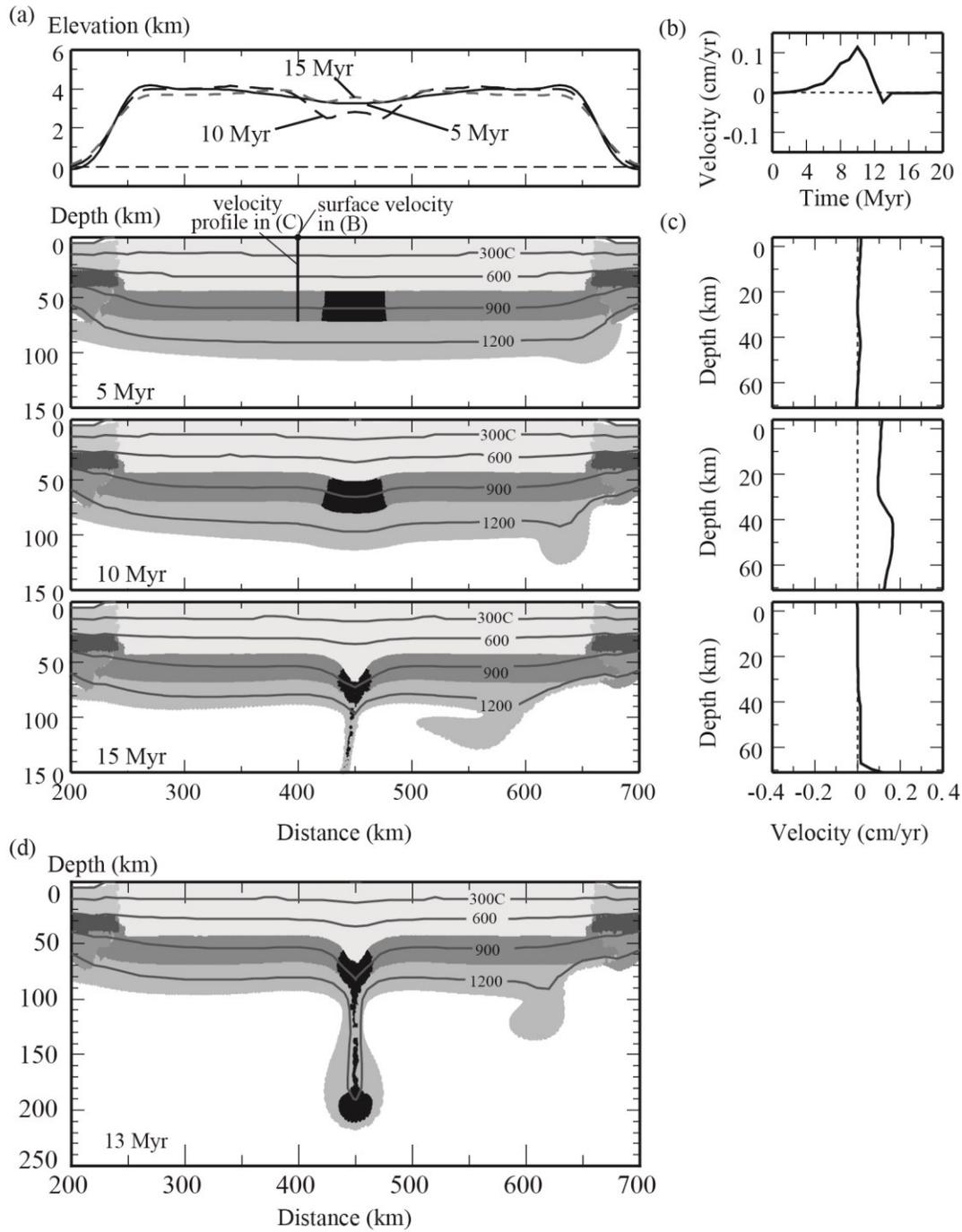
Figure 3.3. Evolution of Reference Model A1. (a) Surface topography and model geometry at the given times after the start of the model run. (b) Evolution of the horizontal surface velocity at x=400 km. (c) Crustal flow velocity profile at x=400 km at the times in Fig. 3.3a. (d) Model geometry at 13 Myr when the drip is undergoing necking and detachment.
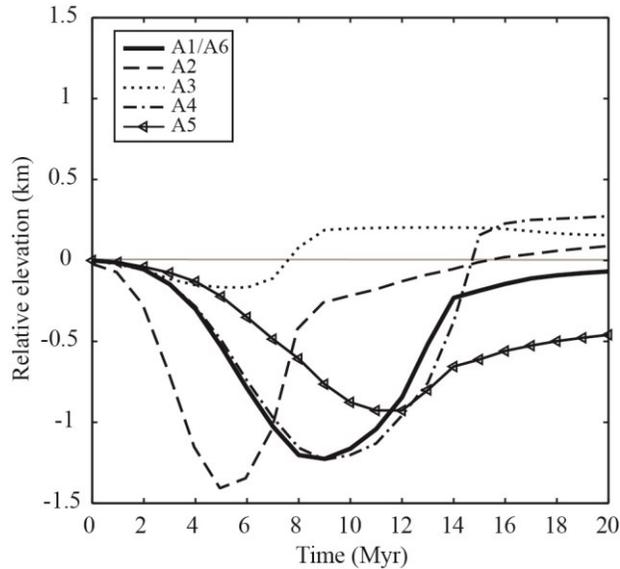
Figure 3.4. The evolution of the depth of the basin for a lower crust instability (Model Set A). The basin depth is the difference between the average elevation of the plateau and the elevation at the center of the surface deflection.

The development of the basin is also associated with contraction at the surface. Figure 3.3b shows the horizontal surface velocity at a fixed point 400 km from the left model boundary. Note that the model is symmetric about the center of the basin (x=450 km). From 0 to 12 Myr, the velocity of the crustal flow is positive (toward the center of the basin), with a maximum velocity at 10 Myr; in other words, the basin is experiencing contraction. After 10 Myr, the horizontal velocity decreases and there is a small negative velocity as the root detaches at 13 Myr, indicating minor extension.

In this model, the maximum basin depth and surface contraction occur before the root is fully removed. This is a consequence of entrainment of the crust by the drip. Figure 3.3c shows a vertical velocity profile through the crust at x=400 km. At 5 Myr, there is little crustal flow. At 10 Myr, the entire crust has a positive velocity as it undergoes contraction during growth of the root instability, with larger velocities in the deep crust. The enhanced velocities are associated with flow that appears to be driven by the negatively buoyant root, which induces a horizontal pressure gradient in the

crust. This results in crustal thickening above the root, and by 10 Myr, crustal flow is sufficient to cause basin inversion and surface uplift prior to root detachment (Figure 3.4). After the root detaches, the rate of surface uplift decreases and there is little flow within the crust (Figure 3.3c).

Model A1 shows that the presence and removal of a dense crustal root can create a transient basin at surface. The density of the root is one important factor that controls its dynamics. The densification rate of the root depends on the efficiency of the eclogite phase change, which is not well-constrained. Model A2 uses a densification rate of 80 kg/m^3/Myr, twice that of Reference Model A1; all other parameters are unchanged. With the greater densification rate, the root undergoes instability and removal more rapidly, and the root detaches at ~8 Myr. At the surface, the dense root results in the formation of a basin with a maximum depth of ~1.4 km at 5 Myr (Figure 3.4), which produces a shorter-lived and slightly deeper basin than in the reference model A1. Again, surface uplift is observed prior to root removal, owing to crustal thickening above the root.

3.4.3 Variations in viscous strength (Models A3 and A4)

The strength of the crust and mantle lithosphere are also important factors that control the dynamics of root removal. We first examine variations in crustal viscous strength, which primarily affects the deep regions of the crust (Figure 3.2c). For crust and mantle, the viscous strength at a given temperature is a function of both composition and degree of hydration. Here, we use the scaling factor f (Equation 2.9) to study the effect of variations in viscous strength. Reference Model A1 uses a relatively strong crust (Table 3.2). Model A3 has a weaker crust, corresponding to more hydrated conditions or a more felsic composition. The strength is changed by decreasing f to 1 for the upper-mid-crust (i.e., the base wet quartzite rheology of Gleason and Tullis, 1995) and 0.1 for the lower crust (10 times weaker than dry Maryland diabase rheology;

Mackwell et al., 1998). The other parameters are the same as in Model A1, with a root densification rate of 40 kg/m^3/Myr.
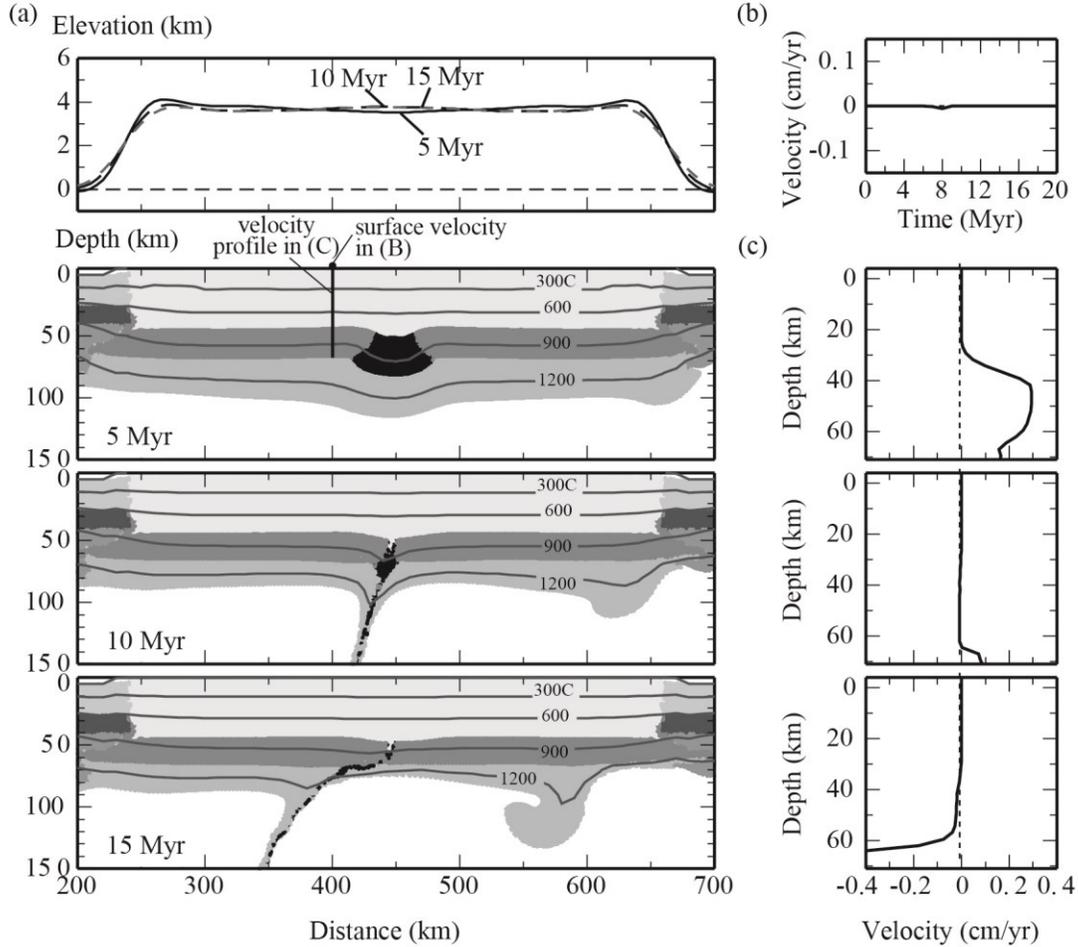
Figure 3.5. Evolution of Model A3. (a) Surface topography and model geometry at the given times after the start of the model run. (b) Evolution of the horizontal surface velocity at x=400 km. (c) Crustal flow velocity profile at x=400 km at the times in Fig. 3.5a.

With the weaker crust, the root detaches at ~9 Myr (Figure 3.5a), which is ~4 Myr earlier than in the reference model. At the surface, there is little deflection in the either vertical (Figure 3.4) or horizontal directions (Figure 3.5b). The vertical velocity profile (Figure 3.5c) shows that the weak crust is more easily entrained by the dripping root. As the root destabilizes, the flow velocity is ~0.3 cm/yr in the deep crust at 5 Myr,

leading to thickening of the crust. Velocities decreases to ~0 cm/yr at 10 Myr after the root is removed. At 15 Myr, there is negative velocity flow in the deep lower crust. This is caused by both relaxation of the thick, weak crust (i.e., flow driven by differential pressures associated with lateral variations in Moho depth) and shearing by flow in the underlying sublithospheric mantle.
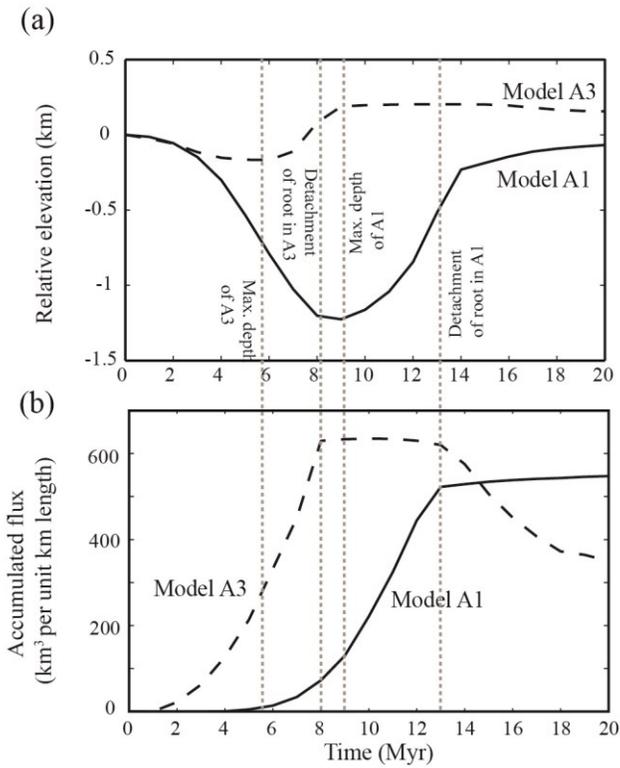
Figure 3.6. (a) The relative elevation of the center basin for Models A1 and A3 (as in Fig. 3.4). (b) The cumulative crustal volume flowing through a vertical profile at x=400 km per unit km length perpendicular to the model plane.

Figure 3.6 compares the depth of the center of the basin and the cumulative crustal flux at x=400 km (calculated by integrating the crustal flow velocities over the vertical direction and time, Figures 3.3c and 3.5c). In Model A1, most crustal flow occurs between 7 and 13 Myr, corresponding to gravitational removal of the root. At 9

39

Myr, when the basin has its maximum depth, the accumulated crustal volume is ~120 km^3 per km along strike and it continues to increase until the root detaches at 13 Myr. As a result, surface uplift associated with crustal thickening is greater than surface subsidence related to root removal, and basin inversion occurs prior to root detachment. Figure 3.6 also shows that the weaker crust of Model A3 is more easily entrained by the detaching root. Crustal flow begins as early as 1 Myr, and by 6 Myr the accumulated crustal volume is ~300 km^3 per km along strike. With the enhanced crustal flow, there is little surface deflection associated with root removal.

In addition to crustal strength, root removal also depends on mantle lithosphere strength because the root must descend through the mantle lithosphere. Model A4 has identical parameters to the reference model, but the mantle lithosphere is five times stronger (f=10) (Tables 3.2 and 3.3) to test the effect of a more water-poor mantle lithosphere. In this model, the strong mantle lithosphere reduces the instability growth rate and root detachment occurs at ~15 Myr, ~2 Myr later than in the reference model. Figure 3.4 shows a similar subsidence history of the two models. The only difference is that Model A4 has longer rebound time and greater uplift; at 20 Myr, the surface is at ~0.2 km higher than the surroundings. This may be due to a greater amount of crustal thickening above the root, owing to the stronger coupling between the crust and mantle lithosphere in this model.

3.4.4 Variations in frictional-plastic strength (Models A5 and A6)

Deformation of the near-surface rocks (here called "upper crust") is controlled by their frictional-plastic strength (Equation 2.7; Figure 3.2c). In the above models, frictional-plastic strain softening was included through a decrease in ϕ_{eff} with accumulated strain, consistent with laboratory and field observations that suggest that rocks may weaken during deformation (e.g., Huismans and Beaumont, 2003, Paterson and Wong, 2005). We now test models with no strain softening. Models A5 and A6

correspond to a strong upper crust (ϕ_{eff} =15°) and weak upper crust (ϕ_{eff} =2°), respectively (Figure 3.2c); other parameters are the same as in Model A1 (Tables 3.2 and 3.3). A lower ϕ_{eff} may be related to high pore fluid pressure in the upper crust due to hydration (Babeyko and Sobolev, 2005 and references therein).

In Models A5 and A6, the root removal process is similar to that in Model A1. The main difference between the models is in the wavelength of surface deflection (Figure 3.7). In Model A5, the upper crust remains strong throughout model evolution, and the surface deflection has a long wavelength. The basin in Model A5 is ~300 km wide, approximately three times that of Model A1. In addition, the basin subsides more slowly and attains its maximum depth of ~1 km at 12 Myr (Figure 3.4). In contrast, there is little difference in the behaviour of Models A1 and A6. In Model A6, the upper crust is weak throughout the model evolution, whereas the upper crust in Model A1 weakens during deformation to the same strength. In both, the surface subsides to ~1.2 km at 9 Myr and the width of the basin is ~100 km. These results demonstrate that the frictional-plastic strength of the crust strongly influences the geometry of the basin but has little effect on the dynamics of root removal; a narrower basin requires weak near-surface rocks.
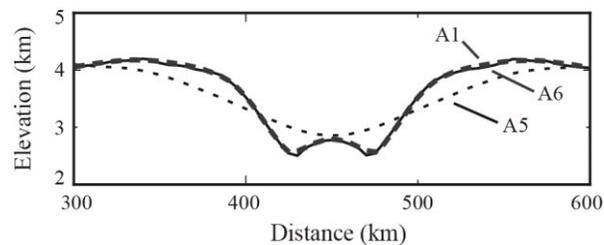
Figure 3.7. Surface topography for Models A1, A5 and A6 at 9 Myr, 11 Myr and 9 Myr respectively, when the basin reaches its maximum depth in each model. Note the longer deflection wavelength for Model A5, in which the frictional-plastic strength is highest.

3.4.5 Sedimentation effects (Models A7, A8 and A9)

The previous models examine the development of a basin associated with lithosphere dynamics (i.e., tectonic subsidence). In nature, the basins are locations of sediment deposition. The introduction of sediments provides a surface load, which will increase basin depth. The thickness of the sediments depends on sedimentation rate, which is controlled by a number of factors, including erosion rate, the nature of the rocks in the source terranes, climate, and basin capacity. Another important factor is the sediment density, which will vary with composition and sediment porosity and may increase with depth due to compaction.

We examine the effect of sediment loading by adding sediments to the basin in Model A1. For simplicity, we fill the basin to capacity at each time step, and we have tested two different sediment densities, 2000 kg/m^3 (Model A7) and 2400 kg/m^3 (Model A8) (Table 3.2). The lower value represents more porous sediments that fill the basin to capacity or can be taken as a proxy for denser sediments that do not completely fill the basin. The latter value is comparable to the average value for 2-5 km thick sediments in North America (Mooney and Kaban, 2010). Other properties in these models are as the same as those in Model A1.

Figure 3.8 shows the evolution of Model A7, with sediment (black material at surface) deposited in the basin as it forms. The width of the sediment layer is ~100 km by ~10 Myr, which is consistent with the basin width in Model A1. The root removal process is also similar to the Model A1, and there are only minor differences in the surface contraction rate and crustal flow velocities. However, the gravitational load of the sediment increases the depth of the basin. The thickness of the sediment increases with time, with the maximum thickness of ~2.9 km at ~11 Myr (Figure 3.9). The change in subsidence rate at 4-5 Myr appears to be caused by the weakening of the upper crust through frictional-plastic strain softening. A sediment density of 2400 kg/m^3 (Model

A8) results in a deeper basin (~4.1 km at ~11 Myr) due to the greater surface load. The

surface of the models undergoes isostatic rebound following root removal. Owing to the

additional thickness of low-density sediments, the basin region becomes a topographic

high, with elevations of ~1.2 km and ~0.8 km higher than the surroundings in Models

A7 and A8, respectively. Finally, Model A9 tests the influence of sedimentation for a

model with a greater root densification rate, based on the parameters in Model A2

(Table 3.2). The overall removal timescale is similar to that in Model A2, but the

additional sediment load leads to a deeper basin, with a depth of ~3.7 km at 6 Myr

(Figure 3.9).
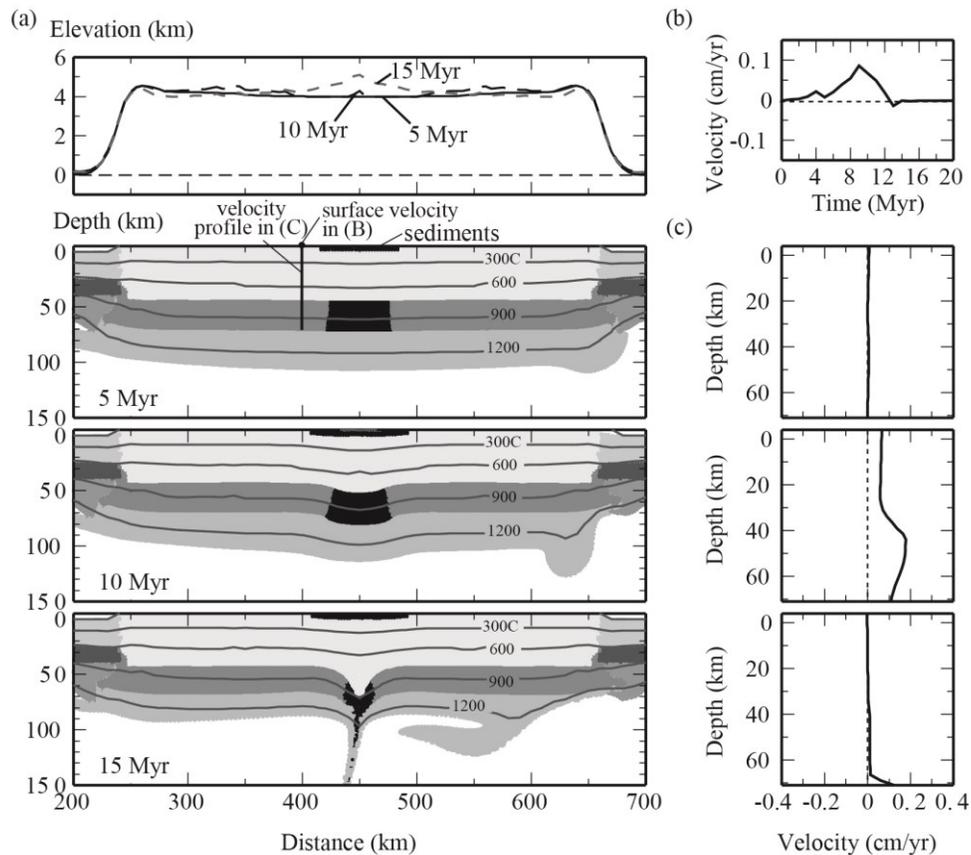
Figure 3.8. Evolution of Model A7. (a) Surface topography and model geometry at the given times after

the start of the model run. (b) Evolution of the horizontal surface velocity at x=400 km. (c) Crustal flow

velocity profile at x=400 km at the times in Fig. 3.8a.
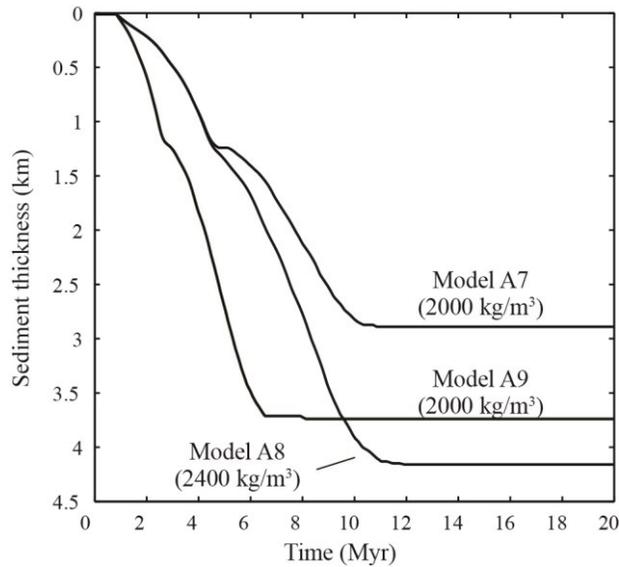
Figure 3.9. Accumulated sediment thickness over time at the center of the basin. Sediment density is 2000 kg/m^3 in Models A7 and A9, and 2400 kg/m^3 in Model A8.

3.5 Mantle lithosphere instability

3.5.1 Origin of the mantle lithosphere instability

The high-density material could also locates in the mantle lithosphere of the orogen through thermal contraction or formation of dense rocks (e.g., eclogite) (Block B in Figure 3.2a), instead of the lower crust. In Model Set B, we consider a mantle lithosphere density anomaly associated with either magmatic eclogite or a lithospheric thickness perturbation. Magmatic eclogite can be produced from mantle-derived mafic magmas which pond near the base of the crust, as the crust acts as a density filter and prohibits ascent to the surface. Partial melting and differentiation lead to the development of a high density eclogitic residue below the Moho, while the low density, felsic melts rise up to shallower crustal levels (Richards, 2003; Saleeby et al., 2003). In our models, we assume that this process occurs in a ~50 km wide region in the mantle lithosphere (Block B in Figure 3.2), and that the densification rate of this region

depends on the rate of magma production and segregation. In Cordilleran volcanic arcs, 60-90 km^3/Myr of magma are erupted at the surface per km along-strike arc length, and there may be 1 to 3 times more residual eclogite at depth (Ducea, 2002; Ducea and Barton, 2007). As magmatic eclogite (density 3550 kg/m^3) replaces mantle lithosphere in the root region, the density of the root should increase at a rate of 22 to 99 kg/m^3/Myr. In the models below, we use a densification rate of 40 kg/m^3/Myr, which is the same as the reference value used in Model Set A. We focus on the dynamics of high-density material in the mantle lithosphere and therefore the models do not include the simultaneous formation of a low-density crustal batholith; inclusion of this is expected to enhance surface uplift of the models following root removal. It should be noted that this mechanism of root formation requires volcanism prior to basin development. There is evidence for arc-type magmatism across much of the Altiplano-Puna plateau since 25 Ma (Trumbull et al., 2006), possibly associated with changes in dip of the subducting plate (Kay and Coira, 2009). The Arizaro basin itself has been in close proximity to the volcanic arc since the Miocene (e.g. Kay and Coira, 2009).

Another possibility is that the high-density mantle lithosphere is a block of perturbed mantle lithosphere that is locally thicker than the surrounding lithosphere. A perturbation to the mantle lithosphere can become gravitationally unstable, leading to further thickening over time and then removal as an RT-drip (Houseman and Molnar, 1997; Molnar and Houseman, 2004; Göğüş and Pysklywec, 2008). Our models approximate a growing instability by increasing the density in a small region of the mantle lithosphere (Block B), instead of imposing variations in lithosphere thickness. The main purpose is to investigate the surface expression of the removal process, rather than a detailed assessment of the origin of the density anomaly.

3.5.2 Effects of a local mantle lithosphere instability (Model B1)

Reference Model B1 has the same parameters as Model A1 (Table 3.1), except

that the high density root (black material) is placed in the mantle lithosphere. Because the root region starts with the same density as the underlying mantle, it becomes gravitationally unstable as soon as its density is increased. The instability grows quickly and the majority of the root detaches from the lithosphere at ~2 Myr (Figure 3.10a). During the removal process, the surface is hardly deflected and no basin forms (Figures 3.10a and 3.11). In addition, the root has little effect on the crustal dynamics, with negligible surface contraction or crustal flow (Figures 3.10b and 3.10c).
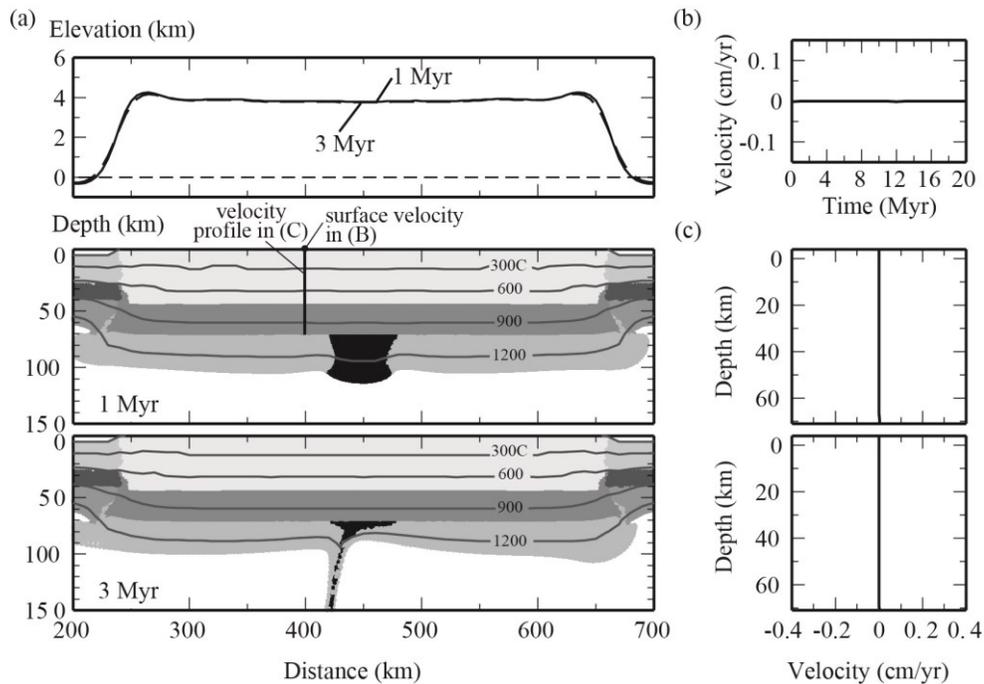
Figure 3.10. Evolution of Reference Model B1, in which the high-density (black) instability originates in the mantle lithosphere. (a) Surface topography and model geometry at the given times. (b) Evolution of the horizontal surface velocity at x=400 km. (b) Crustal flow velocity profile at x=400 km at the times in Fig. 3.10a.

3.5.3 Variations in viscous strength (Models B2, B3 and B4)

We have also tested variations in the viscous strength of the mantle lithosphere and the crust. Model B2 has the same strong crust as Model B1, but the viscosity of the

mantle lithosphere is five times larger (f=10) (Table 3.2). The same rheology is used for both the root region and adjacent mantle lithosphere. With the stronger mantle lithosphere, root removal is slightly delayed, with detachment at ~4 Myr. The longer duration of the root in the lithosphere provides a greater negative buoyancy force on the base of the crust, causing the surface to be deflected downward and creating a basin with a maximum depth of ~0.3 km at 3 Myr. As seen in Model Set A, the basin starts to rebound prior to root removal, as a result of induced horizontal crustal flow and thickening.

We also consider the case in which the crust has a weaker rheology than the reference model, for both the reference mantle lithosphere (Model B3) and the stronger mantle lithosphere (Model B4) (Table 3.2). The time of root removal in these models is the similar to that seen in Models B1 and B2. As the root undergoes gravitational removal, the lateral pressure gradient induces crustal flow in the weak crust. Flow velocities are sufficient to cause crustal thickening and surface uplift above the root (Figure 3.11). In both cases, the surface is uplifted by ≤0.3 km, with greater uplift in Model B4. Following root removal, the surface subsides to its original elevation, as the weak crust flows outward from the topographic high (i.e., topography-induced crustal flow; Beaumont et al., 2006).

Overall, density anomalies located in the mantle lithosphere do not have a significant surface expression in our models. The maximum surface subsidence in mantle lithosphere instability models is ~0.3 km, which is much less than that of the Arizaro basin (~1.5 km tectonic subsidence). If the crust is weak, the gravitational instability induces crustal flow and surface uplift above the root.
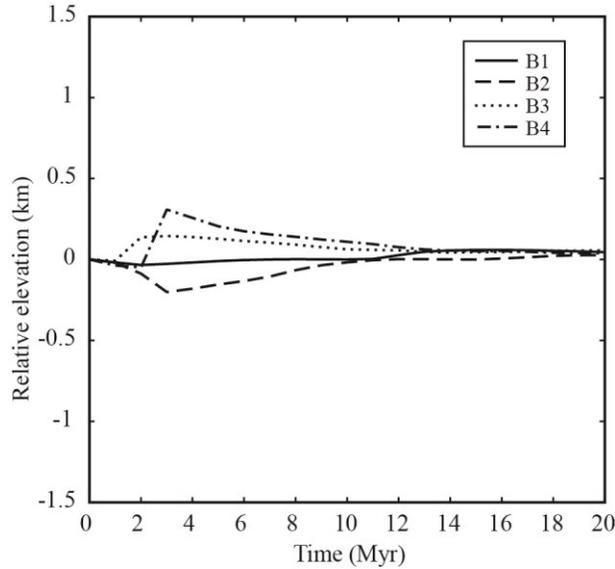
Figure 3.11. The evolution of the relative surface elevation above the R-T drip for a mantle lithosphere instability (Model Set B). The basin depth is the difference between the average elevation of the plateau and the elevation at the center of the surface deflection (at x=450 km).

3.6 Subduction model

In this section, we expanded the numerical models to include an oceanic plate (slab) which subducts below the continental plate, as found below the central Andes. This is motivated by the question of whether a subducting plate will act as a barrier to lithosphere removal (e.g., Kay and Coira, 2009). It also allows for a test of the effects of a realistic mantle flow (corner flow) on the foundering of a dense root. In this case, the mantle flow velocity and geometry are controlled by the dynamics of the subducting slab, rather than being artificially imposed as in the models shown above.

3.6.1 Model setup

We present a preliminary subduction model to investigate the effects of the slab and corner flow on the continental lithosphere removal. As in previous models, we place a dense root in the continental lithosphere to initiate lithosphere removal process. The initial geometry of the model is shown in Figure 3.12. The model domain has a

width of 2000 km and a depth of 900 km, extending from the Earth's surface to the lower mantle. The upper mantle extends to 660 km depth and overlies the lower mantle. The model consists of a 90 km thick oceanic plate with 9 km oceanic crust and a 100 km thick continent plate with 40 km crust (25 km upper crust and 15 km lower crust). A 112 km thick and 400 km wide plateau region is placed in the continental plate, assuming that this is the geometry that would be formed after shortening and thickening by subduction; the process of shortening is not modeled here. In the plateau block, the crust is 76 km thick (with a 48 km upper crust and 28 km lower crust) and 36 km thick mantle lithosphere, which is identical to Models A1 and A2 (Figure 3.3). An eclogite root is placed in the lower crust (with 50 km width and 28 km height). As in Model A2, the density of the root region starts at 3000 kg/m^3 (i.e., the density of the lower crust), and the root density is increased at 80 kg/m^3/Myr (to a maximum density of 3550 kg/m^3) to initiate lithosphere removal process.

At the side boundaries, the oceanic plate enters the model domain at 5 cm/yr (V_{oc}) and continent plate enters at 2 cm/yr (V_{cont}), giving a total convergence rate of 7 cm/yr, similar to the average velocities of Nazca and South America Plates (Oncken et al., 2006). A uniform outflux velocity is applied to the side boundaries of the sublithospheric mantle to maintain the constant mass in the model. A weak seed, ten times weaker than the continental upper crust, is placed between the oceanic plate and continent plate to initiate the subduction.

Table 3.3 shows the rheology and density structure of the model materials. In the model shown below, the continental forearc and craton are 10 times stronger than the plateau. The oceanic crust changes into eclogite when it enters the metamorphic eclogite stability field (Hacker et al., 2003). As the slab penetrates into the lower mantle, all the materials change to lower mantle material. This assumes that the mantle transition zone does not impede slab subduction. By "absorbing" materials into the lower mantle, the interactions between these materials and the model boundaries is reduced, allowing

subduction to run for a long period of time and for the slab geometry to reach a steady-state (Currie et al., 2008). This is clearly a simplification, and future models should address how the mantle transition zone may affect the slab geometry and evolution of the subduction zone.
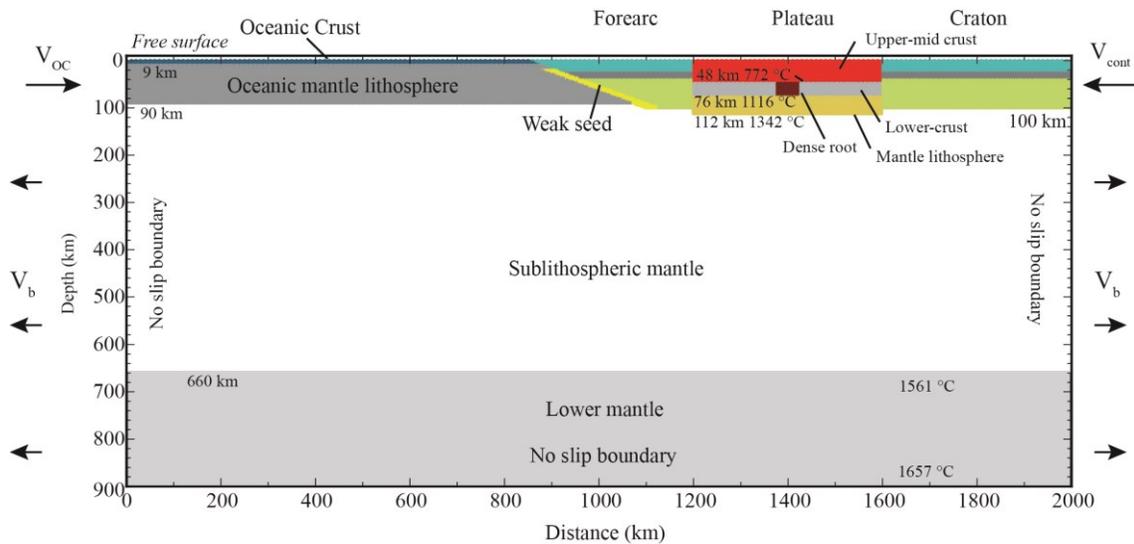
Figure 3.12. Initial geometry and boundary conditions for the full subduction model. The mesh (horizontal × vertical) is 5 km × 2.5 km in the upper 140 km of model, and 5 km × 10 km in the lower part of model.

Table 3.3. Material parameters in the numerical models

	Plateau upper-mid crust	Plateau lower crust	Plateau mantle lithosphere	Oceanic crust	Oceanic mantle lithosphere	Sublithospheric mantle
Plastic rheology						
c_0 (MPa)	20	0	0	1	0	0
ϕ_{eff}	15°	15°	15°	1°	15°	15°
Viscous rheology						
f	1	0.1	10	1	15	1
A (Pa^{-n} s^{-1})	1.10×10^{-28}	5.05×10^{-28}	3.91×10^{-15}	5.05×10^{-28}	3.91×10^{-15}	3.91×10^{-15}
B* (Pa s$^{1/n}$)^a	2.92×10^{6}	1.91×10^{5}	1.92×10^{4}	1.91×10^{5}	1.92×10^{4}	1.92×10^{4}
n	4.0	4.7	3.0	4.7	3.0	3.0
Q (kJ mol^{-1})	223	485	430	485	430	430
V* (cm^{3}mol^{-1})	0	0	10	0	10	10
Thermal parameters						
k (W m^{-1} K^{-1})	2.25	2.25	2.25	2.25	2.25	2.25
A_T (µW m^{-3})	1.15	0.55	0	0	0	0
c_p (J kg^{-1} K^{-1})	750	750	1250	750	1250	1250
Density						
ρ_0 (kg m^{-3})	2800	3000	3250	3000	3250	3250
T_0 (°C)	900	900	900	273	900	900
α (K^{-1})	3.0×10^{-5}	3.0×10^{-5}	3.0×10^{-5}	3.0×10^{-5}	3.0×10^{-5}	3.0×10^{-5}

^{a} $B^* = \left(2^{(1-n)/n}3^{-(n+1)/2n}\right)A^{-1/n}$. The term in brackets converts the pre-exponential viscosity parameter from uniaxial laboratory experiments (A) to the tensor invariant state of stress of the numerical models

3.6.2 Model results

The subduction model is run in three phases. The first phase is isostatic balancing. The model starts with a horizontal top boundary, but as the oceanic plate is denser than the continental plate, it will sink ~4 km to bring the two plates into isostatic balance. Phase 2 is subduction initiation using the imposed convergence velocities V_{oc} =2 cm/yr and V_{cont}=0 cm/yr. In this phase, the continental plate is 50 times stronger than the rheology given in Table 3.3 in order to prevent deformation in upper plate. During

subduction initiation, the weak seed descends into sublithospheric mantle and does not affect the subsequent evolution of the upper plate. In Phase 3, the velocities of oceanic and continental plate are changed to V_{oc} =5 cm/yr and V_{cont}=2 cm/yr as observed in the central Andes (Oncken et al., 2006). The rheology of the two plates is that given in Table 3.3.

Figure 3.13 shows the evolution of the model in Phase 3, where the listed time is the time since the start of this phase. The oceanic plate subducts below the continental plate at an angle of ~40° at 100-200 km depth. A corner flow with velocity at ~5 cm/yr is induced in the mantle wedge beneath plateau (Figure 3.13a). The velocity field is plotted every 14 Eulerian nodes. The greater corner flow imposes a stronger shear stress at base of lithosphere than that in Model Set A (which has an imported mantle flow velocity of 2 cm/yr). As subduction proceeds, the density in the eclogite root (dark red material) is increased at a rate of 80 kg/m^3/Myr. At 3.1 Myr, the density of the root is equal to that of mantle, and it becomes gravitationally unstable after this time. The root begins to visibility descend at ~6 Myr, and by ~8 Myr, a clear Rayleigh-Taylor instability has formed (Figure 3.13b). As the root destabilizes, it is sheared and carried toward the wedge corner by mantle flow. It then gets carried downward along the top of the subducting slab (Figure 3.13c). By 10 Myr, the head of the drip is in the deep upper mantle (>300 km depth), and by 14 Myr, nearly the entire root has been removed (Figure 3.13d).

At the surface, the thick crust of the plateau region has an elevation of ~4 km above the adjacent regions at the start of Phase 3 (Figure 3.13a). As the root becomes denser, the surface above the root subsides. At 8 Myr, the basin reaches its maximum depth of ~2.2 km relative to the surrounding plateau (Figure 3.13b). Then, the surface starts to uplift. Note that the uplift occurs while the root is still in the process of being removed (Figure 3.13c). At this time, uplift is due to crustal thickening above the root. After the root is removed (Figure 3.13d), the surface then undergoes isostatic uplift.

The topographic response to root removal is similar to that seen in the models with no subducting plate (e.g., Figure 3.3). However, the timescales and magnitudes are slightly different because of differences in the lithosphere structure and mantle flow geometry.

This model demonstrates that the subducting plate does not act as a barrier to removal, as previously suggested (e.g., Kay and Coira, 2009). Instead, the subduction-induced corner flow aids in the removal process by "sweeping" the root away. The root is carried into the deeper mantle by both its own negative buoyancy and by entrainment by the subduction-induced flow. It should be noted that the model here has a steep subducting slab. Further work is needed to determine how root removal may be affected if the subducting slab has a sub-horizontal geometry at shallow depth.
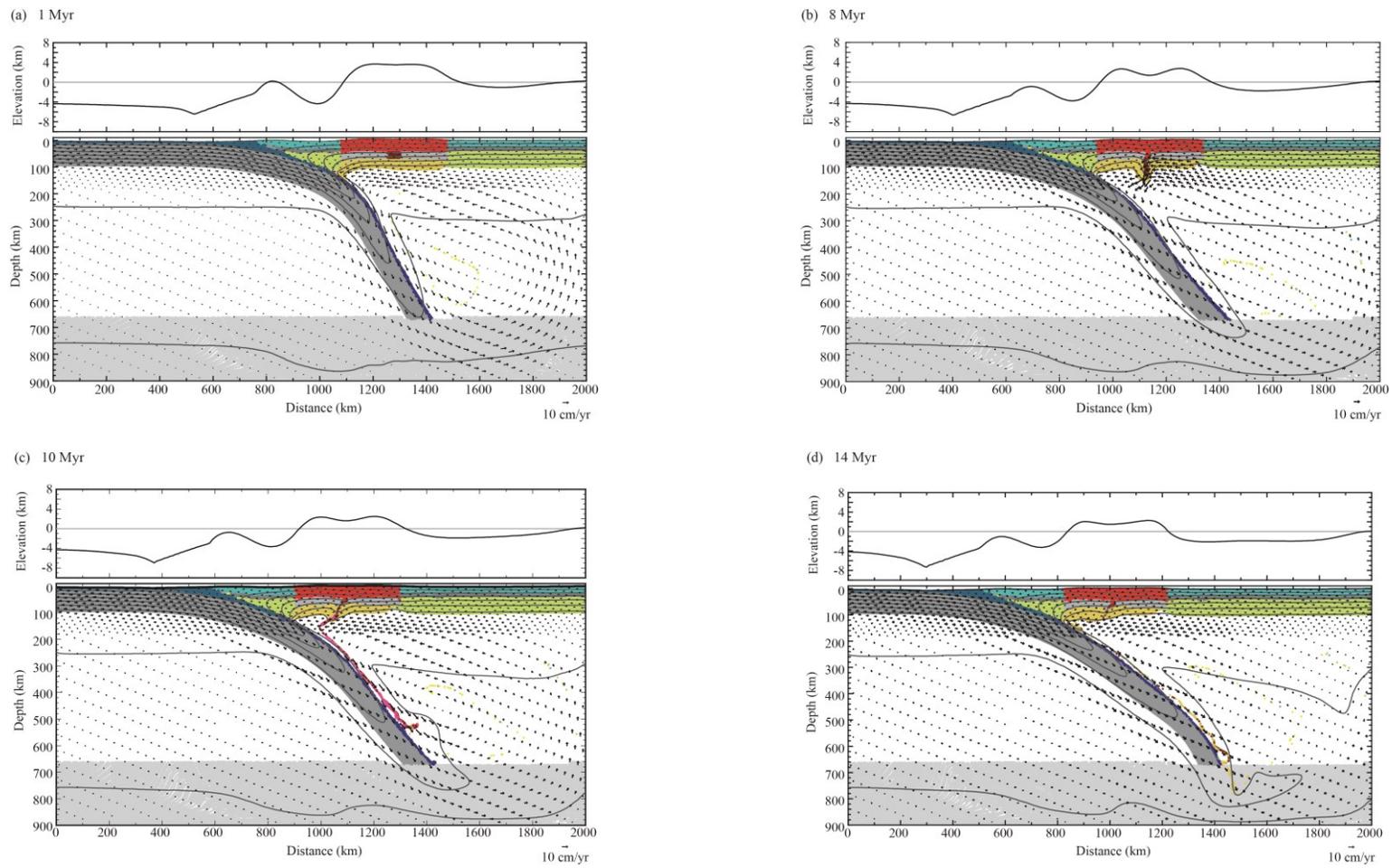
Figure 3.13. The evolution of the subduction model at (a) 1 Myr, (b) 8 Myr, (c) 10 Myr, and (d) 14 Myr since the start of phase three of the models (i.e., start of full subduction).

3.7 Discussion and conclusions

Local hinterland basins of the Altiplano-Puna plateau are enigmatic features that cannot be clearly linked to orogenic deformation or thrust loading (Garzione et al., 2006; Jordan et al., 2007; Horton, 2012; DeCelles et al., 2015). These basins appear to be transient features, as demonstrated by the sedimentary record of the Miocene Arizaro basin. The present Puna plateau contains several internally drained basins, such as the Salar de Arizaro, Salar de Pocitos, and Salar de Atacama basins. An analysis of the isostatic gravity field, derived from satellite gravity observations, shows that these basins are characterized by positive isostatic gravity anomalies (Figure 3.1c), consistent with high-density material beneath the surface. The wavelength of the gravity anomaly is generally 100-200 km, indicating a lithosphere origin for the density anomaly. It is proposed that hinterland basins may be related to local gravitational removal of high-density lithosphere as an RT-drip instability (e.g., DeCelles et al., 2015). This would explain both the gravity observations and the transient nature of the basins.

3.7.1 Summary of modeling results

The main goal of our study is to assess the dynamics of lithosphere removal and its surface expression, for cases in which the density anomaly ("root") is located in either lower crust (Model Set A) or mantle lithosphere (Model Set B). In our models, the root density increases over time to simulate the formation of high-density material through metamorphic or magmatic processes. In all cases, the root region undergoes gravitational removal as an RT-drip within 10 Myr of the time at which its density exceeds that of the underlying mantle. Longer removal times are observed in models in which the root densification rate is low or the root and underlying mantle lithosphere have a high viscosity. These timescales are consistent with the observed timescales for lithospheric RT-drips in other modeling studies (e.g., Houseman and Molnar, 1997; Jull and Kelemen, 2001; Elkins-Tanton, 2007; Göğüş and Pysklywec, 2008).

Table 3.4 summarizes the results of our models. To first order, the presence of the high-density root induces a subsidence of the overlying surface, followed by uplift as the density anomaly is gravitationally removed.   Initial subsidence occurs as an isostatic response to the development of the root, with more rapid subsidence occurring with a higher densification rate.   However, with a high densification rate, the root becomes gravitationally unstable at an earlier time and therefore the duration of subsidence is reduced. The geometry of the root also affects the surface expression. Subsidence is greater for a root located at a relatively shallow depth.   In additional models not presented here, we found that an increase in the width of the root increases the magnitude of surface subsidence and the width over which subsidence occurs but slightly decreases the duration of subsidence, owing to the enhanced negative buoyancy of the larger root region.

An important result from the models is that the crust overlying the root may undergo deformation during root removal, which can significantly alter the surface expression. The strength of the near-surface rocks primarily affects the wavelength over which the surface is deflected. If the near-surface rocks are relatively weak, surface deflection is more localized and is primarily controlled by the width of the dense root. A weak upper crust may be the result of an intrinsic low frictional-plastic strength associated with a high pore fluid pressure or weakness developed during deformation (e.g., Huismans and Beaumont, 2003). The surface expression of an RT-drip also depends on the strength of the deep crust, which is controlled by its viscous rheology. If the deep crust is relatively weak, the lateral pressure gradients associated with the presence of the high-density root can induce crustal flow. This is analogous to horizontal crustal flow that is driven by lateral pressure gradients associated with topographic variations (e.g., Beaumont et al., 2006 and references therein).   Flow velocities increase for either a weaker crust or denser root, leading to crustal thickening above the root and a diminished surface deflection. Such flow has been observed in

previous studies of RT-drips (e.g., Neil and Houseman, 1999, Pysklywec and Beaumont, 2004; Elkins-Tanton, 2007).

Table 3.4. Effects of key parameters on surface topography and crustal flow in numerical models of RT-drips. The number of the check marks indicates the magnitude of each the effect; more check marks indicates a greater effect. ML=mantle lithosphere.

Parameter change	Example of models	Surface elevation			Wavelength of basin	Duration of basin		Velocity of crustal flow	
		Greater subsidence	Limited subsidence	Uplift	Increase	Increase	Decrease	Increase	Decrease
Increase the depth of root	Set A vs. Set B		√√	√√			√√		√√
Increase the densification rate of root	A1 vs. A2	√					√√	√	
Increase the width of root					√√				
Weaken the crust	A1 vs. A3; B1 vs. B3; B2 vs. B4;		√√	√√			√	√√	
Strengthen the ML (weak crust)	B3 vs. B4			√		√		√	
Strengthen the ML (strong crust)	A1 vs. A4; B1 vs. B2	√				√		√	
Strengthen the near-surface rock	A1/A6 vs. A5		√		√√				
Add sedimentation	A1 vs. A7/A8 A2 vs. A9	√√				√			
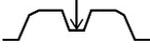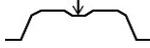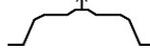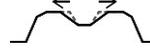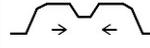
3.7.2 Surface expressions of RT-drips

Overall, we find that the two main controls on the surface expression of an RT drip are the depth of the high-density root and the strength of the crust overlying the root. Three main surface expressions are observed in the models: (1) surface subsidence of >500 m, followed by uplift (Figure 3.14a), (2) little surface subsidence (<200 m) (Figures 3.14b and 3.14c), and (3) surface uplift followed by collapse (Figure 3.14d).
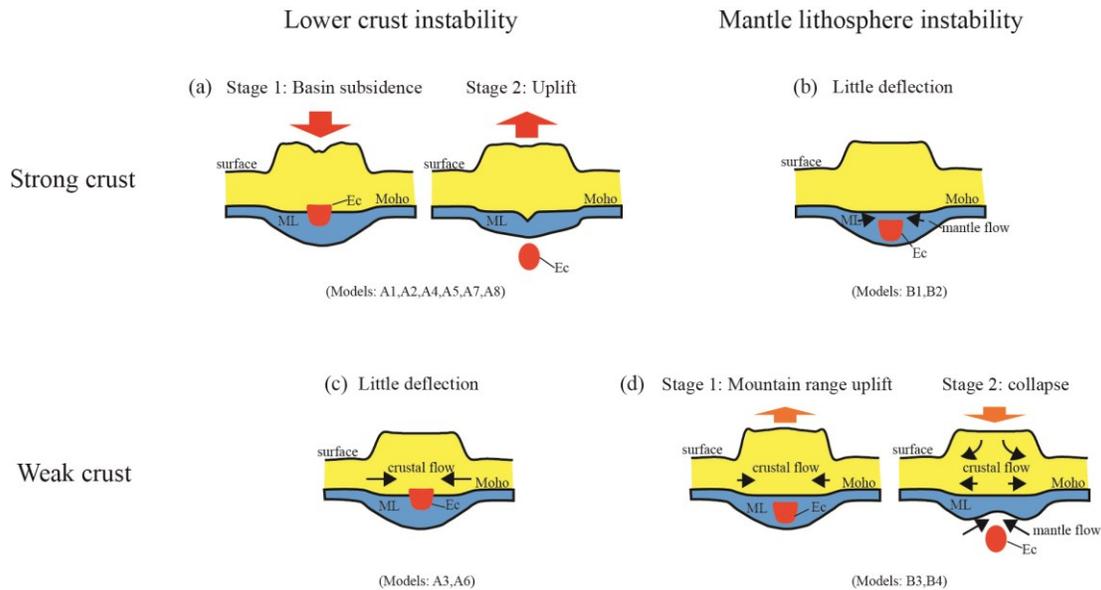
Figure 3.14. End-member models for the surface effects of Rayleigh-Taylor instabilities. (a) Lower crust instability with a viscously strong crust. The high density lower crustal root is removed as a RT-drip. The surface first subsides and then undergoes uplift as the crust thickens and the root is removed. (b) Mantle lithosphere instability with a viscously strong crust. Stresses associated with removal of the mantle lithosphere root are localized in the deep lithosphere and there is little surface deflection. (c) Lower crust instability with a viscously weak crust. Root removal induces crustal flow and there is little surface deflection. (d) Mantle lithosphere instability with a viscously weak crust. Root removal induces crustal thickening which uplifts the surface. After root removal, the topographic high collapses. Ec- eclogite; ML=mantle lithosphere.

The surface deflection depends on the degree of coupling between the root and the surface, which in part depends on the depth of the root. The viscous strength of the crust decreases with depth, owing to increasing temperatures (Figure 3.2c), and therefore a shallower root is overlain by relatively strong material, allowing greater

coupling between the root and near-surface material. Figure 3.15 compares the lithosphere strain rate field during root removal for Models A1 and B1; the only difference between the models is the root depth. For the model times shown, the roots in Model A1 and B1 have similar densities, 3360 kg/m^3 and 3420 kg/m^3 respectively. However, the crustal strain rate in Model A1 is significantly higher (Figure 3.15a), with a zone of high strain rate that originates from the dense crustal root and extends from the near-surface to the base of the lithosphere. The surface is depressed by stresses associated with root dynamics and a basin forms (Figure 3.14a). In contrast, a dense root located in the mantle lithosphere results in deformation localized in the deep crust and mantle lithosphere, with low strain rates in the shallower crust above the root (Figure 3.15b). In this case, the root dynamics are decoupled from the shallower crust, and there is little deflection of the surface (Figure 3.14b).
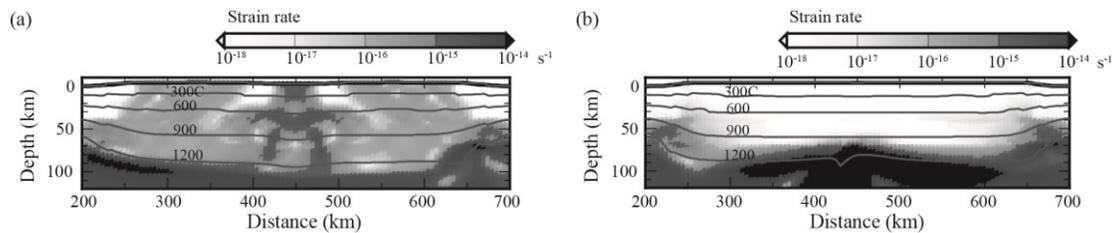
Figure 3.15. Strain rate field at the time of maximum basin depth for: (a) Model A1 (lower crust root) at 9 Myr, (b) Model B1 (mantle lithosphere root) at 3 Myr.

The other factor that determines coupling between the root and surface is the crustal viscosity. The reference models (A1 and B1) use rheological laws representative of dry, strong crustal rocks. If the crust is weaker than assumed, owing to a more felsic composition, hydration, or higher temperatures, the coupling stress between the root and surface decreases. For the weak crust end-members examined in this study, horizontal flow is induced in the weak crust, leading to crustal thickening above the root. For a crustal root, the rate of crustal flow approximately balances the rate at which the root descends and there is little surface deflection (Figure 3.14c). If the root is located in the mantle lithosphere, the rate of crustal thickening is sufficient to cause surface uplift of a few hundred metres (Figure 3.14d). Once the root is removed, the crust relaxes and the surface collapses to its original elevation.

Our models consider gravitational instabilities in a deformed and thickened but thinned orogen. In our models, the crust is thick (~70 km) and the Moho temperature is ~955°C, and therefore the deep crust is relatively weak, even for the strongest rheology tested in our study. As a result, a mantle lithosphere instability is only weakly coupled to the shallower crust, leading to a minor surface deflection. Models with thin crust and relatively thick lithosphere may give different results. In this case, the Moho temperature may be lower (<400°C) and the crust is strong, which increases the coupling between the crust and mantle lithosphere and enhances surface subsidence (e.g. Göğüş and Pysklywec, 2008). Such models may be important for understanding the origin of basins in continental interiors.

3.7.3 Comparison with the Miocene Arizaro basin

We now compare our model results with the geological record of the Miocene Arizaro Basin, which is taken as a representative example of a transient hinterland basin. DeCelles et al. (2015) summarize the evolution of the Arizaro basin. The subsidence history of the basin is given in Figure 3.16. Basin subsidence occurred from 21 to 8 Ma, to a maximum depth of ~3400 m, with an inferred ~1600 m of tectonic subsidence. The basin was subsequently exhumed and today its surface is ~500 m higher than its surroundings. Also shown on Figure 3.16 is the surface elevation above the RT drip for Models A2 and A9. Both models use the same parameters: a strong crustal rheology with frictional-plastic strain softening, and a crustal root with a densification rate of 80 kg/m^3/Myr; the difference is that Model A9 includes sedimentation (Table 3.2). These two models provide the best fit to the Arizaro basin observations including: (1) A symmetric basin of ~100 km width is formed, with greatest subsidence in the center. In 3D, this basin would exhibit a roughly circular shape. (2) A sigmoidal subsidence record is seen, with low subsidence during the first 1-3 Myr, followed by accelerating subsidence and then a decrease. Model A2 exhibits a maximum subsidence of ~1400 m. With the addition of sediments (Model A9), the total subsidence is ~3700 m. Small differences between the observed and modeled subsidence histories can be reduced with minor changes in the densification rate of the root and in the sediment thickness/density. (3) The basin undergoes minor internal

shortening (contraction) during formation. (4) The basin is then uplifted to a higher elevation than its surroundings. Uplift occurs as an isostatic response to removal of the dense root, low density associated with crustal thickening above the root and the presence of low-density basin sediments.
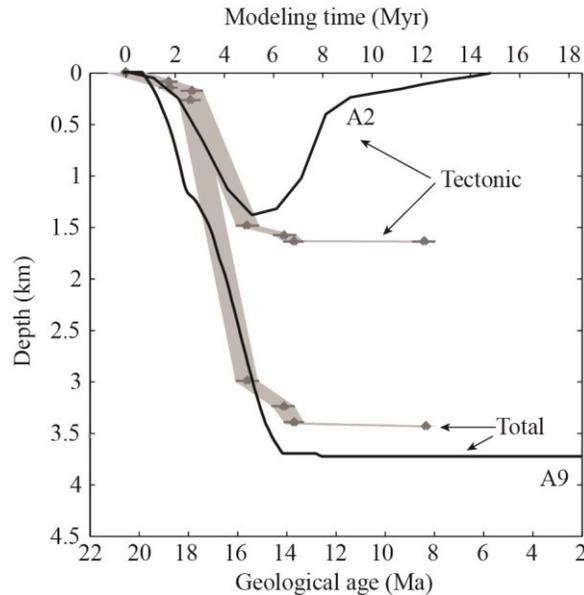
Figure 3.16. Comparison of the modeling results (Model A2 and A9, solid lines) with the subsidence history of Miocene Arizaro basin (grey circles). The grey envelop and error bars are uncertainties in the tectonic component of subsidence and total sediment accumulation of Arizaro basin (DeCelles, et al., 2015).

Both the overall subsidence pattern of the Arizaro Basin and its localized distribution are consistent with the surface deformation associated with gravitational removal of anomalously dense lithosphere. The Arizaro basin formed after the basement rocks of this part of the Puna plateau had already experienced orogenic shortening and crustal thickening (Carrapa et al., 2009). Our models demonstrate that in regions of thick crust, gravitational removal of a dense root will only create a significant surface deflection if the root is located within the crust and the crust is relatively strong (Figure 3.14a). Therefore, we favour a crustal origin for the root, possibly related to progressive metamorphic eclogitization of metastable granulitic crust or the emplacement of eclogitic magmatic restites (e.g., Kay and Kay, 1993; Leech,

2001; Kay and Coira, 2009). Even with a strong crust, gravitational instability of the root can induce flow in the deep crust if the temperature is relatively high. As a result, the crust will thicken as the root destabilizes, and the maximum subsidence and the onset of basin inversion may predate the time of root detachment.

Our study has primarily focussed on the topographic expression associated with an RT-drip. There are a number of other observations that may also be used to constrain the dynamics of this process. For example, after root detachment, the crust may be characterized by a V-shaped Moho with thickened crust in the former root region (e.g., Figure 3.3). This geometry has been proposed to explain seismic data for the Sierra Nevada region of California, where root detachment has been inferred (Zandt et al., 2004). For the Arizaro region, ambient noise tomography images show that the lower crust has a low velocity and could be formed by downwelling of lower crust under the basin (Beck et al., 2015). Other seismic studies suggest that the crust may actually be thinner than surrounding regions (Yuan et al., 2002; Bianchi et al., 2012). However, these studies have only sparse data coverage of this area and may not be able to resolve Moho variations on lateral scales less than 50 km. Removal of a dense root may also be associated with magmatism, produced by melting of the descending root material, decompression melting of upwelling asthenosphere, and melting of the remaining continental lithosphere (e.g., Elkins-Tanton, 2007; Chapter 6). Geochemical data for mafic magmatism in parts of the Altiplano-Puna plateau are consistent with small-scale (<50 km width) convective instabilities over timescales of 1-5 Myr (Ducea et al., 2013). This is consistent with the scale and timing of the instabilities in our models, but further work is needed to assess whether the material in our models will melt.

Chapter 4

Topographic expressions of Rayleigh-Taylor instability

Abstract

Two-dimensional thermal-mechanical numerical models show that Rayleigh-Taylor-type (RT) gravitational removal of high-density lithosphere may produce significant surface deformation (vertical deflection >1000 m) in the interior of a continental plate. A reasonable range of crustal strengths and thicknesses, representing a variation from a stable continental interior with thin crust to a hot orogen with a thick crust, is examined to study crustal deformation and the surface deflection in response to an RT instability. In general, three types of surface deflection are observed during the RT drip event: (1) subsidence and negative topography; (2) uplift and positive topography; (3) subsidence followed by uplift and inverted topography. One key factor that determines the surface expression is the crustal thickness. Models with a thin crust mainly show subsidence and develop a basin. In the thick crust models, surface expressions are more variable, depending on the crustal strength and depth of high-density anomaly. With weak crust and a deep high-density anomaly, the RT drip is decoupled from the overlying crust, and the surface exhibits uplift or little deflection, as the RT drip induces contraction and thickening of the overlying crust. In contrast, with a strong crust and shallow anomaly, the surface is more strongly coupled with the drip and undergoes subsidence, followed by uplift.

4.1 Introduction

For many continental plates, significant deformation has occurred in the interior of the plate, far from the plate boundary. In some cases, the deformation can not be clearly linked to plate tectonic processes. For example, anomalous surface subsidence has been observed in several cratonic regions, such as the Williston, Illinois and Michigan basins in North America (e.g., Naimark and Ismail-Zadeh, 1995) and the Congo basin in Africa (Downey and Gurnis, 2009). In the interior of Australia, a range of vertical surface motions has been observed, including subsidence in the Canning basin in western Australia and uplift of Mt. Isa in northern Australia (Pysklywec and Beaumont, 2004 and references therein). Significant vertical surface deflection has also been observed in the interior of orogenic belts. The Wallowa Mountains in western North America and the Arizaro basin in the central Andes are local areas (~100 km wide) where geological data shows that the surface first underwent subsidence and then was uplifted and eroded (Hales et al., 2005; DeCelles et al., 2015). In both cases, the total surface deflection is more than 1 km, and it does not appear to be related to orogenic deformation processes.

In recent years, geodynamic studies have shown that the Earth's surface can be significantly perturbed by subsurface convective processes, including foundering of cold and dense deep lithosphere and upwelling of hot mantle (e.g. Neugebauer, 1983; Houseman and Molnar, 1997; Pysklywec and Beaumont, 2004; Elkins-Tanton, 2007), and internal crustal deformation, such as ductile flow in hot, weak crust (Beaumont et al., 2006). These factors induce a stress on the Earth's surface, which can create a surface deflection which can occur within the interior of a tectonic plate. In this study, we focus on surface deflections associated with gravitational foundering of dense lower lithosphere, which is argued to be an important process for recycling the lithosphere into the deeper mantle. As described below, such foundering can occur within the interior of a continental plate, and therefore this may be a mechanism for inducing intraplate deformation and anomalous subsidence/uplift.

Previous studies have shown that high density regions of the lithosphere may undergo gravitational instability and removal as a Rayleigh-Taylor-type downwelling or RT drip (e.g., Houseman et al., 1981; Houseman and Molnar, 1997). This type of

removal is distinct from delamination which involves lithosphere removal through peeling along a weak layer within the lithosphere (Bird, 1979). Numerical models of delamination show that this produces a wave of surface uplift and subsidence that migrates with the detachment point of the delaminating lithosphere (Sobolev et al., 2006; Göğüş and Pysklywec, 2008; Krystopowicz and Currie, 2013). In contrast, an RT drip does not migrate laterally and can produce an observable near-circular deflection of the Earth's surface above the drip (Neil and Houseman, 1999; Göğüş and Pysklywec, 2008). An RT drip is driven by the density contrast between dense lithosphere and the less dense asthenosphere. Lithosphere is cooler and therefore it is intrinsically more dense than the hotter asthenosphere. Gravitational removal as an RT drip can be induced by any lateral variation in thermal structure (e.g., a perturbation of the lithosphere and asthenosphere boundary (LAB); Houseman and Molnar, 1997). High density may also arise from variations in composition, such as the formation of high density eclogite through metamorphic phase changes or arc magmatic processes (Kay and Kay, 1993; Conrad and Molnar, 1997; Elkins-Tanton, 2007).

In the regions discussed above, the local nature of the deformation and the near-circular shape of the surface deflection suggest that the anomalous surface uplift/subsidence may be related to an RT drip. The overall vertical motion associated with an RT drip depends on the dynamics of the drip, as well as the strength of the crust. To first order, the surface deflection is the sum of isostatic and dynamic factors. Lateral density variations will produce variations in surface topography through isostatic adjustment, resulting in subsidence above the dense body. As the RT drip develops, the dynamic stresses associated with lithosphere destabilization may also deflect the surface. Initially, the surface should subside, but then may undergo uplift as the drip is removed and low density material upwells to fill the space (e.g. Göğüş and Pysklywec, 2008; Molnar and Houseman, 2013).

However, the surface response is modulated by crustal deformation induced by the RT drip. As the dense body destabilizes, the dynamic stresses may be large enough to cause lateral crustal deformation (Pysklywec and Shahnas, 2003). Neil and Houseman (1999) used analytic models to calculate the crustal deformation caused by an RT instability for a two-layer lithosphere (crust and mantle), with a uniform density

and viscosity for each layer. They found that if the crust is relatively weak (no more than 13 times stronger than the mantle lithosphere), it may experience thickening and contraction as dense mantle lithosphere downwells. Crustal thickening will counteract the surface subsidence produced by the RT drip and lead to surface uplift.

The feedback between the RT drip and crustal deformation has been demonstrated to be important in modifying the surface expression (e.g. Neil and Houseman, 1999; Pysklywec and Beaumont, 2004). The crustal response to the RT drip not only depends on the crustal viscosity but also the crustal thickness. In continental plates, crustal thickness varies from ~20 km in extensional regions to ~80 km in collision orogens. To date, most geodynamic studies of RT drips have focused on regions with a thin crust (~40 km thick) that is relatively cool and strong, representative of continental interior regions; in these studies there is little crustal deformation associated with the drip (e.g., Pysklywec and Beaumont, 2004; Göğüş and Pysklywec, 2008). For significant deformation to occur, an additional weakening mechanism (e.g. crustal heating through local radiogenic heat production) is needed (Pysklywec and Beaumont, 2004).

As noted above, RT drips may also occur in orogenic belts, where the crust is 60-80 km thick. DeCelles et al. (2014) suggest that RT drips may be the cause of transient basins that are found in the hinterland of the central Andes. These basins are local regions which experienced anomalous subsidence, internal contraction and uplift, with no apparent link to regional orogenic deformation. Magmatic records from Tibet have been interpreted to reflect lithosphere removal through an RT drip, but there does not appear to be an obvious surface deflection (Turner et al., 1996).

In this study, we present numerical models to demonstrate the range of surface deflections that may occur as lithosphere is removed through an RT drip. The numerical models have a stress-free upper boundary, which allows surface topography to develop self-consistently above the RT drip. We investigate the effect of crustal thickness on the surface expression of lithosphere removal, including models with a thin crust (i.e., continental interior) and a thick crust (i.e., orogen). Kruse et al. (1991) showed that crustal thickness controls the deformation that may be induced by lateral variations in surface topography; increased crustal thickness results in greater crustal

deformation. Here, we assess whether crustal thickness affects the deformation caused by an RT drip. We also consider the effect of the origin of the density anomaly (mantle or crust) that drives the RT drip. Most previous studies have considered that the density anomaly is in the mantle lithosphere. However, regions with thick crust may contain dense eclogitized lower crust (e.g., Kay and Kay, 1993), which may initiate an RT drip. To date, there have only been limited studies of crustal RT drips (e.g., Wang et al., 2015; see Chapter 3). Through a systematic series of numerical model tests, we quantify the surface response (uplift or subsidence) to an RT drip for variations in crustal thickness, crustal strength and the depth of the density anomaly. We show that the surface deflection can be explained by examining the feedback between the dynamics of the RT drip and crustal deformation induced by the removal event.

4.2 Numerical modeling methodology

4.2.1 Model geometry and material properties

The numerical models are designed to study the dynamics of the crust and upper mantle during gravitational removal of a high density region in the lithosphere. The model domain is 900 km wide and 400 km deep, with a 60 km thick continental lithosphere (25 km thick upper crust, 15 km lower crust and 20 km mantle lithosphere) overlying sublithospheric mantle (Figure 4.1a). The lithosphere is divided into an 800 km wide central region, with two 50 km wide blocks at either side, which are five times stronger than the central region. Tests show that the presence of these blocks does not affect the dynamics of the RT drip or the response of the crust and surface. The top surface of our model is stress-free, such that topography can develop in response to the underlying dynamics. The side boundaries have no vertical velocity and the basal boundary is free slip.

In the models below, we vary the crustal strength of the central region to study how this affects the surface response to an RT drip. We consider two crustal thicknesses: Model Set A has a crustal thickness of 40 km, typical of continental interior regions and Model Set B has a crustal thickness of 76 km, consistent with orogenic areas such as the central Andes and Tibetan Plateau. This set of models includes an initial phase of crustal thickening. The model starts with the geometry

shown in Figure 4.1 (40 km thick crust), and strong lithosphere is introduced through the side boundaries of the model. Deformation is localized in the weaker central region, resulting in pure shear thickening. After 380 km of shortening, the crust is 76 km thick. Owing to the thicker crust, the surface isostatically uplifts to ~3.8 km above its original elevation. At this point, shortening is stopped and a density anomaly is introduced to generate an RT drip (see below).
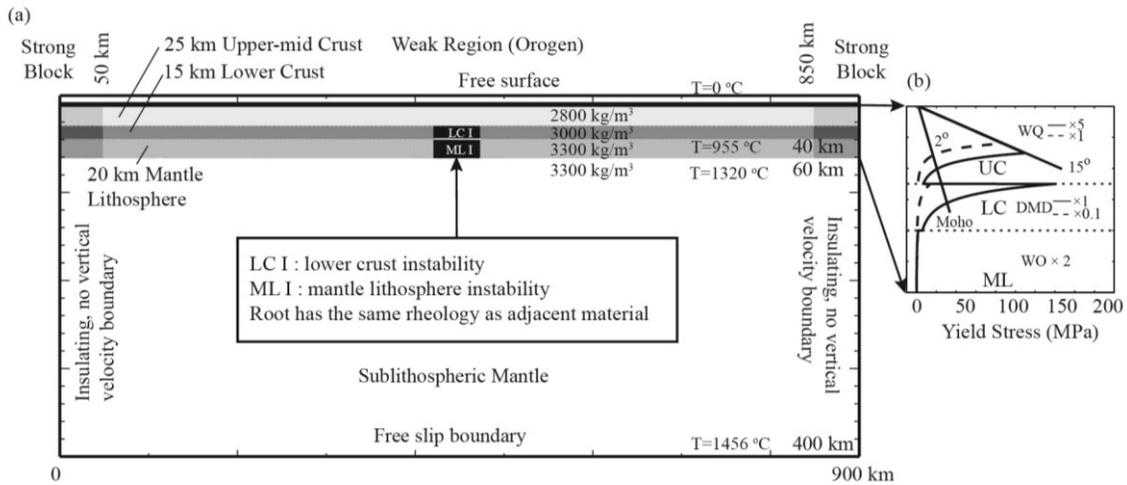
Figure 4.1. Numerical model set-up. (a) Initial model geometry and thermal-mechanical boundary conditions. Material parameters are given in Table 4.1. (b) The strength profiles for orogen lithosphere. The lines, 15º and 2º, show the frictional-plastic yield stress for unsoftened and softened materials, respectively. Solid lines show the viscous rheology used for strong crust models; dashed lines are weak crust models, based on variations in the scaling factor f. The model thermal structure and a strain rate of 10^{-15} s^{-1} are used for the calculations. UC=upper-mid crust; LC=lower crust; ML=mantle lithosphere; WQ=wet quartzite; DMD=dry Maryland diabase; WO=wet olivine.

We use the finite element code SOPALE to calculate the coupled 2D thermal-mechanical evolution of lithosphere and upper mantle, under the assumptions of incompressibility, plain strain and zero Reynolds number (Fullsack, 1995). The modeling uses an arbitrary Lagrangian-Eulerian approach, in which calculations are performed on an Eulerian grid and material properties are advected using Lagrangian points. The Eulerian mesh has 180×56 elements with a resolution of 5 km $\times$ 2.5 km in the upper 140 km of the model, and 180×26 elements with a resolution of 5 km $\times$ 10

km in the lower 260 km.

Table 4.1 gives the thermal properties of all model materials. The initial temperature structure of the model is calculated using these properties, a constant temperature of 0°C at surface, and 1456°C at the base of the model. This yields a surface heat flow of 72 mW/m^2, with a Moho temperature of 955°C and a temperature of 1320°C at the base of the lithosphere (Figure 4.1a). Note that this thermal structure is much hotter than expected for an average continental interior (Currie and Hyndman, 2006). As discussed below, we also vary the rheology of the crustal materials. The strong end-member can be taken to represent the behavior of cooler crust. The sublithospheric mantle has an artificially high thermal conductivity to approximate heat transfer by a convecting mantle, which is not explicitly modeled here (Pysklywec and Beaumont, 2004). This maintains a nearly constant heat flux into the base of the lithosphere and an adiabatic thermal gradient of 0.4°C/km in the sublithospheric mantle.

The materials in the model have a temperature-dependent viscous-plastic rheology (Fullsack, 1996; Willett, 1999), using parameters in Table 4.1. These parameters are consistent with those used in previous modeling studies of continental lithosphere dynamics (e.g., Beaumont et al., 2006) and have been chosen from a few reliable laboratory studies. At stresses above the frictional-plastic yield, material deformation follows a Drucker-Prager yield criterion. We include frictional strain softening to approximate rock weakening due to pore fluid variations, fault gouge formation and mineral reactions during deformation (Huismans and Beaumont, 2002 and 2003; Warren et al., 2008). At lower stresses, the material deforms through viscous creep. The upper crust, lower crust and mantle use the parameters for wet quartzite (Gleason and Tullis, 1995), dry Maryland diabase (Mackwell et al., 1998) and wet olivine (Karato and Wu, 1993), respectively. We include a scaling parameter (*f*) (Equation 2.9) to linearly scale the model viscosity relative to the base laboratory rheologies (Beaumont et al., 2006). This allows us to test reasonable variations in material strength that may arise from moderate changes in composition, water content, and temperature or uncertainties in the rheological parameters.

Table 4.1. Material parameters in the reference numerical models

	Upper crust	Lower crust	Mantle lithosphere	Sublithospheric mantle
Model geometry				
Thickness in Thin Crust Model (km)	25	15	20	340
Thickness in Thick Crust Model (km)	48	28	36	292
Plastic rheology[a]				
c_0 (MPa)	2	2	0	0
ϕ_{eff}	15° - 2°	15° - 2°	15°	15°
Viscous rheology[b]				
f	5	1	2	1
A (Pa^{-n} s^{-1})	1.10×10^{-28}	5.05×10^{-28}	3.91×10^{-15}	3.91×10^{-15}
B* (Pa s$^{1/n}$)^{c}	2.92×10^6	1.91×10^5	1.92×10^4	1.92×10^4
n	4.0	4.7	3.0	3.0
Q (kJ mol^{-1})	223	485	430	430
V* (cm^3 mol^{-1})	0	0	10	10
Thermal parameters				
k (W m^{-1} K^{-1})	2.25	2.25	2.25	102.5
A_T (μW m^{-3})	1	0.4	0	0
c_p (J kg^{-1} K^{-1})	750	750	1250	1250
Density[d]				
ρ_0 (kg m^{-3})	2800	3000	3300	3300
T_0 (K)	900	900	900	900
α (K^{-1})	3.0×10^{-5}	3.0×10^{-5}	3.0×10^{-5}	3.0×10^{-5}

Note: [a] Frictional-plastic deformation follows a Drucker-Prager yield criteria with cohesion (c_0) and effective internal angle of friction (ϕ_{eff}): $J_2' = P\sin\phi_{eff} + c_0\cos\phi_{eff}$. Strain softening is implemented by decreasing ϕ_{eff} from 15° to 2° over accumulated strain of 0.5 to 1.5.

[b] Viscous deformation follows a temperature-dependent power-law rheology, with an effective viscosity given by: $\eta_{eff}^v = f(B^*)(\dot{I}_2')^{\frac{1-n}{n}}\exp((Q + PV^*)/nRT_K)$, where f is a scaling factor (see text), $\dot{\varepsilon}_{ij}$ is the strain rate, R is the gas constant, T_K is the temperature in degrees Kelvin, and B*, n, Q, and V* are the pre-exponential viscosity parameter, stress exponent, activation energy and activation volume from laboratory experiments.

[c] $B^* = (2^{(1-n)/n}3^{-(n+1)/2n})A^{-1/n}$. The term in brackets converts the pre-exponential viscosity parameter from uniaxial laboratory experiments (A) to the tensor invariant state of stress of the numerical models

[d] All materials have a temperature-dependent density, given by $\rho(T) = \rho_0[1 - \alpha(T - T_0)]$ where ρ_0 is the reference density at temperature T_0 and α is the volumetric thermal expansion coefficient.

We have tested two crustal strengths (Figure 4.1b). The reference model uses a strong crust, with *f*=5 for upper crust and *f*=1 for lower crust to approximate a strong, dry quartzo-feldspathic upper crust and a strong lower crust with refractory, intermediate granulite rocks. This could also represent a region with a wet, silica-rich

crust that has lower temperatures than in our models. For example, in the upper crust, viscosity can be increased by a factor of 5 by decreasing temperatures by ~110°C, and in the lower crust, viscosity can be increased by a factor of 10 by decreasing temperatures by ~120°C. We also test the effects of a weaker crust, possibly related to higher fluid content or a composition change, using f=1 and f=0.1 for upper and lower crust respectively. In all models, the sublithospheric mantle has f=1 and the mantle lithosphere has f=2, assuming that it is relatively water-poor due to dehydration and melt depletion effects during lithosphere formation.

4.2.2 Origin of the density anomaly

An RT drip is modeled by introducing a high density region (root) in either the mantle lithosphere or lower crust (Figure 4.1a). A mantle lithosphere root may be attributed to either the presence of high density magmatic rocks or a perturbation of the LAB. As magmatic rocks are emplaced in the mantle lithosphere, partial melting of the surrounding lithosphere and melt differentiation may produce an eclogite-rich residue within the lithosphere (e.g., Ducea, 2001; Richards, 2003). The density of the residue can be as much as 3500 to 3600 kg/m^3 (Jull and Kelemen, 2001; Ducea, 2002), which is 250-300 kg/m^3 higher than the underlying mantle. The presence of a high density magmatic lens has been proposed to explain the occurrence of intracratonic basins in North America (Naimark and Ismail-Zadeh, 1995). The other possibility is that an RT-type instability may be induced by perturbation of the LAB (Houseman and Molnar, 1997; Molnar and Houseman, 2004). In this case, the driving mechanism of the RT-instability is the thermal downwelling of the LAB, forming a locally cool and dense mantle lithosphere. In our models, we use a high density root in the mantle lithosphere to simulate a growing instability, instead of imposing perturbation at the LAB.

In the lower crust, the high-density region may reflect either magmatic eclogite that has been formed through magmatic differentiation within the crust, or a local area of crust that has undergone metamorphic eclogitization. Eclogitized crust can have a density of up to 3550 kg/m^3 (e.g., Christensen and Mooney, 1995; Bousquet et al., 1997), making it denser than the mantle. Metamorphic eclogitization usually requires temperatures >400 °C and pressures > 1.2 GPa in the lithosphere (e.g., Bousquet et al.,

1997), and thus it may be limited to areas with a crustal thickness greater than ~45 km. Field and laboratory data indicate that the eclogite phase change requires the presence of water, which may lead to local zones of eclogitization, adjacent to unreacted rocks (e.g., Austrheim, 1991; Leech et al., 2001; Jackson et al., 2004).

In our study, we focus on the effects of a density anomaly in the mantle lithosphere or lower crust, rather than the mechanism of formation. A root is placed in either the mantle lithosphere or lower crust (Figure 4.1a). Initially, this region has the same density and rheological properties as the adjacent material. Its density is then gradually increased at a prescribed rate to simulate either progressive eclogitization through magmatic or metamorphic processes, or a growing LAB perturbation. The maximum root density is the density of pure eclogite, 3550 kg/m^3. In all cases, once the root becomes denser than the underlying mantle, it is gravitationally unstable and undergoes removal as an RT drip. Our goal is to assess how variations in the location of the drip and crustal thickness and strength affect the evolution of surface topography as the high-density material is removed. Table 4.2 lists all the models presented in this Chapter.

4.3 Results

4.3.1 Thin crust models

In Model Set A, we test the effects of a localized high density root in a region with thin crust. The root is located in the mantle lithosphere and undergoes densification at a rate of 50 kg/m^3/Myr. Figure 4.2a shows the dynamics of Model A1 (Table 4.2), in which the crust is relatively strong (Table 4.1). Because the root material begins with the same density of the mantle, it becomes gravitationally unstable as soon as its density increases. Its negative buoyancy causes it to descend. By ~3 Myr, the lower part of the root has detached from the lithosphere. Some of the adjacent mantle lithosphere is entrained by the drip. The uppermost part of the root remains in the lithosphere, owing to the strong coupling with the crust.

Table 4.2. List of models showing parameter variations tested in this study. Changes in crustal strength are implemented through variations in the viscosity scaling factor (f) for crust materials. ML is mantle lithosphere and LC is lower crust.

Model	Model type	Parameter	Upper crust	Lower crust	Mantle lithosphere
MODEL SET A: Thin crust (40 km thick – average continental crust)					
A1 (reference)	Strong crust & ML instability	f	5	1	2
A2	Weak crust & ML instability	f	1	0.1	2
MODEL SET B: Thick crust (76 km thick – orogen crust)					
B1	Strong crust & ML instability	f	5	1	2
B2	Weak crust & ML instability	f	1	0.1	2
B3	Strong crust & LC instability	f	5	1	2
B4	Weak crust & LC instability	f	1	0.1	2

Figures 4.2a and 4.3 show that the presence and removal of the high-density root lead to a shallow basin above the drip. The surface initially undergoes subsidence, primarily as an isostatic response to the root. Subsidence is slow at first, but then increases to a maximum at 1-2 Myr, resulting in a maximum basin depth of ~94 m. As the root detaches between 2 and 3 Myr, the subsidence rate decreases and there is a minor uplift of the surface. By 20 Myr, well after drip detachment, the surface in this region is still ~57 m lower than the surroundings. This is likely related to the residual root material. Figure 4.2c shows the horizontal velocity of the surface and Figure 4.2d shows the vertical velocity profile of the crust at distance 420 km (i.e., at the edge of the root). In both plots, the velocity is zero during root removal, indicating that there is no internal deformation of the crust.
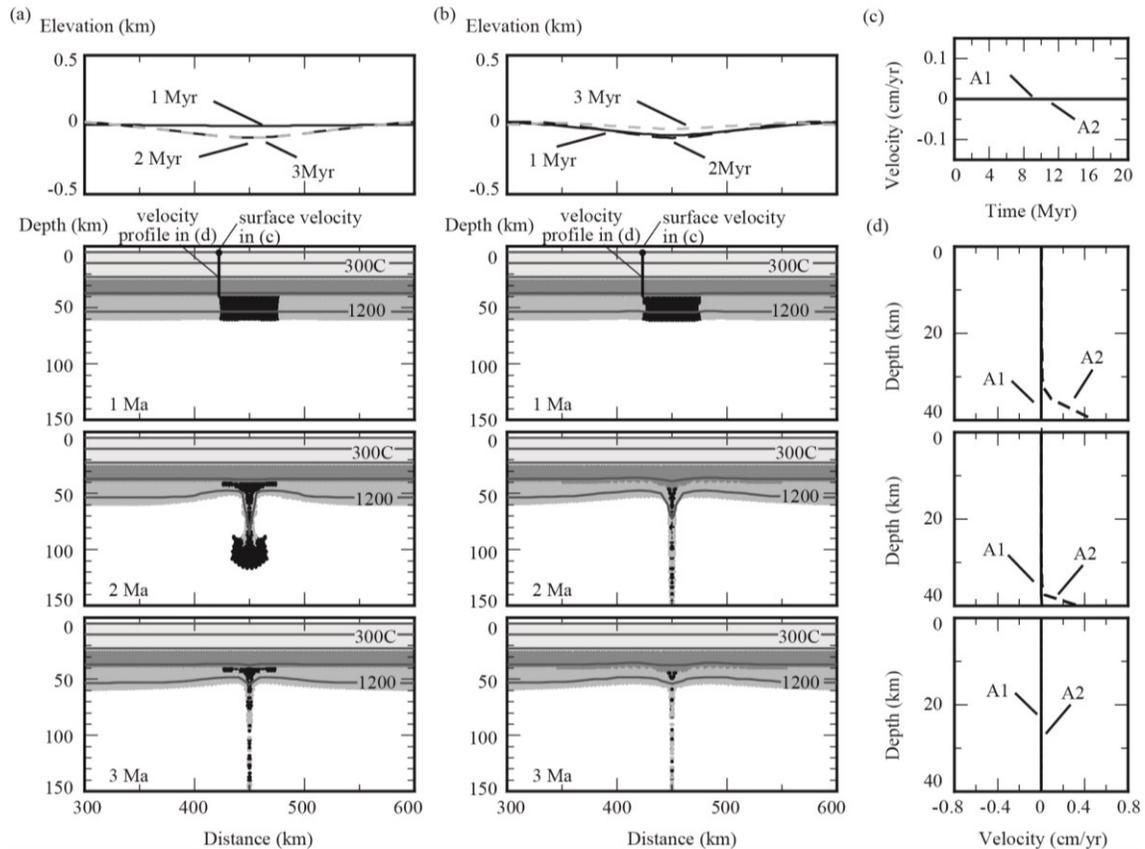
Figure 4.2. (a) Surface topography and model geometry of Model A1 at the given time after the start of the model run. (b) Surface topography and model geometry of Model A2 at the given time after the start of the model run. (c) Evolution of the horizontal surface velocity at x=420 km. (d) Crustal flow velocity profile at x=420 km at the time given in Figure 4.2a and 4.2b.

We have also tested a model in which the crust is weak (Model A2), by decreasing the viscosity scaling factor (*f*) for the upper and lower crust (Table 4.2). The other model parameters are the same as in Model A1. Figure 4.2b shows the evolution of Model A2. With the increasing density, the root becomes unstable and is removed by ~2 Myr; the weaker crust enables more rapid root detachment than in Model A1. Because of the weaker coupling between the crust and mantle lithosphere, less residual root is left at the base of the crust compared to Model A1. As the root is removed, the surface above it subsides to a maximum of ~95 m. After 2 Myr, the surface begins to uplift. Between 2 and 3 Myr, the uplift rate is fast, ~65 m/Myr, and then it slows down to ~2m/Myr. At 20 Myr, the surface sits at almost same elevation as its surroundings

(Figure 4.3a). As shown in Figure 4.2b, the lower crust is thickened during the root foundering process. Figure 4.2d shows a positive crustal flow at the base of lower crust, along with the downwelling of root. The crustal thickening reduces the surface depression and then contributes to surface uplift following root removal. Models in this Chapter do not have sedimentation process, which will deepen the basins (studied in the Chapter 3).
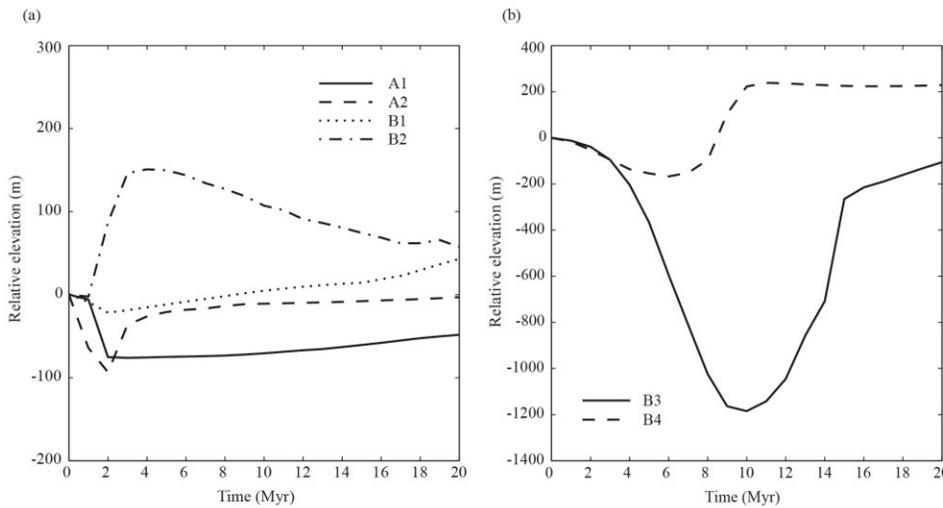
Figure 4.3. Relative elevation of the surface directly above the center of the RT drip. The elevation is relative to the elevation of the surrounding region (Negative means basin; Positive means mountain). (a) Model A1, A2, B1 and B2. (b) Model B3 and B4.

4.3.2 Thick crust models

In Model Set B, we examine an RT drip in a region where the crust is ~76 km thick and the elevation is ~3.8 km, i.e., an orogen. The plot of Model B1 at 0 Myr (Figure 4.4a) shows the lithospheric structure at the start of the model, after the lithosphere has been thickened. We first test the effect of a high-density root in the mantle lithosphere, where the root has the same width as that in the thin crust models (Models A1 and A2). As the thickness of the root has increased during lithosphere shortening, we increase the density of the root at 26.3 $kg/m^3/Myr$, such that the root has the same negative buoyancy as the root in the thin crust models.

We have tested models with a strong and a weak crust, using the same

parameters as in Model Set A (Table 4.2). In Model B1, the crust is strong and the dense root is gravitationally removed at 2 Myr (Figure 4.4a). Above the root, the surface subsides to only ~22 m at the time of root removal, followed by slow surface uplift to an elevation ~40 m higher than the original elevation (Figure 4.3a). This is primarily an isostatic response to lithospheric thinning in this region. In Model B2, the weaker crust allows the root to detach at a slightly earlier time than in Model B1, and root removal causes the crust to thicken (Figure 4.4b). There is initially little surface deflection above the root, but at 1 Myr, the surface begins to uplift owing to crustal thickening (Figure 4.3a). At 4 Myr, after the root has detached, the surface above the root is ~150 m higher than its surroundings. It then starts to subside, as the thickened crust deflates (Figure 4.4b).
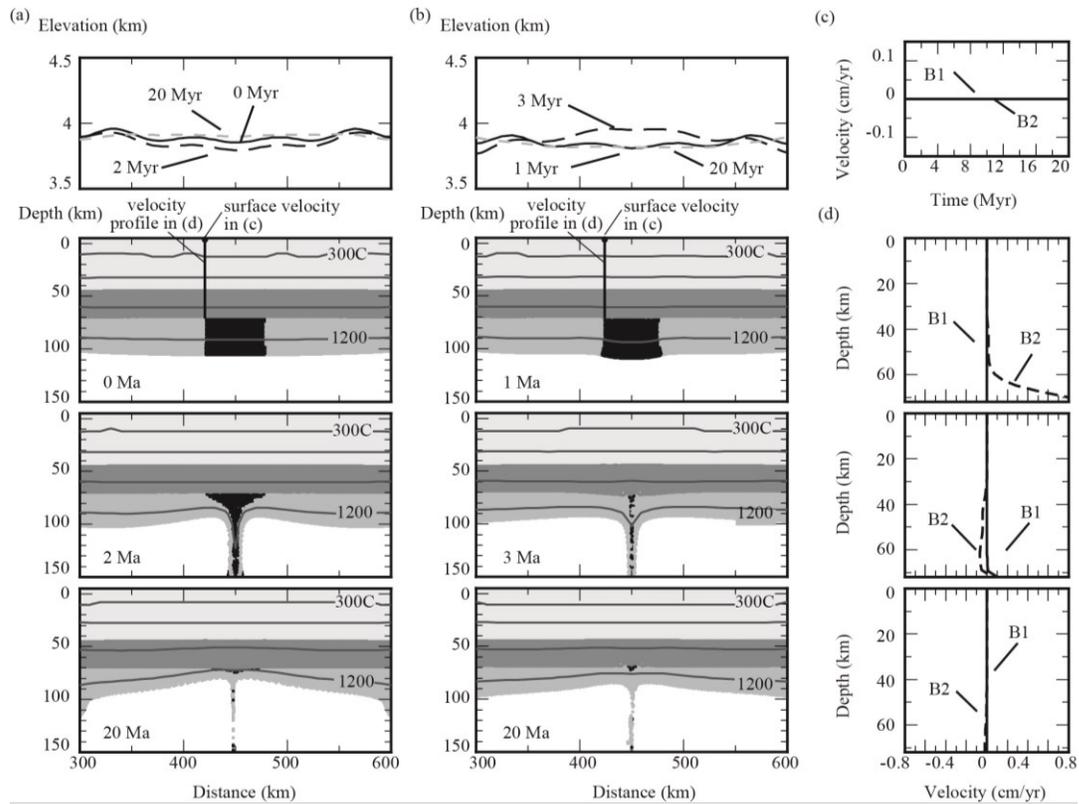

Figure 4.4. (a) Surface topography and model geometry of Model B1 at the given time after the start of the model run. (b) Surface topography and model geometry of Model B2 at the given time after the start of the model run. (c) Evolution of the horizontal surface velocity at x=420 km. (d) Crustal flow velocity profile at x=420 km at the time in Figure 4.4a and 4.4b.

Overall, we find that with a mantle lithosphere root, there is less surface deflection in the thick crust models compared to the thin crust models. With the thicker crust, the density anomaly in the mantle lithosphere is at a greater depth, and therefore the stress from the root must be transmitted through a greater thickness of crust to produce surface deflection. Some of this stress is absorbed by the crust, causing crustal deformation and contraction, especially if the crust is weak. As a result, surface subsidence is reduced, and crustal deformation is enhanced, which further counteracts the surface subsidence and may even produce surface uplift. With a strong crust (Model B1), the surface first subsided and then underwent uplift. With a weak crust (Model B2), there was no subsidence, and the root stresses caused sufficient crustal thickening that the surface uplifted during root removal.

4.3.3 Thick crust models with crustal density anomaly

As noted above, in thick orogenic crust, a high-density anomaly may form in the lower crust, through eclogitization by magmatic or metamorphic processes. To investigate this, we have tested models with a 60 km wide lower crustal root, where the root thickness is the same as that of the adjacent lower crust. The assumption is that this is a local region of lower crust that is either the site of magmatism or that the conditions here are such that metamorphic eclogitization is triggered (e.g., it is more hydrated than surrounding regions; Austrheim, 1991). The root density is initially that of lower crust, and progressive eclogitization is simulated by increasing its density at 35.1 kg/m^3/Myr, in order to keep its negative buoyancy consistent with the earlier models.

Figure 4.5a shows the development of lower crust instability in Model B3, which uses a strong crustal viscosity (Table 4.2). At ~9 Myr, when the root is denser than the underlying mantle, it becomes gravitationally unstable and begins to descend. The root and some mantle lithosphere are removed by 15 Myr as an RT drip. At the surface (Figure 4.3 and 4.5a), the subsidence rate is slow in the first 3 Myr and then increases until 9 Myr. This is primarily the isostatic response to root densification, as the root is less dense than the underlying mantle. From 9 to 10 Myr, the subsidence rate

decreases to zero. The maximum basin depth is ~1200 m at 10 Myr; this is 4-5 Myr earlier than the time at which the root detaches. As the root undergoes gravitational removal, the surface starts to uplift. The maximum uplift rate is observed at ~15 Myr, as the root detaches. After this, the uplift rate decreases and at 20 Myr, the surface above the drip is only ~130 m lower than the surroundings.
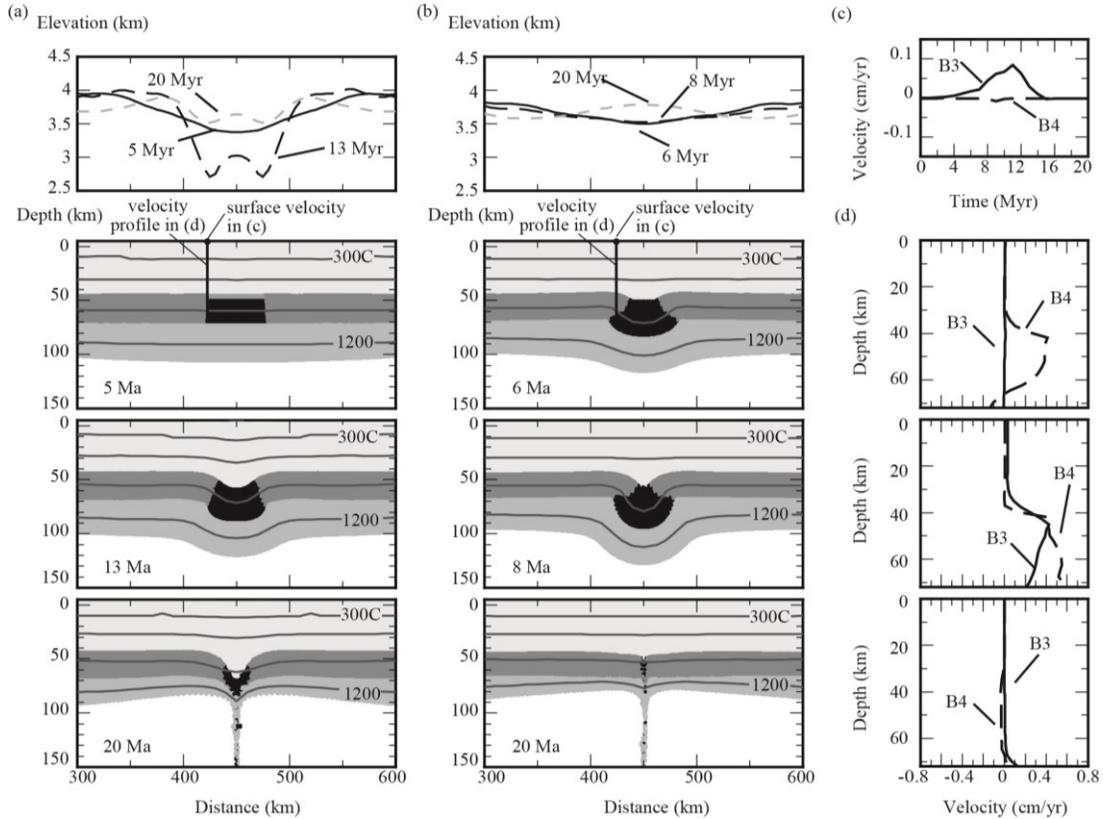
Figure 4.5. (a) Surface topography and model geometry of Model B3 at the given time after the start of the model run. (b) Surface topography and model geometry of Model B4 at the given time after the start of the model run. (c) Evolution of the horizontal surface velocity at x=420 km. (d) Crustal flow velocity profile at x=420 km at the time given in Figure 4.5a and 4.5b.

The observed surface behaviour can be understood by examining the crustal deformation during root instability and detachment. During root detachment, the deep upper crust and lower crust adjacent to the root undergo flow toward the root region, with velocities of ~0.4 cm/yr (Figure 4.5d). As a result, the upper crust above the root starts to thicken, which causes the surface to uplift as the root descends. After root

detachment, the crustal flow ceases. The surface also exhibits horizontal velocities as the root destabilizes. As shown in Figure 4.5c, the surface adjacent to the root has a positive velocity from 4 to 14 Myr, meaning that the surface above the root is undergoing contraction. The maximum velocity is ~0.085 cm/yr at 11 Myr. The rate then decreases and after the root detaches at 14 Myr, there is little horizontal surface velocity.

In Model B4, we test the effects of a lower crustal root for an orogen with a weak crust (Table 4.2). In this case, the weak crust allows the root to detach at ~9 Myr and there is little residual root in the lithosphere, compared to Model B3 with a strong crust. Above the root, the surface initially subsides, reaching a maximum depth of ~200 m at 6 Myr (Figure 4.3b), which is ~3 Myr before root detachment. The surface then begins to uplift during root detachment, and is ~220 m higher than its surroundings at 20 Myr. As shown in Figure 4.5d, the root detachment induces flow in the deep crust, resulting in crustal thickening above the root. This reduces the surface subsidence above the root. In addition, there is little lateral motion of the ground surface (Figure 4.5c). This model shows with a weak crust, root removal induces deformation within the deep crust. As a result, the surface is more strongly decoupled from the dynamics of root removal.

4.4 Discussion and conclusions

As shown in the models above, foundering of continental lithosphere through an RT drip can create observable deflection of the surface, creating both localized basins (subsidence) and mountains (uplift). Such RT instabilities are a type of intraplate tectonics, and therefore may explain the origin of anomalous continental deformation that does not appear to be related to plate boundary interactions.

4.4.1 Summary of modeling results

In previous geodynamic studies, both subsidence and uplift of the Earth's surface has been observed during removal of the deep lithosphere as at RT drip (e.g., Neil and Houseman, 1999; Pysklywec and Beaumont, 2004; Elkins-Tanton, 2007; Göğüş and Pysklywec, 2008). In our models, we find the similar styles of vertical

surface deflection. Our work addresses RT drips in different tectonic settings, from a stable continental interior with thin crust to an orogen with thick crust. By using a common approach for all models, we are able to systematically address the controls on the surface deflection and identify the feedbacks between RT drip dynamics, crustal deformation and surface deflection. The evolution of surface topography above an RT drip depends on both an isostatic adjustment in response to lateral density variations and a dynamic component that is related to both the dripping process and crustal deformation induced by the RT drip. Overall, we find that three types of surface deflection are observed (Figure 4.6):
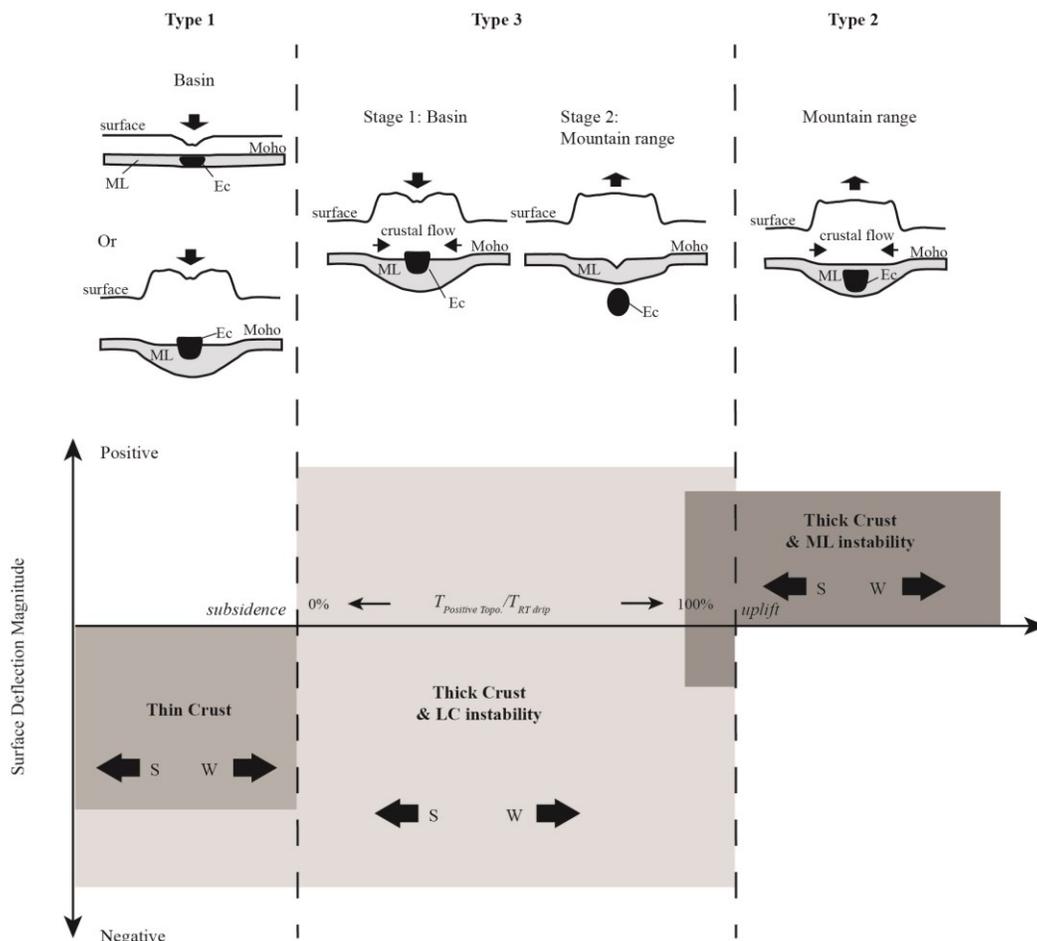
Figure 4.6. The three types of surface deflection associated with an RT drip (upper diagram). The lower diagram qualitatively shows the relative magnitude and temporal evolution of the surface deflection for each type, as a function of crustal strength and depth of the instability. ML=mantle lithosphere; S= strong crust (high strength); W= weak crust (low strength).

Type 1) Subsidence and negative topography (Models A1, A2 and B3);

In these models, the surface response is strongly coupled to the dynamics of the high-density root. In Models A1 and A2, the crust is thin and in Model B3, the crust is strong and thick, with a root in the lower crust. In these models, the surface initially subsides as an isostatic response to the presence of the dense root. As the root destabilizes, further subsidence arises from stresses produced by the descending root. The magnitude of the subsidence depends on the normal stress due to the dense anomaly and the lithospheric flexural strength. For models with thin crust, the normal stress causes surface subsidence, with slightly more subsidence for the model with a weaker crust (Model A2) (Figure 4.2). When the crust is strong (Models A1 and B3), the upper part of the root remains within the lithosphere, which reduces the surface uplift following root removal. In these models, crustal deformation has only a minor effect on the surface response. In Model A1, the crust does not deform. In Models A2 and B3, the deep crust is entrained by the root, resulting in crustal thickening above the root. This means that the maximum subsidence rate occurs prior to root removal. However, the crustal flow is not sufficient to balance the subsidence, and the surface remains at negative elevation (lower than its surroundings).

Type 2) Uplift and positive topography (Model B2);

Previous studies have shown that surface subsidence above an RT drip can be compensated by lateral crustal flow induced by the drip (Neil and Houseman, 1999; Pysklywec and Beaumont, 2004). Crustal flow is induced in two ways: 1) by shearing of the lowermost crust by the convective instability (Couette flow) and 2) by flow caused by the lateral pressure gradient in the deep crust associated with the presence of the high-density material (Poiseuille flow). Model B2 has a thick, weak crust, and removal of the dense mantle lithosphere root causes both Poiseuille and Couette flow in the crust. This results in crustal contraction and thickening above the drip. Deformation is enhanced in the lower crust owing to its Non-Newtonian rheology, and this helps to decouple the dense drip and the surface. Crustal thickening acts to uplift the surface at a rate which exceeds the rate of subsidence associated with the RT drip.

Following drip detachment, the thickened buoyant crust results in further isostatic uplift. This model demonstrates the importance of crustal thickness in the surface response to an RT drip. The only difference between Models A2 and B2 is that Model B2 has a thick crust, which allows a greater crustal flow. As a result, Model B2 undergoes surface uplift to positive topography (higher elevation than surroundings) during the RT drip, whereas Model A2 exhibits subsidence and basin development.

Type 3) Subsidence followed by uplift to positive topography (Models B1 and B4);

These models show a hybrid behaviour, where the crust undergoes some deformation during the RT drip. In the initial stages of root removal, the uplift caused by induced crustal flow does not completely compensate for the isostatic and dynamic subsidence related to the drip. As a result, the surface first undergoes subsidence. However, over time, the effects of the drip are reduced and/or the accumulation of thickened crust above the drip allow the surface to uplift, causing a basin inversion. After removal, the surface sits at relatively high elevation.

This type of surface deflection is intermediate between Types (1) and (2). For the same lithospheric geometry (e.g. crustal thickness, depth of instability), the crustal viscosity determines the surface response to an RT drip. For models with a thick crust and a mantle lithosphere instability, a strong crust (Model B1) has only a minor crustal flow and undergoes subsidence followed by uplift, whereas a weaker crust (Model B2) has greater crustal flow which produces surface uplift throughout the removal event. For a lower crustal instability in thick crust, Models B3 and B4 both experience induced crustal flow through a combination of the Couette and Poiseuille flow. In Model B3, the crust is strong, which reduces the amount of crustal deformation. As a result, the surface does uplift, but it is not enough to create a region of positive topography. In contrast, the weaker crust in Model B4 undergoes greater flow, producing positive topography above the drip.

Figure 4.6 summarizes the three types of behaviour observed of RT drip in our models. The lower plot quantifies both the vertical magnitude (y-axis) and the temporal evolution (x-axis) of surface deflection. In Type (1), the surface has negative

topography throughout the drip event (100% subsidence) and the magnitude of deflection is relatively low (<100 m). In Type (2), the surface always has positive topography (100% uplift) with a low magnitude (<200 m). In Type (3), the surface has negative topography (subsidence), followed by positive topography (uplift), and the magnitude of the deflection can be >1000 m. The temporal evolution is plotted on the x-axis of Figure 4.6 by normalizing the duration of positive topography by the time scale for the RT drip:

$$x = T_{Positive\ Topo.}/T_{RT\ drip} = T_{Positive\ Topo.}/(2T_{Detachment}) \qquad (4.1)$$

To simplify, we define the RT drip time scale as 2 times the time required for detachment of the dense root ($T_{Detachment}$). In general, as the strength of the crust decreases, the crustal deformation and the duration of positive topography increase.

In our study, we have focused on crustal thickness and strength, as well as the location of the root. We find a gradation in surface deflection from subsidence to uplift, corresponding to decreased coupling between the root and surface as the crust becomes weaker and/or thicker and as the depth of the root increases. A number of other factors may affect the surface response. For example, the density of the root determines its negative buoyancy. An increased densification rate will decrease the timescale for root removal (Houseman and Molnar, 1997) and increase the normal stress on the lithosphere. Variations in the densification rate by a factor of 2 for Model B3 show that a denser root initially cause a greater magnitude of surface subsidence, but the enhanced crustal flow then causes the surface uplift to a higher elevation (Wang et al., 2015). The magnitude of surface deflection scales with the normal stress of the root, but the overall surface expression (subsidence vs. uplift) does not change.

The strength of the mantle lithosphere will also affect both the drip timescale and surface response. With a stronger mantle lithosphere than in our models, the drip removal time will increase. The stress on the base of the crust that is produced by root removal will also be amplified. To demonstrate this, we tested Model A2 (thin, weak crust) with a mantle lithosphere that is 10 times stronger (f=20) than that in Figure 4.2b. With the stronger mantle lithosphere, the drip induces greater crustal flow in the weak, thin crust. As a result, the surface initially subsides and then uplifts, producing positive topography (Type 2).

4.4.2 Implications for intraplate deformation

The numerical models presented here have implications for the origin of intraplate deformation on Earth. There are several basins in continental interiors, where the crust is thin and relatively cool, e.g., Michigan basin, Williston basin, Illinois basin (Naimark and Ismail-Zadeh, 1995 and references therein), and Congo basin (Downey and Gurnis, 2009). These have been previously suggested to be related to a high density material in the deep lithosphere (Naimark and Ismail-Zadeh, 1995 and references therein; Downey and Gurnis, 2009). Our model results are consistent with this interpretation. The lithosphere temperature in these cratonic regions is cooler than that in our models, which should result in stronger crust than in our models. This should further reduce the susceptibility of the crust to deformation, and therefore, it is predicted that the surface response to a high-density body should be subsidence. The long duration of the basin, and observations of little to no uplift, suggest that either high-density material is still attached in the lithosphere or that deformation in the crust was limited due to its high strength (e.g., Model A1).

The models with a thick crust demonstrate that RT drips may exhibit all three types of surface expression, depending on the crustal strength and the location of the high-density root (Figure 4.6). In the central Andes, the Arizaro basin formed through Miocene subsidence (21-9 Ma), but since then, the basin has undergone inversion and now sits several hundred meters above its surroundings (DeCelles et al., 2015). Similarly, the Wallowa mountain in northeast Oregon, experienced subsidence at ~12 Ma and then uplift since ~8 Ma and now sits at high elevation (Hales et al., 2005). Both of these cases are consistent with formation by an RT drip that caused significant crustal thickening during removal (Type 2 surface expression).

In contrast to the central Andes, where there are numerous examples of transient hinterland basins, the Tibetan plateau has a relatively low surface relief and there is no evidence of such basins (e.g., Horton, 2012; DeCelles et al., 2014). Turner et al. (1996) propose that the magmatic record in Tibet is consistent with the occurrence of RT drips. One possible explanation for the lack of surface expression is that the crust is thick and weak. As a result, any normal stress associated with an RT drip is decoupled from the

surface and RT drip removal induces the deep crustal flow, leading to little surface deflection (i.e., as seen in Models B1 and B4). This is consistent with independent seismic and magnetotelluric studies that show that there is a viscously weak layer in the crust (e.g. Wang et al., 2007; Zhang et al., 2010; Zhao et al., 2012). The presence of a weak crustal layer may allow topographically-induced crustal channel flow (Clark and Royden, 2000). This layer may also decouple the surface from the dynamics of foundering dense lithosphere.

In summary, our numerical models show that RT drips can cause an observable deflection at the Earth's surface, with a magnitude ranging from 10's of m to >1000 m. Our results demonstrate that RT instabilities have different expressions at the surface, depending on the crustal strength, thickness and depth of the instability. If the crust is thin, the RT drip usually causes surface subsidence (Type 1). The surface deflection for a thick crust is more variable. Within the range of crustal viscosity that we have tested, models with a lower crust instability show surface deflections of Types (1) or (2). These types are characterized by surface subsidence and basin formation; the basin may undergo subsequent inversion to positive topography if the crust is weak enough (Type 2). A mantle lithosphere instability below thick crust produces surface deflections of types (2) or (3), with positive topography (surface uplift) appearing in both cases.

Chapter 5

Crustal channel flow and surface deflection induced by lithospheric removal

5.1 Introduction

Geodetic and geological observations indicate that significant surface vertical deflection has occurred in the interior regions of many continental plates. Deformation ranges from subsidence and the creation of sedimentary basins (e.g., the Williston basin; Naimark and Ismail-Zadeh, 1995) to surface uplift (e.g., southern Sierra Nevada; Fay et al., 2008) and intercontinental orogeny (e.g., the Tian Shan orogeny; Molnar and Houseman, 2004). These observations contrast with the classical view of rigid tectonic plates, where deformation is limited to narrow plate boundaries (e.g., Kreemer et al., 2003). There are three main causes of intraplate deformation: (1) stresses originating from the dynamics of the sublithospheric mantle (e.g., McKenzie, 1977), (2) stresses transmitted from distal plate boundaries to a region of relatively weak lithosphere (e.g., Kusznir and Park, 1984; Mazzotti and Hyndman, 2002), and (3) stresses associated with gravitational removal of lower lithosphere (e.g., Neil and Houseman, 1999; Pysklywec and Shahnas, 2003; Molnar and Garzione, 2007).

In this study, we address the surface deflection caused by the third mechanism. Lithosphere removal is driven by high densities in the deep, resulting from either the cool lithospheric temperatures (e.g., Houseman et al., 1981; Houseman and Molnar, 1997; Conrad and Molnar, 1999) and/or the presence of high-density assemblages (e.g. eclogitic rocks associated with crustal metamorphism or magmatic emplacement) (e.g., Kay and Kay, 1993; Jull and Kelemen, 2001; Lee et al., 2006). This dense material may undergo gravitational removal as a Rayleigh-Taylor instability (RTI), in which the dense lithosphere descends into the deeper mantle as a "drip" (e.g., Houseman and Molnar, 1997). An alternate style of removal is delamination, which involves peeling of a dense material along a shallower detachment layer (e.g., Bird, 1979; Göğüş and Pysklywec, 2008). Here, we focus on RTI-style removal.

Gravitational lithosphere removal has been proposed to have occurred in a number of regions based on geophysical and geochemical data. For example, seismic tomography observations show small-scale (diameter 30-100 km) high-velocity "blobs" in the shallow upper mantle, which are interpreted as fragments of detached lithosphere (e.g., Schurr et al., 2006; Sine et al., 2008; West et al., 2009; Saleeby et al., 2012). Lithosphere removal has also been proposed to explain anomalous magmatism that can

not be linked to normal tectonic processes (Kay and Kay, 1993; Turner et al., 1996; Gao et al., 2004; Elkins-Tanton, 2007; Ducea et al., 2013).

Gravitational removal alters the density structure of the lithosphere, and therefore removal should be accompanied by a vertical deflection of the Earth's surface. As the dense material destabilizes and sinks, a downward normal stress will be exerted on the overlying material, causing the surface to subside. This may be followed by the isostatically-driven surface uplift, after the density anomaly detaches. Lithosphere foundering as an RTI has been invoked to explain the origin of several sedimentary basins, including the Williston basin in central North America (Naimark and Ismail-Zadeh, 1995), Tulare basin in California (Saleeby et al., 2012), and the Arizaro basin in the central Andes (DeCelles et al., 2015). However, there are also places where lithosphere foundering has been linked with either minor (<0.5 km) surface subsidence or surface uplift, such as the Wallowa Mountains in the northern Oregon (Hales et al., 2005), Tien Shan in the western China (Houseman and Molnar, 2001), the Southern Island in New Zealand (Stern et al., 2000), and Isan orogeny in Australia (Pysklywec and Beaumont, 2004).

In areas with surface uplift, it appears that the uplift is accompanied by crustal contraction and thickening (e.g., Zandt et al., 2004; DeCelles et al., 2015). This raises the question: how does the foundering lower lithosphere couple to the overlying crust, and hence affect the surface deflection? Neil and Houseman (1999) use linear stability analysis to investigate RTI removal for a two-layer lithosphere consisting of constant viscosity crust and constant viscosity mantle lithosphere. They find that when the crust is more than 13 times stronger than the mantle, lithosphere removal is accompanied by surface subsidence, but a weaker crust will thicken during removal, leading to surface uplift. Pysklywec and Shahnas (2003) show that crustal thickening may be induced by a shear stress at the base of the crust due to the downwelling RTI. Crustal thickening and uplift is also observed in studies that use a more realistic rheological structure for the crust; in this case, deformation occurs in the weakest region of the crust (e.g., Pysklywec and Beaumont, 2004; Göğüş and Pykslywec, 2008; Wang et al., 2015; see Chapters 3 and 4). Most of these studies use a complex crustal rheology and are designed for a specific region, making it difficult to extrapolate the results to other

areas.

In this study, we investigate the topographic expression and crustal deformation induced by an RTI. Specifically, we examine the effect of a crust with vertical strength variations. As shown below, for certain temperatures and compositions, the mid-crust and/or lower-crust may represent a low viscosity region (i.e., a "jelly sandwich", Burov and Watts, 2006). We first address the conditions under which a weak crustal channel may form. We then present simplified numerical models of three end-member crustal structures: (A) a strong crust, (B) a mid-crustal channel, and (C) a lower-crustal channel. Through this, we assess how the stress associated with an RTI transmits through a crustal channel and how the location of the channel (mid-crust or lower-crust) affects the surface deflection.

5.2 The origin of weak crustal channels

The crust is usually considered to be a rigid, strong layer, owing to its low temperatures (e.g., Kohlstedt et al., 1995). However, geophysical observations suggest the presence of a weak, low viscosity channel in the deep crust in a number of locations. One place where a mid-crustal channel may occur is in southern Tibet, where the crustal thickness is ~75 km. Reflection bright spots in seismic studies (Makovsky et al., 1996; Nelson et al, 1996) and high electrical conductivities in a magnetotelluric study (Li et al., 2003) are interpreted to indicate a weak channel between 15 and 40 km depth. The conductances suggest viscosities of 2.5×10^{18} to 3×10^{20} Pa s in this channel (Rippe and Unsworth, 2010). In other places, a weak channel has been inferred in the lower-crust. For example, the topographic evolution of the central Andes suggests a ~40 km thick weak layer with a viscosity at $\sim 10^{19}$ Pa s that extends to the base of the ~65 km thick crust (Gerbault and Herail, 2005). At the boundaries of the Tibetan plateau, a weak lower-crust (viscosity of 10^{18} to 10^{21} Pa s) can explain the gradients in surface topography (Clark and Royden, 2000). In the Basin and Range province of the western United States, where the crustal thickness is ~40 km, long-wavelength gravity anomalies and topographies are consistent with a 25-km thick lower-crust channel with a viscosity of 10^{18} to 10^{20} Pa s (Kruse et al., 1991).

The creation of a low viscosity channel in the deep crust may occur because the

viscous strength of most crustal rocks decreases exponentially with temperature (e.g., Kohlstedt et al., 1995; Ranalli, 1995). At shallow depths, deformation occurs in a brittle manner, and crustal strength increases with depth (Burov and Diament, 1995). However, in the hotter deep crust, rocks may deform viscously. To determine the conditions under which the strength may be sufficiently low for a weak ductile channel to form, we have calculated viscous strength profiles for geotherms that correspond to surface heat flows of 40 to 90 mW/m^2 (Figure 5.1). In the calculations, a strain rate of 10^{-15} s^{-1} is used, which is comparable to the crustal strain rates observed in the numerical models in Section 5.4; a higher strain rate will yield lower effective viscosities than shown in Figure 5.1. We only consider the effects of temperature and composition on viscous strength. If temperatures are high enough for partial melting, the crust will further weaken (Rosenberg and Handy, 2005), enhancing the development of a channel.

The top row in Figure 5.1 shows the results for 60 km thick (orogenic) crust and the bottom row is for a 40 km crust. The geotherms are shown in Figures 5.1a and 5.1d. For a thick crust (Figure 5.1a), heat flows greater than 70 mW/m^2 give extremely high deep crustal temperatures, and therefore temperatures are capped at the value of a 1300°C adiabat. Figures 5.1b and 5.1e show the strength profiles for crust consisting of a felsic upper-mid crust and a mafic lower-crust (Ranalli and Murphy, 1987), using the rheological parameters of dry granite (Ranalli, 1995) and dry Maryland diabase (Mackwell et al., 1998), respectively. Figures 5.1c and 5.1f show the strength profiles assuming that the entire crust is felsic (Gao et al., 1998) and has a dry granite rheology (Ranalli, 1995).
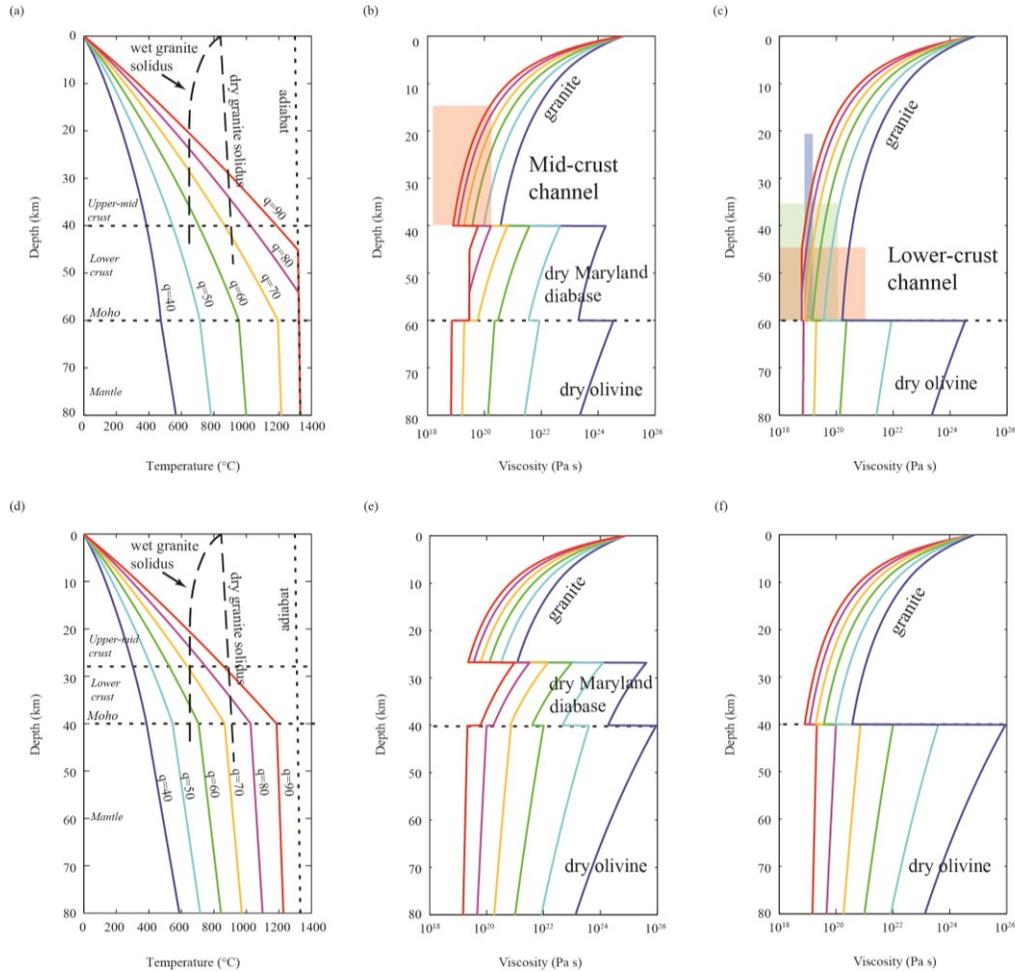
Figure 5.1. Geotherms and viscosity profiles for mid-crustal and lower-crustal channel, for a 60 km crust (top row; consisting of a 40 km upper-mid crust and 20 km lower-crust) and 40 km crust (bottom row; with 27 km upper-mid crust and 13 km lower-crust). (a, d) Geotherms for different surface heat flows (q, in mW/m^2). These are calculated with a thermal conductivity of 3.0 W m^{-1} K^{-1} in the upper-mid crust and 2.5 W m^{-1}K^{-1} in the lower-crust and mantle and radiogenic heat production of 1.3 μWm^{-3} in the top 10 km of the crust, and 0.4 μWm^{-3} in the rest of the crust and 0 μWm^{-3} in the mantle (Currie et al., 2004). The dry and wet granite solidus lines are from Chapman (1986). (b, e) Effective viscosity profiles calculated for each geotherm in plots a and d (using same line colours) and assuming a felsic upper-mid crust and mafic lower-crust. Rheology parameters for upper-mid crust is dry granite (Ranalli, 1995), lower-crust is dry Maryland diabase (Mackwell et al. 1998), and the mantle is dry olivine (Hirth and Kohlstedt, 1996). The red rectangle in (b) shows the inferred location and visocosity for a mid-crustal channel in southern Tibet (see main text). (c, f) Effective viscosity profiles assuming that the entire crust is felsic. The red rectangle is the inferred lower-crustal channel at the edge of Tibet (Clark et al., 2000); the green rectangle shows the conditions for the lower-crust channel under Nevada (Kruse et al., 1991); and blue line shows the depths and viscosity in the central Andean plateau (Gerbault and Herail, 2005).

In all cases, strength decreases with depth owing to increased temperatures, with greater weakening for hotter geotherms. To create a mid-crustal channel, the crust must have a layered rheology such that the mid-crust is felsic, while the lower-crust is mafic and therefore strong (Figures 5.1b, 5.1e). A weak mid-crustal channel (viscosity $<10^{20}$ Pa s) can be formed if mid-crustal temperatures are >500°C, corresponding to surface heat flow >50 mW/m^2 for a 60 km thick crust (Figure 5.1b) and >60 mW/m^2 for 40 km thick crust (Figure 5.1e). A lower-crustal channel (viscosity $<10^{20}$ Pa s) requires either that the lower-crust is warm (>500°C) and felsic, or hot (>1000°C) and mafic. With thick crust, this can occur for heat flows greater than 40 mW/m^2 and 60 mW/m^2, for a felsic and mafic lower-crust, respectively (Figures 5.1b; 5.1c). With thin crust, a lower-crustal channel would likely only occur if the deep crust is felsic and surface heat flow is >50 mW/m^2 (Figure 5.1f). A mafic lower-crust would require an extremely high heat flow >80 mW/m^2 (Figure 5.1c). Overall, these calculations demonstrate that a weak channel may form in the mid-crust or lower-crust for a fairly broad range of conditions.

5.3 Numerical model setup

We now use two-dimensional numerical models to study the behavior of the crust and surface topography as lithosphere is gravitationally removed through as an RTI. The goal is to examine how a weak crustal channel may affect the crustal response to an RTI. The model domain is 1000 km wide and 1000 km deep, with a 110 km thick continental lithosphere (60 km thick crust and 50 km mantle lithosphere) overlying sublithospheric mantle (Figure 5.2). The models investigate gravitational instabilities in orogenic regions with thick crust, although, as discussed in Section 5.4.5, the results are applicable to areas with thinner crust. The surface boundary of the models is stress free, which allows surface topography to develop self-consistently in response to the underlying dynamics. The side and basal boundaries are free slip, and there is no material transfer through them. As drip-style removal is symmetric, only half of the drip is modeled, with the left model boundary being the line of symmetry.

All layers in the models are horizontal and have a constant density and viscosity, as shown in Figure 5.2. The use of constant values allows us to demonstrate the first-

order relationship between lithosphere removal, crustal deformation and surface deflection. In the first model (Model A), the crust has a higher viscosity than the mantle, assuming that the crust is both cool and mafic (e.g., Figure 5.1). In later models, we test the effect of a weak channel by placing a 10 km thick weak layer in either the mid-crust or lower-crust. Gravitational removal is initiated by introducing a 50 km wide high density region (root) in the mantle lithosphere at the left side of the model domain, extending through the entire thickness of mantle lithosphere (50 km). The density of the root is 40 kg/m^3 greater than that of the mantle. This approximates a gravitationally unstable region created by either a magmatic eclogite root or a perturbation at the base of lithosphere. As the magma intrudes the lithosphere, melt differentiation can produce an eclogitic residue that is 50-250 kg/m^3 more dense than mantle (e.g., Ducea, 2001; Jull and Kelemen, 2001; Richards, 2003). Gravitational instability can also be initiated through a perturbation to base of the lithosphere (Houseman and Molnar, 1997; Molnar and Houseman, 2004). Lithospheric mantle is on average 200-600°C cooler than the underlying mantle (Currie and Hyndman, 2006), resulting in densities that are 20-70 kg/m^3 higher owing to thermal contraction. In this case, the high density root can be taken as a proxy for cool lithosphere that has been locally perturbed (thickened), initiating instability.
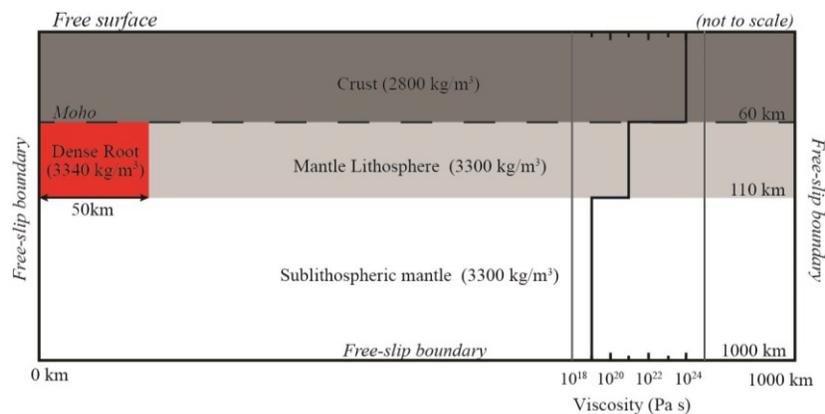
Figure 5.2. Numerical model set-up. The model is symmetric about the left hand boundary. See text for details of modeling parameters and boundary conditions.

The finite element computer code SOPALE is used to calculate the mechanical evolution of crust and mantle during lithosphere removal, under assumptions of incompressibility and plane strain (Fullsack, 1995; Beaumont et al., 2006). The modeling uses an arbitrary Lagrangian-Eulerian approach, in which material properties are advected by Lagrangian nodes. At each time step, the properties are interpolated onto an Eulerian grid, which is used for the thermal-mechanical calculations. The Eulerian mesh has resolution of 5 km × 2.5 km (horizontal × vertical) in the upper 140 km, except at 30-60 km depth where the Eulerian mesh is 5 km × 1 km. The smaller elements ensure adequate resolution of the crustal channel dynamics. In the lower 860 km, the mesh is 5 km × 10 km. Tests show that this resolution is sufficient to resolve growth rates of Rayleigh-Taylor instabilities to within 6% of their expected value (e.g., Houseman and Molnar, 1997).

Below, we present three models to demonstrate the general behaviour for (A) a uniformly strong crust, (B) a crust with a weak channel in the mid-crust and (C) a crust with a weak lower-crust. In the second case, the mid-crustal channel is decoupled from the underlying mantle dynamics, whereas the lower-crustal channel is directly coupled to the descending mantle drip.

5.4 Model results

5.4.1 Model with no ductile channel (Model A)

Model A examines lithosphere removal with a strong crust that has a uniform viscosity of 10^{24} Pa s. The root is gravitationally unstable and it descends, forming a drip shape at the base of lithosphere by 15 Myr after the start of the model (Figure 5.3b). This is followed by necking and detachment from the lithosphere at ~23 Myr. Figure 5.3a shows the surface topography above the drip, and Figure 5.4 shows the surface elevation at the centre of the basin. The surface initially subsides as an isostatic response to the presence of the dense root, creating a basin with a half-width of 150-200 km. The basin is bounded by a low-amplitude bulge at its edge, formed as the result of the flexural strength of the lithosphere. During the first ~4 Myr, the surface subsides rapidly to a depth of ~0.2 km. The subsidence rate then decreases, but subsidence continues as the dense root is removed. A maximum subsidence of 0.34 km at ~23 Myr

coincides with detachment of the drip. After detachment, the surface begins to uplift. At 30 Myr, the surface stabilizes at an elevation that is ~0.17 km lower than surroundings. Some residual root material remains below the crust in the centre of the root region, and the final elevation is consistent with the expected isostatic elevation for a residual root thickness of ~33 km, as observed (Figure 5.3b).

Figure 5.3c shows the horizontal velocities along a vertical profile through the crust at a distance of 200 km from the centre of the drip (i.e., at the edge of basin). The velocity is zero throughout the root removal process, indicating that there is no lateral deformation of the crust. Overall, Model A shows when the entire crust is strong, lithosphere removal is accompanied by surface subsidence, followed by partial uplift after the dense root detaches. This behaviour is consistent with the theoretical calculation of Neil and Houseman (1999) which shows that lithosphere gravitational instability results in surface subsidence if the crustal viscosity is more than a factor of 100 greater than that of the mantle; in this model, the crust is 1000 times more viscous than the mantle. The vertical normal stresses associated with the instability are efficiently transferred through the crust, resulting in surface subsidence.
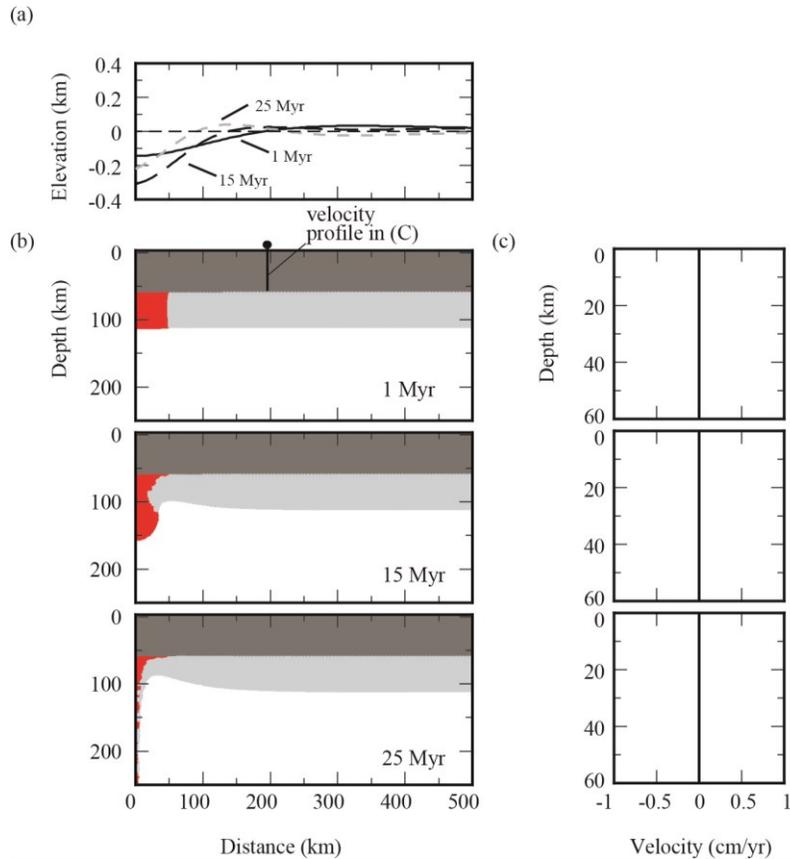
Figure 5.3. Evolution of Model A. (a) Surface topography and (b) model geometry at the given times after the start of the model run. (c) Horizontal crustal flow velocity profile at x=200 km at given times in Fig. 5.3b.
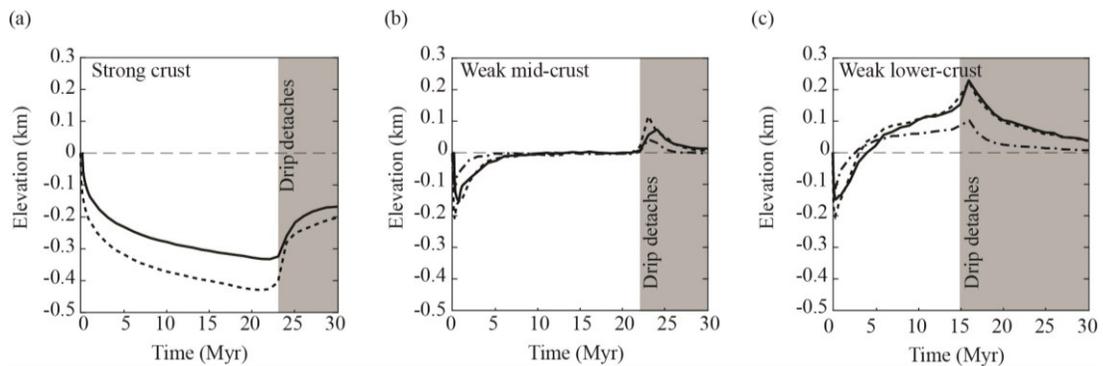
Figure 5.4. The evolution of surface elevation above the centre of drip in (a) Model A, (b) Model B, and (c) Model C. Solid lines are for models with 60 km thick crust (and 10 km thick channel in b and c). Dashed lines are for models with 40 km thick crust (and 10 km thick channel in b and c). Dash-dot lines in b and c are for models with 60 km thick crust and 15 thick channel.

5.4.2 Mid-crustal channel

5.4.2.1 Numerical modeling results (Model B)

In Model B, the effect of a weak mid-crustal channel is examined. This represents a case in which the crust is relatively hot and is comprised of a felsic upper-mid crust and mafic lower-crust (Figure 5.1b). A 10 km thick layer with a viscosity of 10^{18} Pa s is placed at 30 to 40 km depth (Figure 5.5). All other parameters are the same as in Model A. As seen in Model A, the dense root is gravitationally unstable and founders as an RT drip within ~22 Myr. The evolution of topography and crustal deformation during lithosphere removal can be divided into three stages. Initially, the surface rapidly subsides to a maximum depth of ~0.16 km, and a basin with a half-width of ~200 km is formed (Figure 5.5a and Figure 5.4b). At the same time, significant crustal flow occurs within the weak mid-crustal channel, with a maximum velocity of ~0.5 cm/yr toward the drip; there is no horizontal velocity in the strong crust outside the channel (Figure 5.5c). In the second stage, between 0.6 and 10 Myr, the surface begins to uplift and the mid-crustal flow velocity gradually decreases to ~0 cm/yr. Meanwhile, the crust above the drip thickens by ~2.5 km at 10 Myr. At this time, the downwelling root is still attached to the lithosphere. At 10 Myr, the surface elevation is close to its original height and it remains at this height until the drip detaches at ~22 Myr (Figure 5.4b). During this period, surface topography does not change, which contrasts with the dynamical processes occurring in the deeper lithosphere. Figure 5.5d shows the Lagrangian mesh of the model at 15 Myr. The vertical elongated mesh in the channel above the drip indicates the crust has been thickened in this region. The final stage of the model corresponds to isostatic response of the lithosphere following drip detachment at ~22 Myr. In the 2 Myr following detachment, the surface rapidly uplifts to a maximum elevation of 0.07 km above the surroundings. Uplift is driven by both the removal of the dense root and the enhanced thickness of the crust above the drip. Topography then begins to relax to its initial state, as the mid-crustal flow outward from the drip region thins the crust to its original thickness (Figure 5.5c).

(a)

(b)

(c)

(d)
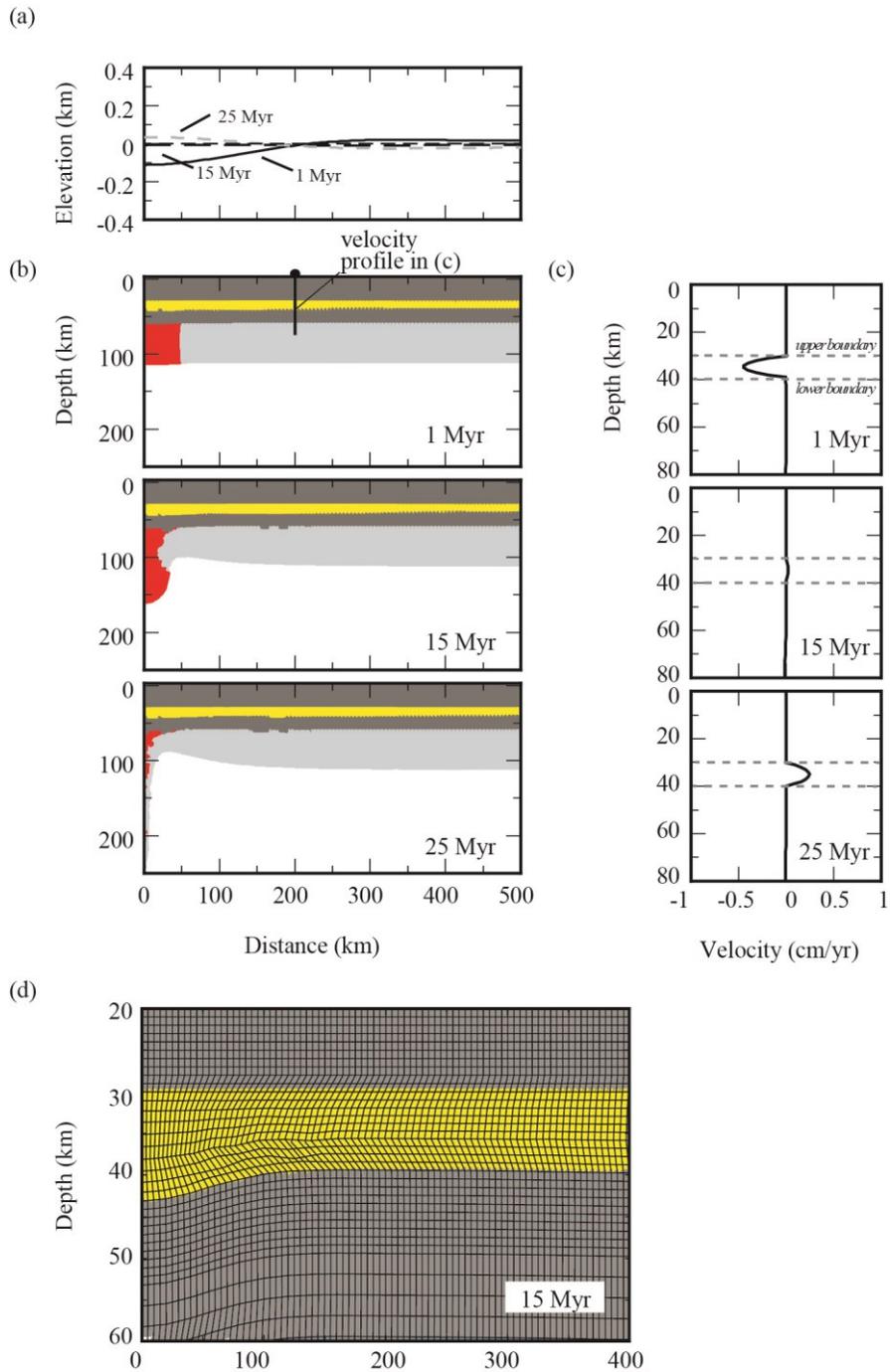
Figure 5.5. Evolution of Model B. (a) Surface topography and (b) model geometry at the given times after the start of the model run. The yellow region is the weak mid-crustal channel. (c) Horizontal crustal flow velocity profile at x=200 km at the given times in Fig. 5.5b. Dashed lines show the positions of the weak channel. (d) Lagrangian mesh of Model B at 15 Myr. The original shape of the mesh is rectangular.

5.4.2.2 Comparison between numerical model and theoretical calculation

The presence of a weak mid-crustal channel in Model B leads to a reduced maximum subsidence compared to Model A and surface uplift that occurs prior to root detachment. The surface response is the result of flow within the weak channel. Flow is driven by the lateral pressure gradient in the crust, similar to that seen in orogenic regions (e.g., Bird, 1991; Clark and Royden, 2000; Beaumont et al., 2006). This occurs because the dense root causes an initial isostatic subsidence of the region above it, resulting in a region of relatively low pressure in the crust above the root. The lateral pressure gradient is sufficient to induce flow within the mid-crustal channel. This leads to crustal thickening and surface uplift above the root.

We can analyze the evolution of Model B in terms of a pressure/gravitationally-driven channel flow. The mid-crustal channel is bounded by strong upper and lower boundaries, which can not be deformed laterally. All flow is confined to the weak channel, and the velocity profile (Figure 5.5c) corresponds to that of Poiseuille flow, in which the flow is symmetric about the centre of the channel and velocity decreases from a maximum at the centre to zero at the upper and lower boundaries of the channel (Turcotte and Schubert, 2002). As shown in the Appendix (Section 5.7), the average flow velocity in the channel ($\bar{v}$) is related to the lateral gradient in surface topography:

$$\bar{v} = \frac{h_{ch}^2}{12\eta_{ch}}\rho_c g \frac{S}{L_{basin}} \qquad (5.1)$$

where h_{ch} and η_{ch} are the thickness and viscosity of the ductile channel, ρ_c is the crustal density, g is the gravitational acceleration, S is the magnitude of the surface deflection (the elevation difference between the centre and edge of the basin) and L_{basin} is the half-width of basin. The surface deflection (S) is the result of the combined effects of the vertical stresses caused by the dense root and isostatic uplift as the crust thickens.

Equation 5.1 predicts a linear relationship between the average channel flow velocity and the surface deflection. Figure 5.6 shows the evolution of observed average channel flow velocity at the edge of the basin and surface deflection for Model B, as well as the expected relationship based on Equation 5.1. The modeling result is in a good agreement with the theoretical analysis, showing that the observed mid-crustal channel flow is consistent with a pressure-driven flow.
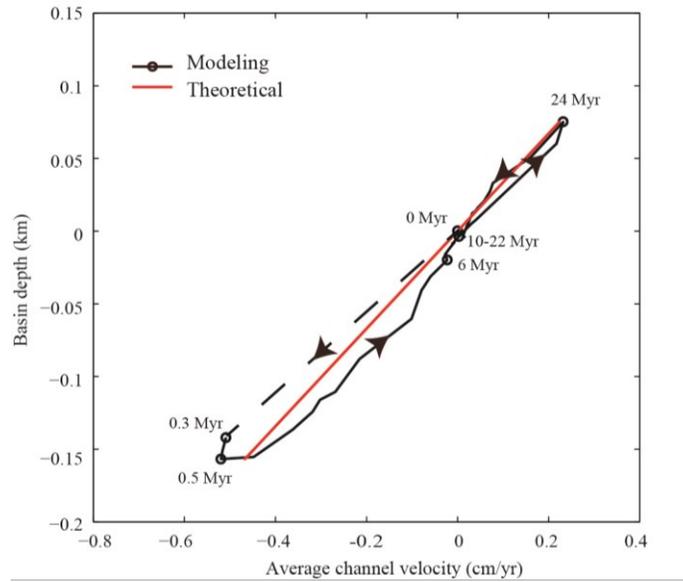
Figure 5.6. The relation between the surface elevation above the centre of drip and the average lateral velocity at x=200 km in the mid-crust channel. The black line is the modeling result (Model B) and the red line is the theoretical approximation based on the model parameters.

Equation 5.1 also shows that mid-crustal channel flow will occur if there is a gradient in surface topography and that channel flow will cease if the surface is flat (S=0). The channel flow is driven by the negative buoyancy of the root, and therefore the crust above the root can only thicken until it fully isostatically balances the effect of the dense root. If channel flow is rapid, this means that the surface can return to its initial elevation before the root detaches; it is not possible to create a topographic high above the dense root. At this point, the surface will have a deflection of S=0 and all channel flow will stop. In Model B, this occurrs between 10 and 22 Myr (Figure 5.4b).

5.4.3 Lower-crustal channel
5.4.3.1 Numerical modeling results (Model C)

The third model (Model C) examines the effect of a weak lower-crustal channel. A weak channel with a viscosity of 10^{18} Pa s is placed in the lower 10 km of the crust (50-60 km depth), and therefore it is in direct contact with the mantle lithosphere and the gravitationally unstable root. This corresponds to a case where the deep crust is either moderately hot and felsic (Figure 5.1c) or very hot and mafic (Figure 5.1b).

Other parameters are the same as those in the previous models. The model evolution is shown in Figure 5.7. The dense root is removed as an RTI and detaches from the overlying lithosphere at ~15 Myr. The earlier detachment time in this model compared to Models A and B is due to the reduced coupling between the root and weak lower-crust. In the first 0.3 Myr, the surface above the root rapidly subsides to a depth of ~0.15 km and a basin with a half-width of ~200 km is formed (Figure 5.4c and Figure 5.7a). The width and the maximum depth of the basin are similar to the model with the weak mid-crust (Model B). Following this, the surface rapidly uplifts and reaches a positive topography at 5 Myr (Figure 5.4c). The uplift rate decreases as the surface elevation increases. Before the drip detaches at ~15 Myr, the surface above the drip is at an elevation of ~0.13 km. After detachment, the surface uplifts rapidly to ~0.23 km, followed by a decrease toward its initial elevation.

The topographic response to root removal is related to flow of the weak lower-crust during lithosphere removal. In the initial stages of removal, the lower-crust flows towards the root (Figure 5.7c). Flow is driven by both the lateral variation in pressure within the weak channel (as in Model B) and by shearing of the lower boundary of the weak crust by mantle lithosphere that is entrained by the drip. The induced flow leads to a thickening of the crust above the drip and this causes surface uplift. The surface uplifts above its original elevation, as the basal shearing results in an over-thickening of the crust. This is similar to the behaviour observed by Neil and Houseman (1999) for a uniformly weak crust. In our model, crustal flow and thickening is confined to the lower-crustal channel. At 5 Myr, the crust is thickened above the drip as shown in the Lagrangian mesh (Figure 5.7d). At 10 Myr, the deep channel exhibits flow toward the drip, driven by basal shearing, while the upper part of the channel shows a small flow outward from the drip. The outward flow is driven by the high topography above the drip. The Lagrangian mesh shows that the upper channel above the drip thins and ascends; while the lower part thickens and sinks (Figure 5.7d). After drip detachment at 15 Myr, the thickened crust starts to deflate, as exhibited by outward crustal flow (Figure 5.7c) and topographic collapse (Figure 5.4c). At this time, the high topography and weak crust are no longer dynamically supported by basal shearing.
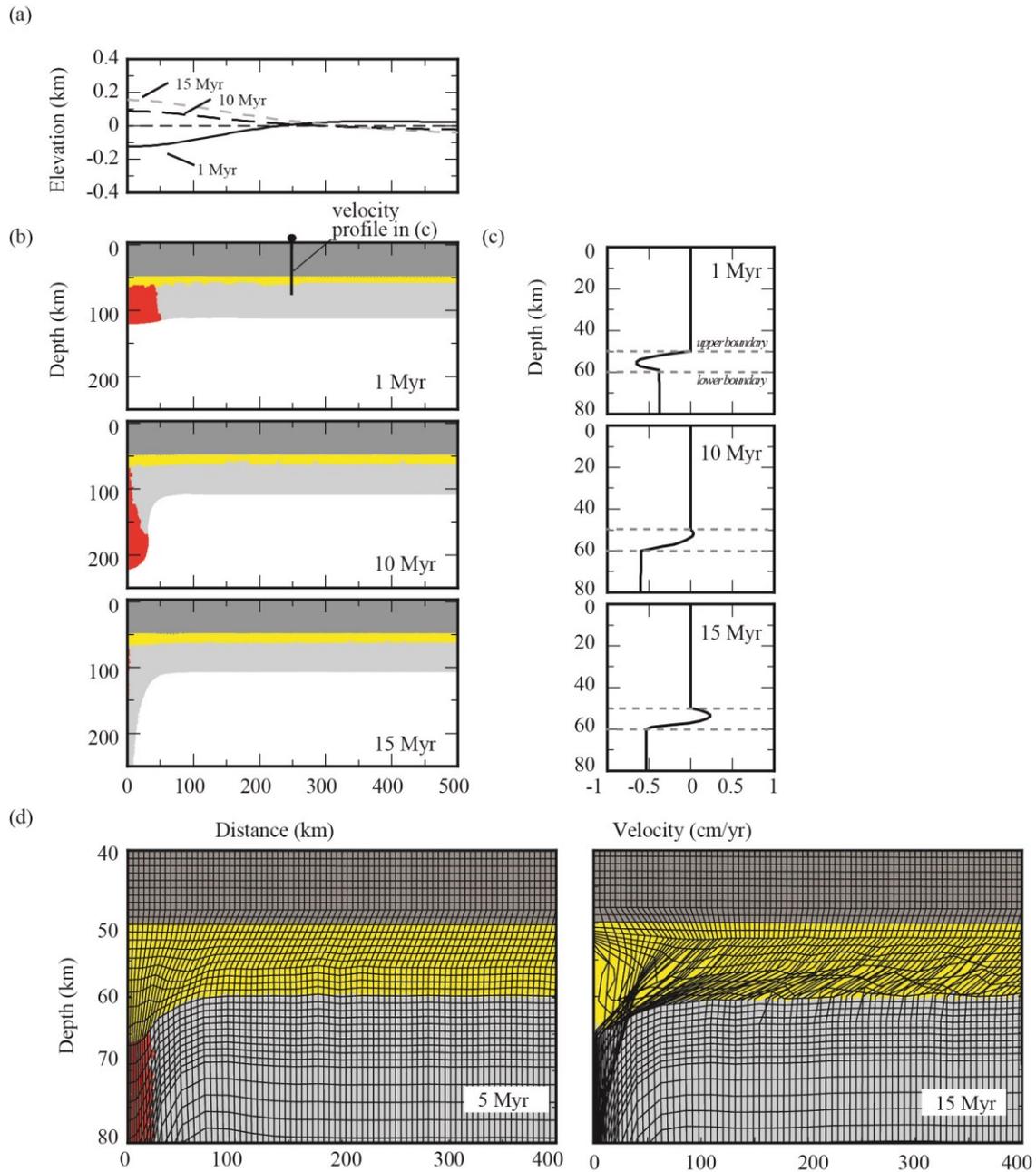
Figure 5.7. Evolution of Model C. (a) Surface topography and (b) model geometry at the given times after the start of the model run. The yellow region is the weak lower-crustal channel. (c) Horizontal crustal flow velocity profile at x=200 km at given times in Fig. 5.7b. Dashed lines show the positions of the weak channel. (d) Lagrangian mesh of Model C at 5 Myr and 15 Myr. The original shape of the mesh is rectangular.

It should be noted that this model has a thick lithosphere in the vicinity of the root after the drip detaches. This is due to the weak lower-crust, which allows a greater

area of lithosphere to be entrained by the drip; the velocities profiles show that the mantle lithosphere at the edge of the basin has a non-zero velocity (Figure 5.7c). In contrast, Models A and B exhibit lithospheric thinning following drip removal (Figure 5.3b and Figure 5.5b). In these models, lower-crust is strong enough to resist horizontal deformation, and this restricts the amount of mantle lithosphere that is carried laterally by the drip.

5.4.3.2 Comparison between numerical model and theoretical calculation

Gravitational removal of the mantle lithosphere in this model produces a short-lived basin at the surface, followed by an inversion to a topographic high. This is related to crustal thickening above the dense root, where thickening is driving by flow in the weak lower-crustal channel. Flow arises from a combination of pressure-driven Poiseuille flow associated with topographic variations and by basal shearing, which creates Couette flow (e.g., Turcotte and Schubert, 2002). As a result, the velocity at the base of the channel is not zero, flow velocities are not symmetric about the centre of the channel, and most crustal flow is in the deep channel (Figure 5.7c). This leads to an average flow velocity in the channel ($\bar{v}$) of

$$\bar{v} = \frac{h_{ch}^2}{12\eta_{ch}}\rho_c g \frac{S}{L_{basin}} + \frac{1}{2}v_0 \tag{5.2}$$

where v_0 is the horizontal velocity at the lower boundary. The first term corresponds to topographically-driven flow and the second term corresponds to the average Couette flow in the channel (see Section 5.7 for details).

For a given basal velocity (v_0), this equation predicts a linear relationship between the surface deflection and average crustal flow velocity. Figure 5.8a shows the observed surface deflection and channel velocity for Model C. The poor linear relationship is due to the fact that the basal velocity of the channel increases over time (Figure 5.8b), as expected for a gravitational instability (e.g., Houseman and Molnar, 1997). In Figure 5.8c, the component of Poiseiulle flow is isolated from the observations (Figure 5.8a) by subtracting half of the velocity of the lower boundary (Figure 5.8b). With this, there is a clear linear relationship between the surface deflection and flow velocity that agrees well with the expected value. This confirms

that the channel flow in this model is driven by both lateral pressure variations and basal shearing.
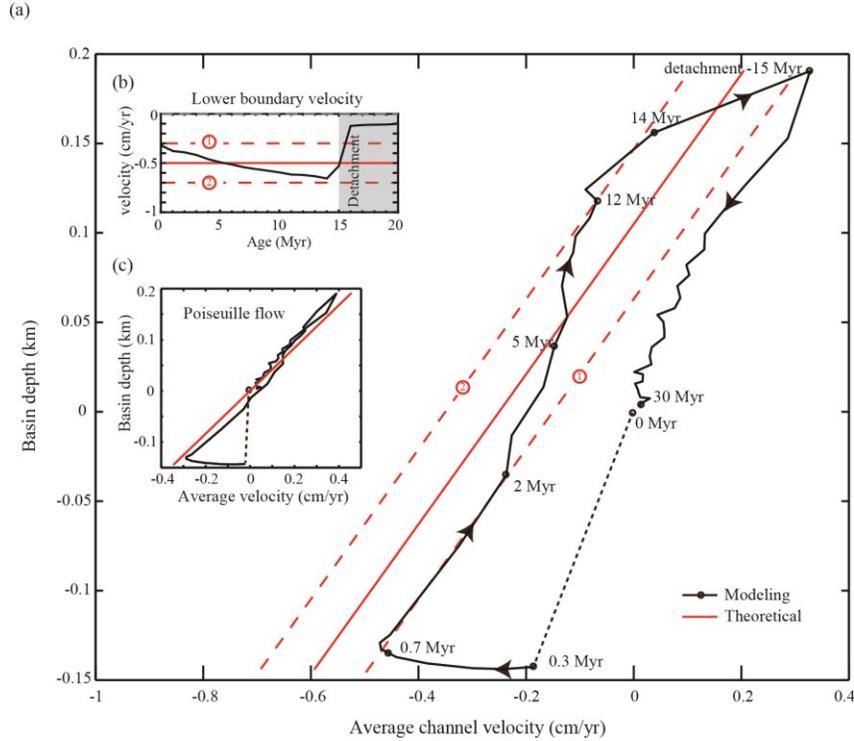
Figure 5.8. Comparison of observed and theoretical lateral velocity of crustal flow. (a) The relation between the surface elevation above the centre of the drip and the average lateral velocity at x=200 km in the lower-crustal channel. The black line is the modeling result (Model C) and the red lines are the theoretical approximations. The red solid and two dashed lines with labels ① and ② use the values of v_0 shown in Figure 5.8b in the same line pattern. (b) The velocity of the lower boundary of the channel observed in Model C over time. (c) The relation between the surface elevation above the centre of drip and the average lateral velocity of Poiseuille flow. This is calculated by subtracting half of the velocity of the lower boundary (Figure 5.8b) from the observed average channel velocity (black line in Figure 5.8a). The red line is the theoretical approximation based on the model parameters.

With a lower-crustal channel, the surface above the dense root can form a topographic high. The Poiseuille flow is driven by the surface deflection created by lateral density variations; as argued above, this isostatic balancing can only uplift the surface above the root to its initial elevation. On the other hand, the Couette flow is induced by the descending root, and this can lead to enhanced shearing and thickening

106

of the crust above the root (Pysklywec and Shahnas, 2003). It is the Couette flow that provides the additional force to elevate the topography above the surrounding areas. From Equation 5.2, the channel will have an average velocity of 0 when the surface elevation is

$$S = -6\frac{\eta_{ch}}{h_{ch}^2}\frac{L_{basin}}{\rho_c g}v_0 \qquad (5.3)$$

where the negative sign indicates that the surface deflection (S) above the root is a topographic high. At this time, the Couette flow contribution (which is always directed toward the root) is balanced by the Poiseuille flow that is directed outward from the topographic high. Equation 5.3 therefore shows the maximum elevation that can be created above the dense root. Once the dense root is removed and v_0 goes to zero, the topographic high will relax (Figure 5.7c).

5.4.4 Variations in root density and channel viscosity

Models B and C demonstrate that the presence of a weak crustal channel can significantly modify the surface expression of lithosphere drip-style removal. These models represent end-member cases of a strong crust with an extremely weak crustal channel in either the mid-crust (Model B) or lower-crust (Model C). In this section, we examine the effect of a more viscous channel and variations in the density of the root. The root density provides the driving force for removal and induces the lateral pressure gradient in the crust. The crustal viscosity determines how easily the crust will flow in response to the presence of the dense root. This leads to a complex dynamical system; a denser root will cause greater subsidence of a strong crust, but when the crust contains a weak channel, the denser root will induce more crustal flow, which can lead to greater crustal thickening and surface uplift. Thus, the surface expression of root removal is hard to predict. We have tested a suite of models with root densities that are 20 to 240 kg/m^3 greater than that of underlying mantle, and crustal channel viscosities of 10^{18} to 10^{21} Pa s. Both mid-crustal and lower-crustal channels are considered, with a 10 km channel thickness for each case.

5.4.4.1 Mid-crustal channel

Figure 5.9 shows the model results for a mid-crustal channel. From top to

bottom, these plots show the magnitude of initial surface subsidence above the dense root (z_{max}) (Figure 5.9a), the elevation of the surface at the time of root detachment (z_{td}) (Figure 5.9b), the uplift ratio (defined as (z_{td}-z_{max})/|z_{max}|; an uplift ratio of 1 corresponds to full recovery of the initial subsidence) (Figure 5.9c), and the amount of crustal thickening above the root (Figure 5.9d). In all models, the surface initially subsides as an isostatic response to the presence of the dense root. The later evolution of the surface depends on whether the crust is weak enough that crustal flow is induced. A weaker channel leads to a decreased amount of initial surface subsidence and an increased amount of surface uplift as the root detaches.

To understand the model behaviour, we define two timescales: (1) the drip timescale (t_d), which is the time taken for the root to detach from the upper plate, and (2) the crustal flow timescale (t_c), which is the time required for the crustal thickening to completely counteract the subsidence associated with the drip (i.e., the length of time needed for the surface to rebound to an elevation of 0 km). For a mid-crustal channel, t_d decreases with increasing root density (note that t_d also depends on the dimensions and the viscosity of the root and surrounding mantle, which we have not varied). The time t_d therefore sets the length of time over which crustal flow and deformation can occur in response to root dynamics. The crustal flow timescale (t_c) depends on the velocity of flow within the channel, which in turn depends on the driving force for flow (i.e., the density of the root) and the viscosity of the channel.

From the model results in Figure 5.9, three main behaviours are observed. One end-member behaviour corresponds to the case of a high viscosity channel (10^{20} Pa s or greater) and a moderately dense root (>60 kg/m^3 more dense than mantle). Here, the induced crustal flow and associated crustal thickening are relatively minor over the timescale of root detachment ($t_c \gg t_d$). The initial subsidence increases with increasing root density, and the surface remains as a topographic low throughout root removal, with an uplift ratio of less than 0.1.
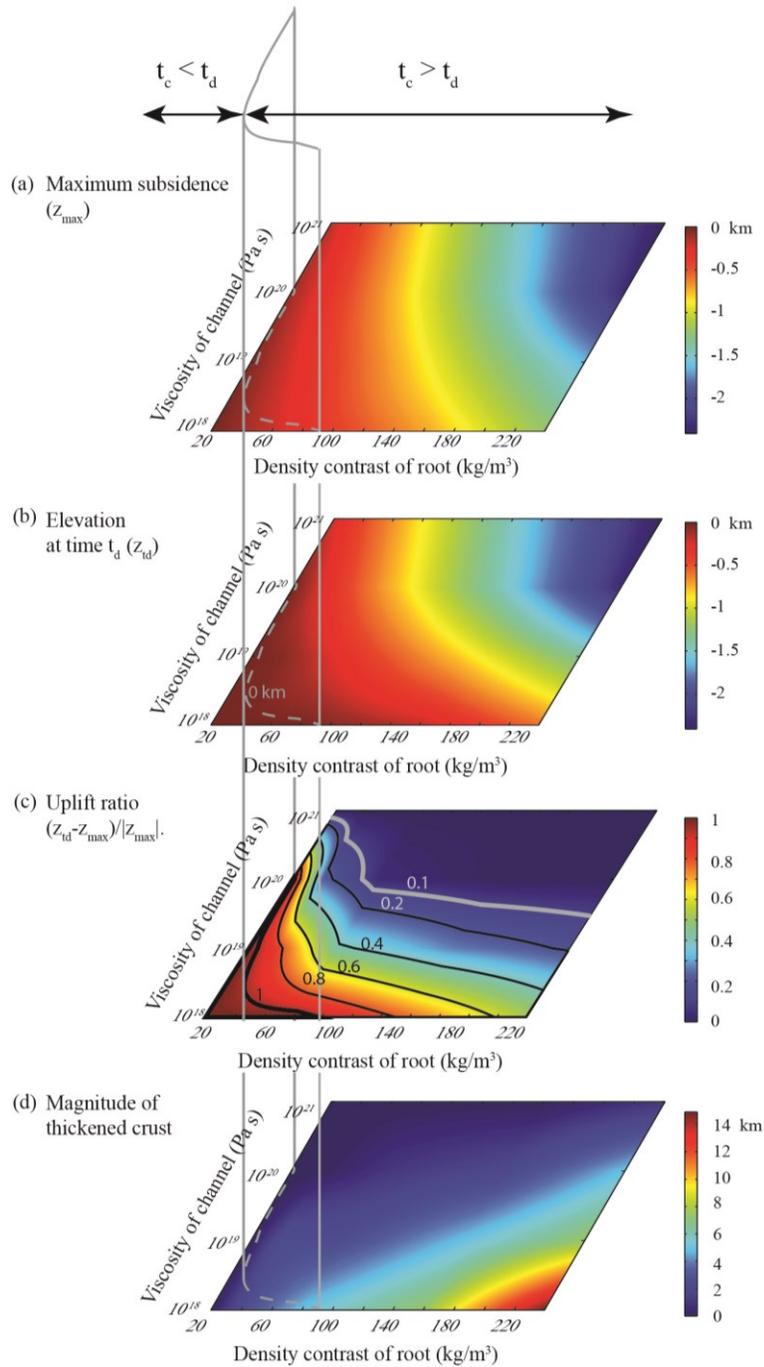
Figure 5.9. Surface elevation and crustal deformation in models with a mid-crustal channel during the Rayleigh-Taylor instability. (a) The elevation at the time of maximum surface subsidence (z_{max}). (b) The elevation at the time of root detachment (z_{td}). (c) The surface uplift ratio ((z_{td}-z_{max})/|z_{max}|). (d) The magnitude of crustal thickening above the root. t_c and t_d are the timescales for crustal flow and drip detachment (see text for discussion).

The other end-member is where the crustal flow is sufficiently rapid that there is only a short-lived basin, which undergoes 100% uplift prior to drip detachment. This corresponds to the case $t_c < t_d$, and it is observed in models where the channel viscosity is low (and hence t_c is small) and where the root density is relatively low (t_d is large). This is confined to models where the channel viscosity is less than 10^{19} Pa s and root densities are 60 kg/m^3 or less. In this case, the surface remains at zero elevation during the final stages of root removal (Figure 5.4b). Following root detachment, the surface uplifts and then subsides as the thick crust in the weak channel relaxes.

Between these end-members, an intermediate response is observed where the surface first subsides and then undergoes slow uplift as induced channel flow results in crustal thickening. Here, $t_c > t_d$, but the crustal flow is too slow to fully uplift the surface before the drip detaches. As a result, the surface remains as a topographic low throughout root removal, and detachment is associated with an increased rate of uplift.

5.4.4.2 Lower-crustal channel

Figure 5.10 shows the suite of model results for a lower-crustal channel. Again, all models show initial surface subsidence (Figure 5.10a). The later behaviour can be divided into the same groups as observed for the mid-crustal channel: (1) negligible surface uplift as the dense root is removed (uplift ratio < 0.1), (2) moderate uplift during root removal (uplift ratio of 0.1 to 1), in which the surface remains a topographic low until is root removed, and (3) full inversion of the basin during root removal (uplift ratio of 1 or greater).

The model behaviour can be understood by comparing the relative timescales of drip removal (t_d) and crustal flow (t_c). In this case, the dense root is in direct contact with the crustal channel, which has two main effects. First, the drip removal timescale now depends on both the root density and the channel viscosity. A lower viscosity allows for more rapid root removal (lower t_d) compared to the case of a mid-crustal channel with a strong lower-crust. Second, the removal of the root induces a shear along the base of the crustal channel, leading to a greater rate of crustal flow. As a result of this, the magnitude of initial subsidence is less and the magnitude of crustal thickening is greater than in models with a mid-crustal channel.
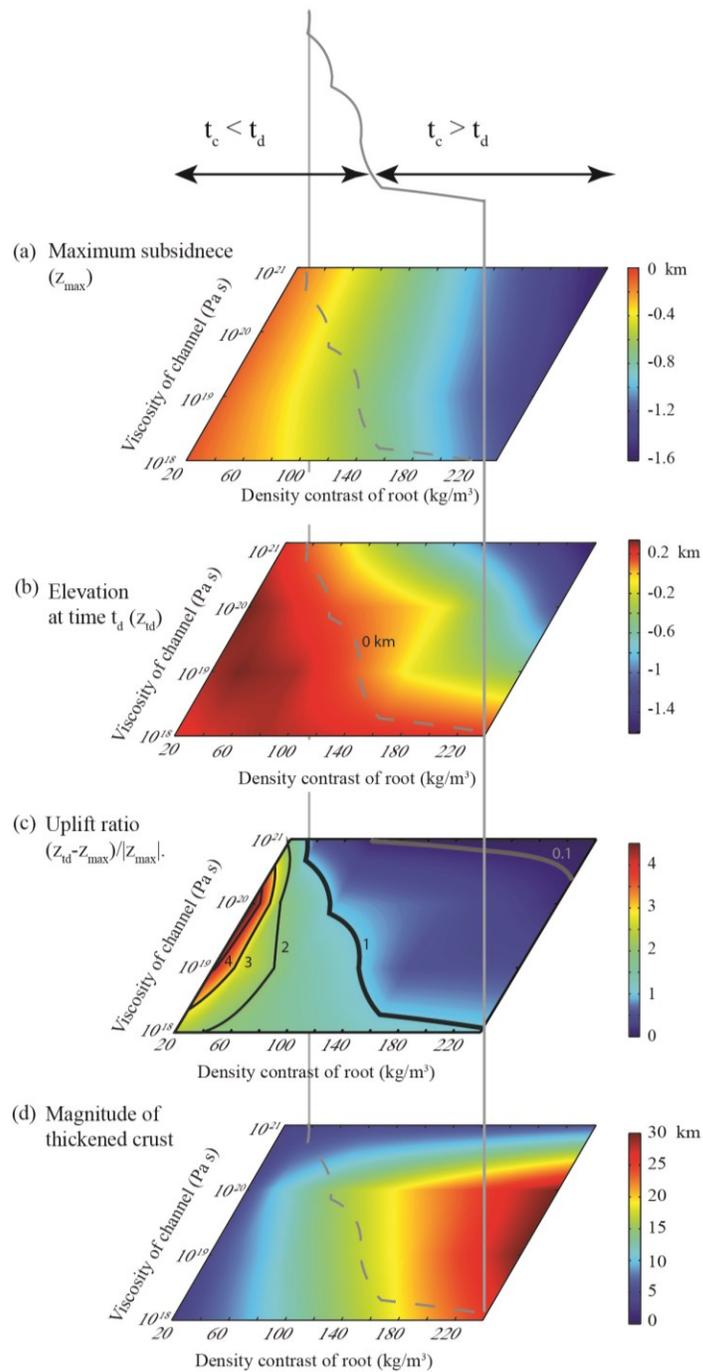
Figure 5.10. Surface elevation and crustal deformation in models with a lower-crustal channel during the Rayleigh-Taylor instability. (a) The elevation at the time of maximum surface subsidence (z_{max}). (b) The elevation at the time of root detachment (z_{td}). (c) The surface uplift ratio (($z_{td}-z_{max}$)/$|z_{max}|$). (d) The magnitude of crustal thickening above the root. t_c and t_d are the timescales for crustal flow and drip detachment (see text for discussion).

Owing to the enhanced crustal flow, a greater range of models exhibit syn-removal uplift. Only models with a high channel viscosity (10^{21} Pa s or greater) and a high root density (>140 kg/m^3 denser than mantle) show an uplift ratio of less than 0.1. There is also an increase in the range of models that exhibit full basin inversion, as channel flow creates enhanced crustal thickening. For some models, the crustal flow is sufficient to over-thicken the crust above the drip, leading to the creation of a topographic high above the dense root (uplift ratio >1). The greatest uplift is observed where the root density is relatively low (<40 kg/m^3 greater than mantle density) and the channel viscosity is 10^{19}-10^{20} Pa s. The low root density and moderate viscosity lead to a moderate drip removal timescale, which allows for sufficient time for the crust to over-thicken. If the channel viscosity is too low, t_d is reduced, and if the channel viscosity is too high, t_c is reduced; in both bases, less surface uplift occurs.

5.4.5 Variations in crustal and channel thickness

In this section, we consider how the surface response to lithosphere removal may be affected if the crust is thinner or the channel is thicker than assumed in the previous models. First, we have rerun Models A, B, and C with a 40 km crust. If the entire 40 km crust is strong (dashed line in Figure 5.4a), the surface response is similar to that seen in Model A, with surface subsidence, followed by uplift after the dense root is removed. The main differences are that the magnitude of the surface deflection is about 0.1 km greater and that the half-width of the basin is about ~50 km narrower than in Model A. This is due to the fact that the density anomaly is closer to the Earth's surface and the thinner crust has a lower flexural strength.

Figures 5.4b and 5.4c (dashed lines) show the surface response for a thin crust with a weak mid-crustal channel (located at 20-30 km depth) and a weak lower-crust (located at 30-40 km depth), respectively. In both cases, the initial subsidence of the surface is greater than for the original models, but the later evolution is similar. All models show rapid inversion of the basin prior to detachment of the root. The timing of uplift for the thin crust models is similar to that seen for the thick crust models. This suggests a slightly greater rate of channel flow and crustal thickening for the thin crust

models, in order to counteract the larger initial subsidence. This is primarily driven by the larger lateral gradient in pressure, as the thinner crust creates a deeper, narrower basin. Overall, the overall surface response to lithosphere removal is not strongly affected by variations in crustal thickness, for a given set of crustal channel and root properties.

We have also tested how the surface response may be affected with a larger channel thickness. For this, we have rerun Models B and C (60 km thick crust) with a 15 km thick channel in the mid-crust and lower-crust, respectively; the lower boundary of the channel is at the same depth as the original models. The surface evolution is shown in Figures 5.4b and 5.4c (dash-dot lines). Again, all models show an initial subsidence followed by full basin inversion before the root detaches. The models with a thicker channel show greater uplift rates and earlier basin inversion. This comes from the fact that the rate of channel flow is proportional to the square of the channel thickness (Equations 5.1 and 5.2), and therefore a thicker channel will allow for more rapid crustal thickening. From this, we conclude that if the channel is thicker than 10 km, crustal thickening, surface uplift and basin inversion may occur for higher channel viscosities than predicted in Figures 5.9 and 5.10.

5.5 Discussion

5.5.1 Intracontinental surface deflections

There are many examples of transient vertical surface deflections that have occurred in continental interiors, far from plate boundaries. In some areas, the deflection has a relatively long wavelength (100's to 1000's of km), suggesting that it is related to the dynamics of the sublithospheric mantle (e.g., Braun, 2010; Flament et al., 2013). However, there are other places where the deflection is more localized, indicating a lithospheric source. One hypothesis is that these deflections may originate from stresses at distal plate boundaries that are transmitted into the interior of the continent plate, causing lateral extension or shortening of the lithosphere (Neil and Houseman, 1999; Raimondo et al., 2014). As a result, the surface subsides for thinned lithosphere or uplifts for thickened lithosphere, creating intracratonic basins and orogens, respectively (Figure 5.11a).

There are also places with short-wavelength surface deflection that is not clearly associated with regional lithospheric deformation, such as the Tulare basin in California (Saleeby et al., 2012), the Arizaro basin in the central Andes (DeCelles et al., 2015), the Wallowa Mountains in northern Oregon (Hales et al., 2005), and the Isa Orogen in Australia (Pysklywec and Beaumont, 2004). In these places, it is proposed that the deflection is caused by the gravitational removal of a density anomaly in the deep lithosphere. It is generally assumed that lithosphere foundering should be accompanied by surface subsidence during removal, followed by isostatic uplift after the dense material detaches. However, many of the cases mentioned above show a more complex surface signature, including surface uplift and intracontinental orogeny during foundering.
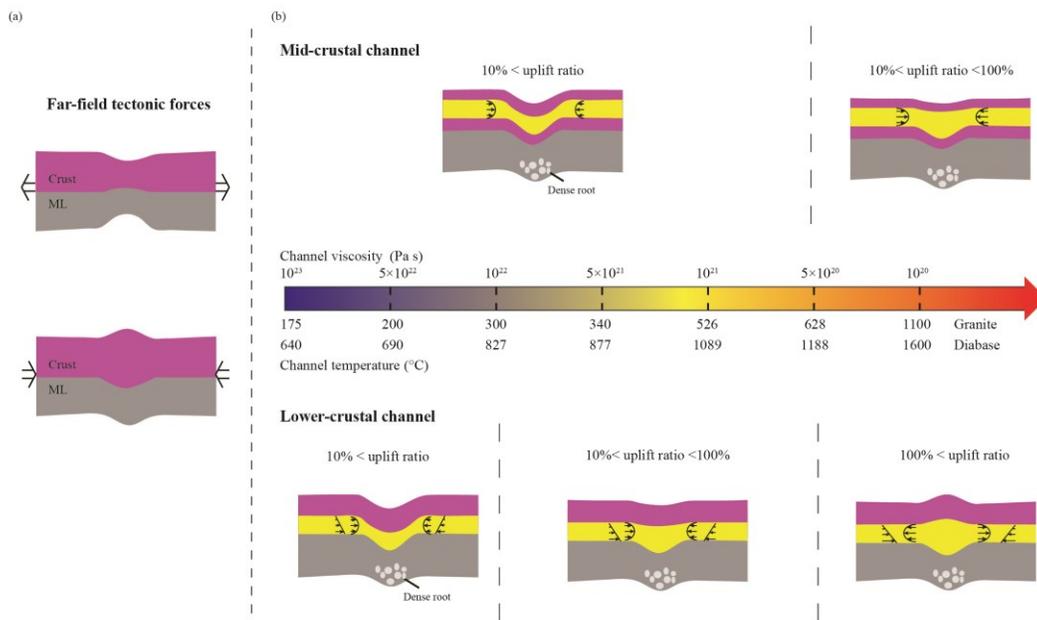
Figure 5.11. Origin of localized surface deflections in continental interiors. (a) Surface subsidence caused by extension and lithospheric thinning (top); surface uplift caused by lateral shortening and lithospheric thickening (bottom). ML=mantle lithosphere. (b) Surface deflections induced by gravitational removal of a dense anomaly (root) in the deep lithosphere, for a mid-crustal channel (top row) and lower-crustal channel (bottom row). The viscosity of the channel decreases from left to right, as shown on the center plot; also shown is the temperature corresponding to each viscosity for a granite rheology (Ranalli, 1995) and a diabase rheology (Mackwell et al., 1998). For a high channel viscosity, root removal is accompanied by surface subsidence. As channel viscosity decreases, the dense root induces flow within the channel, causing the surface to uplift.

Our study demonstrates how the presence of a low density crust modulates the surface deflection associated with removal of the density anomaly. The surface response is the result of the interaction between: (1) the vertical (normal) stresses associated with root removal that cause the surface to subside, and (2) the horizontal stresses in the crust that lead to crustal contraction and thickening, causing the surface to uplift (Pysklywec and Shahnas, 2003). The relative importance of each factor depends on the strength of the crust. Where the crust is strong, vertical stresses are efficiently transferred through the crust and the surface deflection will follow the expected pattern of syn-removal subsidence and post-removal uplift (Figure 5.11). Where the crust is relatively weak, the horizontal stresses become sufficient to deform the crust, complicating the surface response.

Earlier studies assumed a uniform crust in which the entire crust deforms if it is weak enough (e.g., Neil and Houseman, 1999; Pysklywec and Shahnas, 2003). In our models, crustal deformation occurs within a weak channel that is placed either in the mid-crust or lower-crust. This reflects a weak zone that arises from a combination of high temperature and a weak rheology (Figure 5.1). The low-viscosity channel can inhibit stress transmission from the dense drip to the surface (e.g., Burov and Diament, 1992), and thus decouple the upper crust from the dynamics of the deeper mantle (Royden et al., 1997). Using this layered rheology, we demonstrate that crustal deformation in the weak channel has two components: (1) a pressure-driven channel flow caused by lateral variations in topography that arise from the presence of the dense root; this is similar to the topographically-driven flow in orogenic regions (e.g., Kruse et al., 1991; Clark and Royden, 2000; Beaumont et al., 2001, 2004, 2006); and (2) flow that is driven by shearing on the base of the weak channel by the foundering lithosphere (Pysklywec and Shahnas, 2003).

The relative importance of each component depends on the depth of the channel, as well as the properties of the channel (thickness, viscosity) and root (density, volume, viscosity). For a mid-crustal channel, the strong lower-crust is immobile and flow is driven only by the lateral pressure gradient. If the mid-crustal channel is thick and/or weak, crustal flow is sufficient to fully compensate for the presence of the dense root,

leading to only a minor surface deflection (Figure 5.11b). With a lower-crustal channel, flow is induced by both the lateral pressure gradient and basal shear. In this case, channel flow can lead to crustal over-thickening and the creation of a topographic high above the descending root (Figure 5.11b).

The models in this study are simplified in order to demonstrate the first-order crustal dynamics that may occur during gravitational removal of the deep lithosphere. Each layer has a constant density and constant viscosity. The general crustal deformation style (i.e., crustal flow) and associated surface response (subsidence or uplift) have been observed in numerical models that use a more complex rheology (e.g., Pysklywec and Beaumont, 2004; Chapters 3 and 4), but further work is needed to assess how a temperature-dependent density and non-Newtonian rheology may alter the details of the surface response to lithosphere removal. In addition, the dense root is instantaneously emplaced in our models, and therefore the early evolution of the models (first 1-2 Myr) involves rapid isostatic subsidence to compensate for the dense root. In nature, the density anomaly should develop gradually, for example, through progressive metamorphism or the addition of dense magmatic components to the lithosphere. Therefore, the initial subsidence should occur more gradually and the timescale for the gravitational instability (t_d) will be somewhat longer than in our models. This could allow for a wider range of conditions for basin inversion than predicted in Figures 5.9 and 5.10. The gradual emplacement of a dense root was studied in Chapter 3. It was demonstrated that this can lead to flow-induced crustal thickening and surface uplift prior to gravitational removal of the root if the deep crust is weak, as observed in the models in this study.

5.5.2 Implications for intraplate deformation

The numerical experiments show the relationship between crustal strength and the surface deflection induced by lithospheric gravitational removal (Figures 5.9 and 5.10). Here, we use the simplified models to predict the surface deflection for different crustal temperatures and compositions. In particular, we wish to place general constraints on the conditions under which lithosphere foundering will be accompanied by (1) subsidence, (2) subsidence and then syn-removal uplift, and (3) surface uplift to a

topographic high. We note that this is an approximation, as our models use a constant density and viscosity for each lithospheric layer and a fixed 10 km thick crustal channel.

Figure 5.11b shows the types of surface deflection as a function of viscosity in the mid-crust and lower-crust channel. For this, we use the model results for a root that is 40 kg/m^3 denser than mantle. This could reflect a root that is 16% eclogitized (assuming a mafic eclogite density of 3550 kg/m^3; Christensen and Mooney, 1995) or that is ~400°C cooler than the underlying mantle. From Figure 5.9 (mid-crustal channel) and Figure 5.10 (lower-crustal channel), we identify the critical channel viscosities needed for an uplift ratio of <10% (surface remains as a topographic low), an uplift ratio of 10-100% (partial uplift), and an uplift ratio >100% (full uplift to a topographic high). The rheologies of dry granite (Ranalli, 1995) and dry Maryland diabase (Mackwell et al., 1998) are used to link the viscosity to the average temperature in the channel, assuming a strain rate of 10^{-15} s^{-1}. These represent end-member felsic and mafic crustal compositions, respectively.

For a mid-crustal channel (upper row in Figure 5.11b), the model results predict that the removal of a dense root will cause subsidence (<10% uplift) if the channel viscosity is greater than ~5×10^{20} Pa s; at lower viscosities, the surface will partially uplift during root removal. For a felsic composition (i.e., dry granite; Ranalli, 1995), this viscosity corresponds to a temperature of ~628°C. If the mid-crust is hotter than this, then gravitational removal will be accompanied by subsidence followed by uplift. If the mid-crust has a mafic composition (i.e., dry Maryland diabase; Mackwell et al., 1998), the critical viscosity corresponds to a temperature of 1188°C; this is too hot for reasonable crustal geotherms (e.g., Figure 5.1). Further, in order for 100% uplift to occur, a mid-crustal channel viscosity of 3×10^{18} Pa s is needed (Figure 5.9) is needed. This requires temperatures greater than 1300°C for both a felsic and mafic rheology, which are unlikely to occur in nature.

The lower row in Figure 5.11b shows the predicted surface response for difference lower-crustal viscosities. Syn-drip subsidence requires a lower-crustal viscosity greater than ~10^{22} Pa s, corresponding to temperatures less than 300°C for a felsic crust and 827°C for a mafic crust. On the other hand, significant lower-crustal flow, leading to the formation of a topographic high (uplift >100%) occurs if the lower-crustal viscosity

is less than $\sim 5 \times 10^{20}$ Pa s. This corresponds to lower-crustal temperatures greater than $\sim 628°C$ for dry granite, and $\sim 1188°C$ for dry Maryland diabase. For reasonable crustal temperatures (Figure 5.1), it is likely that >100% uplift would only occur if the lower crust is felsic. At intermediate viscosities and temperatures, lithosphere removal will be accompanied by partial (10-100%) surface uplift.

We now link our model predictions to regions where lithosphere density anomalies have been proposed to have caused an observable surface deflection. First, the Williston basin in central North America is a circular basin containing ~ 5 km sediments (Naimark and Ismail-Zadeh, 1995). Subsidence started at 480 Ma. Until present, it remains as a topographic low and there are no indications of uplift (Figure 5.12). Even though, the Williston basin has a long-wavelength (400-700 km), but its large magnitude of subsidence probably indicates that the anomalous stress is located in the lithosphere. The subsidence has been related to the formation of a dense eclogite lens in the lithosphere (Hajnal et al., 1984; Fowler and Nisbet, 1985). In this area, the observed surface heat flow is 50-60 mW/m^2 (Blackwell and Richards, 2004) and the crustal thickness is ~ 55 km (Fowler and Nisbet, 1985). This implies mid-crustal temperatures of $\sim 550°C$ and lower-crustal temperatures of $\sim 700°C$ (slightly cooler than those shown in Figure 5.1a, which represents a 60 km crust). If Williston basin subsidence is due to a lithospheric density anomaly, the observed subsidence indicates little induced crustal deformation. This is requires dry mafic lower-crust (Figure 5.11b). The long time period for subsidence is also consistent with a strong lithosphere in which the rate of gravitational instability growth is extremely low; it may even have stagnated.
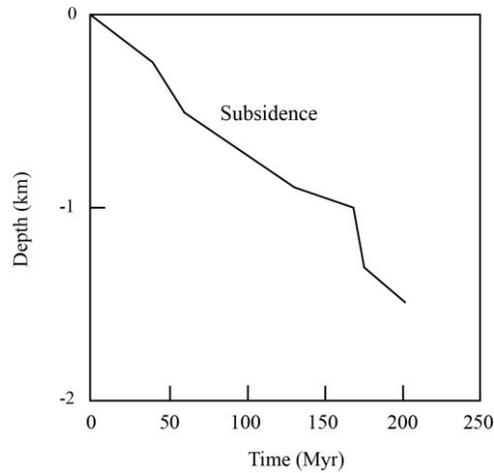
Figure 5.12. Surface history of Williston basin (modified after Naimark and Ismail-Zadeh, 1995). The depth (y-axis) and time (x-axis) are relative to the elevation of this region at the onset of subsidence at 480 Ma.
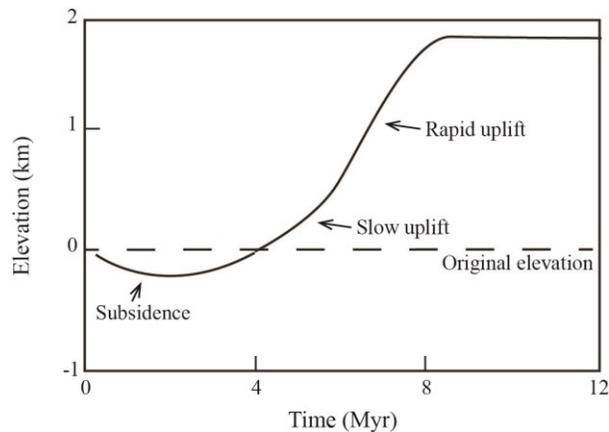
Figure 5.13. Surface history of Wallowa Mountains (modified after Hales et al., 2005). Time start since the basin subsided. The depth (y-axis) and time (x-axis) are relative to the elevation of this region at the onset of subsidence at 12 Ma.

On the other hand, there are areas where lithospheric removal appears to have produced a basin that is then uplifted to become a topographic high during the removal process. For instance, the Wallowa Mountains in northern Oregon is a region with only a minor component of subsidence but a prolonged period of uplift to form a topographic high (Hales et al. 2005; Figure 5.13). The Wallowa Mountains exhibited a small-

119

magnitude subsidence (<0.2 km) from ~12 Ma to ~10 Ma (Hales et al., 2005). Then, the surface deflection reversed, forming a topographic high with a relatively low uplift rate (~0.3 km/Myr) at ~8 Ma. After ~0.3 km of uplift, the rate increased to ~0.6 km/Myr, bringing the surface to its present ~2 km elevation. This surface deflection is proposed to be synchronous with the formation and gravitational instability of a dense magmatic root (Hales et al., 2005; Darold and Humphreys, 2013). Our results suggest that the initial slow uplift and basin inversion are likely caused by lower-crustal flow, followed by a rapid uplift after the dense lithosphere detached (as shown in Figure 5.4c). The crustal thickness is ~40 km in northern Orogen (Darolad and Humphreys, 2013) with a relatively high heat flow (~70 mW/m^2; Blackwell et al., 1982; Blackwell and Richards, 2004). This corresponds to a ~700°C mid-crust and a ~900°C lower-crust (based on Figure 5.1d which represents a 40 km crust). In order for gravitational removal to create a topographic high (>100% uplift), Figure 5.11b implies the lower-crust is probably felsic (e.g., granite).

We note that the observed surface deflection in Williston basin and Wallowa Mountains are one order of magnitude larger than that in numerical models. This could due to the variation of dimension and density of the dense instability and crustal properties (e.g., thickness and rheology). The purpose of this study is to investigate the first-order effects of the crust on the surface deflection, as well as lateral crustal deformation induced by gravitational instability. To fit a specific regional observation, a more realistic model should be developed based on the lithosphere structure of that area (thickness, temperature and density structure). Models should also include a non-Newtonian viscosity and temperature-dependent density.

5.5.3 Rayleigh-Taylor Instability in 3-dimension

All numerical models in this study use 2D plane-strain calculations, in which the deformations are parallel to the model plane. But in 3D, the material deformation and displacement can occur perpendicular to the plane, which complicates the stress and temperature fields in the models.

The Rayleigh-Taylor instability process has been investigated in 3D under the assumption of 2D axisymmetry by Hoogenboom and Houseman (2006). In their

analysis, the drip develops in symmetry about an axis. Because of additional downwelling stresses from all directions around the symmetric axis, the drip in 3D grows and detaches faster than that in 2D. Hoogenboom and Houseman (2006) also find the development of the RT instability in 3D could result in a larger deflection at surface than that in 2D.

In our study, the surface uplift depends on how much the crust can flow and thicken above the descending drip. In 3D, the crust could be thickened more rapidly because (1) the crust can flow from all directions perpendicular to the symmetry axis; and (2) the crust experiences a greater shearing stress towards the drip column from the underlying mantle. As a consequence, in 3D the surface would uplift faster and return back to its original elevation earlier than that in 2D models when the mid-crust is weak. The 3D flow may create a higher orogen when the lower crust is weak. Future work is needed to examine 3D effects quantitatively.

5.6 Conclusions

In this study, we have addressed the topographic expression of gravitational removal of the deep continental lithosphere through Rayleigh-Taylor instability. In accordance with earlier studies (e.g., Neil and Houseman, 2000; Pysklywec and Shahnas, 2003), we find that the presence of a low-density crust above the density anomaly can affect the topographic response to lithosphere removal. The dense root induces three main stresses on the overlying crust: (1) a vertical normal stress owing to the root density, (2) a horizontal shear stress associated with the dynamical removal of the root, and (3) a lateral pressure gradient that arises from the topographic variations created by the presence of the dense root. The first stress acts to cause surface subsidence, while the latter two act to compress and thicken the crust above the root, producing surface uplift. The overall topographic expression depends on the magnitude of these stresses compared to the strength of the crust (Figure 5.11b):

- If the crust is strong enough to resist horizontal compression, it will not deform and the topographic expression directly reflects root dynamics (stress 1); root removal creates surface subsidence, followed by uplift after the root detaches.

- If the crust contains a weak, low viscosity channel surrounded by two strong layers, the dense root can induce Poiseuille flow within the channel owing to lateral pressure variations (stress 3). This leads to crustal thickening and surface uplift while the root is undergoing removal. The maximum amount of uplift corresponds to the topography of the adjacent regions that have no dense root.

- If the lower-crust is weak and is in direct contact with the dense root, crustal deformation can occur due to both basal shearing (stress 2) and lateral pressure variations (stress 3). The crust thickens through a combination of Poiseuille flow and Couette flow. The basal shearing can create over-thicken the crust, creating a topographic high during root removal.

Crustal strength calculations (Figure 5.1) show that a strong crust may be found in areas of low heat flow, especially where the crust is thin. In these areas lithosphere removal is predicted to be accompanied by surface subsidence. A mid-crustal channel can be created in warm, thick crust, in which the upper-mid crust has a rheologically weak composition (e.g., felsic granite) and the lower-crust has a strong mafic composition (e.g., dry Maryland diabase). A weak lower-crustal channel can be created if the crust is hot and felsic. A weak lower-crust can also occur in areas with an enhanced concentration of radioactive elements, crustal hydration and partial melting (e.g., Pysklywec and Beaumont, 2004). In the case of a weak mid-crust or lower-crust, lithosphere removal may be expressed through either a minor surface deflection or through the formation of a topographic high. This range of behaviours is consistent with the range of surface deflections observed in areas where RTI's have been proposed. This suggests that gravitational removal of the lithosphere is a viable process for causing transient topographic variations in intracontinental areas.

5.7 Appendix: Crustal channel flow approximation

5.7.1 Mid-crustal channel

We first consider a ductile channel in the mid-crust. Figure 5.14 shows the simplified two-dimensional model structure. We assume that the upper and lower boundaries (i.e., upper and lower crust) of the ductile channel are strong, such that no

horizontal deformation can occur but they can be deformed vertically. We also assume the whole crust has a constant density and the ductile channel and mantle lithosphere have a constant (Newtonian) viscosity, which allows for a simplified treatment of channel flow and the effect of root foundering.

Lateral variations of mass in the mantle lithosphere or in the crust generate lateral variations of pressure in the ductile crustal channel. This occurs because the presence of a density anomaly (e.g., a dense root) causes a surface deflection through vertical isostatic adjustment. The topographic gradient induces a pressure gradient in the crust, where areas of low topography have a lower-crustal pressure. If the crust is weak enough, this can induce ductile crustal flow from high pressure areas to low pressure areas, in order to reduce the pressure gradient (e.g., Bird, 1991, Kruse et al., 1991).
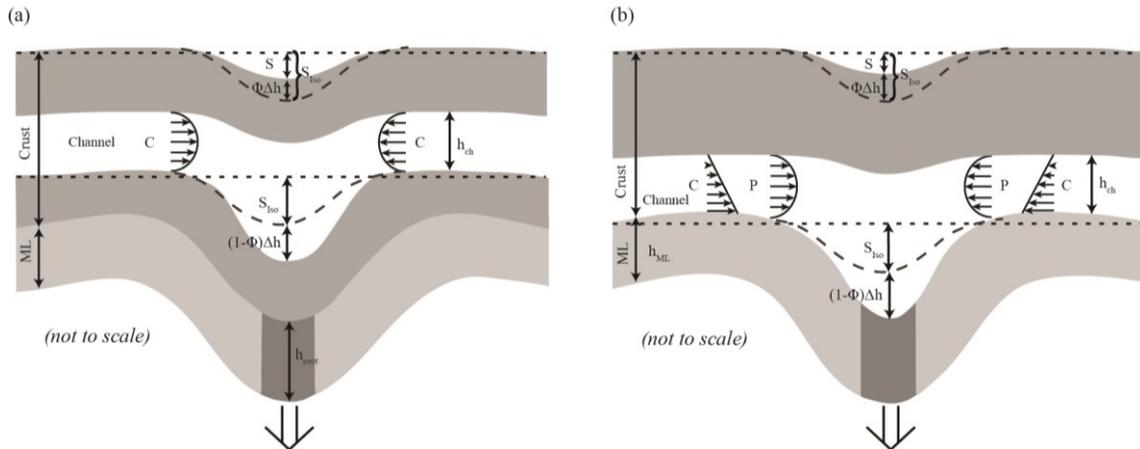
Figure 5.14. Schematic illustrating the channel boundaries and behavior of crustal deformation during the downwelling of a RT drip in mantle. (a) Mid-crustal channel, which is bounded by strong upper crust and lower-crust. Couette flow (C) induced in the mid-crustal channel. (b) Lower-crustal channel, which is directly coupled with lithosphere. Poiseuille flow (P) and Couette flow (C) are induced in the lower-crustal channel. (See text for definition of other symbols).

For a mid-crustal channel, the channel deforms through Poiseuille flow, with no velocity at the upper and lower boundaries and the maximum velocity in the center of the channel. The average channel velocity $\bar{v}$ can be expressed as (Turcotte and Schubert, 2002):

$$\bar{v} = \frac{h_{ch}^2}{12\eta_{ch}} \frac{dP}{dx} \tag{5.4}$$

where η_{ch} and h_{ch} are the viscosity and thickness of channel, respectively, and $\frac{dP}{dx}$ is the horizontal pressure gradient.

In our models, the horizontal pressure gradient arises from the presence of a high density root in the mantle lithosphere. The pressure gradient from the dense root on the crust can be written as:

$$\frac{dP}{dx} = \frac{C_0 \Delta\rho_{root} g h_{root}}{L/2} \tag{5.5}$$

where C_0 is a coefficient that denotes the viscous coupling between the root and overlying crust, $\Delta\rho_{root}$ is the density contrast between the root and the underlying mantle ($\Delta\rho_{root} = \rho_{root} - \rho_m$), g is the gravitational acceleration, h_{root} is the thickness of the root, and L is the horizontal length scale for the channel flow. Airy isostatic adjustment causes the surface above the dense root to subside, as expressed by:

$$C_1 C_0 \Delta\rho_{root} g h_{root} = \rho_m g S_{iso} \tag{5.6}$$

where C_1 is a factor that accounts for lithospheric flexure rigidity and S_{iso} is the magnitude of isostatic subsidence at the surface.

Equation 5.6 shows how subsidence is related to the properties of the root; a thicker or denser root will create a greater surface deflection. In the analysis of our models, the most important factor is the surface deflection that is induced by the presence of the dense root (S_{iso}), as it is the surface deflection that induces a pressure gradient in the crust. The pressure gradient can be written as:

$$\frac{dP}{dx} = \frac{\rho_c g S_{iso}}{L/2} = \frac{\rho_c g S_{iso}}{L_{basin}} \tag{5.7}$$

where ρ_{root} is the crustal density and L_{basin} is the half-width of the basin. Here the length scale for channel flow from high topography to low topography (L) is taken to be approximately the half-width of the basin (L_{basin}).

As a result of channel flow, the crust above the root will thicken. If the crust thickens by Δh, then according to Airy isostatic compensation, the surface will uplift by $\Phi\Delta h$ (where $\Phi = (\rho_m - \rho_c)/\rho_m$) and the lower boundary of the crust (or Moho) will be pushed downward by $(1 - \Phi)\Delta h$, due to the weight of the thickened crust (Kruse et al., 1991; Turcotte and Schubert, 2002). Thus, the surface topography that drives

channel flow depends on both the dense root and the induced crustal thickening, with a total surface deflection of:

$$S = S_{iso} - \Phi \Delta h \qquad (5.8)$$

The pressure gradient in the channel (Equation 5.7) becomes:

$$\frac{dP}{dx} = \frac{\rho_c g S}{L_{basin}} \qquad (5.9)$$

Plugging Equation 5.9 into Equation 5.4, the average velocity of channel flow is:

$$\bar{v} = \frac{h_{ch}^2}{12\eta_{ch}} \rho_c g \frac{S}{L_{basin}} \qquad (5.10)$$

This equation shows that: (1) the rate of flow is proportional to the observed surface deflection S (which accounts for both the effect of the dense root and crustal thickening due to channel flow), and (2) crustal flow ceases when there is no vertical surface deflection (S = 0).

5.7.2 Lower-crustal channel

If the weak channel is located in the lower-crust, we assume that its upper boundary (upper-mid crust) is strong and can not be deformed laterally (Figure 5.14b). The lower boundary is directly attached to the mantle lithosphere and can be deformed both vertically and horizontally as the dense root is removed. Therefore, the channel will have zero velocity on its upper boundary but a non-zero velocity on its lower boundary.

As the dense root founders, it will entrain the adjacent mantle lithosphere, causing shear along the base of the channel towards the dense root. The relative motion between the upper and lower boundaries of the channel induces the Couette flow in the channel, with an average velocity of (Turcotte and Schubert, 2002):

$$\bar{v}_c = \frac{1}{2} v_0 \qquad (5.11)$$

where v_0 is the relative lateral velocity of the lower boundary.

In addition to Couette flow, the channel will exhibit Poiseuille flow associated with the lateral pressure gradient induced by the dense root, as discussed above. Therefore, the net velocity of the lower-crustal channel is the sum of Equations 5.10 and 5.11:

$$\bar{v} = \frac{h_{ch}{}^2 \rho_c g S}{12 \eta_{ch} L_{basin}} + \frac{1}{2} v_0 \qquad (5.12)$$

This shows that the channel flow velocity depends on both the surface deflection and the basal shearing velocity. In addition, the basal shearing velocity creates an additional compressive force on the crust, enabling it to have a greater thickness than can be generated by only the lateral pressure gradient.

Chapter 6

Continental magmatism induced by lithospheric removal

6.1 Introduction

Gravitational removal of lithosphere appears to have occurred in a number of continental regions, causing magmatism sourced from both mantle and crust. A range of geophysical and geochemical observations supports the idea that a significant portion of continental lithosphere has been recycled into the deeper convecting mantle. For example, seismic images show that the mantle lithosphere is abnormally thin and the hot asthenosphere is located less than 20 km below the continental crust in many regions, such as the Altiplano-Puna plateau in South America (Myers et al., 1998; Bianchi et al., 2012; Heit et al., 2014), the western North Island in New Zealand (Stern et al., 2006; Salmon et al., 2011) and the Wallowa Mountains in Oregon (Hales et al., 2005; Darold and Humphreys, 2013). These observations conflict with the expectation that felsic crust should be underlain by thick ultramafic/mafic materials in order to balance geochemical element budgets (Rudnick and Fountain, 1995; Plank, 2005; Lee et al., 2006). Furthermore, seismic studies find high-velocity anomalies in the shallow sublithospheric mantle (100-200 km depth) of the southern Sierra Nevada and the Great Basin in the western United States (West et al., 2005; Saleeby et al., 2012), the western Mediterranean in southern Spain and northern Morocco (Thurner et al., 2014), and the Puna plateau (Schurr et al., 2006; Bianchi et al., 2012). These are interpreted to be pieces of cool lithosphere that have detached from the overlying plate.

Seismic observations provide snapshots of present-day lithosphere removal events. Both ongoing and ancient removal events may be traced through anomalous surface observations that can not be readily explained by regional tectonics. These include the generation of local basins/orogens, crustal contraction/extension, and increased heat flow and magmatism (e.g., Springer, 1999; Farmer et al., 2002; Gao et al., 2008; DeCelles et al., 2015; Schoenbohm and Carrapa, 2014). Of these, magmatism is usually considered to be the clearest evidence, as it indicates a rapid change in the thermal structure of the deep lithosphere (Kay and Kay, 1993). Magmas provide thermal and compositional information of their source region, and therefore they can be used to investigate the mechanism and scale of the lithosphere recycling process (e.g., Kay et al., 1994; Ducea, 2011). However, magma samples from different regions that appear to have had removal events show variations in the source composition and pressure-

temperature (PT) evolution of the melts. In addition, lithospheric removal has been invoked to explain the origin of some intracratonic basins, but there is no magmatism associated with these events (Elkins-Tanton, 2005). To date, there has been little work to understand that dynamical relationship between lithosphere removal and its magmatic expression.

The classical view is that magmatism originates from decompression melting of asthenospheric mantle that upwells to fill the gap created by lithosphere removal (e.g., Kay and Kay, 1993; Kay et al., 1994). In this case, the rising asthenosphere follows a mantle adiabat and its melting temperature and pressure should decrease during the removal process (Kay et al., 1994; Lee et al., 2009). For example, the southern Sierra Nevada, which is proposed to be a region with recent lithospheric foundering (e.g., Ducea and Saleeby, 1996 and 1998; Saleeby et al., 2012), experienced an eruption of small volume, high-potassium mafic magmas in Pliocene. These are interpreted to reflect decompression melting of metasomatized asthenosphere (e.g., Manley et al., 2000; Farmer et al., 2002; Elkins-Tanton and Grove, 2003).

The descending lithosphere may also contribute to the magmatism. Elkins-Tanton (2005; 2007) suggests that the descending lithosphere may devolatilize as it founders, which may trigger melting of the surrounding asthenosphere. Furthermore, Ducea et al. (2013) and Murray et al. (2015) find that the composition of young magmas in the southern Puna plateau has changed over time. Earlier magmatism (at ~1 Ma) appears to have been extracted from lithospheric pyroxentites, whereas more recent magma is consistent with an asthenospheric peridotite source. The melting temperature of lithospheric pyroxenites increases from ~1200°C to ~1300°C within 1 Myr (Ducea et al., 2013). This increasing temperature is contrary to the expected decrease temperature for decompression melting of asthenosphere. They hypothesize that magmatism is related to lithospheric foundering. Initial melts are extracted from conductive heating and melting of small pieces of sinking lithosphere, whereas later melts originate from the upwelling asthenosphere.

The expressions of magmatism are further complicated if the remaining lithosphere (lithospheric mantle and/or crust) also experiences partial melting owing to rapid heating following a removal event. This has been proposed to explain silicic

volcano in the southern Sierra Nevada (Moore and Dodge, 1980), shoshonitic volcanism on the Tibetan plateau (Turner et al., 1993 and 1996; Chung et al., 2003) and felsic ignimbrites in the central Andes (Schilling et al., 2006).

Most inferences of magmatism induced by lithospheric removal are based on geochemical observations. Only a few geodynamics studies have investigated magmatism using forward models. Elkins-Tanton (2005; 2007) studied melting associated with lithosphere removal as a Rayleigh-Taylor instability (one style of lithosphere removal, see Section 6.2), in order to understand how asthenospheric melting may be induced by adiabatic upwelling and devolatilization of the descending lithosphere. Gorczyk and Vogt (2013) examined lithosphere dynamics during regional shortening and found that lithosphere removal and magmatism could occur under some conditions, depending on the pre-existing structure of the lithosphere.

Until now, it is still not well-understood how the magmatic signature of removal may vary depending on the tectonic setting and removal style. In this study, coupled thermal-mechanical models are used to study magmatism and other surface expressions of lithospheric removal, for settings ranging from a hot, thin lithosphere (i.e., back arc or mobile belt) to thick, cool lithosphere (i.e., stable continental interior). The model results demonstrate the potential source regions of magmatism and how magma composition and PT conditions may change during removal.

6.2 Styles of lithospheric removal

Lower lithosphere can detach and sink into the convective mantle in different styles, depending on the rheology and density structure. Generally, continental lithosphere can be recycled in two ways: Rayleigh-Taylor instability and delamination. In a Rayleigh-Taylor instability, the lower lithosphere descends into the deep mantle as a "drip" (e.g., Houseman and Molnar, 1997). In delamination, the lower lithosphere peels away from the upper plate as an intact layer, where decoupling occurs along a weak interface (e.g., Bird, 1979). For delamination to occur, there must be a weak layer within the lithosphere, whereas a Rayleigh-Taylor instability involves the part of the lithosphere that is weak enough to destabilize (e.g., Göğüş and Pysklywec, 2008).

Lithospheric removal is driven by the gravitational instability of high-density

materials in the lower lithosphere. The presence of pyroxenite, the second-most abundant mineral in the lithospheric mantle (Lee et al., 2011), is a common cause of gravitational instability in the upper plate (e.g., DeCelles et al., 2009; Ducea et al., 2013). Pyroxenite rocks can be generated from the formation of cumulates and/or residues of ancient magmas (Lee et al., 2006; 2011). When they are in the garnet stability field (depth >40 km; Rapp and Watson, 1995), most garnet pyroxenite rocks are denser than the underlying asthenosphere (Ducea et al., 2013 and reference therein). Garnet pyroxenites (loosely referred to as eclogites; Lee et al., 2006 and 2011) may be 50-250 kg/m^3 denser than the underlying peridotite mantle (e.g., Ducea and Saleeby, 1998; Jull and Kelemen, 2001; Horodyskyj et al., 2007). A xenolith study shows a garnet pyroxenite root, which was ~40 km thick and 200 kg/m^3 denser than the asthenospheric peridotites, existed beneath central Sierra Nevada before the removal event in Pliocene (Ducea and Saleeby, 1998).

The link between pyroxenite rocks and lithosphere removal is further supported by magmatic evidence. In several regions where lithospheric removal has been inferred, the magmas appear to have a pyroxenite source, such as the Puna plateau (Ducea et al., 2013; Murray et al., 2015) and the North China Craton (Gao et al., 2008). The solidus of pyroxenite is suggested to be ~150 °C lower than that of peridotite (Hirschmann and Stolper, 1996; Pertermann and Hirschmann, 2003; Lambart et al., 2009). Therefore, the pyroxenites are more likely than peridotites to melt as they descend into the hot asthenosphere.

Peridotites (with or without garnet) in the mantle lithosphere could also be gravitationally unstable, owing to their low temperature (e.g., Houseman and Molnar, 1997). Lithosphere that is 100-400°C cooler than asthenosphere will be 10-40 kg/m^3 more dense, assuming no compositional difference between the two. In this case, removal via Rayleigh-Taylor instability may be limited to the lowermost lithosphere where the viscosity is low enough for removal (e.g., Conrad and Molnar, 1999). Removal of the entire thickness of mantle lithosphere could occur through delamination, which requires the presence of a pre-existing weak layer at the base of the crust. In the following models, we assume lithosphere removal is initiated by the presence of a dense pyroxenite anomaly and trace the resultant magmatism. However,

the models also provide insight into gravitational removal of cool peridotite, as we examine the effect of different density contrasts between the lithosphere and asthenosphere (Section 6.5.1).

6.3 Numerical methods

6.3.1 Modeling approach

We use two-dimensional numerical models to investigate continental magmatism caused by lithosphere removal. We test models with either a thin (75 km) or thick (115 km) lithosphere, in order to explore how magmatism varies with lithosphere thickness and therefore thermal structure. In both cases, a 40 km thick crust is used. The thin lithosphere model has a 35 km mantle lithosphere, which leads to high temperatures (979°C) at the Moho (Figure 6.1a). This is designed to approximate a tectonically-active region, such as a continental back arc, in which lithosphere has been thinned and heated by asthenospheric mantle convection (Currie and Hyndman, 2006). The thick lithosphere model has a 75 km mantle lithosphere, with a 610°C Moho (Figures 6.1b and 6.1c). This is comparable to average Phanerozoic continental lithosphere and is somewhat warmer than a stable cratonic region (e.g., Jaupart and Mareschal, 1999). As shown below, this lithosphere is too cool to melt during gravitational removal, and therefore an even colder lithosphere would also not melt.

The numerical models use the finite element code SOPALE, which calculates the coupled thermal-mechanical evolution of the lithosphere-upper mantle system based on arbitrary Eulerian-Lagragian techniques, assuming incompressibility and plane strain (Fullsack, 1995). All models are 400 km deep and 800 km wide. The Eulerian mesh has 321 × 120 elements, with an element width of 2.5 km for the entire model domain. The element height is 2.5 km in the top 35 km, 1.25 km between 35 and 120 km depth and 10 km at greater depths. The smaller elements are used to ensure a well-resolved sinking lithosphere and upwelling asthenosphere. Boundary conditions for the models are shown in Figure 6.1, and the material parameters for each material are given in Table 6.1. The top boundary of the model domain has a constant temperature of 0°C and is stress free, which allows it to be deflected in response to subsurface dynamics. The side boundaries are free slip and have no heat or material transfer. The thermal

structure in the asthenosphere is initially adiabatic, with a gradient of 0.4°C/km and potential temperature of 1300°C (Figure 6.1). The lithosphere thermal structure is determined by varying the surface heat flow until the conductive geotherm in the lithosphere (calculated from the lithosphere thermal properties) intersects the mantle adiabat at the base of the lithosphere.
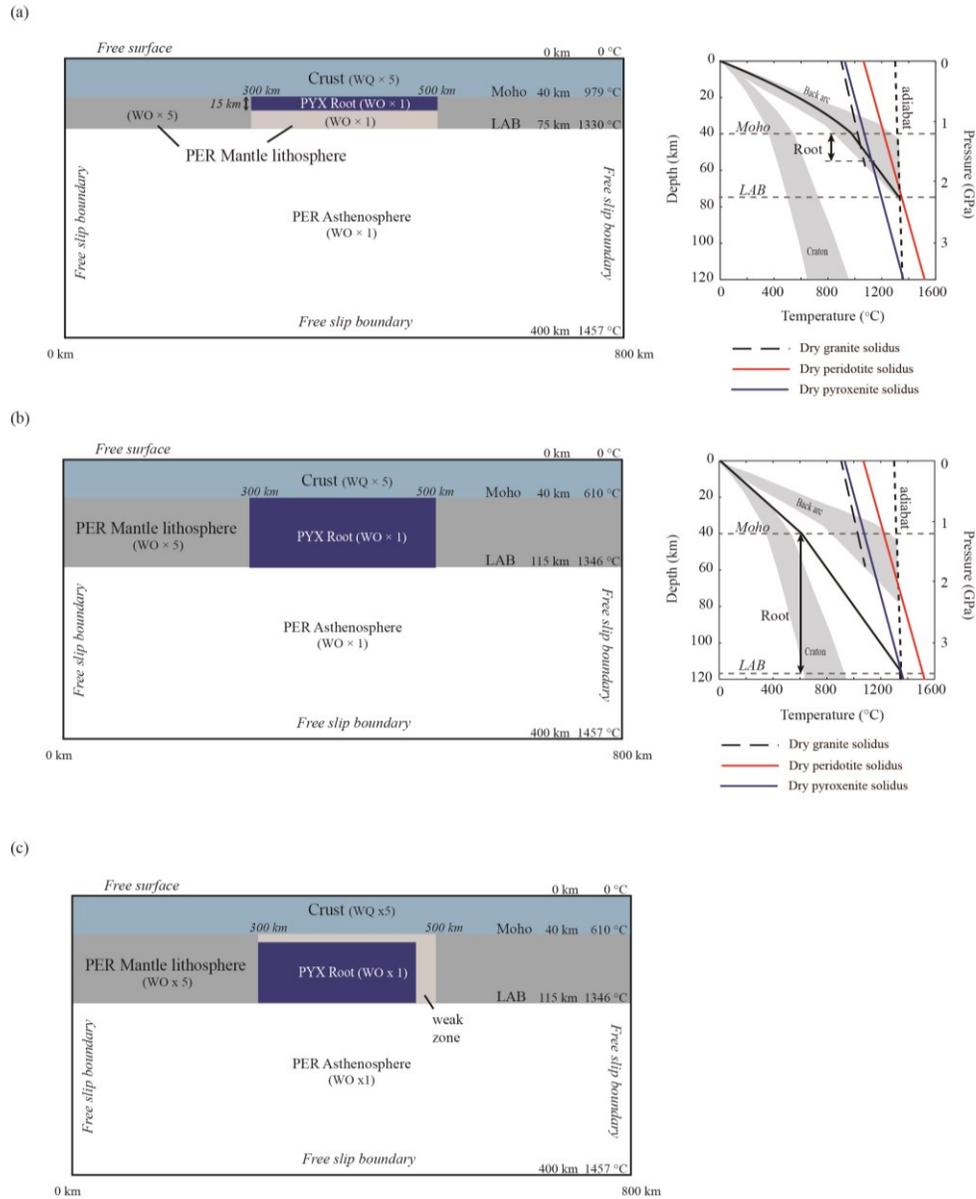
Figure 6.1. Numerical model setup and thermal-mechanical boundary conditions. (a) Model setup for a 75 km thick lithosphere for Rayleigh-Taylor instability (left) and the corresponding thermal structure (right, solid black line). Also shown are the solidus lines for granite, pyroxenite and peridotite, which are used to examine the melting conditions for crust, lithospheric root material, and mantle peridotite, respectively. The shaded grey regions show the thermal conditions for stable continental regions (cratons) and tectonically active continental regions (back arcs) (Currie and Hyndman, 2006). (b) Model setup of a 115 km thick lithosphere for Rayleigh-Taylor instability (left) and its corresponding thermal structure (right). (c) Model setup of a 115 km thick lithosphere for delamination. Delamination is induced by including a weak zone with a constant viscosity of 10^{19} Pa s; the density is the same as the lithospheric root. The thermal structure is the same as in Figure 6.1b. PER: peridotite; PYX: pyroxenite; LAB: lithosphere-asthenosphere boundary; WQ: wet quartzite; WO: wet olivine.

A 200 km wide high-density region ("root") is placed in the mantle lithosphere immediately below the crust. This represents an area that contains garnet pyroxenite. We assume that it is instantaneously emplaced in the lithosphere as our purpose is to examine gravitational removal of this material, rather than its formation processes. The thickness of the root region is 15 km in the thin, hot lithosphere model (Figure 6.1a) and 75 km in the thick, cool lithosphere model (Figures 6.1b and 6.1c). This thickness is based on the maximum depth that a pyroxenite root can remain below its solidus, based on the thermal structure of each lithosphere. The root is 100 kg/m^3 denser than the underlying mantle, consistent with the density contrast between pyroxenite and peridotite (e.g., Jull and Kelemen, 2001). The width of lithosphere removed by gravitational instability varies in different regions. Batholith roots associated with arc magmatism (e.g., Sierra Nevada) are ~100 km wide (e.g., Saleeby et al., 2012). Removal below orogenic belts could affect a 150-600 km wide region (e.g., Hoke and Garzione, 2008; Molnar and Houseman, 2013). Intracratonic basins may be associated with a 100-500 km wide density anomaly (Naimark and Ismail-Zadeh, 1995). In this study, we use a 200 km wide dense root. We have tested widths of 100 to 400 km and find that this does not affect the overall removal dynamics. The wavelength of Rayleigh-Taylor instabilities is less than 100 km for the lithosphere structure in our models, and therefore the root width primarily determines how many drips occur in the model. For both Rayleigh-Taylor instability and delamination, the width of the root controls the lateral extent of lithosphere removal, and therefore the volume of magmatism scales with root width. However, the temporal changes in the composition and PT conditions of the melt for each model are not affected by the root width.

In all models, the high-density root is gravitationally unstable. The presence of the root is sufficient to initiate lithosphere removal as a Rayleigh-Taylor drip. For delamination-style removal, it is necessary to introduce a viscously weak zone, in order to facilitate detachment of this material (e.g., Göğüş and Pysklywec, 2008). In nature, delamination likely occurs at the Moho (e.g., Bird, 1979; Burov and Watts, 2006). In our delamination model, a weak layer with a constant viscosity of 10^{19} Pa s is placed at the right side of the root and along its surface at the base of the crust (Figure 6.1c).

All model materials have a viscous-plastic rheology and a temperature-dependent density (Table 6.1). At stresses above the frictional-plastic yield stress, materials deform following a Drucker-Prager yield criterion:

$$J_2' = P\sin\phi_{eff} + c_0\cos\phi_{eff} \qquad (6.1)$$

where J_2' is the square root of the second invariant of the deviatoric stress σ_{ij}' ($J_2'^2 = \frac{1}{2}\sigma_{ij}'\sigma_{ij}'$), P is the pressure, ϕ_{eff} is the effective internal angle of friction and c_0 is the cohesion. The frictional-plastic deformation is modeled as a viscous creeping flow by defining a viscosity that places the stress on yield (Fullsack, 1995; Willett, 1999).

Table 6.1. Material parameters in the numerical models

	Crust	Mantle lithosphere	Pyroxenite root	Sublithospheric mantle
Plastic rheology				
c_0 (MPa)	20	20	20	20
ϕ_{eff}	15º	15º	15º	15º
Viscous rheology				
f	5	5	1 or 5	1
A (Pa^{-n} s^{-1})	1.10×10^{-28}	3.91×10^{-15}	3.91×10^{-15}	3.91×10^{-15}
B* (Pa s$^{1/n}$)^a	2.92×10^{6}	1.92×10^{4}	1.92×10^{4}	1.92×10^{4}
n	4.0	3.0	3.0	3.0
Q (kJ mol^{-1})	223	430	430	430
V* (cm^3 mol^{-1})	0	10	10	10
Thermal parameters				
k (W m^{-1} K^{-1})	2.25	3.5	3.5	3.5
A_T (µW m^{-3})	1	0	0	0
c_p (J kg^{-1} K^{-1})	750	1250	1250	1250
Density ^{b}				
ρ_0 (kg m^{-3})	2800	3250	3350	3250
T_0 (K)	900	900	900	900
α (K^{-1})	3.0×10^{-5}	3.0×10^{-5}	3.0×10^{-5}	3.0×10^{-5}

^{a} $B^* = \left(2^{(1-n)/n}3^{-(n+1)/2n}\right)A^{-1/n}$. The term in brackets converts the pre-exponential viscosity parameter from uniaxial laboratory experiments (A) to the tensor invariant state of stress of the numerical models (B*)

^{b} All materials have a temperature-dependent density, given by $\rho(T) = \rho_0[1 - \alpha(T - T_0)]$ where ρ_0 is the reference density at temperature T_0 and α is the volumetric thermal expansion coefficient.

At stresses less than the frictional-plastic yield stress, the deformation follows a power law creep rheology:

$$\eta_{eff}^{v} = f(B^*)(\dot{I}_2')^{\frac{1-n}{n}} \exp(\frac{Q+PV^*}{nRT_K}) \qquad (6.2)$$

in which η_{eff}^{v} is the effective viscosity, $\dot{I}_2'^2$ is the square root of the second invariant of the strain rate tensor $\dot{\varepsilon}_{ij}$ ($\dot{I}_2'^2 = \frac{1}{2}\dot{\varepsilon}_{ij}\dot{\varepsilon}_{ij}$), R is the gas constant and T_K is the absolute temperature. The rheology parameters (B*, n, Q, V*; Table 6.1) are derived from laboratory data on rock deformation, and f is the scaling parameter which linearly scales the material viscosity relative to the laboratory results to approximate materials that are stronger or weaker owing to a moderate change in composition, water content, uncertainty in the rheological parameters under the same ambient conditions (Beaumont et al., 2006). The crust in our models uses the rheological parameters of wet quartzite (Gleason and Tullis, 1995), with f=5 to approximate a strong, dry quartzo-feldspathic crust (Beaumont et al., 2004; 2006). The mantle lithosphere, asthenospheric mantle, and high-density root use the rheological parameters of wet olivine (Karato and Wu, 1993). The scaling factor for the mantle lithosphere is varied between f=1 and f=5, which is comparable to the range of lithosphere strengths for different water contents (Hirth and Kohlstedt, 2003) (Figure 6.2). We use f=5 to approximate a strong continental lithospheric mantle which is dehydrated and melt depleted. The rheology of pyroxenite is not well-defined. We use viscosity of wet olivine with f=5 to approximate a strong pyroxenite lithosphere, which is comparable to the strong lithosphere end member (Hirth and Kohlstedt, 2003) and dry eclogite (Zhang and Green, 2007). In the region of the pyroxenite root, the mantle lithosphere may be slightly weaker than the adjacent lithospheric mantle (Elkins-Tanton, 2005 and 2007). In order to examine how a weak pyroxenite root affects this removal and melting process, we also test models with a weak lithosphere mantle (f=1) at the root column, which is also comparable to the weak end member of lithosphere (Hirth and Kohstedt, 2003) and wet eclogite (Jin et al., 2001).
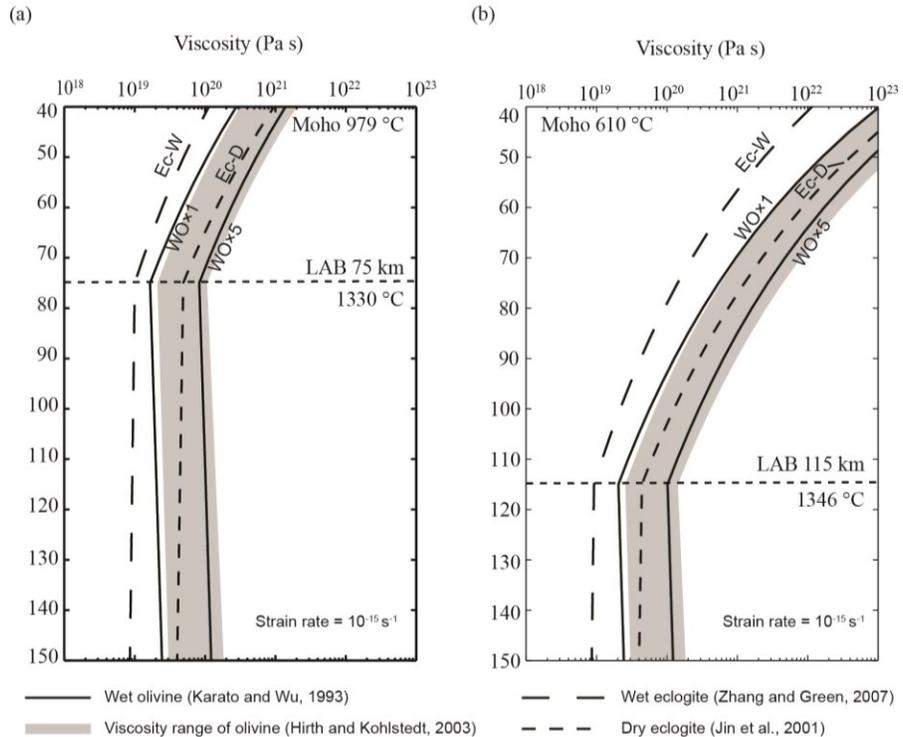
Figure 6.2. Rheology structure of the mantle in the models with (a) a 75 km lithosphere and (b) a 115 km thick lithosphere. The grey area shows the range of effective viscosities for olivine, from a dry olivine to partially hydrated olivine with 1000 $H/10^6Si$ (Hirth and Kohlstedt, 2003). The solid black lines are the two viscosity structures tested in the models, based on a linear scaling of wet olivine (WO, Karato and Wu, 1993). The dashed lines show the viscosity of eclogite for dry conditions (Ec-D, Zhang and Green, 2007) and wet conditions (Ec-W, Jin et al., 2001).

6.3.2 Melt calculations

In this study, we take a simplified approach to determining melting during lithospheric removal, as our goal is to demonstrate the materials that could melt during removal and to assess how different modes of removal may be recognized in the magmatic record. For each model, melting is calculated *a posteriori* using the PT conditions during model evolution. We focus on melting of the mantle lithosphere, asthenospheric mantle and pyroxenite root, assuming that these are dry. In Section 6.5.1, we consider how the results may change if the materials are partially hydrated, and in Section 6.4.3, we assess the conditions under which crustal melting may occur. Melting is calculated for the mantle lithosphere and asthenospheric mantle using the dry peridotite solidus (Katz et al., 2003). Melting of the pyroxenite root is determined by

assuming its solidus is 150°C lower than that of dry peridotite (e.g., Hirschmann and Stolper, 1996). Where melt occurs, the volume of melt is determined assuming 0.3% melt per °C above the solidus (Elkins-Tanton, 2005), which is comparable to the melting fraction of peridotite (Katz et al., 2003) and pyroxenite (Pertermann and Hirschmann, 2003). Note that the rheology and density of materials are not changed due to melting, and there is no melt migration in the models. It is assumed that the melt fraction is sufficiently small that there is a negligible effect on the overall dynamics of the system.

6.4 Results

In this section, we present the results of the numerical models. The first set of models examines lithosphere removal via Rayleigh-Taylor instability (drip), and the second set of models investigates removal through delamination.

6.4.1 Rayleigh-Taylor instability

Model Drip-1. This model uses a thin and hot lithosphere (Figure 6.1a). Figure 6.3a shows that the dense pyroxenite root is gravitationally unstable and immediately starts to founder. The length-scale of foundering depends on the viscosity and density structure (e.g., Houseman and Molnar, 1997; Molnar and Houseman, 2004). In our models, the wavelength scale is ~50 km, and the initial foundering occurs as a symmetric pair of drips at each end of root at ~1.6 Myr. This is followed by a pair of drips in the central part of the root at ~2.2 Myr and a final drip at the centre of the root at ~3 Myr. Each drip has a residual tail that continues to descend after the main drip. The three drip events remove most of the root material, as well as the underlying mantle lithosphere, leaving a ~10 km thick layer of pyroxenite root in the lithosphere. At the same time, hot asthenosphere upwells to fill the space created by root removal. During the model evolution, the surface above the dense root subsides symmetrically, followed by isostatic uplift as root detaches. After detachment, the surface remains as a topographic low, as some root material remains below the crust.
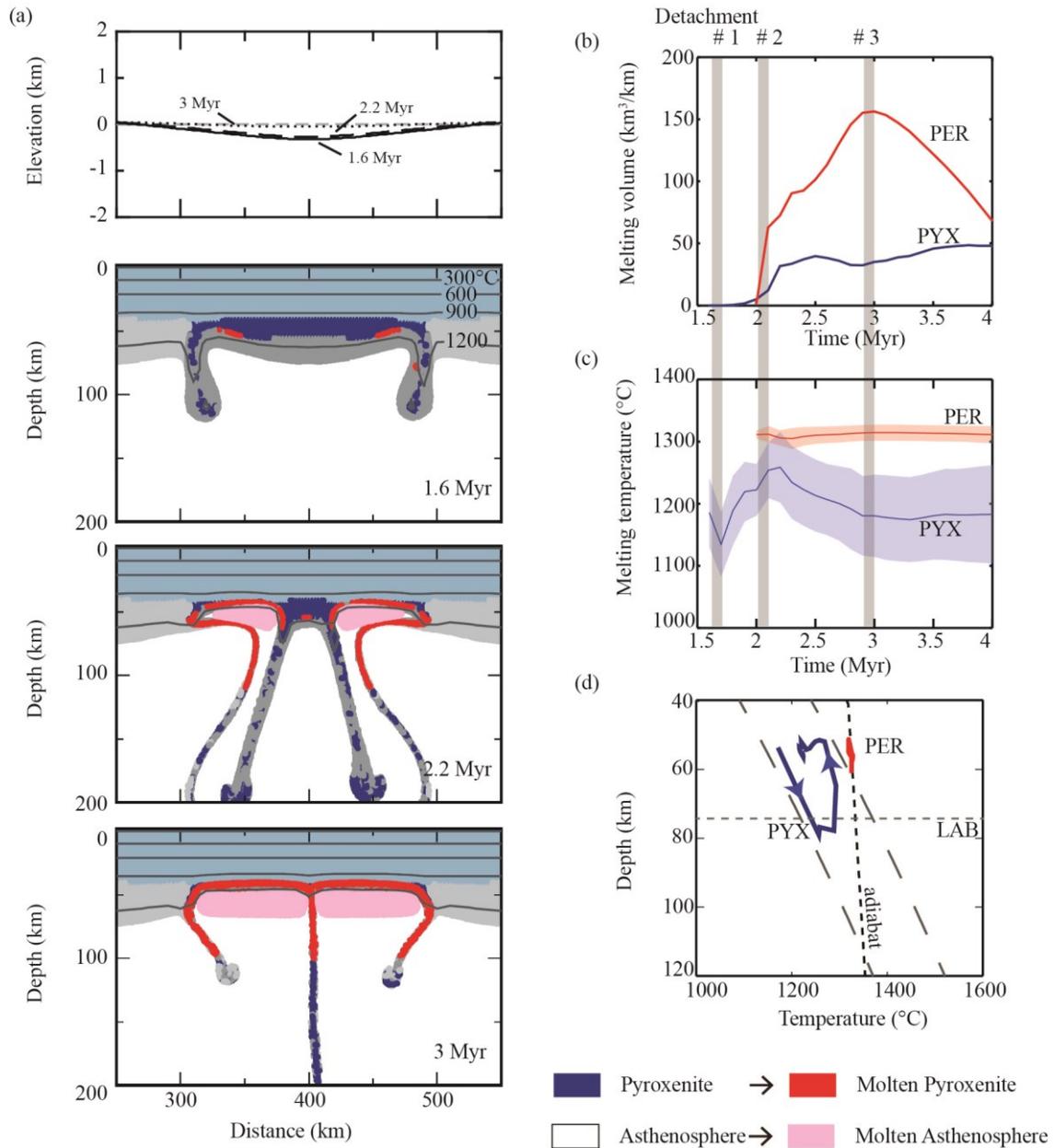
Figure 6.3. Evolution of Model Drip-1. (a) Surface elevation (top plot) and model geometry at the given times. (b) Predicted melting volume (per km along strike) of lithospheric pyroxenite and asthenospheric peridotite during model evolution. (c) The average (solid lines) and standard deviation variation (shaded area) of melting temperatures for lithospheric pyroxenite and asthenospheric peridotite during model evolution. The grey bars show the time at which the drip detaches from the upper plate. (d) Average melting temperature and depth for lithospheric pyroxenite and asthenospheric peridotite. PER: peridotite; PYX: pyroxenite; LAB: lithosphere-asthenosphere boundary.

To show where melt may occur in the model, we change the color of pyroxenite lithosphere from dark blue to red and that of the peridotite asthenosphere from white to pink when they cross their dry solidi (Figure 6.3a). The peridotite mantle lithosphere is also monitored for melting, but it remains below its solidus throughout the model evolution. In this model, the mantle lithosphere and pyroxenite roots descend rapidly, and thus the heads of the drips remain cool and well below their solidus. Starting at ~1.6 Myr, the pyroxenite root within the lithosphere starts to melt as a result of heating associated with lithospheric removal. As more root is removed, the molten pyroxenite extends across the width of the root region. In addition, the narrow pyroxenite tails sink at a low enough rate that they can be conductively heated above their solidus. Melting is observed to a depth of ~115 km. After ~3 Myr, there are no further dripping events, but the residual pyroxenite in the lithosphere is hot enough to melt. Figure 6.3b shows the temporal evolution of the volume of molten pyroxenite (per kilometer perpendicular to the model plane). This shows the onset of melting at ~1.6 Myr, and a rapid increase in the melt volume at ~2 Myr, owing to heating by the upwelling asthenosphere. Melting continues to increase over time, to a maximum of ~50 km^3/km at 3.7 Myr.

The models also predict significant decompression melting of the upwelling asthenosphere during root removal (pink material in Figure 6.3a). Melting starts at ~2 Myr, when there has been sufficient lithosphere removal that the hot asthenosphere can upwell to a depth of ~60 km or less. As shown in Figure 6.3b, the onset of melting of asthenospheric peridotites occurs ~0.4 Myr later than that of lithospheric pyroxenite, but the melting volume increases rapidly, reaching a maximum of ~160 km^3/km at ~3 Myr. After this, the volume of melting decreases, owing to conductive cooling from the overlying lithosphere. The asthenosphere melts are only a few degrees above their solidus and therefore they are much more sensitive to surface cooling than the pyroxenite melts.

Figure 6.3c shows how the temperatures of the molten pyroxenite and peridotite vary over time, and Figure 6.3d shows the average temperature and depth of the melts. In this model, the first melts correspond to pyroxenites, and their average temperature increases from ~1130°C to ~1260°C between ~1.6 and 2.2 Myr, corresponding to the

growth and detachment of the first two pairs of drips. The overall increase in temperature is a result of the fact that the depth of melting is initially at ~50 km depth but then extends to greater depth by 2.2 Myr (Figures 6.3a and 6.3d). The average temperature then decreases to ~1180°C at ~3 Myr and becomes stable (Figure 6.3b). The average depth also decreases over time (Figure 6.3d), reflecting the fact that the majority of melt originates from the residual pyroxenite in the lithosphere (Figure 6.3a). The peridotite melt starts at ~2 Myr, and its temperature is ~1320°C throughout model evolution (Figure 6.3c). This corresponds to decompression melting of near-adiabatic asthenospheric mantle, and melting depths are limited to depths between ~60 km (the intersection of the adiabatic line with the solidus) and ~50 km (the base of the residual lithosphere) (Figure 6.3d).

Model Drip-2. In Model Drip-1, the rheology of lithosphere at the root column is quite weak (Figure 6.2a). Figure 6.3a shows that the weak root is removed through a series of short-wavelength drips. Model Drip-2 tests a stronger mantle lithosphere (f=5), corresponding to the highest viscous strength of olivine from laboratory studies (Figure 6.2; Hirth and Kohlstedt, 2003). The other parameters are identical to those in Model Drip-1. Figure 6.4a shows that the high root strength retards the growth of the gravitational instability, with rapid growth delayed until ~14 Myr. Instability occurs through a single pair of drips that initiate at the edges of the root. The width of the drips is larger than those in Model Drip-1, as expected for an increased root viscosity (e.g., Houseman and Molnar, 1997; Molnar and Houseman, 2004). The drips then merge to form a single drip in the center of root by 17.4 Myr, and this detaches from the lithosphere at 17.8 Myr. The drip removes nearly the entire root area, as well as the underlying mantle lithosphere. In addition, the drip causes lateral entrainment of the adjacent mantle lithosphere and overlying crust, leading to crustal thickening (~5 km) above the drip. The surface above the root initially subsides to a maximum depth of 0.35 km, but at 17.4 Myr, it starts to uplift as a result of crustal thickening. Prior to final root detachment, the surface is a topographic high (~0.1 km).
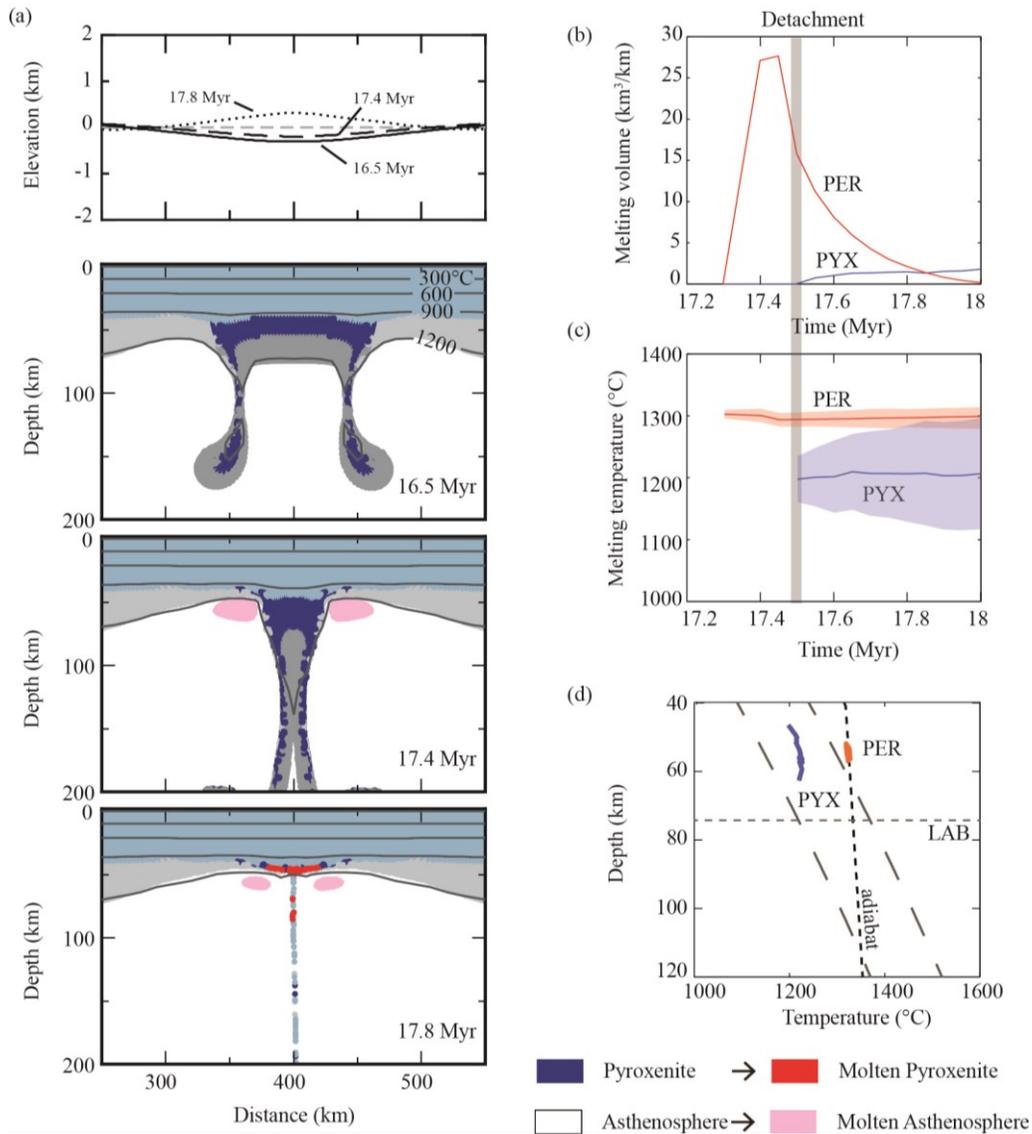
Figure 6.4. Evolution of Model Drip-2. (a) Surface elevation (top plot) and model geometry at the given times. (b) Predicted melting volume (per km along strike) of lithospheric pyroxenite and asthenospheric peridotite during model evolution. (c) The average (solid lines) and standard deviation variations (shaded area) of melting temperatures for lithospheric pyroxenite and asthenospheric peridotite during model evolution. The grey bar show the time at which the drip detaches from the upper plate. (d) Average melting temperature and depth for lithospheric pyroxenite and asthenospheric peridotite. PER: peridotite; PYX: pyroxenite; LAB: lithosphere-asthenosphere boundary.

In this model, the main contribution to the melt is the asthenospheric peridotites that upwell as the dense root is removed. Decompression melting starts at ~17.3 Myr and peaks at ~27 km^3/km before the drip detaches at ~17.5 Myr (Figure 6.4b). After the

drip detaches, there is a small amount of melting (~2 km^3/km) of the residual lithospheric pyroxenites, as they are conductively heated. The average melting temperature of pyroxenites and peridotites is stable at ~1180°C and ~1300°C, respectively (Figure 6.4c), with a melting depth of 46-62 km for the lithospheric pyroxenites and 52-58 km for the asthenospheric peridotites (Figure 6.4d). The reduced peridotite melting in the later stages of the model is due to the conductive cooling from surface.

Model Drip-3. Models Drip-1 and Drip-2 test the Rayleigh-Taylor drip process for a relatively thin lithosphere with a hot Moho, which is similar to that of back arcs and other tectonically active regions (Figure 6.1a). Model Drip-3 examines Rayleigh-Taylor removal for a thicker and cooler lithosphere, representative of average Phanerozoic lithosphere (Figure 6.1b).

Figure 6.5 shows the evolution of this model. Owing to the cooler lithosphere temperatures, only the lower ~40 km of the root participates in the gravitational instability. In the initial stages of removal, two perturbations grow at the edges of the root. These rapidly converge together, with final detachment at ~0.5 Myr. A ~40 km thick root remains in the overriding plate, which continues to seep downward in the ~12 km wide tail created by the initial drip. The tail keeps sinking for ~40 Myr until a new, cold lithosphere mantle is generated by surface cooling. The surface deflection is similar to Drip-1, but with a larger magnitude of subsidence.

In this model, neither lithosphere nor asthenosphere crosses their solidi during the removal event. The drips sink rapidly and have insufficient time for conductive heating. The thick residual lithosphere prevents the asthenosphere from upwelling to a depth where it can undergo decompression melting.
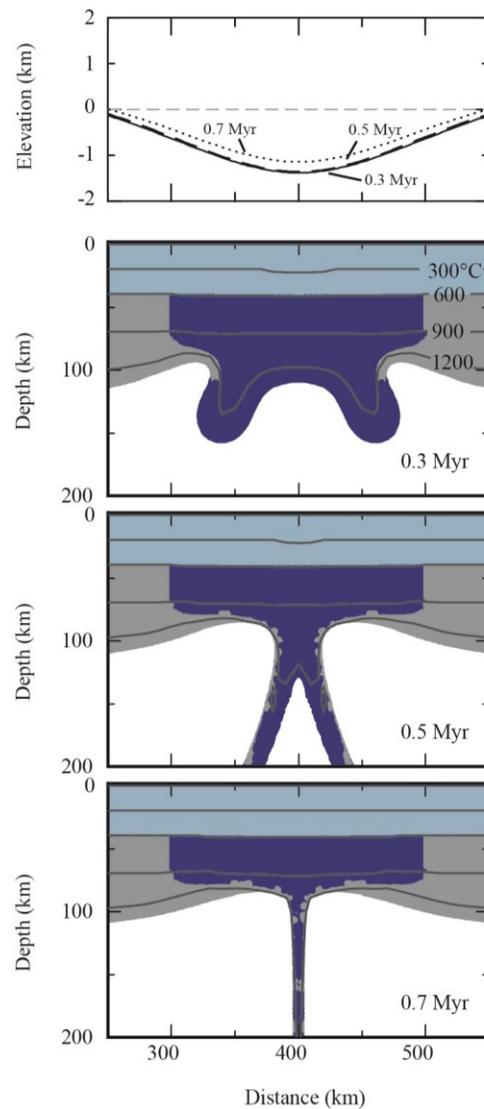
Figure 6.5. Evolution of Model Drip-3. The top plot shows the surface elevation and the lower three plots show the model geometry at the given times. No melting is predicted to occur in this model.

6.4.2 Delamination

The other style of lithosphere removal is delamination. In the models, delamination is induced by placing a weak zone at the right side and top of the dense root (Figure 6.1c). The evolution of this model is shown in Figure 6.6a. Foundering initiates at the weak side of the root, and the detachment point migrates leftward as the dense root peels away from the upper plate. Surface uplifts from a topographic low to be a high above the detached root. This surface rebound migrates laterally as

146

delamination proceeds. The surface deflection is asymmetric that is contrary to the symmetric surface deflection associated with Rayleigh-Taylor removal (e.g., Göğüş and Pysklywec, 2008).

Delamination proceeds quickly, and the entire root is removed within 1.1 Myr. This causes asthenosphere to upwell and come into contact with the base of the crust. The rapid rate of removal means that the pyroxenite root remains below its solidus during detachment. However, widespread decompression melting of the asthenosphere is predicted. The amount of melt increases as the lithosphere detaches, with a maximum of 230 km^3/km at 0.94 Myr (Figure 6.6b). The melt has an average temperature of ~1310°C (Figure 6.6c), and originates at depths of 40-60 km (Figure 6.6d). The volume of peridotite melt in this model is much greater than in the drip models (Figures 6.3b and 6.4b) as delamination efficiently removes the entire root region.

This model predicts that only asthenosphere will melt during delamination (see Section 6.4.3 for a discussion of crustal melt). In order to determine if there are any conditions under which the delaminating lithosphere may melt, we have explored other delamination models using different root densities and lithosphere thermal structures. When the lithosphere is thin and hot (e.g., thermal structure in Drip-1, Figure 6.1a) and the density of pyroxenite root is very low (~20 kg/m^3 more dense than asthenosphere), the delaminating lithosphere sinks slowly. A small portion of the upper part of the delaminated root can cross solidus. In this extreme case, the volume of molten lithosphere pyroxenite is <10 km^3/km, which is insignificant when compared to that of molten asthenosphere (>100's km^3/km). Therefore, asthenosphere sourced magmas dominate in a delamination event.
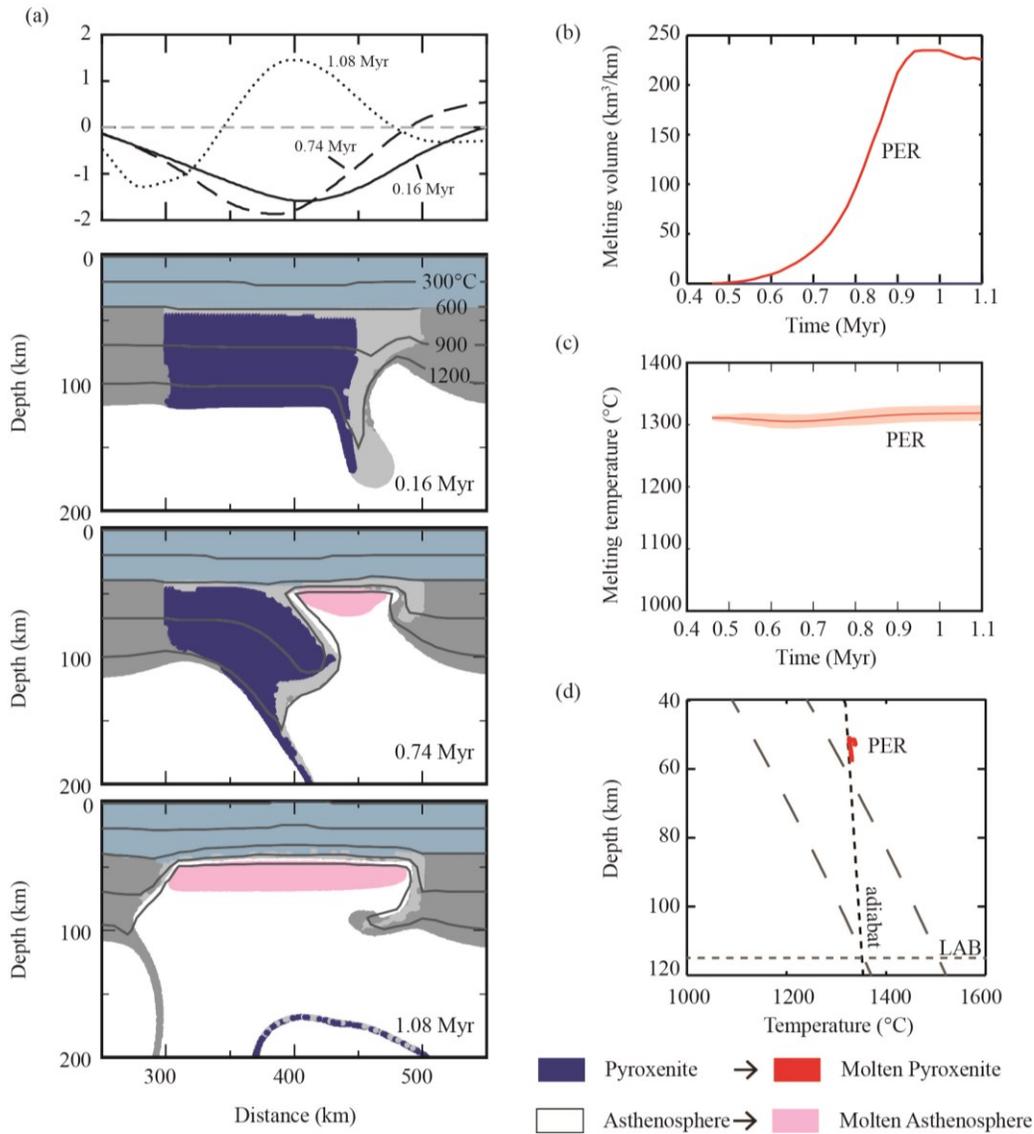
Figure 6.6. Evolution of the delamination model. (a) Surface elevation (top plot) and model geometry at the given times. Only the asthenospheric peridotite is predicted to melt. (b) Predicted melting volume (per km along strike) of asthenospheric peridotite during model evolution. (c) The average (solid lines) and standard deviation variations (shaded area) of asthenospheric peridotite melting temperature during model evolution. (d) Average melting temperature and depth for asthenospheric peridotite. PER: peridotite; LAB: lithosphere-asthenosphere boundary.

6.4.3 Crustal melting

The models presented above demonstrate the dynamics of lithosphere removal and the induced melts in the mantle. In this section, we investigate crustal thermal

148

conditions during lithosphere removal. The upwelling of hot asthenosphere replaces the removed lower lithosphere and advects heat to overlying residual lithosphere. The thickness of residual mantle lithosphere determines the magnitude of conductive heating in the crust; this may provide sufficient heat to melt the crust. Crustal solidus depends on its composition and volatile content, both of which can be highly variable (e.g., Nair and Chacko, 2002). A more felsic and/or hydrated crust would have a lower solidus (e.g., Lindsay et al., 2001). For simplicity, we use the dry granite solidus as the basis of our melt predictions (Elkins-Tanton, 2005; Saleeby et al., 2012).

6.4.3.1 Rayleigh-Taylor instability

A Rayleigh-Taylor drip involves the part of the dense root that is weak enough to be mobilized by the gravitational instability (Conrad and Molnar, 1999). As the viscosity structure of the root depends on temperature, the shallow part of the root may be too viscous to be gravitationally removed, even though it has a high density. The Moho temperature plays an important role in determining the residual lithosphere thickness following a Rayleigh-Taylor removal event (Jagoutz and Behn, 2013). A hotter Moho results in a weaker mantle lithosphere and therefore a greater thickness of material can be gravitationally removed, leaving a thinner residual lithosphere. Indeed, the thickness of residual mantle lithosphere in our models is ~10 km when the Moho temperature is 979°C (Drip-1 and Drip-2) and ~40 km for a 610°C Moho (Drip-3).

As a result of the differing thicknesses of residual mantle lithosphere, the deep crust experiences different magnitudes of heating following removal. Figure 6.7a shows that the Moho temperature is increased by 100-150°C for the hot Moho models (Drip-1 and Drip-2), but only ~50°C for the cold Moho model (Drip-3). Note that heating in Model Drip-3 occurs >20 Myr after drip detachment.

Figure 6.7b shows how the temperature-depth structure changes over time at the centre of the root (distance = 400 km) and 50 km away from the centre (distance=350 km). These are used to assess where crustal melting may occur. For the models with a thin lithosphere (Drip-1 and Drip-2), the temperature profiles at x=350 km show an earlier heating than the profiles at x=400 km. During root removal, the deep crust at x=350 km may become hot enough to melt at ~3 Myr in Model Drip-1, whereas the

crust at x=400 km remains below the solidus. This is consistent with the dynamics of root removal, as removal initially occurs on the edges of the root, and the final removal is at the centre of the root (Figures 6.3a and 6.4a). The centre of the root could have later melting, as it is conductively heated by underlying hot asthenosphere.

In contrast, if a drip occurs for thick and cold lithosphere (model Drip-3), the crust remains below its solidus throughout removal (Figure 6.7d). In this case, only limited magmatism associated with asthenospheric decompression is predicted.
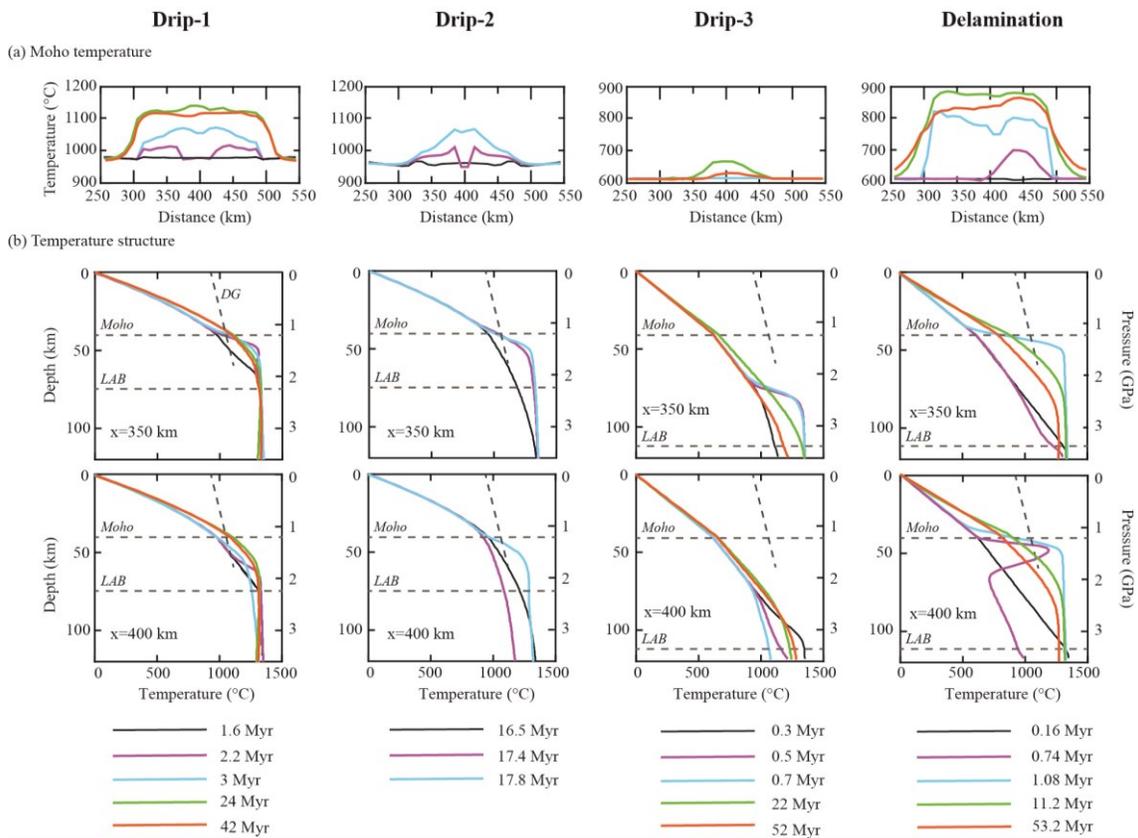

Figure 6.7. Thermal evolution of models Drip-1, Drip-2, Drip-3 and delamination. (a) Moho temperature evolution. (b) Vertical temperature profile along between 0-120 km depth at x=350 km (top plot) and x=400 km (bottom plot; this is the middle of the model domain). The inclined dashed lines in (b) show the solidus for dry granite (DG) which is used to assess melting of the crust.

6.4.3.2 Delamination

If removal occurs through delamination, the entire dense lithospheric mantle can be removed, bringing the hot asthenosphere into direct contact with the deep crust (Figure 6.6). This leads to rapid heating of the crust, which migrates laterally with the detachment point of the delaminating lithosphere (Figures 6.7). If the crust is initially cool, delamination causes deep crustal temperatures to increase by ~300°C. The crust remains below the dry granite solidus throughout delamination. We have also tested delamination for a lithosphere that is initially hot and thin (as in Drip-1 and Drip-2), and in this case, the temperature at the base of crust can increase by ~170°C, and the lower ~6 km of the crust moves above the dry granite solidus. Overall, the models show that delamination induces significant heating of the crust. Under the same initial thermal structure of lithosphere, delamination could produce larger volumes of crustal melting than Rayleigh-Taylor drip.

6.5 Discussion

6.5.1 Effect of hydration and composition on melt predictions

The models presented above examine the magmatism expressions that may occur during the gravitational removal of dense lithosphere. An important assumption in the melt calculations is that the materials are dry. The addition of water to either the lithosphere or asthenosphere will decrease the solidus, enhancing the possibility of melt. We first consider the effect of hydration on asthenospheric melts. The loss of the lower lithosphere by either Rayleigh-Taylor instability or delamination causes passive upwelling of the asthenosphere along the mantle adiabat, and melting will occur at the depths where the adiabat lies above the peridotite solidus. For dry peridotite and a 1300°C mantle adiabat, the melting threshold depth is ~67 km (Figure 6.8). Therefore, dry decompression melting will occur if the lithosphere is thinned to less than this depth; in the above models, this requires either a Rayleigh-Taylor instability of a rheologically weak lithosphere (Drip-1 and Drip-2; Figures 6.3 and 6.4) or delamination along the Moho (Figure 6.6). Hirth and Kohlstedt (1996) suggest that the hydrated upper mantle contains ~50 ppm H_2O in olivine, which lowers the solidus by ~144°C (Katz et al., 2003). The corresponding to melting threshold depth is ~115 km (Figure

6.8). In this case, decompression melting is predicted for all three Rayleigh-Taylor models, even model Drip-3 which has a thick residual lithosphere (~75 km) after the removal event. Owing to the increased depth range for melting, a greater volume of magma may be created for Rayleigh-Taylor drip models with a thin residual lithosphere (Drip-1 and Drip-2) and the delamination model.
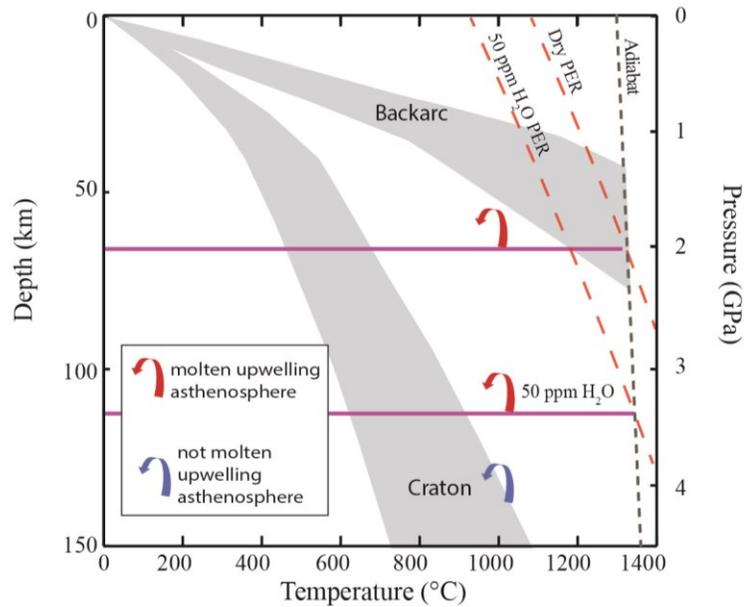
Figure 6.8. Melting conditions for asthenosphere. Horizontal, purple lines show the critical depths for decompression melting of asthenosphere. Above 67 km depth, the dry asthenospheric peridotite crosses its solidus; and above 115 km, the wet asthenospheric peridotite with 50 ppm H_2O in olivine can melt. The two inclined red dashed lines show the solidus of dry peridotite and wet peridotite with 50 ppm H_2O in olivine respectively (calculated based on Katz et al., 2003). The shaded grey regions show the thermal conditions for stable continental regions (cratons) and tectonically active continental regions (back arcs) (Currie and Hyndman, 2006). PER: peridotite.

Hydration will also affect the melting behavior of the dense root material. Melting requires that the root be conductively heated above its solidus before sinking to the deeper mantle. The above models assume a dry pyroxenite composition, and root melting is predicted to occur only for Rayleigh-Taylor style removal, if the size of the drip is relatively small (e.g. Drip-1 with a weak rheology, Figure 6.3). For most model parameters, delamination occurs too rapidly for root melting to occur. It is possible that

the pyroxenite root may be partially hydrated. A xenolith study of the garnet pyroxenite root of the Sierra Nevada batholith indicates water contents of 1% H_2O in melt (Ducea, 2002). The effects of water on the pyroxenite solidus are not well-known. For peridotite, 1% water fraction in melt can lower the solidus by 43°C (Katz et al., 2003). If the pyroxenite solidus is reduced by a similar amount, the maximum melting depth for pyroxenite lithosphere increases from 115 km to 133 km. Therefore, a greater volume of sinking pyroxenite materials can move above the solidus line and contribute to melting models with an initially hot lithosphere (Drip-1 and Drip-2). For the cold model (Drip-3), the PT of sinking lithosphere approaches the solidus, but still does not cross it.

Finally, we consider the case that the root has a peridotite composition, rather than pyroxenite. Peridotitic lithosphere can be denser than the underlying asthenosphere due to thermal contraction and/or the presence of dense components (e.g., garnet) (e.g., Houseman and Molnar, 1997), and this can drive gravitational removal. If the root is composed of dry peridotite, the solidus temperature will be ~150°C higher than that of pyroxenite (Hirth and Kohlstedt, 1996; Pertermann and Hirschmann, 2003). For all the models shown above, as well as additional models with a lower root density, the mantle lithosphere remains below its solidus and it is predicted that there would be no melting of a dry peridotitic lithosphere for either Rayleigh-Taylor instability or delamination. When the root has a lower density, only the deepest lithosphere that is hot and weak can be removed. Therefore, the residual lithosphere is thicker, which results in less melting of the upwelling asthenosphere. A low density root sinks more slowly. However it sinks from a large depth and therefore there is insufficient time for conductive heating. If the root is composed of partially hydrated lithosphere (i.e., 50 ppm H_2O in olivine), the solidus temperature can be reduced by ~144°C (Katz et al., 2003) and the predicted melting is similar to that in Figures 6.3, 6.4, 6.5 and 6.6; only small-scale drips will undergo melting.

6.5.2 Summary of model results

On the basis of the numerical models, we suggest that there are four types of melting associated with lithosphere removal, depending on the removal style and which components melt (Figure 6.9):

Type 1: Lithosphere and asthenosphere melts induced by Rayleigh-Taylor instability. In this type, the lithosphere is removed in a series of small-scale drips, which undergo melting as they descend. If a significant fraction of the lithosphere is removed, the upwelling asthenosphere can undergo decompression melting. This may also trigger melting of the deep crust if the asthenosphere is in close proximity to the base of the crust. The models demonstrate that small-scale drips are favoured if the root material is warm and has a weak rheology (e.g., Drip-1 and Drip-2, Figures 6.3 and 6.4). Therefore, this type of melting may be limited to regions that have an initially thin lithosphere. The higher initial temperature of the root will make it easier for it to be heated above its solidus during removal. In addition, the sinking lithosphere should be partially hydrated. This will weaken the lithosphere and lower its solidus temperature, leading to the formation of small-scale drips that are prone to melting.
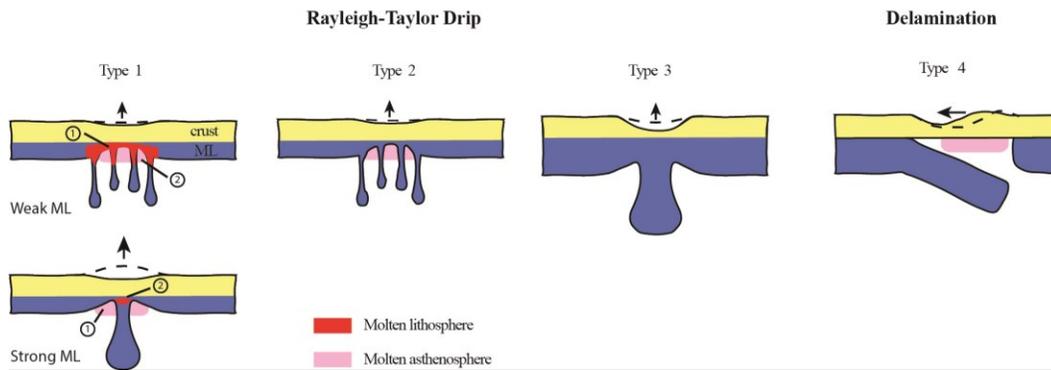

Figure 6.9. Four types magmatism and surface deflection caused by lithosphere removal (see text for details). Number ① and ② denote the time sequence of melting lithosphere and asthenosphere. ML: mantle lithosphere.

If the foundering root is quite weak (i.e., it is warm or hydrated), the root material will melt first, followed by asthenospheric melting (e.g., Drip-1, Figure 6.3).

154

This will be accompanied by subsidence of the surface above the drip, and then uplift after drip removal. If the root is somewhat stronger, the size of the drips and the timescale for removal increase (e.g., Drip-2, Figure 6.4). This may delay the onset of root melting, and therefore the asthenosphere could melt before lithospheric melting. In this case, the root is more strongly coupled to the crust, and root destabilization may lead to crustal thickening and surface uplift during drip removal (e.g., Neil and Houseman, 1999; Pysklywec and Beaumont, 2004; Chapter 5). In both cases, melting should initiate at the edges of the root region and migrate toward the centre (Figure 6.7). In 3D, this would correspond to ring-shaped melting and that converges radially. The surface topography should also be symmetric above the foundering lithosphere.

Type 2: Only asthenospheric melts induced by Rayleigh-Taylor instability. Here, the lithosphere still founders in relatively small drips, but the drips do not melt during descent. However, the lithosphere thins enough to induce decompression melting of the asthenosphere. This corresponds to a case where either the lithosphere is initially cooler than in Type 1 and/or its solidus temperature is higher. For example, if the foundering lithosphere is composed of dry peridotite, it may not melt during destabilization owing to its high solidus temperature. Another possibility is that the initial lithosphere is slightly cooler than in Type 1, and therefore the drips can not be sufficiently heated during removal. Therefore, the pyroxenite in the lithosphere does not contribute to magmatism in this case. Both the distribution of asthenospheric magmas and surface deflection will be symmetric about the foundering root. Depending on the magnitude of lithosphere thinning and the initial temperature and composition of the crust, the crust may or may not melt.

Type 3: No melt associated with Rayleigh-Taylor instability. This type will occur if both the foundering lithosphere and upwelling asthenosphere remain below their solidus. This type will be associated with regions that have an initially thick and cool lithosphere. The low lithosphere temperature increases the strength of the root, causing it to founder in large drips (e.g., Drip-3, Figure 6.5), which descend too rapidly to be heated above their solidus. In addition, the low temperature limits the amount of root that can be gravitationally removed and therefore thick residual lithosphere prevents the upwelling asthenosphere from melting. This also prohibits significant

crustal heating and therefore crustal melts are not expected. Owing to the cool temperatures, the root and crust will be strongly coupled, which will lead to significant subsidence that is symmetric about the drip, followed by partial uplift after drip detachment.

Type 4: Only asthenosphere melts induced by delamination. Delamination occurs when the entire thickness of mantle lithosphere is removed through peeling along a weak layer at the Moho (e.g., Bird, 1979). For most lithosphere densities and rheologies, delamination is a rapid process. Therefore it is unlikely that the delaminating lithosphere root will melt, unless it is initially quite hot or hydrated. However, delamination will be accompanied by widespread decompression melting of the asthenosphere (e.g., Figure 6.6). This will also lead to rapid heating of the deep crust, which could produce melting. This type of melting can be differentiated from Type 2 by both the volume of asthenospheric melt and the spatial distribution of melting. Delaminating lithosphere is removed asymmetrically. Therefore, melting should migrate laterally with the detachment point. This style of removal may also be recognized by a migrating wave of surface subsidence followed by uplift (e.g., Göğüş and Pysklywec, 2008; Figure 6.6).

6.5.3 Initial lithosphere thermal structure and Rayleigh-Taylor melting regimes

Types 1, 2, and 3 are associated with melting induced by Rayleigh-Taylor instability, and they are differentiated based on whether melting involves foundering lithosphere and asthenosphere (Type 1), only asthenosphere (Type 2) or whether lithosphere removal is amagmatic (Type 3) (Figure 6.9). As argued above, the initial thermal structure of the lithosphere plays a key role in determining the distribution of melting. This provides a first-order control on lithosphere strength and it determines how much heating is required for the foundering lithosphere to melt. Here, we present a simplified analysis to constrain the lithosphere thermal conditions under which the three types of melting may occur.

Peridotite melting. First, we consider how much lithospheric thinning can occur via Rayleigh-Taylor instability. This controls the shallowest depth to which adiabatic asthenosphere upwells; in order for decompression melting to occur, the

upwelling asthenosphere must reach a depth which places it above its solidus. The amount of thinning depends on lithosphere strength, which in turn depends on its temperature (Jagoutz and Behn, 2013). We have run a series of models with initial lithosphere thermal structures that range between the two end-members shown in Figure 6.1a and 6.1b. The model parameterization follows that in Drip-1 and Drip-3, where the lithosphere contains a root that is weak (f=1) and is 100 kg/m^3 more dense than the asthenosphere. We tested lithosphere thermal structures that range in thickness from 75 km to 160 km (corresponding to Moho temperatures of 400°C to 1000°C). Each model was run until the lithospheric root was removed, and the final thickness was measured; this is termed the decoupling depth. Figure 6.10 shows the measured decoupling depth as a function of Moho temperature. Along the top of the plot, the initial lithosphere temperature at the decoupling depth for each model is given. Models that start with an initially hot lithosphere (e.g., similar to a back arc thermal regime) exhibit a decoupling depth of 50-60 km, whereas cooler models can only be thinned to >120 km. Owing to its temperature-dependent rheology, an initially cool lithosphere has a relatively strong mantle lithosphere. Only the lowest lithosphere that is sufficiently weak will participate in the removal process. Conrad and Molnar (1999) term this unstable material as "available buoyancy". In a hot lithosphere, the mantle lithosphere is weak and a large portion of it has the mobility to be removed.
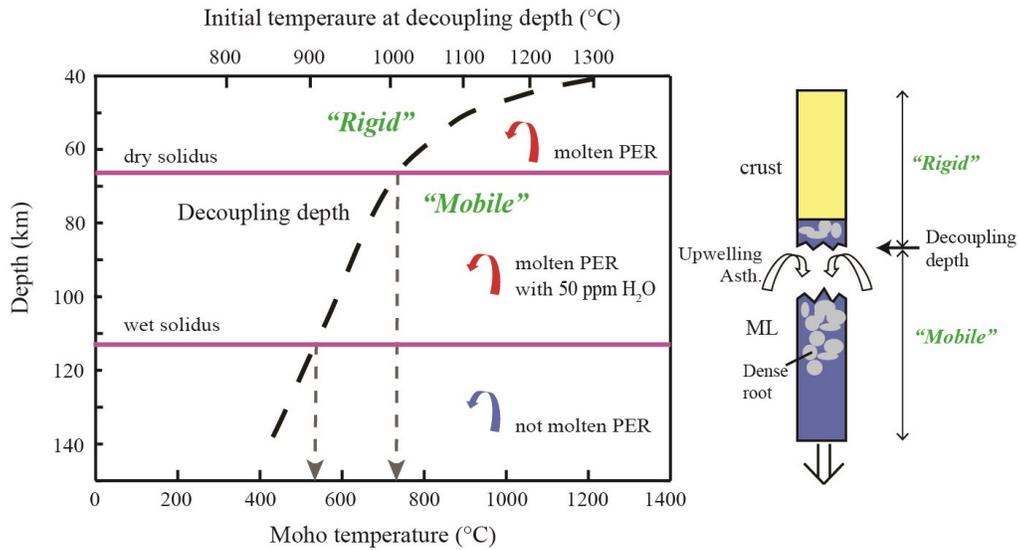
Figure 6.10. Decoupling depth of a Rayleigh-Taylor instability as a function of Moho temperature (assuming crust is 40 km thick, left panel). Schematic lithospheric column of decoupling in lithosphere removal process (right panel). Above the decoupling depth, the lithosphere is rigid and stable in the upper plate; below the decoupling depth, the dense root is gravitationally unstable and has the mobility to be recycled into the deep mantle. Horizontal purple lines show the critical melting depth for dry and wet asthenospheric peridotite (derived from Figure 6.8). When the decoupling depth is above the critical melting depth, the upwelling asthenosphere can cross the solidus. For lithosphere with a Moho temperature >740°C, the lithosphere decoupling depth is above 67 km, which will allow decompression melting of upwelling dry asthenosphere. When the Moho temperature is >530°C, the decoupling depth is >115km and the wet asthenospheric peridotite may melt. For a cold lithosphere with Moho temperature <530°C, the decoupling depth is >115 km and no asthenosphere can melt. PER: peridotite. Asth.: asthenosphere.

As discussed in Section 6.5.1, a dry, adiabatic asthenosphere must upwell to a depth less than 67 km in order to melt. Figure 6.10 shows that this will occur for lithospheres with an initial Moho temperature greater than ~740°C.   If the asthenosphere is partially hydrated (50 ppm H_2O in olivine; Hirth and Kohlstedt, 1996), upwelling must reach a depth less than 115 km, and thus the lithosphere must have an initial Moho temperature greater than ~530°C in order to thin enough to enable asthenospheric decompression melting.   These Moho temperatures mark the critical

temperatures for peridotite melting; for cooler lithospheres, gravitational removal will not produce asthenospheric melt (i.e., Type 3, Figure 6.9).

Pyroxenite melting. The other component to be considered is the foundering lithosphere; can this material melt as it is removed? Following Elkins-Tanton (2005), we approximate the sinking root as a sphere that falls through a hot, constant viscosity asthenosphere. The Stokes flow equation (Turcotte and Schubert, 2002) is used to calculate the sinking velocity of the sphere:

$$U = \frac{(d/2)^2 g(\rho_{root} - \rho_{asth})}{3\mu_{asth}} \qquad (6.3)$$

where d is the diameter of sphere, g is the gravitational acceleration (9.81 m/s), ρ_{root} is the density of dense root (3350 kg/m^3), ρ_{asth} is the density of asthenosphere (3250 kg/m^3), and μ_{asth} is the viscosity of asthenosphere (10^{19} Pa s).

As the sphere falls, it is conductively heated by the surrounding asthenosphere, with heating given by (Turcotte and Schubert, 2002):

$$\frac{T(t) - T_{asth}}{T_0 - T_{asth}} = \text{erfc}\frac{y}{2\sqrt{kt}} \qquad (6.4)$$

where T(t) is the temperature of sphere at time t, T_{asth} is the temperature of asthenosphere (taken as the adiabatic temperature: 1300 °C + 0.4 °C/km × depth), y is the distance from the edge of sphere towards its centre, and k is the thermal diffusivity (10^{-6} m^2/s).

We track the thermal evolution of a series of spheres that start at a given depth and temperature and fall to a depth of 150 km (i.e., well below the intersection of the pyroxenite solidus and the mantle adiabat). The temperature of the sphere is compared to the solidus for dry and partially hydrated pyroxenite (see Section 6.5.1) to determine if melting will occur.

Note that these calculations are greatly simplified relative to a real Rayleigh-Taylor instability. For example, they assume a constant descent velocity, whereas a gravitational instability will increase in velocity over time. They also assume that the sphere is fully surrounded by adiabatic mantle; therefore, the amount of heating may be overestimated. Nonetheless, they are useful for demonstrating the range of conditions under which a small fragment of lithosphere may melt.
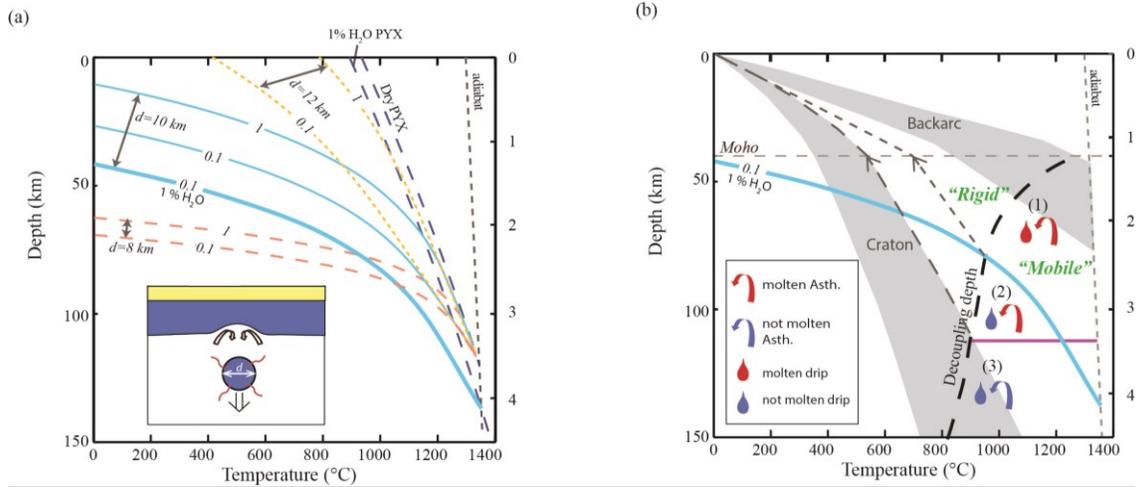
Figure 6.11. Melting conditions for lithospheric pyroxenite and asthenospheric peridotite. (a) Curved lines show the maximum temperature and depth at which a sphere must start falling in order to melt. A schematic sinking lithospheric sphere is shown in the panel at the lower left corner. Contours of melting volume (0.1 or 1) are shown in different colors in order to distinguish different diameters (d) of the sphere. See text for details. Inclined dashed blue lines are the solidi for dry pyroxenite and pyroxenite with 1% H_2O (Ducea, 2002; pyroxenite solidus for 1% H_2O is calculated based on Katz et al., 2003). (b) Relation between the melting conditions and initial thermal structure of lithosphere. The decoupling depth line (derived from Figure 6.10) is shown as the bold black dashed line for the temperature and depth at the decoupling depth; the arrows show the Moho temperature. The blue contour shows the maximum temperature and depth needed for a 10 km sphere of wet pyroxenite to undergo 10% melting. The purple line shows the threshold depth of peridotite with 50 ppm water in olivine to undergo decompression melting.

Figure 6.11a shows the results of these calculations for spheres with diameters of 8, 10 and 12 km. The x and y axes denote the initial temperature and depth for a sphere. The curved lines show the boundary that defines the maximum initial depth that a sphere can start with a given temperature and undergo melting. Any sphere that starts at the depth and temperature above these lines may melt during descent. Three melt possibilities are shown: 100% melting of a dry pyroxenite sphere, 10% melting volume of a dry pyroxenite sphere and 10% melting volume of a partially hydrated pyroxenite sphere. The lines are curved because spheres that have an initially low temperature must start falling from a shallower depth in order to sufficiently heat, while hotter

spheres require less time (and thus less falling distance) to melt. The rate of falling is strongly affected by the diameter of the sphere (Equation 6.3) and it is predicted that only spheres with diameters of ~12 km or less will melt. This is consistent with the numerical modeling results that show that only the thin (~10 km width) and hot tails of the drips melt (e.g., Drip-1 and Drip-2, Figures 6.3 and 6.4). Further, a hydrated pyroxenite will melt over a wider range of initial conditions (greater depth and cooler temperature), as expected given its lower solidus.

Figure 6.11b combines the results of the analysis of peridotite melting (Figure 6.10) and pyroxenite melting (Figure 6.11a), assuming that both the peridotite and pyroxenite are partially hydrated and that the lithosphere is gravitationally removed as small-scale (10 km wide) drips. As discussed above, whether the upwelling asthenosphere can undergo decompression melting depends on the decoupling depth of the Rayleigh-Taylor instability. For melting of wet asthenosphereic peridotite (with 50 ppm H_2O in olivine), the maximum decoupling depth is 115 km. The geothermal boundary of lithosphere for this decoupling is shown with a grey, dashed line with an arrow pointing to the corresponding Moho temperature at 530°C. This thermal structure of lithosphere is close to the boundary of cratonic thermal conditions, suggesting lithosphere hotter than a craton could be thinned to <115 km depth and the upwelling asthenosphere can melt during Rayleigh-Taylor instability. Note that this assumes that only temperature controls the decoupling depth. Compositional variations are not considered.

Melting of lithospheric pyroxenite also depends on the decoupling condition, as the small-scale drip (i.e., tail of drip) sinks from below the base of "rigid" lithosphere. The decoupling line on Figure 6.11b denotes the initial depth and temperature of this small-scale drip. If the decoupling line is above the melting boundary of pyroxenite (bold blue line; derived from Figure 6.11a), the sinking lithosphere could melt. The upper grey, short dashed line shows the coldest geotherm of lithosphere for pyroxenite melting, corresponding to a ~700°C Moho.

Figure 6.11b shows how the magmatism resulting from a Rayleigh-Taylor instability depends on the initial thermal structure of lithosphere. Consistent with the numerical modeling and analysis results shown in Figure 6.9, three types of magmatism

are predicted. The grey dashed lines in Figure 6.11b denote the boundaries for the corresponding lithospheric geotherm: (1) in a hot lithosphere with Moho temperature >700°C (e.g., back arc or other tectonically-active Phanerozoic area), both asthenosphere and lithosphere melt; (2) in a relative warm lithosphere with Moho temperature 530°C to 700°C (e.g., relatively cold Phanerozoic lithosphere), only asthenosphere melt; (3) in a cold and thick lithosphere with Moho temperature <530°C (e.g., craton), no magmatism could occur.

6.5.4 Geological implications

Our numerical models demonstrate how lithosphere removal may be recognized in the magmatic record. Removal via Rayleigh-Taylor instability and delamination can be differentiated by the spatial distributions of magmatism. In a Rayleigh-Taylor instability, magmatism initiates at the edges of the instability and migrates toward the center (Figures 6.3 and 6.4). In 3D, this would correspond to ring-shaped magmatism and that converges radially. This pattern has been recognized in magmas that have erupted at the edge of the Colorado plateau in the last ~25 Ma, suggesting a link with convective dripping of the lower lithosphere (e.g., Roy et al., 2009; van Wijk et al., 2010). In contrast, delamination occurs asymmetrically and thus, magmatism should migrate laterally as the lithosphere detaches (Figure 6.6). This is consistent with observations from the North Island of New Zealand, where a lateral migration of surface subsidence/uplift and magmatism have been proposed to be related to lithosphere delamination (Kear, 2004; Stern et al., 2013).

Another result from the models is that both the style of removal and the pre-exiting thermal structure of the lithosphere strongly control the resulting magmatism. This may explain the diversity of magmatism observations for areas with lithosphere removal, from the absence of magmatism in cratonic regions (e.g., Elkins-Tanton, 2005) to widespread magmatism in other areas (e.g., Kay et al., 1994; Farmer et al., 2002).

Here, we compare our Rayleigh-Taylor model results with observations from the southern Puna plateau in South America. This region has a long history of magmatism with diverse compositions, including those that are inconsistent with typical subduction-related magmas (e.g., Kay and Kay, 1993; Kay et al., 1994). Ducea et al. (2013) and

Murray et al. (2015) use the Zn/Fe ratio to understand the origin the young (last 5 Myr) magmas in this region. They find that the magmatism includes both asthenospheric peridotite and lithospheric pyroxenite. During the first ~1 Myr of magmatism, the magmas are primarily sourced from lithospheric pyroxenite, and the source temperature increases from 1200°C to 1300°C (Figure 6.12). After this, the magma composition indicates an asthenospheric peridotite source with a temperature of ~1300°C. Ducea et al. (2013) suggest that the origin of magmatism and the temporal shift in composition and temperature are caused by small-scale Rayleigh-Taylor drips.
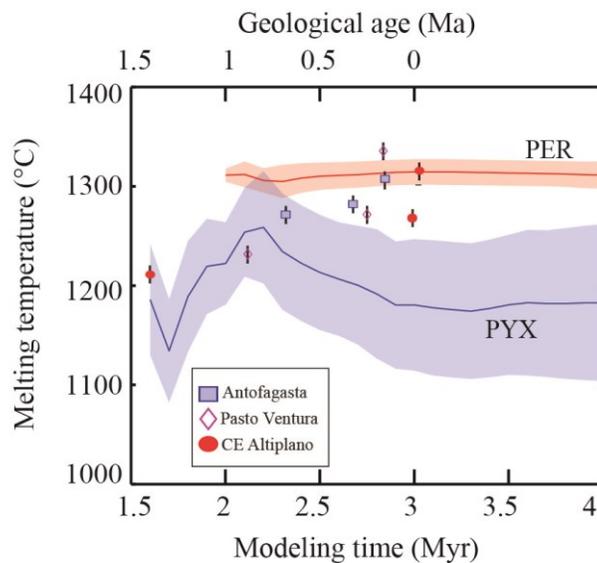
Figure 6.12. Comparison of the modeling results (solid lines and shaded areas) with the evolution of melting temperature and source composition of magmas in Puna plateau (red circles, blue squares and pink diamonds; from Ducea et al., 2013). PYX=pyroxenite, PER=peridotite.

The observations and interpretation by Ducea et al. (2013) are consistent with our Type 1 magmas, especially if the dense lithospheric pyroxenite has a relatively weak rheology (Figure 6.12). This requires that the lithosphere is initially warm. The southern Puna plateau has a relatively thick crust, but the underlying mantle lithosphere is thin (<30 km) (Babeyko et al., 2002; Schurr et al., 2006; Bianchi et al., 2012). Further, the mid-crust is inferred to be 700-800°C at 20-25 km depth (Babeyko et al., 2002 and reference therein), which indicates even higher temperatures at the Moho. It is suggested that the hot, thin lithosphere is a long-lived feature (e.g., Babeyko et al.,

2002), which pre-dates the recent foundering event. Our models show that if a warm lithosphere undergoes convective destabilization, the dense pyroxenite root will sink as small-scale drips that are conductively heated as they fall. If these melt, the average melting temperature of the pyroxenite lithosphere will increase over time (Figure 6.3c). Lithosphere removal induces passive upwelling of the asthenosphere, which may undergo decompression melting. At this point, the main magma source will change from lithosphere to asthenosphere. This sequence of events requires that the lithospheric root destabilizes in a series of small drips. We suggest that the Puna lithosphere is both relatively hot and partially hydrated due to its position above the subducting Nazca plate. As a result, the lithosphere has a relatively weak rheology, which favours smaller drip sizes. In addition, hydration decreases the solidus temperature of the foundering lithosphere, making the drips more susceptible to melting.

The southern Sierra Nevada (California) is another place where recent lithosphere removal has been proposed (e.g., Ducea and Saleeby, 1996; Saleeby et al., 2003). Pliocene magmas are found at the eastern side of southern Sierra Nevada and they appear to be derived from metasomatized asthenospheric peridotites at 40-100 km depth (Farmer et al., 2002; Elkins-Tanton and Grove, 2003). However, a xenolith study shows that the lithosphere was >100 km thick before the Pliocene and that the lithosphere was rich in garnet pyroxenites (~200 kg/m^3 denser than asthenosphere) between 40-75 km depth (Ducea and Saleeby, 1998; Ducea, 2001; Saleeby et al., 2003). The Pliocene magmatism was accompanied by significant vertical deflection of the Earth's surface, with a Pliocene uplift at the eastern side and a Pliocene-Quaternary subsidence at the western side (e.g., the subsidence of the Tulare basin) (Saleeby et al., 2012 and references therein).

Our models show lithosphere delamination is a possible explanation for observations in this region, including melting of asthenosphere right beneath crust and the asymmetric surface deflection. If this is right, the mantle lithosphere beneath the eastern side of the Sierra Nevada probably detached in the Pliocene, likely driven by the presence of the dense garnet pyroxenite root. The root itself may be a remnant of earlier arc magmatism associated with Farallon Plate subduction (e.g., Ducea, 2001). Detachment occurred at the base of the crust, and this allowed the asthenosphere to

upwell to shallow depths where it melted through decompression. The temporal variations in uplift and subsidence of the Earth's surface suggest that lithosphere detachment has migrated westward across the Sierra Nevada. Our model suggests the magmatism should also migrate along with the delamination hinge. The spatial variation of Cenozoic volcanism in the southern Sierra Nevada is not well-known (Farmer et al., 2002). But Saleeby et al., (2012 and 2013) suggest that the 0-4 Ma volcanism mainly resides in the area with Pliocene surface uplift, while the present anomalous thermal transient has the most recent rock uplift. Seismic tomography studies of this region show an eastward dipping high-velocity anomaly beneath this region, called the "Isabella anomaly" (e.g., Zandt and Carrigan, 1993; Jones et al., 1994; Saleeby et al., 2012). The high-velocity anomaly is interpreted to be the mantle lithosphere (e.g., Saleeby et al., 2012), and its geometry is consistent with lithosphere delamination. Below the Tulare Basin (western Sierra Nevada), the mantle lithosphere is still coupled to the crust; under the eastern Sierra Nevada, the mantle lithosphere is detached from the crust and is found at ~200 km depth. At the detached region, the magmas are extracted from asthenosphere first with melting depth changing from ~100 km to 40-75 km; then magmas have more silicic compositions in Quaternary (Moore and Dodge, 1980; Saleeby et al., 2012). The melting source and depth shift is consistent with the prediction of delamination model, in which the melt first extracts from the upwelling asthenosphere and later extends into the lower crust.

6.6 Conclusions

Magmatism in the interior regions of continental plates may be associated with gravitational removal of the deep lithosphere (e.g., Kay and Kay, 1993; Elkins-Tanton, 2005 and 2007). Such magmatism carries information about ancient and ongoing lithospheric removal events, but until now, there have only been a few geodynamic studies that have specifically examined the relationship between lithosphere removal and magmatism (e.g., Elkins-Tanton 2005 and 2007; Gorczyk and Vogt, 2013). Our forward numerical models investigate the possible magma sources and the pressure-temperature evolution of magmatism associated with lithosphere removal via Rayleigh-Taylor instability or delamination. Our models show that the lithosphere thermal

structure strongly affects the magmatic expression of a Rayleigh-Taylor instability. Destabilization of a hot, thin lithosphere (e.g., back arc or other tectonically-active Phanerozoic area) can induced melting of lithospheric pyroxenites through conductive heating and melting of asthenospheric peridoties through decompression. Small-scale drips (width <10 km) that grow from a weak mantle lithosphere are especially prone to melting. For a relatively cold lithosphere (e.g., relative cold Phanerozoic lithosphere), magmas are mainly extracted through decompression melting of the asthenosphere. However, when the lithosphere is cold and thick (e.g., craton lithosphere), gravitational removal is limited to the lowermost lithosphere and no magmatism can be generated. The results are also dependent on the water content of the lithosphere and asthenosphere. With hydration, the solidus temperature of each composition is reduced, and therefore, melting can occur for a greater range of thermal conditions and the melt volume will increase. Crustal melting can occur if the Rayleigh-Taylor instability results in significant thinning of the mantle lithosphere; this appears to be confined to regions with lithosphere that is warm and rheologically weak.

In delamination, the entire mantle lithosphere detaches by peeling along the Moho (Bird, 1979). This causes significant decompression melting as the asthenosphere upwells to fill the gap created by detachment. The deep crust can be rapidly heated, which may result in widespread melting. The detaching lithosphere sinks rapidly and it is unlikely to melt. In the magmatic record, delamination may be recognized by a spatial migration in magmatism, where melting followed the detachment hinge. In contrast, magmatism induced by Rayleigh-Taylor instability will be symmetric about the drip and may migrate radially toward the center as the drip detaches.

Chapter 7

Conclusions and future work

7.1 Main conclusions

The main objective of this thesis is to study the dynamics of lithosphere removal for continental plates. Many geophysical studies suggest that a significant part of lithosphere has been removed and that the base of lithosphere has a heterogeneous structure over wavelengths of 50-100 km, in places such as Wallowa Mountains, southern Sierra Nevada and Great Basin in North America, and the central Andes in South America (e.g., Hales, et al., 2005; West et al., 2009; Bianchi et al., 2012; Saleeby et al., 2012). Furthermore, present-day continental crust growth occurs primarily through magmatic basalt addition (Lee et al., 2006). Geochemistry studies show that the crustal composition is inconsistent with that of the parental basalt; the mafic compositions are "missing" in the lithosphere (e.g., Plank, 2005). Gravitational removal has been proposed to explain these observations. Mafic lithosphere (mantle lithosphere and/or lower crust) can be denser than the underlying asthenosphere, and therefore it is prone to gravitational instability, which causes it to be recycled into the deeper mantle.

Gravitational lithosphere removal will induce deformation in the mantle and crust. Observable surface effects include surface subsidence/uplift, crustal contraction/extension, and magmatism. Studying this evidence provides a window to study the dynamics of removal and the lithosphere rheology structure. This thesis examines three main topics to gain insight into the continental destabilization and thinning process:

(a) **The origin of sedimentary basins in the central Andean hinterland (Chapter 3)**: Numerous transient sedimentary basins have developed in the central Andean plateau, and their formation cannot be directly linked to regional plate tectonics (DeCelles, et al., 2015). The Arizaro basin, one example of these basins, is characterized by a localized geometry (diameter of ~100 km) and a short-lived history (subsidence followed by uplift within the last ~20 Myr) (DeCelles, et al., 2015). In addition, the lithosphere in this region is abnormally thin, which is proposed to be the result of gravitational removal (e.g., Kay and Kay, 1993; Schurr et al., 2006). In this study, numerical models were used to investigate whether such transient basins can be created through foundering of lower lithosphere. We find that formation of dense lower crust (e.g., eclogite

formed through metamorphic processes) can generate a localized basin. However, if the crust is weak, the foundering dense lower crust can induce lateral crustal flow, leading to crustal thickening and the formation of a topographic high. In order to create a topographic low, the crust must be relatively strong and resistant to lateral flow. The results demonstrate that lithosphere removal can generate localized, transient sedimentary basins that have been observed in the central Andean hinterland.

(b) **Crustal deformation and topographic expression of lithosphere removal (Chapters 4 and 5)**: The second part of this thesis considers the range of surface deflections that may be caused by lithosphere removal. Chapter 4 tests how the initial lithospheric structure and thickness affect crustal deformation and the surface deflection. The results show that with a thin crust, the dense instability (root) is strongly coupled to the overlying crust, leading to surface subsidence and basin formation. After the root detaches, the surface undergoes isostatic uplift. With a thick and weak crust, the dense lower lithosphere is decoupled from the shallow crust. Foundering of lower lithosphere causes lateral crustal flow and crustal thickening, leading to surface uplift prior to root detachment.

Chapter 5 investigates the details of crustal deformation and surface deflection induced by lithosphere removal. Using both numerical modeling and analytic analysis, it is demonstrated that a weak crustal layer (channel) may undergo lateral flow. The dense lithosphere root first depresses the overlying surface. Before the root detaches, the surface has two expressions of uplift, depending on the properties of weak crustal channel. The presence of the dense root induces a lateral pressure gradient in the crust. For a weak mid-crustal channel, this causes a Poiseuille flow in the channel, which thickens the buoyant crust and partially uplifts surface. This behavior may occur in regions where the mid-crust is felsic and relatively weak (i.e., temperatures >628°C), and where the lower crust is mafic and strong. If a weak channel is located in the lower crust, flow is induced by both the lateral pressure gradient (Poiseuille flow) and by

shearing of the base of the channel by the foundering root (Couette flow). This allows significant channel flow, such that the crust can over-thicken and a topographic high can be created. This behavior requires that the lower crust is hot (temperatures >628°C) and has a felsic/intermediate composition.

(c) **Magmatism associated with lithosphere removal (Chapter 6)**: The last part of the thesis uses numerical models to predict the relationship between lithosphere removal and magmatism. The results show that there may be three sources of magmatism: (1) melting of the foundering lithosphere as it sinks through the hot asthenosphere; (2) decompression melting of upwelling asthenosphere; and (3) melting of the residual lithosphere (mantle lithosphere and/or crust) by heating from the underlying asthenosphere. The details of melting depend on the style of lithosphere removal and the initial thermal structure of the lithosphere. For removal via Rayleigh-Taylor instability, all three sources of melting may be observed in a hot and thin lithosphere (e.g., back arcs or tectonically active regions); in a moderately warm lithosphere (e.g., average Phanerozoic lithosphere), only decompression melting of asthenosphere may occur; in a cold and thick lithosphere (e.g., craton), no magmatism can be induced. If removal occurs through delamination, the dense lithosphere peels along the Moho and sinks rapidly. In this case, only the upwelling asthenosphere may melt during removal. After delamination, the hot asthenosphere is immediately below the crust, which may induce melting of the crust.

7.2 Future work

Unlike lithospheric recycling at subduction zones, the process of lithosphere recycling in the interior of continental plates is still not well-defined. Gravitational removal of lithosphere not only causes significant deformation of the continental plate but also plays an important role in how the upper plate evolves. Below are some suggested directions for future work on lithosphere dynamics.

First, a global compilation of places with inferred lithosphere removal should be

made, in order to examine the similarities/differences and identify any patterns in their occurrence. Most studies to date have focussed on individual regions that may have lithosphere removal. The big picture of where, when and how gravitational removal occurs globally is unclear. Organizing the statistics of lithosphere removal cases could answer some fundamental geological questions, such as: does lithosphere removal favour specific tectonic provinces? Do areas with more lithosphere removal events have a more geochemically evolved lithosphere? Does lithosphere removal occur with a certain frequency or spatial dimension, and what controls this?

Second, numerical modeling results should be compared in more detail with specific geological and geophysical observations. (a) The decoupling depth (see Chapter 6) indicates the thickness of stable lithosphere root for a given lithosphere thermal structure. Thickening the lithosphere root below the decoupling depth (through surface cooling, magmatism addition etc.) may lead to gravitational instability and lithosphere removal. Therefore, lithosphere is stable above the decoupling depth, and mobile below the decoupling depth. The numerically modeled decoupling depth can be compared to observed data (such as surface topography or surface heat flow) to see how the observed lithosphere thickness correlates with continental plate stability. For example, if a region is thicker than the predicted decoupling depth, is there evidence that it is prone to instability or that it is in the process of foundering?

(b) This thesis has focussed on the crustal and magmatic expressions of lithosphere removal. However, the removal process is also expressed in other observational data sets, such as seismic velocity. Lithosphere removal disrupts the temperature and composition structure in mantle, with cold lithosphere material sinking into sublithospheric mantle and hot asthenosphere replacing the removed lithosphere. This disruption will affect the seismic velocity structure of the region. For example, tomographic studies show a high-velocity block at 100-200 km depth beneath the Puna plateau, which is interpreted to be a fragment of detached continental lithosphere (Schurr et al., 2006; Bianchi, et al., 2012). The numerical models presented in this study could be used to analyze how lithosphere removal may be expressed in seismic tomography studies. Using the methodology in the studies of van Wijk et al. (2008) and Hyndman et al. (2009), the temperature, pressure and composition of the models can be

used to calculate the seismic velocity structure at each time step. The synthetic seismic image can then be compared to observed seismic data (which represents a present-day snapshot of mantle structure), in order to assess the dimensions of the detached lithosphere, as well as the details of its detachment (e.g., time of removal and initial temperature).

(c) Under some circumstances, lithosphere removal can thicken and heat the overlying crust. Chapters 5 and 6 show that the thickness and temperature of crust can be increased by 30 km and 300°C during the removal process. The thermal perturbation in the crust should last for 30-50 Myr after lithosphere detachment. Both the thickness and temperature variations will affect the seismic velocity structure of the crust, and therefore crustal seismic data may provide clues about past removal events in a region. For example, the crust in the Puna plateau shows "bull's eye" zones of low shear wave velocity, which are interpreted to represent thermal anomalies caused by lithosphere removal (Beck et al., 2015). Synthetic crustal seismic maps can be derived from numerical models, which can then be used to constrain the scale, depth and time of lithosphere removal.

Third, the numerical models could be improved. (a) The models in this study are two-dimensional cross-sections through the Earth. An important direction is to develop full three-dimensional models. For a Rayleigh-Taylor drip, pseudo-3D models can be constructed by assuming an axisymmetric two-dimensional model domain (e.g., Elkins-Tanton, 2005; Hoogenboom and Houseman, 2006). However, delamination requires a full 3D model domain. The development of 3D models is especially important for the detailed comparison between the model predictions and geophysical observations.

(b) The role of surface processes is another important modeling direction, as sedimentation and erosion will modify surface topography. In Chapter 2, the effect of sediment deposition on the formation of hinterland basins was examined. When lithosphere removal induces surface subsidence, sedimentation will deepen the basin and cause more contraction in near-surface crust. In the future, the erosion process could also be added into numerical models. In the central Andean plateau, the erosion rate is 0.5-3 m/yr over the last 60 Myr (Pelletier et al., 2010 and references therein).

Rapid erosion will flatten the surface and decrease the elevation. However, moderate erosion will reduce the lithostatic load, induce crustal extrusion and uplift the surface during the orogen-building process (e.g., Avouac and Burov, 1996; Beaumont et al., 2004). Therefore, the surface expressions of lithosphere removal could be significantly modified by sedimentation and erosion. In addition, the surface processes may also have some feedback on the dynamics of the deeper lithosphere and underlying mantle (Pysklywec, 2006).

Lastly, the numerical models should be extended to consider the relationship between local lithosphere removal and regional tectonics. (a) The models in this study assume a static continental plate, but in some areas (e.g., the Puna plateau) lithosphere removal occurs at the same time as continental shortening. Therefore, models should be developed in which the upper plate undergoes active shortening and deformation, in order to assess how the dynamics of removal may be affected. An important consideration is the numerical implementation of shortening. In most numerical models, plate deformation is modelled using imposed velocities on the side model boundaries (including models with no shortening; the boundary velocities are assigned to have a velocity of zero). In reality, deformation is driven by forces that originate from plate tectonics. Therefore, numerical models should use constant force conditions on the side boundaries. In this way, the upper plate will deform self-consistently according to localized dynamics and regional stresses, which will make the models more compatible with nature.

(b) The effect of an underlying subducting plate should be studied in more detail. Preliminary subduction models were explored in Chapter 3. However, one thing that was not tested was temporal variations in the dip of the subducting plate (slab). Kay and Coira (2009) suggest that a flat or low-angle slab could act as a barrier to the foundering of lithosphere. Subsequent steepening of the slab may trigger lithosphere removal, leading to widespread melting and surface uplift. This may have occurred for the Sierra Nevada in the western United States (DeCelles et al., 2009; 2015). More sophisticated subduction models (including 3D models) should be used to assess how subduction and variations in slab dip affect the dynamics of the upper plate and the surface expressions of lithosphere removal.

References

Austrheim, H., 1991, Eclogite formation and dynamics of crustal roots under continental collision zones: Terra Nova, v. 3, p. 492-499, doi: 10.1111/j.1365-3121.1991.tb00184.x.

Avouac, J. P., and Burov, E. B., 1996. Erosion as a driving mechanism of intracontinental mountain growth. Journal of Geophysical Research: Solid Earth (1978–2012), 101(B8), 17747-17769.

Babeyko, A. Y., Sobolev, S. V., Trumbull, R. B., Oncken, O., and Lavier, L. L., 2002. Numerical models of crustal scale convection and partial melting beneath the Altiplano–Puna plateau, Earth and Planetary Science Letters. v. 199, p. 373-388.

Babeyko, A. Y., and Sobolev, S. V., 2005. Quantifying different modes of the late Cenozoic shortening in the central Andes, Geology, v. 33, p. 621-624.

Babeyko, A. Y., Sobolev, S. V., Vietor, T., Oncken, O., and Trumbull, R. B., 2006. Numerical study of weakening processes in the central Andean back-arc. InThe Andes (pp. 495-512). Springer Berlin Heidelberg.

Bao, X., Eaton, D. W., and Guest, B. 2014. Plateau uplift in western Canada caused by lithospheric delamination along a craton edge. Nature Geoscience,7(11), 830-833.

Beaumont, C., Jamieson, R. A., Nguyen, M. H., and Lee, B., 2001. Himalayan tectonics explained by extrusion of a low-viscosity crustal channel coupled to focused surface denudation. Nature, 414(6865), 738-742.

Beaumont, C., Jamieson, R. A., Nguyen, M. H., and Medvedev, S., 2004. Crustal channel flows: 1. Numerical models with applications to the tectonics of the Himalayan-Tibetan orogen. Journal of Geophysical Research: Solid Earth (1978–2012), 109(B6).

Beaumont, C., Nguyen, M.H., Jamieson, R.A., and Ellis, S., 2006, Crustal flow modes in large hot orogens: Geological Society, London, Special Publications, v. 268, p. 91–145, doi: 10.1144/GSL.SP.2006.268.01.05.

Beck, S. L., Zandt, G., Myers, S. C., Wallace, T. C., Silver, P. G., and Drake, L., 1996.

Crustal-thickness variations in the central Andes, Geology, v. 24, p. 407-410.

Beck S. L. and Zandt, G., 2002, Nature of orogenic crust in the central Andes, Journal Geophysical Research, v. 107, p. 2230, doi:10.1029/2000JB000124.

Beck, S. L., Zandt, G., Ward, K. M., and Scire, A., 2015. Multiple styles and scales of lithospheric foundering beneath the Puna Plateau, central Andes.Geological Society of America Memoirs, 212, MWR212-03.

Bianchi, M., Heit, B., Jakovlev, A., Yuan, X., Kay, S.M., Sandvol, E., Alonso, R.N., Coira, B., and Kind, R., 2012, Teleseismic tomography of the southern Puna plateau in Argentina and adjacent regions: Tectonophysics, v. 586, p. 65-83.

Bird, P., 1979, Continental delamination and the Colorado Plateau: Journal of Geophysical Research, v. 84, no. B13, p. 7561–7571.

Bird, P., 1991. Lateral extrusion of lower crust from under high topography in the isostatic limit. Journal of Geophysical Research: Solid Earth (1978–2012), 96(B6), 10275-10286.

Blackwell, D. D., Bowen, R. G., Hull, D. A., Riccio, J., and Steele, J. L., 1982. Heat flow, arc volcanism, and subduction in northern Oregon. Journal of Geophysical Research: Solid Earth (1978–2012), 87(B10), 8735-8754.

Blackwell, D. D., and M. Richards, 2004, Geothermal map of North America, 1 sheet, scale 1:6,500,000, Am. Assoc. Pet. Geol., Tulsa, Okla.

Bousquet, R., Goff, B., Henry, P., Le Pichon, X., and Chopin, C., 1997, Kinematic, thermal and petrological model of the Central Alps: Lepontine metamorphism in the upper crust and eclogitisation of the lower crust: Tectonophysics, v. 273, p. 105–127.

Braun, J., 2010. The many surface expressions of mantle dynamics. Nature Geoscience, 3(12), 825-833.

Burov, E. B., and Diament, M., 1992. Flexure of the continental lithosphere with multilayered rheology. Geophysical Journal International, 109(2), 449-468.

Burov, E. B., and Diament, M., 1995. The effective elastic thickness (Te) of continental lithosphere: What does it really mean?. Journal of Geophysical Research: Solid Earth (1978–2012), 100(B3), 3905-3927.

Burov, E. B., and Watts, A. B., 2006. The long-term strength of continental lithosphere:"

jelly sandwich" or" crème brûlée"?. GSA today, 16(1), 4.

Calkins, J. A., Zandt, G., Girardi, J., Dueker, K., Gehrels, G. E., and Ducea, M. N. 2010. Characterization of the crust of the Coast Mountains Batholith, British Columbia, from P to S converted seismic waves and petrologic modeling. Earth and Planetary Science Letters, 289(1), 145-155.

Canavan, R., Clementz, M., Carrapa, B., Quade, J., DeCelles, P.G., Schoenbohm, L.M., and Boyd, J., 2010, Paleoelevation of the Puna Plateau, northwestern (NW) Argentina inferred from deuterium isotopic analyses of volcanic glass: AGU Fall Meeting, Abstracts, PP13B-1525, v. 1, p. 1525.

Canavan, R., Clementz, M., Carrapa, B., Quade, J., DeCelles, P.G., and Schoenbohm, L.M, 2011. Paleoelevation of the Puna Plateau (Northwest Argentina) inferred from geochemical analyses of volcanic glass: 2011 GSA Annual Meeting in Minneapolis.

Carrapa, B., and DeCelles, P.G., Reiners, P.W., Gehrels, G.E., and Sudo, M., 2009, Apatite triple dating and white mica 40Ar/39Ar thermochronology of syntectonic detritus in the Central Andes: A multiphase tectonothermal history: Geology, v. 37, no. 5, p. 407-410, doi: 10.1130/G25698A.1.

Carrapa, B., Reyes-Bywater, S., DeCelles, P.G., Mortimer, E., and Gerhels, G., 2011, Cenozoic synorogenic basin evolution in the Eastern Cordillera of northwestern Argentina (25°-26°S): Regional implications for Andean orogenic wedge development: Basin Research, v. 23, p. 1–20, doi: 10.1111/j.1365-2117.2011.00519.x

Chapman, D. S., 1986. Thermal gradients in the continental crust. Geological Society, London, Special Publications, 24(1), 63-70.

Christensen, N.I., and Mooney, W.D., 1995, Seismic velocity structure and composition of the continental crust: A global view: Journal of Geophysical Research, v. 100, no. B6, p. 9761-9788, doi: 10.1029/95JB00259.

Chung, S. L., Liu, D., Ji, J., Chu, M. F., Lee, H. Y., Wen, D. J., ... and Zhang, Q., 2003. Adakites from continental collision zones: melting of thickened lower crust beneath southern Tibet. Geology, 31(11), 1021-1024.

Chung, S. L., Chu, M. F., Zhang, Y., Xie, Y., Lo, C. H., Lee, T. Y., ... and Wang, Y. 2005.

Tibetan tectonic evolution inferred from spatial and temporal variations in post-collisional magmatism. Earth-Science Reviews, 68(3), 173-196.

Clark, M.K., and Royden, L.H., 2000. Topographic ooze: Building the eastern margin of Tibet by lower crustal flow. Geology, 28(8): 703-706.

Conrad, C.P., and Molnar, P., 1997. The growth of Rayleigh—Taylor-type instabilities in the lithosphere for various rheological and density structures. Geophysical Journal International, 129(1): 95-112.

Conrad, C. P., and Molnar, P., 1999. Convective instability of a boundary layer with temperature-and strain-rate-dependent viscosity in terms of 'available buoyancy'. Geophysical Journal International, 139(1), 51-68.

Currie, C. A., Wang, K., Hyndman, R. D., and He, J., 2004. The thermal effects of steady-state slab-driven mantle flow above a subducting plate: the Cascadia subduction zone and backarc. Earth and Planetary Science Letters, 223(1), 35-48.

Currie, C.A., and Hyndman, R.D., 2006, The thermal structure of subduction zone back arcs: Journal of Geophysical Research, v. 111, no. B08404, doi: 10.1029/2005JB004024.

Currie, C. A., Huismans, R. S., and Beaumont, C., 2008. Thinning of continental backarc lithosphere by flow-induced gravitational instability. Earth and Planetary Science Letters, 269(3), 436-447.

Currie, C. A., and Beaumont, C., 2011. Are diamond-bearing Cretaceous kimberlites related to low-angle subduction beneath western North America?.Earth and Planetary Science Letters, 303(1), 59-70.

Darold, A., and Humphreys, E., 2013. Upper mantle seismic structure beneath the Pacific Northwest: A plume-triggered delamination origin for the Columbia River flood basalt eruptions. Earth and Planetary Science Letters, 365, 232-242.

DeCelles, P. G., Ducea, M. N., Kapp, P., and Zandt, G., 2009. Cyclicity in Cordilleran orogenic systems. Nature Geoscience, 2(4), 251-257.

DeCelles, P.G., Carrapa, B., Horton, B.K., McNabb, J, and Boyd, J., 2011. Cordilleran hinterland basins as recorders of lithospheric removal in the Central Andes: AGU Fall Meeting, Abstracts T13I-06, v. 1, p. 06.

DeCelles, P. G., Carrapa, B., Horton, B. K., McNabb, J., Gehrels, G. E., and Boyd, J. , 2015. The Miocene Arizaro Basin, central Andean hinterland: Response to partial lithosphere removal?. Geological Society of America Memoirs, 212, 359-386.

Delft Gravity Model, release 1, Satellite-only (DGM-1S): http://www.citg.tudelft.nl/index.php?id=52752 (April 2013).

Djomani, Y. H. P., O'Reilly, S. Y., Griffin, W. L., and Morgan, P., 2001. The density structure of subcontinental lithosphere through time. Earth and Planetary Science Letters, 184(3), 605-621.

Downey, N.J., and Gurnis, M., 2009. Instantaneous dynamics of the cratonic Congo basin. Journal of Geophysical Research: Solid Earth (1978–2012), 114(B6).

Ducea, M. N., and Saleeby, J. B., 1996. Buoyancy sources for a large, unrooted mountain range, the Sierra Nevada, California: Evidence from xenolith thermobarometry. Journal of Geophysical Research: Solid Earth (1978–2012),101(B4), 8229-8244.

Ducea, M., and Saleeby, J., 1998. A case for delamination of the deep batholithic crust beneath the Sierra Nevada, California. International Geology Review, 40(1), 78-93.

Ducea, M., 2001. The California arc: Thick granitic batholiths, eclogitic residues, lithospheric-scale thrusting, and magmatic flare-ups. GSA today, 11(11): 4-10.

Ducea, M.N., 2002, Constraints on the bulk composition and root foundering rates of continental arcs: A California arc perspective: Journal of Geophysical Research, v. 107, no. B11, 2304, doi: 10.1029/2001JB000643.

Ducea, M.N., and Barton, M.D., 2007, Igniting flare-up events in Cordilleran arcs: Geology, v. 35, no. 11, p. 1047-1050, doi: 10.1130/G23898A.1.

Ducea, M. N., 2011. Fingerprinting orogenic delamination. Geology, 39(2), 191-192.

Ducea, M. N., Seclaman, A. C., Murray, K. E., Jianu, D. and Schoenbohm, L. M., 2013, Mantle-drip magmatism beneath the Altiplano-Puna plateau, central Andes, Geology, publish on line June 20, 2013, doi: 10.1130/G34509.1.

Elkins‑Tanton, L. T., and Hager, B. H. 2000. Melt intrusion as a trigger for lithospheric foundering and the eruption of the Siberian flood

basalts.Geophysical Research Letters, 27(23), 3937-3940.

Elkins‑Tanton, L. T., and Grove, T. L., 2003. Evidence for deep melting of hydrous metasomatized mantle: Pliocene high‑potassium magmas from the Sierra Nevadas. Journal of Geophysical Research: Solid Earth (1978–2012),108(B7).

Elkins-Tanton, L. T., 2005. Continental magmatism caused by lithospheric delamination. Geological Society of America Special Papers, 388, 449-461.

Elkins-Tanton, L. T., 2007. Continental magmatism, volatile recycling, and a heterogeneous mantle caused by lithospheric gravitational instabilities, Journal of Geophysical Research: Solid Earth, v. 112, B03405, doi:10.1029/2005JB004072.

Farmer, G. L., Glazner, A. F., and Manley, C. R., 2002. Did lithospheric delamination trigger late Cenozoic potassic volcanism in the southern Sierra Nevada, California?. Geological Society of America Bulletin, 114(6), 754-768.

Fay, N. P., Bennett, R. A., and Hreinsdóttir, S., 2008. Contemporary vertical velocity of the central Basin and Range and uplift of the southern Sierra Nevada. Geophysical Research Letters, 35(20).

Flament, N., Gurnis, M., and Müller, R. D., 2013. A review of observations and models of dynamic topography. Lithosphere, 5(2), 189-210.

Fowler, C. M. R., and Nisbet, E. G., 1985. The subsidence of the Williston Basin. Canadian Journal of Earth Sciences, 22(3), 408-415.

Fullsack, P., 1995, Arbitrary Lagrangian-Eulerian formulation for creeping flows and its application in tectonic models: Geophysical Journal International, v. 120, no. 1, p. 1-23.

Gao, S., Luo, T. C., Zhang, B. R., Zhang, H. F., Han, Y. W., Zhao, Z. D., and Hu, Y. K., 1998. Chemical composition of the continental crust as revealed by studies in East China. Geochimica et Cosmochimica Acta, 62(11), 1959-1975.

Gao, S., Rudnick, R. L., Yuan, H. L., Liu, X. M., Liu, Y. S., Xu, W. L., Ling, W., Ayers, J., Wang, X., and Wang, Q. H., 2004. Recycling lower continental crust in the North China craton. Nature, 432(7019), 892-897.

Gao, S., Rudnick, R. L., Xu, W. L., Yuan, H. L., Liu, Y. S., Walker, R. J., ... and Yang, J., 2008. Recycling deep cratonic lithosphere and generation of intraplate

magmatism in the North China Craton. Earth and Planetary Science Letters, 270(1), 41-53.

Garzione, C.N., Molnar, P., Libarkin, J.C., and MacFadden, B.J., 2006, Rapid late Miocene rise of the Bolivian Altiplano: evidence for removal of mantle lithosphere. Earth and Planetary Science Letters, v. 241, p. 543–556.

Gerbault, M., Martinod, J., and Hérail, G., 2005. Possible orogeny-parallel lower crustal flow and thickening in the Central Andes. Tectonophysics, 399(1), 59-72.

Gemmer, L., and Houseman, G. A. 2007. Convergence and extension driven by lithospheric gravitational instability: evolution of the Alpine–Carpathian–Pannonian system. Geophysical Journal International, 168(3), 1276-1290.

Gleason, G.C., and Tullis, J., 1995, A flow law for dislocation creep of quartz aggregates determined with the molten salt cell: Tectonophysics, v. 247, no. 1, p. 1-23, doi: 10.1016/0040-1951(95)00011-B.

Gök, R., Pasyanos, M. E., and Zor, E. 2007. Lithospheric structure of the continent—continent collision zone: eastern Turkey. Geophysical Journal International, 169(3), 1079-1088.

Göğüş, O.H., and Pysklywec, R.N., 2008, Near-surface diagnostics of dripping or delaminating lithosphere: Journal of Geophysical Research, v. 113, no. B11404, doi: 10.1029/2007JB005123.

Gorczyk, W., Hobbs, B., and Gerya, T. 2012. Initiation of Rayleigh–Taylor instabilities in intra-cratonic settings. Tectonophysics, 514, 146-155.

Gorczyk, W., and Vogt, K., 2013. Tectonics and melting in intra-continental settings. Gondwana Research.

Götze, H.J., and Krause, S., 2002, The Central Andean gravity high, a relic of an old subduction complex ?: Journal of South American Earth Sciences, v. 14, p. 799–811, doi: 10.1016/S0895-9811(01)00077-3.

Gutiérrez-Alonso, G., Murphy, J. B., Fernández-Suárez, J., Weil, A. B., Franco, M. P., and Gonzalo, J. C. 2011. Lithospheric delamination in the core of Pangea: Sm-Nd insights from the Iberian mantle. Geology, 39(2), 155-158.

Hacker, B. R., Abers, G. A., and Peacock, S. M., 2003. Subduction factory 1. Theoretical mineralogy, densities, seismic wave speeds, and H2O

contents.Journal of Geophysical Research: Solid Earth (1978–2012), 108(B1).

Hales, T.C., Abt, D.L., Humphreys, E.D., and Roering, J.J., 2005. A lithospheric instability origin for Columbia River flood basalts and Wallowa Mountains uplift in northeast Oregon. Nature, 438(7069): 842-845.

Hajnal, Z., Fowler, C. M. R., Mereu, R. F., Kanasewich, E. R., Cumming, G. L., Green, A. G., and Mair, A., 1984. An initial analysis of the Earth's crust under the Williston Basin: 979 Cocrust Experiment. Journal of Geophysical Research: Solid Earth (1978–2012), 89(B11), 9381-9400.

Heit, B., Koulakov, I., Asch, G., Yuan, X., Kind, R., Alcozer, I., Tawackoli, S. and Wilke, H., 2008, More constraints to determine the seismic structure beneath the Central Andes at 21°S using teleseismic tomography analysis, Journal of South American Earth Science, v. 25, p. 22–36.

Heit, B., Bianchi, M., Yuan, X., Kay, S. M., Sandvol, E., Kumar, P., ... and Comte, D., 2014. Structure of the crust and the lithosphere beneath the southern Puna plateau from teleseismic receiver functions. Earth and Planetary Science Letters, 385, 1-11.

Heidlauf, D. T., Hsui, A. T., and Klein, G. D. 1986. Tectonic subsidence analysis of the Illinois Basin. The Journal of Geology, 779-794.

Hirschmann, M. M., and Stolper, E. M., 1996. A possible role for garnet pyroxenite in the origin of the "garnet signature" in MORB. Contributions to Mineralogy and Petrology, 124(2), 185-208.

Hirth, G., and Kohlstedt, D. L., 1996. Water in the oceanic upper mantle: implications for rheology, melt extraction and the evolution of the lithosphere.Earth and Planetary Science Letters, 144(1), 93-108.

Hirth, G., and Kohlstedt, D., 2003. Rheology of the upper mantle and the mantle wedge: A view from the experimentalists. Inside the subduction Factory, 83-105.

Hoke, L., and Lamb, S., 2007. Cenozoic behind-arc volcanism in the Bolivian Andes, South America: implications for mantle melt generation and lithospheric structure. Journal of the Geological Society, 164(4), 795-814.

Hoke, G. D., and Garzione, C. N., 2008. Paleosurfaces, paleoelevation, and the mechanisms for the late Miocene topographic development of the Altiplano

plateau, Earth and Planetary Science Letters, v. 271, p. 192-201.

Hoogenboom, T., and Houseman, G. A., 2006. Rayleigh–Taylor instability as a mechanism for corona formation on Venus. Icarus, 180(2), 292-307.

Horodyskyj, U. N., Lee, C. T. A., and Ducea, M. N., 2007. Similarities between Archean high MgO eclogites and Phanerozoic arc-eclogite cumulates and the role of arcs in Archean continent formation. Earth and Planetary Science Letters, 256(3), 510-520.

Horton, B.K., 2012, Cenozoic evolution of hinterland basins in the Andes and Tibet, in Busby, C.J., and Azor, A., eds., Tectonics of Sedimentary Basins: Recent Advances, First Edition, Blackwell Publishing Ltd., p. 427-444.

Houseman, G. A., McKenzie, D. P., and Molnar, P., 1981. Convective instability of a thickened boundary layer and its relevance for the thermal evolution of continental convergent belts. Journal of Geophysical Research: Solid Earth (1978–2012), 86(B7), 6115-6132.

Houseman, G.A., and Molnar, P., 1997, Gravitational (Rayleigh-Taylor) instability of a layer with non-linear viscosity and convective thinning of continental lithosphere: Geophysical Journal International, v. 128, no. 1, p. 125-150, doi: 10.1111/j.1365-246X.1997.tb04075.x.

Houseman, G., and Molnar, P., 2001. Mechanisms of lithospheric rejuvenation associated with continental orogeny. Geological Society, London, Special Publications, 184(1), 13-38.

Huismans, R.S., and Beaumont, C., 2002, Asymmetric lithospheric extension: The role of frictional plastic strain softening inferred from numerical experiments: Geology, v. 30, no. 3, p. 211-214.

Huismans, R.S., and Beaumont, C., 2003, Symmetric and asymmetric lithospheric extension: Relative effects of frictional-plastic and viscous strain softening: Journal of Geophysical Research, v. 108, no. B10, 2496, doi: 10.1029/2002JB002026.

Hyndman, R. D., Currie, C. A., Mazzotti, S., and Frederiksen, A., 2009. Temperature control of continental lithosphere elastic thickness, Te vs Vs. Earth and Planetary Science Letters, 277(3), 539-548.

Jackson, J. A., Austrheim, H., McKenzie, D., and Priestley, K., 2004, Metastability, mechanical strength, and the support of mountain belts: Geology, v. 32, no. 7, p. 625-628, doi: 10.1130/G20397.1.

Jagoutz, O., and Behn, M. D., 2013. Foundering of lower island-arc crust as an explanation for the origin of the continental Moho. Nature, 504(7478), 131-134.

Jaupart, C., and Mareschal, J. C., 1999. The thermal structure and thickness of continental roots. Developments in Geotectonics, 24, 93-114.

Jin, Z.M., Zhang, J., Green, H.W., and Jin, S., 2001, Eclogite rheology: implications for subducted lithosphere: Geology, v. 29, no. 8, p. 667-670.

Jones, C. H., Kanamori, H., and Roecker, S. W., 1994. Missing roots and mantle "drips": Regional Pn and teleseismic arrival times in the southern Sierra Nevada and vicinity, California. Journal of Geophysical Research: Solid Earth (1978–2012), 99(B3), 4567-4601.

Jordan, T.E., Mpodozis, C., Munoz, N., Blanco, N, Pananont, P., and Gardeweg, M., 2007, Cenozoic subsurface stratigraphy and structure of the Salar de Atacama Basin, northern Chile: Journal of South American Earth Sciences, v. 23, p. 122-146.

Jull, M., and Kelemen, P.B., 2001, On the conditions for lower crustal convective instability: Journal of Geophysical Research, v. 106, no. B4, p. 6423–6446.

Karato, S.I., and Wu, P., 1993, Rheology of the upper mantle: a synthesis: Science, v. 260, no. 5109, p. 771-778.

Katz, R. F., Spiegelman, M., and Langmuir, C. H., 2003. A new parameterization of hydrous mantle melting. Geochemistry, Geophysics, Geosystems, 4(9).

Kay, R.W., and Kay, S.M., 1993, Delamination and delamination magmatism: Tectonophysics, v. 219, p. 177-189.

Kay, S. M., Coira, B., and Viramonte, J., 1994, Young mafic back-arc volcanic rocks as indicators of continental lithospheric delamination beneath the Argentine Puna Plateau, Central Andes, Journal of Geophysical Research, v. 99, p. 24,323–24,339, doi: 10.1029/94JB00896.

Kay, S.M., and Coira, B.L., 2009, Shallowing and steepening subduction zones, continental lithospheric loss, magmatism, and crustal flow under the Central

Andean Altiplano–Puna Plateau: Geological of America Memoir, v. 204, no. 11, p. 229-260, doi: 10.1130/2009.1204(11).

Kear, D., 2004. Reassessment of Neogene tectonism and volcanism in North Island, New Zealand. New Zealand Journal of Geology and Geophysics, 47(3), 361-374.

Kohlstedt, D. L., Evans, B., and Mackwell, S. J., 1995. Strength of the lithosphere: Constraints imposed by laboratory experiments. Journal of Geophysical Research: Solid Earth (1978–2012), 100(B9), 17587-17602.

Kreemer, C., Holt, W. E., and Haines, A. J., 2003. An integrated global model of present-day plate motions and plate boundary deformation. Geophysical Journal International, 154(1), 8-34.

Kruse, S., McNutt, M., Phipps-Morgan, J., Royden, L., and Wernicke, B., 1991. Lithospheric extension near Lake Mead, Nevada: A model for ductile flow in the lower crust. Journal of geophysical Research, 96(B3): 4435-4456.

Krystopowicz, N. J., and Currie, C. A., 2013. Crustal eclogitization and lithosphere delamination in orogens. Earth and Planetary Science Letters, 361, 195-207.

Kusznir, N. J., and Park, R. G., 1984. Intraplate lithosphere deformation and the strength of the lithosphere. Geophysical Journal International, 79(2), 513-538.

Krystopowicz, N. J., and Currie, C. A., 2013. Crustal eclogitization and lithosphere delamination in orogens. Earth and Planetary Science Letters, 361, 195-207.

Lambart, S., Laporte, D., and Schiano, P., 2009. An experimental study of pyroxenite partial melts at 1 and 1.5 GPa: Implications for the major-element composition of Mid-Ocean Ridge Basalts. Earth and Planetary Science Letters,288(1), 335-347.

Lee, C. T. A., Cheng, X., and Horodyskyj, U., 2006. The development and refinement of continental arcs by primary basaltic magmatism, garnet pyroxenite accumulation, basaltic recharge and delamination: insights from the Sierra Nevada, California. Contributions to Mineralogy and Petrology, 151(2), 222-242.

Lee, C. T. A., Luffi, P., Plank, T., Dalton, H., and Leeman, W. P., 2009. Constraints on the depths and temperatures of basaltic magma generation on Earth and other

terrestrial planets using new thermobarometers for mafic magmas. Earth and Planetary Science Letters, 279(1), 20-33.

Lee, C. T. A., Luffi, P., and Chin, E. J., 2011. Building and destroying continental mantle. Annual Review of Earth and Planetary Sciences, 39, 59-90.

Leech, M.L., 2001, Arrested orogenic development: eclogitization, delamination, and tectonic collapse: Earth and Planetary Science Letters, v. 185, no. 1, p. 149-159, doi: 10.1016/S0012-821X(00)00374-5.

Leier, A., McQuarrie, N., Garzione, C., and Eiler, J., 2013. Stable isotope evidence for multiple pulses of rapid surface uplift in the Central Andes, Bolivia, Earth and Planetary Science Letters, v. 371, p. 49-58.

Li, S., Unsworth, M. J., Booker, J. R., Wei, W., Tan, H., and Jones, A. G., 2003. Partial melt or aqueous fluid in the mid-crust of Southern Tibet? Constraints from INDEPTH magnetotelluric data. Geophysical Journal International, 153(2), 289-304.

Lindsay, J. M., Schmitt, A. K., Trumbull, R. B., De Silva, S. L., Siebel, W., and Emmermann, R., 2001. Magmatic evolution of the La Pacana caldera system, Central Andes, Chile: compositional variation of two cogenetic, large-volume felsic ignimbrites. Journal of Petrology, 42(3), 459-486.

Mackwell, S.J., Zimmerman, M.E., and Kohlstedt, D.L., 1998, High-temperature deformation of dry diabase with application to tectonics on Venus: Journal of Geophysical Research, v. 103, no. B1, p. 975-984.

Makovsky, Y., Klemperer, S. L., Huang, L., and Lu, D., 1996. Structural elements of the southern Tethyan Himalaya crust from wide‐angle seismic data. Tectonics, 15(5), 997-1005.

Manley, C. R., Glazner, A. F., and Farmer, G. L., 2000. Timing of volcanism in the Sierra Nevada of California: Evidence for Pliocene delamination of the batholithic root?. Geology, 28(9), 811-814.

Manthei, C. D., Ducea, M. N., Girardi, J. D., Patchett, P. J., and Gehrels, G. E., 2010. Isotopic and geochemical evidence for a recent transition in mantle chemistry beneath the western Canadian Cordillera. Journal of Geophysical Research: Solid Earth (1978–2012), 115(B2).

Mazzotti, S., and Hyndman, R. D., 2002. Yakutat collision and strain transfer across the northern Canadian Cordillera. Geology, 30(6), 495-498.

McKenzie, D., 1977. Surface deformation, gravity anomalies and convection.Geophysical Journal International, 48(2), 211-238.

Middleton, M. F. 1989. A model for the formation of intracratonic sag basins.Geophysical Journal International, 99(3), 665-676.

Molnar, P., Houseman, G.A., and Conrad, C.P., 1998, Rayleigh-Taylor instability and convective thinning of mechanically thickened lithosphere: effects of non-linear viscosity decreasing exponentially with depth and of horizontal shortening of the layer: Geophysical Journal International. v. 133, no. 3, p. 568-584.

Molnar, P., and Houseman, G.A., 2004, The effects of buoyant crust on the gravitational instability of thickened mantle lithosphere at zones of intracontinental convergence: Geophysical Journal International, v. 158, no. 3, p. 1134-1150, doi: 10.1111/j.1365-246X.2004.02312.x.

Molnar, P., and Garzione, C. N., 2007. Bounds on the viscosity coefficient of continental lithosphere from removal of mantle lithosphere beneath the Altiplano and Eastern Cordillera. Tectonics, 26(2).

Molnar, P., and Houseman, G.A., 2013. Rayleigh‐Taylor instability, lithospheric dynamics, surface topography at convergent mountain belts, and gravity anomalies. Journal of Geophysical Research: Solid Earth, 118(5): 2544-2557.

Mooney, W.D., and Kaban, M.K., 2010, The North American upper mantle: Density, composition, and evolution: Journal of Geophysical Research, v. 115, B12424, doi: 10.1029/2010JB000866.

Moore, J. G., and Dodge, F. C., 1980. Late Cenozoic volcanic rocks of the southern Sierra Nevada, California: I. Geology and petrology: Summary.Geological Society of America Bulletin, 91(9), 515-518.

Murray, K. E., Ducea, M. N., and Schoenbohm, L., 2015. Foundering-driven lithospheric melting: The source of central Andean mafic lavas on the Puna Plateau (22° S–27° S). Geological Society of America Memoirs, 212, 139-166.

Myers, S., Beck, S., Zandt, G., and Wallace, T., 1998, Lithospheric-scale structure across the Bolivian Andes from tomographic images of velocity and attenuation

for P and S waves, Journal of Geophysical Research, v. 103, p. 21,233–21,252.

Naimark, B.M., and Ismail‑Zadeh, A.T., 1995. Numerical models of a subsidence mechanism in intracratonic basins: Application to North American basins. Geophysical Journal International, 123(1): 149-160.

Nair, R., and Chacko, T., 2008. Role of oceanic plateaus in the initiation of subduction and origin of continental crust. Geology, 36(7), 583-586.

Neil, E.A., and Houseman, G.A., 1999, Rayleigh-Taylor instability of the upper mantle and its role in intraplate orogeny: Geophysical Journal International, v. 138, no. 1, p. 89-107, doi: 10.1046/j.1365-246x.1999.00841.x.

Nelson, K. D., Zhao, W., Brown, L. D., Kuo, J., Che, J., Liu, X., ... and Edwards, M., 1996. Partially molten middle crust beneath southern Tibet: synthesis of project INDEPTH results. Science, 274(5293), 1684-1688.

Oncken, O., Hindle, D., Kley, J., Elger, K., Victor, P., and Schemmann, K., 2006, Deformation of the central Andean upper plate system: Facts, fiction and constraints for plateau models, in Oncken, O., et al., eds., The Andes: Active Subduction Orogeny: Berlin, Springer-Verlag, Frontiers in Earth Sciences, v. 1, p. 3-28.

Paterson, M.S., and Wong, T.F., 2005, Experimental rock deformation - The brittle field, 2nd edition: Berlin, Springer, 348 p.

Pelletier, J. D., DeCelles, P. G., and Zandt, G., 2010. Relationships among climate, erosion, topography, and delamination in the Andes: A numerical modeling investigation. Geology, 38(3), 259-262.

Pertermann, M., and Hirschmann, M. M., 2003. Partial melting experiments on a MORB-like pyroxenite between 2 and 3 GPa: Constraints on the presence of pyroxenite in basalt source regions from solidus location and melting rate.Journal of Geophysical Research: Solid Earth (1978–2012), 108(B2).

Plank, T., 2005. Constraints from thorium/lanthanum on sediment recycling at subduction zones and the evolution of the continents. Journal of Petrology,46(5), 921-944.

Pysklywec, R. N., and Shahnas, M. H., 2003. Time-dependent surface topography in a coupled crust–mantle convection model. Geophysical Journal

International, 154(2), 268-278.

Pysklywec, R.N., and Beaumont, C., 2004, Intraplate tectonics: feedback between radioactive thermal weakening and crustal deformation driven by mantle lithosphere instabilities: Earth and Planetary Science Letters, v. 221, no. 1, p. 275-292, doi: 10.1016/S0012-821X(04)00098-6.

Pysklywec, R. N., 2006. Surface erosion control on the evolution of the deep lithosphere. Geology, 34(4), 225-228.

Quade, J., M. P. Dettinger, B. Carrapa, P. DeCelles, K. E. Murray, K. W. Huntington, A. Cartwright, R. R. Canavan, G. Gehrels, and M. Clementz. The growth of the central Andes, 22° S–26° S. Geological Society of America Memoirs 212 (2014): MWR212-15

Raimondo, T., Hand, M., and Collins, W. J., 2014. Compressional intracontinental orogens: Ancient and modern perspectives. Earth-Science Reviews, 130, 128-153.

Ranalli, G., and Murphy, D. C., 1987. Rheological stratification of the lithosphere.Tectonophysics, 132(4), 281-295.

Ranalli, G., 1995. Rheology of the Earth. Springer.

Rapp, R. P., and Watson, E. B., 1995. Dehydration melting of metabasalt at 8–32 kbar: implications for continental growth and crust-mantle recycling. Journal of Petrology, 36(4), 891-931.

Richards, J.P., 2003, Tectono-magmatic precursors for porphyry Cu-(Mo-Au) deposit formation: Economic Geology, v. 98, no. 8, p. 1515-1533.

Rippe, D., and Unsworth, M., 2010. Quantifying crustal flow in Tibet with magnetotelluric data. Physics of the Earth and Planetary Interiors, 179(3), 107-121.

Rosenberg, C. L., and Handy, M. R., 2005. Experimental deformation of partially melted granite revisited: implications for the continental crust. Journal of metamorphic Geology, 23(1), 19-28.

Roy, M., Jordan, T. H., and Pederson, J., 2009. Colorado Plateau magmatism and uplift by warming of heterogeneous lithosphere. Nature, 459(7249), 978-982.

Royden, L. H., Burchfiel, B. C., King, R. W., Wang, E., Chen, Z., Shen, F., and Liu, Y.,

1997. Surface deformation and lower crustal flow in eastern Tibet.science, 276(5313), 788-790.

Rudnick, R. L., and Fountain, D. M., 1995. Nature and composition of the continental crust: a lower crustal perspective. Reviews of Geophysics, 33(3), 267-309.

Saleeby, J., Ducea, M.N., and Clemens-Knott, D., 2003, Production and loss of high-density batholithic root, southern Sierra Nevada, California: Tectonics, v. 22, no. 6, 1064, doi: 10.1029/2002TC001374.

Saleeby, J., Le Pourhiet, L., Saleeby, Z., and Gurnis, M., 2012. Epeirogenic transients related to mantle lithosphere removal in the southern Sierra Nevada region, California, part I: Implications of thermomechanical modeling.Geosphere, 8(6), 1286-1309.

Saleeby, J., Saleeby, Z., and Le Pourhiet, L., 2013. Epeirogenic transients related to mantle lithosphere removal in the southern Sierra Nevada region, California: Part II. Implications of rock uplift and basin subsidence relations.Geosphere, 9(3), 394-425.

Salmon, M. L., Stern, T. A., and Savage, M. K., 2011. A major step in the continental Moho and its geodynamic consequences: the Taranaki-Ruapehu line, New Zealand. Geophysical Journal International, 186(1), 32-44.

Sandiford, M., and Hand, M. 1998. Controls on the locus of intraplate deformation in central Australia. Earth and Planetary Science Letters, 162(1), 97-110.

Schilling, F. R., Trumbull, R. B., Brasse, H., Haberland, C., Asch, G., Bruhn, D., ... and Vietor, T., 2006. Partial melting in the Central Andean crust: a review of geophysical, petrophysical, and petrologic evidence. In The Andes (pp. 459-474). Springer Berlin Heidelberg.

Schoenbohm, L.M., and Carrapa, B., 2011, Evidence from the timing of contraction, extension, sedimentation and magmatism for small-scale lithospheric foundering in the Puna Plateau, NW Argentina: AGU Fall Meeting, Abstracts, T13I-07, v. 1, p. 07.

Schoenbohm, L. M., and Carrapa, B., 2014. Miocene–Pliocene shortening, extension, and mafic magmatism support small-scale lithospheric foundering in the central Andes, NW Argentinae. Geological Society of America Memoirs,212,

MWR212-09.

Schurr, B., Rietbrock, A., Asch, G., Kind, R., and Oncken, O., 2006, Evidence for lithospheric detachment in the central Andes from local earthquake tomography: Tectonophysics, v. 415, no. 1, p. 203-223, doi: 10.1016/j.tecto.2005.12.007.

Sine, C. R., Wilson, D., Gao, W., Grand, S. P., Aster, R., Ni, J., and Baldridge, W. S., 2008. Mantle structure beneath the western edge of the Colorado Plateau. Geophysical Research Letters, 35(10).

Springer, M., and Förster, A., 1998. Heat-flow density across the Central Andean subduction zone, Tectonophysics, v. 291, p. 123-139.

Springer, M., 1999. Interpretation of heat-flow density in the Central Andes.Tectonophysics, 306(3), 377-395.

Sobel, E. R., and Arnaud, N. 2000. Cretaceous–Paleogene basaltic rocks of the Tuyon basin, NW China and the Kyrgyz Tian Shan: the trace of a small plume.Lithos, 50(1), 191-215.

Stern, T., Molnar, P., Okaya, D., and Eberhart‐Phillips, D., 2000. Teleseismic P wave delays and modes of shortening the mantle lithosphere beneath South Island, New Zealand. Journal of Geophysical Research: Solid Earth (1978–2012), 105(B9), 21615-21631.

Stern, T. A., Stratford, W. R., and Salmon, M. L., 2006. Subduction evolution and mantle dynamics at a continental margin: Central North Island, New Zealand.Reviews of Geophysics, 44(4).

Stern, T., Houseman, G., Salmon, M., and Evans, L., 2013. Instability of a lithospheric step beneath western North Island, New Zealand. Geology, 41(4), 423-426.

Thurner, S., Palomeras, I., Levander, A., Carbonell, R., and Lee, C. T., 2014. Ongoing lithospheric removal in the western Mediterranean: Evidence from Ps receiver functions and thermobarometry of Neogene basalts (PICASSO project). Geochemistry, Geophysics, Geosystems, 15(4), 1113-1127.

Trumbull, R.B., Riller, U., Oncken, O., Schueber, E., Munier, K., and Hongn, F., 2006, The time-space distribution of Cenozoic arc volcanism in the Central Andes: A new data compilation and some tectonic considerations, in Oncken, O., et al., eds., The Andes: Active Subduction Orogeny: Berlin, Springer-Verlag, Frontiers

in Earth Sciences, v. 1, p. 29-44.

Turcotte, D. L., and Schubert, G., 2002. Geodynamics. Cambridge University Press.

Turner, S., Hawkesworth, C., Liu, J., Rogers, N., Kelley, S., and van Calsteren, P., 1993. Timing of Tibetan uplift constrained by analysis of volcanic rocks. Nature, 364(6432), 50-54.

Turner, S., Arnaud, N., Liu, J., Rogers, N., Hawkesworth, C., Harris, N., Kelley, S., Van Calsteren, P., and Deng, W., 1996. Post-collision, shoshonitic volcanism on the Tibetan Plateau: implications for convective thinning of the lithosphere and the source of ocean island basalts. Journal of Petrology, 37(1): 45-71.

Tsumura, N., Ikawa, H., Ikawa, T., Shinohara, M., Ito, T., Arita, K., ... and Ikawa, T. 1999. Delamination☐wedge structure beneath the Hidaka Collision Zone, central Hokkaido, Japan inferred from seismic reflection profiling. Geophysical Research Letters, 26(8), 1057-1060.

Van Wijk, J., Van Hunen, J., and Goes, S., 2008. Small-scale convection during continental rifting: Evidence from the Rio Grande rift. Geology, 36(7), 575-578.

Van Wijk, J. W., Baldridge, W. S., Van Hunen, J., Goes, S., Aster, R., Coblentz, D. D., Grand, S. P., and Ni, J., 2010. Small-scale convection at the edge of the Colorado Plateau: Implications for topography, magmatism, and evolution of Proterozoic lithosphere. Geology, 38(7), 611-614.

Wang, C.Y., Han, W.B., Wu, J.P., Lou, H., and Chan, W.W., 2007. Crustal structure beneath the eastern margin of the Tibetan Plateau and its tectonic implications. Journal of Geophysical Research: Solid Earth (1978–2012), 112(B7).

Wang, H., Currie, C. A., and Zhan, Y., 2014. Surface Expressions of Rayleigh‐Taylor Instability in Continental Interiors. Acta Geologica Sinica (English Edition), 88(3), 1004-1016.

Wang, H., Currie, C. A., and DeCelles, P. G., 2015. Hinterland basin formation and gravitational instabilities in the central Andes: Constraints from gravity data and geodynamic models. Geological Society of America Memoirs, 212, 387-406.

Warren, C.J., Beaumont, C., and Jamieson, R.A., 2008, Deep subduction and rapid exhumation: Role of crustal strength and strain weakening in continental subduction and ultrahigh-pressure rock exhumation: Tectonics, v. 27, no. 6,

TC6002, doi: 10.1029/2008TC002292.

West, J. D., Fouch, M. J., Roth, J. B., and Elkins-Tanton, L. T., 2009. Vertical mantle flow associated with a lithospheric drip beneath the Great Basin. Nature Geoscience, 2(6), 439-444.

Whitman, D., 1999, The isostatic residual gravity anomaly of the Central Andes, 12° to 29° S: A guide to interpreting crustal structure and deeper lithospheric processes: International Geology Review, v. 41, no. 5, p. 457-475, doi: 10.1080/00206819909465152.

Willett, S.D., 1999, Rheological dependence of extension in wedge models of convergent orogens: Tectonophysics, v. 305, no. 4, p. 419-435.

Yuan, X., Sobolev, S.V., and Kind, R., 2002, Moho topography in the central Andes and its geodynamic implications: Earth and Planetary Science Letters, v. 199, no. 3, p. 389-402, doi: 10.1016/S0012-821X(02)00589-7.

Zandt, G., and Carrigan, C. R., 1993. Small-scale convective instability and upper mantle viscosity under California. Science, 261(5120), 460-463.

Zandt, G., 2003. The southern Sierra Nevada drip and the mantle wind direction beneath the southwestern United States. International Geology Review, 45(3), 213-224.

Zandt, G., Gilbert, H., Owens, T. J., Ducea, M., Saleeby, J., and Jones, C. H., 2004. Active foundering of a continental arc root beneath the southern Sierra Nevada in California, Nature, v. 431, p. 41-46.

Zhang, J., and Green, H.W., 2007. Experimental investigation of eclogite rheology and its fabrics at high temperature and pressure: Journal of Metamorphic Geology, v. 25, p. 97-115.

Zhao, G., Unsworth, M.J., Zhan, Y., Wang, L., Chen, X., Jones, A.G., Tang, J., Xiao, Q., Wang, J., Cai, J., Li, T., Wang, Y., and Zhang, J., 2012. Crustal structure and rheology of the Longmenshan and Wenchuan Mw 7.9 earthquake epicentral area from magnetotelluric data. Geology, 40(12): 1139-1142.